THE UNIVERSITY OF CHICAGO

HYBRID QUANTUM SYSTEMS OF NITROGEN-VACANCY CENTERS IN DIAMOND COUPLED TO MAGNETIC INSULATOR MATERIALS

A DISSERTATION SUBMITTED TO
THE FACULTY OF THE PRITZKER SCHOOL OF MOLECULAR ENGINEERING
IN CANDIDACY FOR THE DEGREE OF
DOCTOR OF PHILOSOPHY

BY
MASAYA FUKAMI

CHICAGO, ILLINOIS
JUNE 2022

For SS

Table of Contents

List of Figures

This dissertation represents the motivations and findings in the following works:

[1] Surface-magnon mediated self interaction of spin qubits in diamond revealed by longitudinal relaxometry, **M. Fukami**, J. Karsch, L. Weiss, and D. D. Awschalom, *in preparation* (2022)

[2] Opportunities for long-range magnon-mediated entanglement of spin qubits via on- and off-resonant coupling, **M. Fukami**, D. R. Candido, D. D. Awschalom, and M. E. Flatté, *PRX Quantum* **2**, 040314 (2021)

[3] Spatiotemporal mapping of a photocurrent vortex in monolayer MoS_2 using diamond quantum sensors, B. B. Zhou, P. C Jerger, K.-H. Lee, **M. Fukami**, F. Mujid, J. Park, and D. D. Awschalom, *Physical Review X* **10**, 011003 (2020)

[4] All-optical cryogenic thermometry based on nitrogen-vacancy centers in nanodiamonds, **M. Fukami**, C. G. Yale, P. Andrich, X. Liu, F. J. Heremans, P. F. Nealey, and D. D. Awschalom, *Physical Review Applied* **12**, 014042 (2019)

Acknowledgments

The work presented in this dissertation would have been impossible without the support of my mentors, colleagues, friends, and family. First and foremost, I am grateful to my dissertation committee. Their advice and feedback have greatly elevated the quality of my research and contributed invaluably to my education in quantum information science. As my primary advisor and the chair of my dissertation committee, David Awschalom has challenged me to broaden my vision, improve research design, and learn new methods. I'm consistently inspired by his faith in science and deep insight into physics. I cannot imagine a better place for me to have done my PhD other than the Awschalom group. I also benefit greatly from the wide-ranging expertise and support of Peter Maurer and Giulia Galli. They encouraged me to become a more thoughtful physicist as well as a more precise communicator.

Discussion with the Awschalom group members has been the core of my graduate study. When I joined the group, Joe Heremans helped me set up my first experiment. I would like to thank him for always being patient and open to my ideas and sometimes stupid questions. Chris Yale showed me all the basics of the optical experiments, including how to align laser paths and adjust mirrors. What I learned from him has been absolutely essential in my research. Working in the same room in LL215 of ERC, Brian Zhou has been a role model for me in so many ways. He has not only novel ideas about impactful research, but also the ability to design and execute practical experiments. Paul Jerger is very knowledge about NV center physics. He was willing to spend time helping me overcome some of the most frustrating technical difficulties. Chris Anderson is a talented physicist with great intuition.

I really enjoyed our conversation on physics and everything else, including the one about a rubber duck. Alex Crook has been extremely kind to me. He answered my questions with the best intention and the most sincerity. I missed our joyful chats after a busy day of attending conference talks in Hong Kong and Boston. Kevin Miao encouraged me when I was at a low point of my PhD journey. I had a lot of fun solving a simulation problem with him. Jonathan Karsch has outstanding experiment skills. I was fortunate to work with him closely, especially on some magnonics projects. I'd also like to thank all the current and former members of the Awschalom group, including Gary Wolfowicz, Andrew Yeats, David Christle, Leah Weiss, Sean Sullivan, Nazar Delegan, Yeghishe Tsaturyan, Mouktik Raha, Jonghoon Ahn, Sam Whiteley, Peter Mintun, Paolo Andrich, Charles de las Casas, Berk Diler Kovos, Alex Bourassa, Erzsebet Vincent, Jacob Feder, Pratiti Deb, Ben Soloway, Joseph Blanton, Grant Smith, Elena Glen, Cyrus Zeledon, Yizhi Zhu, Will Burke, Swathi Chandrika, Marquis McMillan, and Chris Egerstrom. I will always remember watching the sunrise at the top of Mount Fuji after our 2016 summer conference and having group dinner in the pouring rain because we had to sit in an open space during COVID.

I'm immensely thankful to my coauthors: Michael Flatté, Denis Candido, Paul Nealey, Xiaoying Liu, Kazuya Ando, Yuma Tateno, Takaharu Tashiro, and Koji Sekiguchi. My research is the fruit of these productive collaborations. Besides, I received excellent administrative support from Mary Pat McCullough, David Taylor, and JulieAnn Scherer.

In addition, I'd like to express my heartfelt appreciation to my dear family. I dedicate this dissertation to my wife Yutian. Her devotion, encouragement, and unwavering support provided the much-needed emotional foundation throughout my PhD days. It was a pleasant surprise that she, as an intelligent economist, was able to provide numerous insights into my physics experiments, including some concrete research suggestions. Her contribution should be acknowledged in all my first-authored papers. I feel so lucky to have her as my partner. Last but not least, I thank my parents for their unconditional trust and everlasting love. I hope they are proud of my work.

Abstract

Nitrogen-vacancy (NV) centers in diamond have been known as excellent solid-state qubit platforms in quantum information science. Hybrid quantum systems of NV centers and magnetic insulator materials are of particular interest in recent years due to their great potential in computing and sensing applications. In this dissertation, we explore several experimental and theoretical aspects of the hybrid (or composite) quantum system of NV centers and yttrium iron garnet (YIG). YIG is a ferrimagnetic insulator material extensively studied in the field of spintronics and magnonics. It shows exceptionally low magnetic damping that leads to nontrivial magnon related phenomena such as the spin Seebeck effect.

The first section of this dissertation focuses on the fundamentals of quantum physics. Chapter 1 provides an introduction to quantum information science and engineering. Chapter 2 describes the basics of NV centers. Chapter 3 features the concept of boson-mediated interaction of qubits.

In Chapter 4, we show that the NV center can serve as a nanoscale temperature probe of the YIG substrate and is potentially useful for the study of the spin Seebeck effect. Employing an all-optical ratiometric thermometry technique, we find that the NV-based temperature sensing can function down to liquid nitrogen temperatures without a deterioration of its temperature sensitivity, which is ideal for the sensing application of YIG. With an array of NV centers embedded into a polymer membrane, we map out a temperature gradient of YIG as a demonstration of this all-optical temperature sensing.

Chapter 5 pursues a potential of the hybrid quantum architecture of NV centers and

magnons in YIG, with the expectation that long-distance two-qubits gates of NV centers will be enabled. We perform a theoretical study of a practical hybrid quantum system of NV centers interacting with magnons in YIG waveguide and bar structures. With both a semi-analytic analysis and a numerical analysis, we construct a framework to compute the NV-magnon coupling strength and the NV-NV effective coupling strength mediated by magnons. This will guide future experiments and device fabrications.

Lastly in Chapter 6, we use a diamond membrane that hosts ensemble of NV centers placed on top of a YIG slab and experimentally explore the coupling between the NV centers and magnons. We employ a device geometry where surface spin waves are prominent and are expected to interact with NV centers efficiently. With the longitudinal relaxometry experimental measurements, we estimate the NV-magnon coupling strength in terms of the real part of the self-susceptibility of an NV center mediated by magnons. This scheme of experimentally characterizing the hybrid quantum system's relevant parameters will be of great use in future exploration of the NV-magnon hybrid quantum architectures.

Chapter 1

An emerging field of quantum information science and engineering

In the past few decades, the field of quantum information science and engineering (QISE) has witnessed significant advances in both theories and experiments based on various physical realizations, including photons in linear optics [5–7], trapped ions [8–10], neutral atoms [11–13], superconducting qubits [14–16], quantum dots [17–19], and dopants/defects in solids [20–22]. To utilize the full capabilities of quantum physics in applications such as computing, communication, and sensing, the field of QISE has tied together multiple previously distinct communities of science in a common interdisciplinary field. For example, speaking different technical languages, researchers of optical computers, physicists studying atomic or molecular structures, engineers of semiconductor devices, and scholars of nuclear magnetic resonances may not sit together to discuss the same scientific topic effectively without the field of QISE. Now, they are collectively working to achieve a common goal with their idiosyncratic yet complementary approaches and specialties. This interdisciplinary nature of QISE has certainly boosted the remarkable recent development in quantum technologies [10, 13, 16].

1.1 Quantum advantage over classical technologies

Quantum technologies take advantage of what appears to be an underlying layer of the physical world described by the quantum physics and promote its fundamental features into applications. Based on the laws of quantum physics, wave functions, instead of probability distributions, are the fundamental unit that represents the physical world. Although the wave functions themselves are not directly observable, they construct probability distributions for measurement outcomes of arbitrary measurements. Therefore, we refer to this structure as the underlying layer, the feature of which is sometimes phrased as "the strange property of quantum mechanics". The very fact that the physical state is represented by the wave functions, together with the special characteristics of the wave functions, is essentially the basis of the advanced computational power of the quantum computing, security of the quantum communication, and the high precision of the quantum sensing.

The comparison between the quantum and classical technologies are made more explicit by highlighting the comparison between the quantum and classical computation as an example. In classical computation, the fundamental unit of information is represented by a binary quantity called a bit b, which takes either zero (false) or one (true):

$$b = 0; \quad b = 1. \tag{1.1}$$

In contrast in quantum computation, where physical states are represented by vectors in a Hilbert space written as $|\cdots\rangle$, the fundamental unit of information is a quantum bit $|q\rangle$ which can be a sum (superposition) of two orthogonal unit vectors representing the zero and one classical states $|0\rangle$ and $|1\rangle$, respectively:

$$|q\rangle = \alpha|0\rangle + \beta|1\rangle, \tag{1.2}$$

where α and β are complex numbers. As the physical states are more specifically described by the ray of the vector $|q\rangle$, we can impose the normalization condition $\langle q|q\rangle = (\alpha^*\langle 0| + \beta^*\langle 1|)(\alpha|0\rangle + \beta|1\rangle) = |\alpha|^2 + |\beta|^2 = 1$, where $\langle\cdots|$ is a dual vector of $|\cdots\rangle$, and eliminate overall phase factor by identifying $|q\rangle \leftrightarrow e^{i\theta}|q\rangle$ for real number θ and $i = \sqrt{-1}$. Eliminating two degrees of freedom out of the four degrees of freedom of the two complex numbers (α and β) allows us to map the qubit state into a point on a unit sphere in the three-dimensional real space as shown in Fig. 1.1. In this figure, the vector $\langle\vec{\sigma}\rangle$ points to a position on the unit sphere and is calculated from the qubit state $|q\rangle$ via the quantum-mechanical expectation:

$$\langle\vec{\sigma}\rangle = \langle q|\vec{\sigma}|q\rangle, \tag{1.3}$$

$$\vec{\sigma} = \hat{x}\sigma_x + \hat{y}\sigma_y + \hat{z}\sigma_z, \tag{1.4}$$

where we define coordinate independent Pauli operators:

$$\begin{aligned}
\sigma_x &= [|0\rangle\ |1\rangle] \begin{bmatrix} 0 & 1 \\ 1 & 0 \end{bmatrix} \begin{bmatrix} \langle 0| \\ \langle 1| \end{bmatrix}, \\
\sigma_y &= [|0\rangle\ |1\rangle] \begin{bmatrix} 0 & -i \\ i & 0 \end{bmatrix} \begin{bmatrix} \langle 0| \\ \langle 1| \end{bmatrix}, \\
\sigma_z &= [|0\rangle\ |1\rangle] \begin{bmatrix} 1 & 0 \\ 0 & -1 \end{bmatrix} \begin{bmatrix} \langle 0| \\ \langle 1| \end{bmatrix}.
\end{aligned} \tag{1.5}$$

This is clearly different from the classical bit: the quantum bit is represented by a point on the sphere while the classical bit takes binary value. The sphere in Fig. 1.1 is called the Bloch sphere.

There are a few points to be addressed to avoid confusion on the distinction between the quantum and classical states. One may suspect, for example, that the quantum state is more like an analog state because Eq. (1.2) and Fig. 1.1 seem to be parametrized by a continuous variables. This is inaccurate, as measurements of the qubit state result in binary outcomes: if we measure the quantity σ_z for the qubit state $|q\rangle$, we find the qubit is either

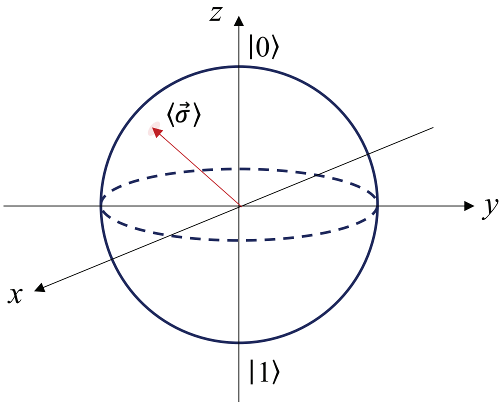

Figure 1.1: Bloch sphere and the vector $\langle\vec{\sigma}\rangle$ representing the quantum state.

in the state $|0\rangle$ or in the state $|1\rangle$ with probabilities $|\langle 0|q\rangle|^2$ and $|\langle 1|q\rangle|^2$, respectively. In a sense, a quantum state is an intermediate object of classical digital and analog states, which is essentially the particle-wave duality. For example, the measurement of σ_z for the state $|q\rangle = (|0\rangle + |1\rangle)/\sqrt{2} \equiv |+\rangle$ results in the outcomes of $\sigma_z = 1$ (i.e., the qubit state is $|0\rangle$) and $\sigma_z = -1$ (i.e., the qubit state is $|1\rangle$) with equal probabilities 1/2. This qubit state $|+\rangle$ is sometimes called as a state which is 0 and 1 at the same time, or the superposition of 0 and 1. One should not confuse this superposition and a classical state with randomness or statistical probabilities. In fact, one can add classical statistical probabilities on top of the quantum probabilities, in which case the state is called a mixed state and described by a density matrix (density operator) ρ defined by

$$\rho = \sum_k p_k \, |\psi_k\rangle \, \langle\psi_k| \,, \tag{1.6}$$

where k labels (pure) quantum states $|\psi_k\rangle$ and p_k is the statistical probability for the given mixed state to be in the quantum state $|\psi_k\rangle$ (more generally, the density operator is a hermitian positive semi-definite operator with trace one). Graphically, the mixed state ρ of a qubit is mapped to a vector inside the unit sphere drawn in Fig. 1.1, which is called the Bloch vector, with the definition of the following statistical and quantum-mechanical expectation (which is the generalization of Eq. (1.3)):

$$\langle \vec{\sigma} \rangle = \mathrm{Tr}[\vec{\sigma}\rho]. \tag{1.7}$$

There is a one-to-one correspondence between the qubit density operator ρ and the Bloch vector $\langle \vec{\sigma} \rangle$ via the above equation and the following:

$$\rho = (I + \langle \vec{\sigma} \rangle \cdot \vec{\sigma})/2. \tag{1.8}$$

For the pure quantum state $|+\rangle$, for example, its density matrix is written as

$$\rho_{|+\rangle} = [|0\rangle \ |1\rangle] \begin{bmatrix} 1/2 & 1/2 \\ 1/2 & 1/2 \end{bmatrix} \begin{bmatrix} \langle 0| \\ \langle 1| \end{bmatrix}, \tag{1.9}$$

and drawn as a point $(x, y, z) = (1, 0, 0)$ on the Bloch sphere in Fig. 1.1. In contrast, a mixed state of being in $|0\rangle$ and $|1\rangle$ with equal probabilities 1/2 is, which can also be described by the classical bit $b = 0, 1$ with randomness, given by

$$\rho_{\mathrm{classical}} = [|0\rangle \ |1\rangle] \begin{bmatrix} 1/2 & 0 \\ 0 & 1/2 \end{bmatrix} \begin{bmatrix} \langle 0| \\ \langle 1| \end{bmatrix}, \tag{1.10}$$

and is drawn as a point $(x, y, z) = (0, 0, 0)$ (i.e., the origin) in Fig. 1.1. The difference between the quantum state Eq. (1.9) and the classical state Eq. (1.10) shows up in the off-diagonal component of the density matrix, which is called the coherence in this context. Graphically, the qubit is in a pure state when $|\langle \vec{\sigma} \rangle| = 1$ and mixed when $|\langle \vec{\sigma} \rangle| < 1$, which can be due to the loss of the coherence. In most of the real-world quantum applications, it is difficult to preserve this off-diagonal component (coherence) over a long time, which is one of the major challenges in quantum technologies.

We note that a general quantum state ρ can be detected as a pure or a mixed state by checking the following quantity called a purity:

$$\text{(purity)} = \mathrm{Tr}\left[\rho^2\right]. \tag{1.11}$$

When the state is pure, we obtain $\text{(purity)} = 1$, and when it is mixed, we obtain $\text{(purity)} < 1$. This captures how quantum (pure) the given state is.

So far, we have discussed the difference between a single classical bit and a single qubit. However, the origin of the advanced computational power of quantum computation can be found more concretely by focusing on multi-qubit case. Classically, when there are two bits, we can represent one of the following four states with a two-bit register x:

$$x = 00;\ x = 01;\ x = 10;\ x = 11. \tag{1.12}$$

On the other hand, the quantum state represented by two qubits is represented by

$$|\psi\rangle = \alpha|00\rangle + \beta|01\rangle + \gamma|10\rangle + \delta|11\rangle, \tag{1.13}$$

where $\{\alpha, \beta, \gamma, \delta\}$ are complex numbers with $\langle\psi|\psi\rangle = |\alpha|^2 + |\beta|^2 + |\gamma|^2 + |\delta|^2 = 1$. Note that the state $|ab\rangle$ needs to be understood as a tensor product $|ab\rangle = |a\rangle \otimes |b\rangle$. Clearly, the quantum state can represent a state of being $|00\rangle$, $|01\rangle$, $|10\rangle$, and $|11\rangle$ at the same time as a superposition, which is the basis of the advantage over the classical bits that can only represent one out of four states in Eq. (1.12) (with a caveat that the quantum states would also take one of the four states under the measurement of the logical qubit states, which can be treated cleverly in quantum algoriths [23]). When there are n qubits, quantum states can represent 2^n classical digital states at the same time as a superposition, which is the manifestation of the quantum computational power.

We note that one critical property of the quantum multi-qubit state allowing the quantum advantage is the existence of entanglement or entangled states. Entanglement is a special correlation for a certain class of quantum states composed of two (or more) qubits, where the state of the whole qubits cannot be described by specifying the quantum states of individual qubits separately or by introducing the classical randomness (joint probability) into the same number of classical bits. One example of the entangled state is the following Bell state:

$$|\psi_B\rangle = (|00\rangle + |11\rangle)/\sqrt{2}. \tag{1.14}$$

For this state, there is a speciall correlation between the first and the second qubit: when the first qubit is zero (one), the second one is also zero (one). Furtheremore, due to the existence of the coherence, it is different from the state described by the classical joint probabilities. In contrast to this entangled state, the non-entangled state, or the separable state, is written as a tensor product:

$$|\psi\rangle = |q_A\rangle \otimes |q_B\rangle, \tag{1.15}$$

where $|q_A\rangle$ ($|a_B\rangle$) is the state of the left qubit A (right qubit B). More generally, a mixed state described by a density operator ρ is called separable if it can be written as

$$\rho = \sum_k p_k \rho_k^{(A)} \otimes \rho_k^{(B)}, \tag{1.16}$$

where k labels density matrix $\rho_k^{(A)}$ and $\rho_k^{(B)}$ of the system A and B, respectively, with probability p_k. One of the metrics for checking if the given state ρ is entangled or not is the entanglement negativity, based on the Peres-Horodecki criterion [24]:

$$(\text{Negativity}) = \sum_{i|\lambda_i<0} |\lambda_i|, \tag{1.17}$$

where the summation runs over the index i with $\lambda_i < 0$, which is the eigenvalue of the partial transposed density operator:

$$\rho^{T_B} = (I \otimes T)(\rho), \tag{1.18}$$

where T represents the transpose. When the state is separable and written as Eq. (1.16), due to the positive-semidefinite property of the density operator which is not affected by the transposition operation, all the eigenvalues of ρ^{T_B} is positive, and therefore the negativity is zero. On the other hand, when the negativity takes a non-zero positive value, it means the partial transposed density operator has at least one negative eigenvalue and hence the state is entangled.

Lastly, we note that there is a stronger and clearler manifestation of the non-classical correlation of the entanglement called the violation of the Bell inequality [25, 26]. Although the violation of this Bell inequality is sufficient but not necessary condition for a general state to be entangled, it shows how two remote quantum bits can be quantum-mechanically correlated in a way that a classical correlation cannot explain with a local realism. This has been a clear manifestation of nontrivial quantum correlation in a given quantum system and has been demonstrated experimentally in a variety of platforms in QISE [22, 27–30].

1.2 Quantum computing, communication, and sensing

There are three major categories of the applications of the quantum technology, i.e., quantum computing, communication, and sensing. Quantum computing tries to use the quantum coherence and entanglement, as described in the previous section, to enable classically difficult computational tasks more efficiently, such as prime factorization [31], database search [32], and optimization [33, 34]. Quantum communication utilizes the non-classical quantum correlation of the entangled qubits, together with the fact that the quantum state cannot be copied, to realize fundamentally secure communications such as with quantum key distribution [35]. Teleportation of quantum bits [36] and superdense coding [37] could also be under the umbrella of the quantum communication, where information stored in quantum or classical bits are sent between two nodes of communicators in a secure fashion with the use of shared entangled qubits. Quantum sensing [38] exploits the fragility of the quantum states to environment, especially the coherence, to enable high-precision and fast sensing of a small changes in the surrounding physical quantities, such as the magnetic field. In some schemes, entangled qubit states such as the Greenberger-Horne-Zeilinger state (often abbreviated as the GHZ state) are used to further improve the sensitivity.

We note that these categories are not distinct. In the overlapping area of the quantum computation and quantum communication, there are efforts to construct a network of quantum computational nodes (quantum network) [39–41] using the techniques in quantum communication, which will allow distributed quantum computating [42–44]. Similarly, combination of the quantum communication and sensing techniques will allow distributed sensing [45, 46]. Quantum sensing, or the qubit-based sensing in general, would be helpful to characterize new quantum computational architectures, as the qubits in the system can directly be used as a high-sensitivity sensor [47]. In Chapter 6 of this dissertation, we characterize the hybrid-quantum system architecture to engineer a boson-mediated two-qubit gate of spin qubits by probing the relaxation property of the qubit, which may also be regarded as in the intersection of qubit-based sensing and quantum computation.

Chapter 2

The Nitrogen-Vacancy centers in Diamond as a qubit platform

NV centers in diamond are known as one of the most promising qubit platforms. The NV center is an isolated point defect in diamond consisting of a substitutional nitrogen atom and an adjacent vacancy [see Fig. 2.1(a)]. Their optical accessibility and the long spin-coherence time with relatively easy microwave control make NV centers an ideal testbed for quantum information science, especially in sensing and communication applications.

2.1 Level structures

2.1.1 Optical transitions

NV center's orbital (optical) level structures are shown in Fig. 2.1(b)[48, 49]. In this dissertation, we only consider negatively charged NV centers in diamond except for Chapter 4. The optical ground state (GS) of the NV center is orbital singlet and spin triplet (typically labeled as $^3A_2$). The optical excited state (ES) is orbital doublet and spin triplet (typically labeled as ^3E). While the energy difference between GS and ES is approximately 1.945 eV [637 nm, called a zero-phonon line (ZPL)], due to the phonon-assisted transition, transitions

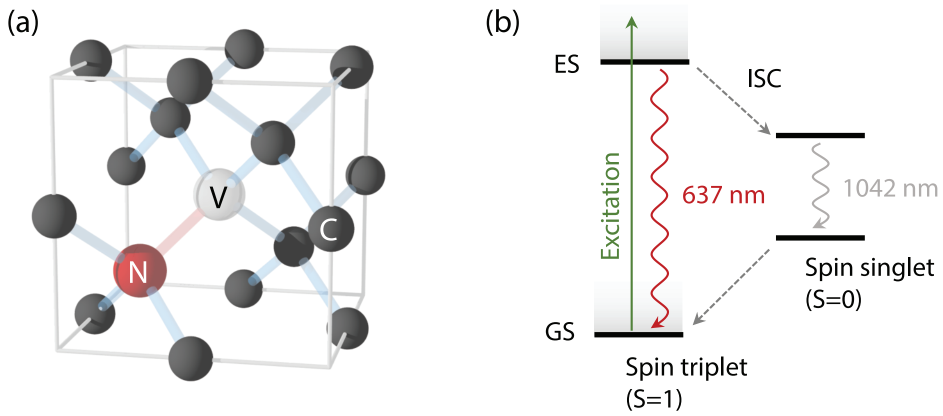

Figure 2.1: (a) Illustration of the nitrogen-vacancy (NV) center in diamond crystal. (b) Optical level structure of the negatively charged NV center in diamond.

occurs under the illumination of a green laser (532 nm), which is widely used in the experiments of NV centers. The photoluminescence spectra under a laser illumination are shown in Chapter 4 and used for temperature sensing. The spectrum consists of a sharp zero-phonon line at 637 nm and a wider phonon sideband in the range approximately from 600 nm to 850 nm.

One of the most practically important features of this optical level structure is the existence of the spin-dependent non-radiative (phonon-assisted) decay through the spin singlet states via the intersystem crossing (ISC), which is drawn as the dashed arrow in Fig. 2.1(b). The origin of this intersystem crossing is the spin-orbit interaction. This non-radiative decay through the intersystem crossing occurs preferentially for $m_s = 0$ state, leading to two important consequences under the 532-nm laser irradiation (note that the laser induced transitions and spontaneous decay have selection rules due to the standard interaction with electromagnetic field, which conserves (does not change) the projection of the spin). One is the spin initialization (optical pumping): GS population with $m_s = \pm 1$ ($m_s = 0$) goes to $m_s = \pm 1$ ($m_s = 0$) states in ES under the 532-nm laser illumination and then more likely to go to the ISC (undergo spontaneous emission) resulting in $m_s = 0$ ($m_s = 0$) spin state in GS [Figs. 2.2(a) and (b)]. The other is the spin-dependent photoluminescence (PL). As $m_s = \pm 1$ states are more likely to go to the ISC than the $m_s = 0$ state does, the PL for $m_s = \pm 1$

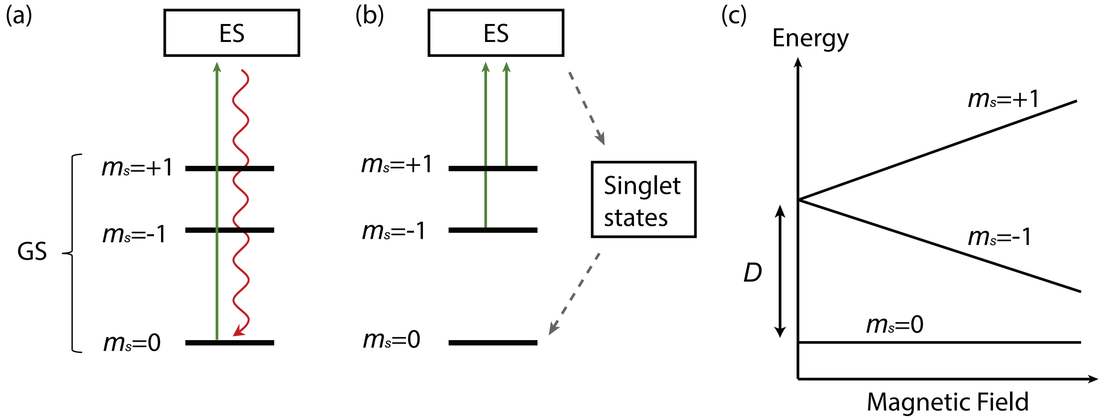

Figure 2.2: (a) Illustration of NV center states under the illumination of a 532-nm laser when the spin state is $|m_s = 0\rangle$. (b) Illustration of NV center states under the illumination of a 532-nm laser when the spin state is $|m_s = \pm 1\rangle$. (c) Magnetic field dependence of the NV center's spin levels.

states is darker as compared to the $m_s = 0$ state (for the time before the initialization is finished)[cite Dohery] [Figs. 2.2(a) and (b)].

2.1.2 Spin Hamiltonian

As mentioned in the previous section, under the optical pumping, the NV center's ground state spin can be initialized to $m_s = 0$ state. Here, the ground state spin Hamiltonian of the NV center is given by:

$$\mathcal{H}_{\text{NV}} = D(\hat{n} \cdot \vec{S})^2 + \gamma \vec{B} \cdot \vec{S}, \tag{2.1}$$

where $D = 2\pi \times 2.87$ GHz iszero-field splitting, $\hat{n}$ is the unit vector along the main symmetry axis of the NV center, i.e., the displacement direction of the nitrogen and the vacancy ($\langle 111 \rangle$ direction of the diamond crystal), $\gamma = 2\pi \times 2.8$ MHz/G is the absolute value of the gyromagnetic ratio, $\vec{B}$ is the external magnetic field, $\vec{S}$ is the spin-one operator of the NV center's electron spin, and we set $\hbar = 1$.

In Fig. 2.2(c), we show the axial magnetic field $\vec{B} \propto \hat{n}$ dependence the three spin levels. Due to the zero-field splitting, the $m_s = \pm 1$ states and the $m_s = 0$ state are not degenerate, and the energy separation is D. This makes the NV centers sensitive to the magnetic field $\vec{B}$ and the zero-field splitting D, which is due to the crystal field and depends on the temperature $D = D(T)$ due to the lattice expansion and contraction as a function of temperature T. Furthermore, the NV is sensitive to electric field crystal strain. This is made more explicit by writing the NV ground state Hamiltonian in the presence of electric field $\vec{E}$ and the effective strain field $\vec{\sigma}$:

$$\mathcal{H}_{\mathrm{NV}} = \left(D(T) + d_{\parallel}\vec{\mathcal{E}} \cdot \hat{n}\right)(\hat{n} \cdot \vec{S})^2 - \vec{\mathcal{E}} \cdot \left(\vec{S} \cdot \overleftrightarrow{d}_{\perp} \cdot \vec{S}\right) + \gamma \vec{B} \cdot \vec{S}, \tag{2.2}$$

$$\overleftrightarrow{d}_{\perp} = \frac{d_{\perp}}{2}\left(\hat{e}_{+} \otimes \hat{e}_{+} \otimes \hat{e}_{+} + \hat{e}_{-} \otimes \hat{e}_{-} \otimes \hat{e}_{-}\right), \tag{2.3}$$

where $d_{\parallel}, d_{\perp}$ are coefficients describing the electric dipole moment, $\hat{e}_{\pm} = \hat{x} \pm i\hat{y}$, $\hat{x}$ and $\hat{y}$ are orthogonal to NV main symmetry axis $\hat{n} = \hat{z}$ with an appropriate coordinate, and we write the rank-three tensor $\overleftrightarrow{d}_{\perp}$ to make the rotational symmetry explicit, i.e., rotating the coordinate (x, y) by $2\pi/3$ around z axis results in the transformation $\hat{e}_{\pm} \rightarrow \hat{e}_{\pm}e^{\pm i2\pi/3}$ and $\overleftrightarrow{d}_{\perp} \rightarrow \overleftrightarrow{d}_{\perp}$.

2.2 Single qubit properties

The NV center has an excellent qubit properties such as coherence time (T_2), dephasing time (T_2^*), and lifetime (T_1). In the following sections, we review these properties of an NV center as single qubit.

In a heuristic quantum mechanical argument, a wave function $\psi(t)$ with frequency ω may evolve in time as, with some decay rate κ,

$$\psi(t) = \psi(0)e^{-i\omega t - \kappa t}, \tag{2.4}$$

and the population of the state-1 will evolve as:

$$|\psi(t)|^2 = |\psi(0)|^2 e^{-2\kappa t}. \tag{2.5}$$

We immediately observe that the decay rate of the population 2κ [Eq.(2.5)] is twice as fast as the decay rate of the phase κ [Eq. (2.4)]. The former is related to the T_1 decay rate (lifetime, longitudinal decay), while the latter is related to the T_2 decoherence or T_2^* dephasing rate (transverse decay rate). In fact, when taking into account the randomness in dynamic phase evolution $i\omega t$, the transverse decay rate becomes faster than κ, which leads to a typical relation

$$\text{(transverse decay rate)} \ \geq \ \text{(longitudinal decay rate)} \ /2. \tag{2.6}$$

In the following sections, we make this discussion more concrete using the two-level system. For NV-center's case, we typically restrict the consideration to two states of the spin-triplet ground state, such as $|m_s = 0\rangle = |g\rangle$ and $|m_s = -1\rangle = |e\rangle$.

2.2.1 Longitudinal relaxation (T_1)

The longitudinal decay of a qubit can be captured by the following Lindblad master equation

$$\partial_t \rho = -i[H, \rho] + \gamma_> \mathcal{L}\left[\sigma_-\right]\rho + \gamma_< \mathcal{L}\left[\sigma_+\right]\rho, \tag{2.7}$$

$$\mathcal{L}[A]\rho = A\rho A^\dagger - \frac{1}{2}\left\{A^\dagger A, \rho\right\}, \tag{2.8}$$

where $H = \omega|e\rangle\langle e|$ is the qubit Hamiltonian, $\sigma_- - |g\rangle\langle e|$, $\sigma_+ = (\sigma_-)^\dagger$, and $\gamma_>$ ($\gamma_<$) is the transition rate for $|e\rangle \to |g\rangle$ ($|g\rangle \to |e\rangle$). As the density operator is one-to-one corresponding to $\langle\vec{\sigma}\rangle = \mathrm{Tr}[\vec{\sigma}\rho]$, it is sufficient to check the time evolution of this Bloch vector $\langle\vec{\sigma}(t)\rangle =$

$\mathrm{Tr}[\vec{\sigma}\rho(t)]$. Solving the differential equation, we obtain

$$\langle\sigma_-(t)\rangle = (\langle\sigma_+(t)\rangle)^* = \langle\sigma_-(0)\rangle\, e^{-i\omega t-(\gamma_>+\gamma_<)t/2}, \tag{2.9}$$

$$\langle\sigma_z(t)\rangle = \big(\langle\sigma_z(0)\rangle - \sigma_{\mathrm{eq}}\big)\, e^{-(\gamma_>+\gamma_<)t} + \sigma_{\mathrm{eq}}, \tag{2.10}$$

where $\sigma_z = |e\rangle\langle e| - |g\rangle\langle g|$ and the equilibrium Bloch vector's z component σ_{eq} is given by

$$\sigma_{\mathrm{eq}} = (\gamma_> - \gamma_<)\,/\,(\gamma_> + \gamma_<)\,. \tag{2.11}$$

Thus, the longitudinal (T_1) decay rate is [from Eq. (2.10)]

$$1/T_1 = \gamma_> + \gamma_<. \tag{2.12}$$

Additionally, the transverse (T_2) relaxation rate is [from Eq. (2.9)]

$$1/T_2 = (\gamma_> + \gamma_<)\,/2 = \frac{1/T_1}{2}, \tag{2.13}$$

which is consistent with Eq. (2.6). The meaning of the two rates $\gamma_>$ and $\gamma_<$ are made more explicit by writing the rate equation for the population $\rho_{ee} = \langle e|\rho|e\rangle$ and $\rho_{gg} = \langle g|\rho|g\rangle$:

$$\partial_t \begin{bmatrix} \rho_{ee} \\ \rho_{gg} \end{bmatrix} = \begin{bmatrix} -\gamma_> & +\gamma_< \\ +\gamma_> & -\gamma_< \end{bmatrix} \begin{bmatrix} \rho_{ee} \\ \rho_{gg} \end{bmatrix}. \tag{2.14}$$

This rate equation explicitly indicates that $\gamma_>$ and $\gamma_<$ are transition rates for $|e\rangle \rightarrow |g\rangle$ and $|g\rangle \rightarrow |e\rangle$, respectively. For NV centers, at room temperature the T_1 time can be as long as 6-7 ms [50, 51]. At lower temperatures, it improves orders of magnitudes [52, 53] and reaches as long as 200 s at 10 K (see supplemental material of [52]).

2.2.2 Dephasing and decoherence (T_2^* and T_2)

In the previous section, the longitudinal relaxation is accompanied by the transverse relaxation. Besides, due to a Markovian noise, there could be additional components for the transverse relaxation. The pure transverse relaxation is reproduced by the following Lindblad master equation:

$$\partial_t \rho = -i[H, \rho] + \frac{\gamma_\phi}{2} \mathcal{L}\left[\sigma_z\right] \rho. \tag{2.15}$$

In this case, the Bloch vector has time evolution of

$$\left\langle \sigma_-(t) \right\rangle = \left(\left\langle \sigma_+(t) \right\rangle \right)^* = \left\langle \sigma_-(0) \right\rangle e^{-i\omega t - \gamma_\phi t}, \tag{2.16}$$

$$\left\langle \sigma_z(t) \right\rangle = \left\langle \sigma_z(0) \right\rangle. \tag{2.17}$$

Thus, the transverse relaxation rate is [from Eq. (2.16)]

$$1/T_2 = \gamma_\phi, \tag{2.18}$$

and there is no longitudinal decay $1/T_1 = 0$ from Eq. (2.17). Furthermore, adding the contribution of Eq. (2.7) and Eq. (2.15), we obtain the equation of motion:

$$\partial_t \rho = -i[H, \rho] + \gamma_> \mathcal{L}\left[\sigma_-\right] \rho + \gamma_< \mathcal{L}\left[\sigma_+\right] \rho + \frac{\gamma_\phi}{2} \mathcal{L}\left[\sigma_z\right] \rho, \tag{2.19}$$

which results in

$$\left\langle \sigma_-(t) \right\rangle = \left(\left\langle \sigma_+(t) \right\rangle \right)^* = \left\langle \sigma_-(0) \right\rangle e^{-i\omega t - \left(\frac{\gamma_2 + \gamma_<}{2} + \gamma_\phi \right) t}, \tag{2.20}$$

$$\left\langle \sigma_z(t) \right\rangle = \left(\left\langle \sigma_z(0) \right\rangle - \sigma_{\mathrm{eq}} \right) e^{-(\gamma_> + \gamma_<) t} + \sigma_{\mathrm{eq}}. \tag{2.21}$$

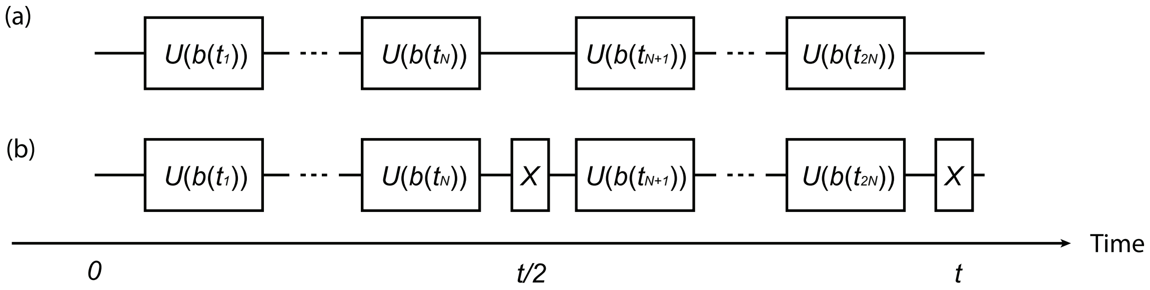

Figure 2.3: (a) Illustration of random magnetic-field noise acting on the NV center. The drawn random gate is $U(b) = e^{-ib(\sigma_z/2)\Delta t}$ with $\Delta t = t/2N$. (b) Schematic of a Hahn-echo like dynamical decoupling sequence, where X gate (π pulse) is applied at time $t/2$ and t.

This is the manifestation of Eq. (2.6), i.e.,

$$1/T_2 = \frac{\gamma_> + \gamma_<}{2} + \gamma_\phi \geq \frac{\gamma_> + \gamma_<}{2} = \frac{1/T_1}{2}. \tag{2.22}$$

So far, we have reviewed the T_2 transverse decay of an exponential form, which is due to Markovian phase noise. Alternative noise would a quasi-stationary frequency detuning $\omega \to \omega + \delta\omega$, where $\delta\omega$ is independent of time in a single qubit time evolution but can take random value in experiment to experiment. Working in the interaction frame (setting $\omega = 0$) and assuming the distribution of $\delta\omega$ is Gaussian with zero mean and variance σ^2, the average time evolution of the transverse component becomes

$$\begin{aligned} \langle \sigma_-(t) \rangle &= \langle \sigma_-(0) \rangle \, \overline{e^{-i(\delta\omega)t}}, \\ &= \langle \sigma_-(0) \rangle \int d(\delta\omega) \frac{1}{\sqrt{2\pi\sigma^2}} e^{-\frac{1}{2}\left(\frac{\delta\omega}{\sigma}\right)^2} e^{-l(\delta\omega)t}, \\ &= \langle \sigma_-(0) \rangle \, e^{-\frac{\sigma^2 t^2}{2}}. \end{aligned} \tag{2.23}$$

Interestingly, we obtained different decay form of the transverse spin. This dephasing, however, can be cancelled by adopting the dynamical decoupling sequence described in Fig. 2.3(b). [Note that the drawn sequence is Hahn echo. The second pulse is not necessary but shown for convenience. In the figure, we consider general time dependency of the noise $b(t)$]. In this figure, the randomness in phase $i\omega t$ is represented by a sequenctial application of a random gate $U(b) = e^{-ib(\sigma_z/2)\Delta t}$, where $\Delta t = t/2N$ [Fig. 2.3(a)]. When the time-dependency of the random variable $b(t)$ is independent of time $b(t) = \delta\omega$, then after the dynamical decoupling sequence (Hahn echo), the contribution cancels out:

$$XU\left(b\left(t_{2N}\right)\right)\cdots U\left(b\left(t_{N+2}\right)\right)U\left(b\left(t_{N+1}\right)\right)X = \left[U\left(b\left(t_{N}\right)\right)\cdots U\left(b\left(t_{2}\right)\right)U\left(b\left(t_{1}\right)\right)\right]^{-1}, \tag{2.24}$$

and we obtain $\langle\sigma_-(t)\rangle = \langle\sigma_-(0)\rangle$, indicating that the noise is cancelled out. For more general time-dependent noise, we have, for the free evolution:

$$\langle\sigma_-(t)\rangle = \langle\sigma_-(0)\rangle\, e^{-i\int_0^t d\tau b(\tau)}, \tag{2.25}$$

and with the Hahn echo, we have:

$$\langle\sigma_-(t)\rangle = \langle\sigma_-(0)\rangle\, \overline{e^{-i\int_0^t \lambda(t)b(t)}}, \tag{2.26}$$

where $\lambda(t) = 1$ for $0 \le \tau < t/2$ and $\lambda(\tau) = -1$ for $t/2 < \tau \le t$. The cancellation of the noise would be imperfect due to the fast oscillating contribution. The averaging $\overline{(\cdots)}$ can be made more explicit for the zero-mean Gaussian noise case:

$$\overline{(\cdots)} = \frac{1}{Z}\int \mathcal{D}[b(t)]e^{-\frac{1}{2}\int_{-\infty}^{\infty} dt_1 dt_2 b(t_1)K(t_1-t_2)b(t_2)}(\cdots), \tag{2.27}$$

where $Z = \int \mathcal{D}[b(t)]e^{-\frac{1}{2}\int_{-\infty}^{\infty} dt_1 dt_2 b(t_1)K(t_1-t_2)b(t_2)}$ is normalization constant, $\int \mathcal{D}[b(t)]$ represents the path integral, and $K(t_1 - t_2)$ is an appropriate integral kernel, which is roughly the inverse matrix of the noise correlation $S\left(t_1 - t_2\right) = \overline{b\left(t_1\right) b\left(t_2\right)}$ of form

$$\int_{-\infty}^{\infty} dt_2 K\left(t_1 - t_2\right) S\left(t_2 - t_3\right) = \delta\left(t_1 - t_3\right). \tag{2.28}$$

For this Gaussian noise case, all the information is contained in this noise correlation $S(t)$.

This is made more explicit by computing the generating function $G[J(\tau)]$:

$$G[J(\tau)] \equiv \overline{e^{i\int_0^t d\tau b(\tau)J(\tau)}} = e^{-\frac{1}{2}\iint_{-\infty}^{\infty} dt_1 dt_2 J(t_1)S(t_1-t_2)J(t_2)}. \tag{2.29}$$

As the Eqs. (2.25) and (2.26) are both in the form of generating function, it is enough to consider the above generating function with an appropriate choice of $J(\tau)$. For example, the free evolution [Eq. (2.25)] is the case with $J(\tau) = \Theta(\tau)(t-\tau)$ with the Heaviside step function Θ. Then we obtain

$$\langle\sigma_-(t)\rangle / \langle\sigma_-(0)\rangle = \overline{e^{-i\int_0^t d\tau b(\tau)}} = e^{-\frac{1}{z}\iint_0^t dt_1 dt_2 S(t_1-t_2)}. \tag{2.30}$$

When the noise is Markovian, we have $S(t_1-t_2) = 2\gamma_\phi\delta(t_1-t_2)$ and obtain

$$\langle\sigma_-(t)\rangle / \langle\sigma_-(0)\rangle = e^{-\gamma_\phi t}. \tag{2.31}$$

When the noise is time independent, we have $S(t_1-t_2) = \sigma^2$ and obtain

$$\langle\sigma_-(t)\rangle / \langle\sigma_-(0)\rangle = e^{-\frac{\sigma^2 t^2}{2}}. \tag{2.32}$$

These equations [Eqs. (2.31) and (2.32)] are consistent with Eqs. (2.16) and (2.23). We call the free (Ramsey) transverse decay time as a dephasing time (T_2^*) and the Hahn echo or the dynamical decoupled transverse decay time as a decoherence time (T_2). For NV center, T_2^* can be as good as 1.5 ms and (Hahn-echo) T_2 can be as good as 2.4 ms at room temperature [54].

2.2.3 Single-qubit gates

One convenient property of the NV center qubit is the control of its spin states with microwaves. Under microwave drive with frequency ω_d, the phase offset φ, and the amplitude

Ω, the NV center's Hamiltonian in the two states in the ground state reads:

$$\begin{aligned}\mathcal{H}_{\mathrm{NV}} &= \omega_{\mathrm{NV}}|e\rangle\langle e| + 2\Omega\sigma_x \cos\left(\omega_{\mathrm{d}}t+\varphi\right), \\ &\approx \omega_{\mathrm{NV}}|e\rangle\langle e| + \Omega\left(\sigma_+ e^{-i(\omega_{\mathrm{d}}t+\varphi)} + \sigma_- e^{+i(\omega_{\mathrm{d}}t+\varphi)}\right), \end{aligned} \tag{2.33}$$

where in the second line we use the rotating-wave approximation. In the rotating frame $[\mathcal{H}_{\mathrm{NV}} \to V(t)\left[\mathcal{H}_{\mathrm{NV}} - i\partial_t\right] V^\dagger(t)$ with $V(t) = e^{i\omega_{\mathrm{d}}t|e\rangle\langle e|}]$, we obtain

$$\begin{aligned}\mathcal{H}_{\mathrm{NV}} &= \left(\omega_{\mathrm{NV}} - \omega_{\mathrm{d}}\right)|e\rangle\langle e| + \Omega\left(\sigma_+ e^{-i\varphi} + \sigma_- e^{+i\varphi}\right), \\ &= \frac{\omega_{\mathrm{NV}} - \omega_{\mathrm{d}}}{2} I + \widetilde{\Omega}\hat{n}\cdot\vec{\sigma}, \end{aligned} \tag{2.34}$$

where we define the unit vector $\hat{n}$ and the rate $\widetilde{\Omega}$ as

$$\hat{n} = \left(\left(\frac{\omega_{\mathrm{NV}} - \omega_{\mathrm{d}}}{2}\right)\hat{z} + \Omega(\hat{x}\cos\varphi + \hat{y}\sin\varphi)\right)/\widetilde{\Omega}, \tag{2.35}$$

$$\widetilde{\Omega} = \sqrt{\left(\frac{\omega_{\mathrm{NV}} - \omega_{\mathrm{d}}}{2}\right)^2 + \Omega^2}. \tag{2.36}$$

The time-evolution operator under this drive becomes

$$U(t) = \exp\left[-i\mathcal{H}_{\mathrm{NV}}t\right] = \exp\left[-i\frac{\omega_{\mathrm{NV}} - \omega_{\mathrm{d}}}{2}t\right]\left(\cos[\widetilde{\Omega}t] - i\hat{n}\cdot\vec{\sigma}\sin[\widetilde{\Omega}t]\right), \tag{2.37}$$

where the relation $\exp[i\theta\hat{n}\cdot\vec{\sigma}] = \cos\theta + i(\hat{n}\cdot\vec{\sigma})\sin\theta$ is used to obtain the last expression, which can be shown in the same way as the proof of the Euler's formula using the relation $(i\hat{n}\cdot\vec{\sigma})^2 = -I$. This gate $U(t)$ is equivalent to the rotation along the direction $\hat{n}$ up to a phase factor. This can be made more explicit by considering the transformation of the Pauli operator vector $\vec{\sigma}$ under the rotation operator:

$$R_{\hat{n}}(\phi) = \exp\left[-i\frac{\phi}{2}\hat{n}\cdot\vec{\sigma}\right]. \tag{2.38}$$

As $\langle\vec{\sigma}\rangle$ is one-to-one corresponding to the single-qubit state, the following equation explicitly show that the unitary operator $R_{\hat{n}}(\phi)$ represents the rotation around axis $\hat{n}$:

$$R^{\dagger}_{\hat{n}}(\phi)\vec{\sigma}R_{\hat{n}}(\phi) = \hat{n}(\hat{n}\cdot\vec{\sigma}) + \cos\phi(-\hat{n}\times(\hat{n}\times\vec{\sigma})) + \sin\phi(\hat{n}\times\vec{\sigma}). \tag{2.39}$$

For on-resonant microwave $\omega_{\text{d}} = \omega_{\text{NV}}$ and and with zero phase offset $\varphi = 0$, Eq. (2.37) realizes the rotation around $\hat{x}$ axis with angular frequency 2Ω. With the choice of the microwave duration $\Omega t = \pi/2$, it becomes the X gate ($X = |e\rangle\langle g| + |g\rangle\langle e|$) up to a factor $-i$. Alternatively, by setting the phase to be $\varphi = \pi/2$, it realizes the Y gate [$Y = i(|g\rangle\langle e| - |e\rangle\langle g|)$] up to a factor $-i$. This phase φ can be controlled by the IQ modulation of the microwaves.

2.3 Two-qubits gates

Surprisingly, it is not very trivial to perform two-qubit gates of NV centers in a scalable fashion, although it is a building block of the quantum technology enabling access to the entangled qubit's subspace. There are two relatively well studied schemes of the NV-center based two-qubit gates and entanglement generation. One of them is the use of the magnetic dipole-dipole interaction, which lead to a controlled phase gate. In NV-center-nuclear spin systems, this dipole-interaction based two qubit gates has been shown to be very promising in quantum computation. However, this magnetic dipole-dipole interaction based two-qubit gates limit the distance between two NV centers within tens of nanometers, and there is a difficulty in scaling up in the number of qubits. The other scheme is the generation of long-distance (> 1 meter) entanglement based on indistinguishable single photons detection, with the use of the spin-to-photon interface of NV centers. This approach has been known be promising for quantum communication research. However, generating entanglement does not mean one has two-qubit gates. To promote the Bell-state generation to two-qubit gates, in each nodes one needs to have access to a nuclear spin quantum memory with long spin-coherence time, two-qubit gates between the NV center and the nuclear spin, single-shot readout of the NV center, and the nuclear spin's single qubit gate based on the measurement outcome of the NV state.

In the remainder of this chapter, we firstly review the two-qubit gates in other platform, and then discuss the dipole-dipole interaction based and detection based two-qubit gate of NV centers.

2.3.1 Two-qubit gates in other platforms

In this section, we briefly review the core concept behind the two-qubit gates in other platforms. In a neutral atom qubit platform, the use of a highly excited atom's Rydberg state is the core of the two-qubit gates. Due to the spreading wave function of the Rydberg state, the neighboring atoms cannot simultaneously occupy the Rydberg state (i.e., we need extra energy to have two neighboring atoms in the Rydberg state). The total Hamiltonian of the system is given by

$$\mathcal{H} = \left(\sum_{i=1,2} \omega_q |e\rangle_i \langle e | + \omega_R | r\rangle_i \langle r| \right) + V|r\rangle_1\langle r| \otimes |r\rangle_2\langle r| + \mathcal{H}_\mathrm{d}, \tag{2.40}$$

$$\mathcal{H}_\mathrm{d} = \sum_{i=1,2} 2\Omega_{\mathrm{d},i}(t) \cos\left(\omega_\mathrm{d} t\right) \left(|r\rangle_i\langle 1| + |1\rangle_i\langle r|\right), \tag{2.41}$$

where ω_q is the excited qubit state energy, ω_R is the energy for the Rydberg state $|r\rangle$, V is the Rydberg blockade energy, $\Omega_{\mathrm{d},i}$ is the drive amplitude for atom $i = 1, 2$, and ω_d is the drive laser frequency. The term V indicates that there is an extra energy needed to excite the second atom to the Rydberg state if the first atom is already in the Rydberg state. An example driving pulse scheme for a two-qubit gate enabled by this Hamiltonian is shown in Fig. 2.4(a). In this figure, firstly $\Omega_{i,\mathrm{d}}$ is turned on with $\omega_\mathrm{d} = \omega_R - \omega_q$ to perform a π rotation $|e\rangle_1 \to |r\rangle_1$. If the first qubit's state is $|g\rangle$, this pulse do nothing due to the frequency mismatch. Then, $\Omega_{\mathrm{d},2}$ is turned on with $\omega_\mathrm{d} = \omega_R - \omega_q$ to perform 2π rotation $|e\rangle_2 \to |r\rangle_2 \to |e\rangle_2$. Importantly, if the first qubit is already in the Rydberg state, this drive

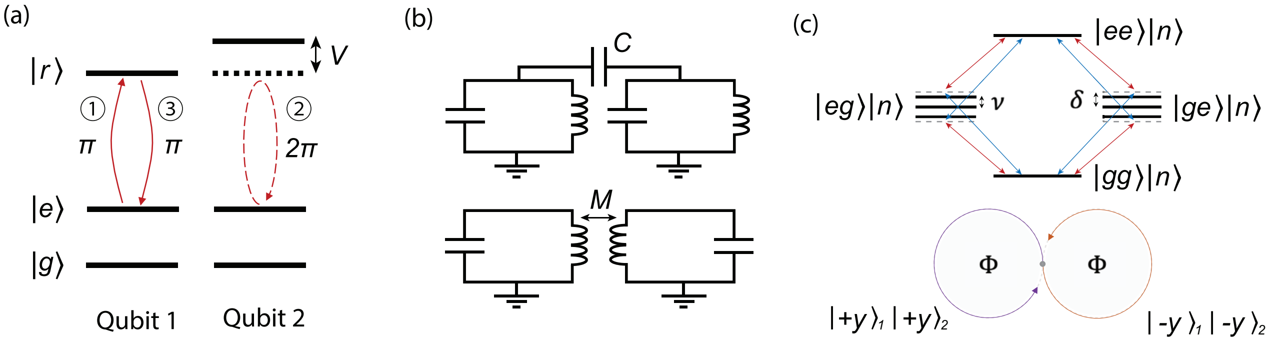

Figure 2.4: (a) Illustration of a type of two-qubit gates in neutral atom platforms with Rydberg interaction V. Gates (π-2π-π) are applied to the qubit 1-qubit 2-qubit 1 ordering. (b) Capacitively (C)or inductively coupled two LC circuits as an example of a two-circuit interaction. The coupling capacitance C and mutual inductance M are drawn. (c) Schematic of the Mølmer-Sørensen gate in a trapped ion plaform. Upper drawing shows the energy diagram, where blue and red lines represent the blue and red detuned lasers, respectively, and $|n\rangle$ is the phonon state. The lower drawing shows the spin dependent displacement of the phonon coherent state $|\alpha\rangle$ accumulating a geometric phase Φ.

do nothing due to the energy increase V (Rydberg blockade). Lastly, another π rotation is applied to return the first qubit's state from $|r\rangle$ to $|e\rangle$.

In a superconducting qubit platform, two-qubit gates are realized by a clever design and control of lumped circuit elements. Although the consideration of a specific type of gates and circuits are beyond our scope here, in Fig. 2.4(b) we illustrate how two LC circuits constituting harmonic oscillators, instead of anharmonic resonators (superconducting qubits), are coupled capacitively or inductively. In the presence of these coupling circuit elements, the original LC circuits' resonant frequencies are modified. The left circuits' current or voltage can affect the right circuit's current or voltage, which is enough to let us guess that more advanced circuit designs can lead to two-qubit gates of superconducting qubits.

In a trapped ion platform, one convenient feature of the system is the coupling to low frequency phonon modes in a drive-laser dependent manner, leading to multiple two-qubit gates. In the following, we outline how one of such gates schemes, Mølmer-Sørensen gate, is performed with the use of this coupling to the low frequency phonon mode. The Hamiltonian describing the coupled system with two ions can be written as

$$\mathcal{H} = \mathcal{H}_0 + \mathcal{H}_{\mathrm{d}}, \tag{2.42}$$

$$\mathcal{H}_0 = \sum_{i=1,2} \omega_q |e\rangle_i \langle e| + \nu a^\dagger a, \tag{2.43}$$

$$\mathcal{H}_{\mathrm{d}} = 2\Omega(t) \cos\left[ikx_0(a^\dagger + a) - i\omega_{\mathrm{d}} t\right] \left(\sigma_x^{(1)} + \sigma_x^{(2)}\right), \tag{2.44}$$

where ω_q is the qubit frequency of state $|e\rangle$, ν is the phonon frequency, a ($a^\dagger$) is the phonon annihilation (creation) operator, k is the wavenumber of the laser, x_0 is the zero-point motion of the phonon, ω_{d} is the drive laser frequency, $\Omega(t)$ is the drive laser amplitude, $\sigma_x = \sigma_+ + \sigma_-$, $\sigma_- = |g\rangle\langle e|$, and $\sigma_+ = (\sigma_-)^\dagger$. When applying bichromatic laser with frequency $\omega_{\mathrm{d}} = \omega_q \pm \delta$ with $\delta \approx \nu$ with the same drive amplitude Ω, as shown in the upper drawning of Fig. 2.4(c), and assuming that k for these two lasers are approximately the same, the drive Hamiltonian in the interaction picture with $\mathcal{H}_0$ becomes :

$$\mathcal{H}_{\mathrm{d}} \approx \Omega(t) \left(e^{-i\delta t} + e^{i\delta t}\right) e^{i\eta(ae^{-i\nu t} + a^\dagger e^{i\nu t})} \left(\sigma_+^{(1)} + \sigma_+^{(2)}\right) + \text{H. c.}, \tag{2.45}$$

where we drop fast oscillating terms proportional to $e^{\pm 2i\omega_q t}$ and define the Lamb-Dicke parameter $\eta = kx_0$. Under the condition $\eta \ll 1$, we can expand the exponential with phonon creation and annihilation operators. As $\delta \approx \nu$, we keep terms proportional to $e^{\pm i\epsilon}$ with $\epsilon = \nu - \delta$, and we obtain

$$\mathcal{H}_{\mathrm{d}} \approx -\eta\Omega(t) \left(ae^{-i\epsilon t} + a^\dagger e^{i\epsilon t}\right) S_y, \tag{2.46}$$

where we define $S_y = \sigma_y^{(1)} + \sigma_y^{(2)}$ with $\sigma_y = i(\sigma_- - \sigma_+)$. The last term means there is a spin (S_y) dependent force on the phonon mode, controlled by the laser amplitude $\Omega(t)$. When the laser drive amplitude is turned on $\Omega(t) = \Omega$ for $t \geq 0$, the time evolution operator under this drive is

$$\begin{aligned} U(t) &= T\exp\left[-i\int_0^t d\tau\mathcal{H}_{\mathrm{d}}(\tau)\right], \\ &= \prod_n D\left(i\eta\Omega S_y e^{i\epsilon t t_n}\Delta t\right), \end{aligned} \tag{2.47}$$

where $D(A) = \exp\left[Aa^\dagger - A^\dagger a\right]$ is the displacement operator and in the second line we divided the time-ordered integration into small increments with duration Δt. The last expression indicates a sequential application of the phonon displacement depending on the spin S_y. The spin operator S_y takes a value of zero if the qubit state is $|\pm y\rangle_1|\mp y\rangle_2$ and ± 2 when $|\pm y\rangle_1|\pm y\rangle_2$, where $|\pm y\rangle$ is the eigenstate of σ_y. Under an appropriate choice of laser irradiation time $t = 2\pi/\epsilon$, the phonon state comes back to the original state, accumulating a spin-dependent geometric phase as shown in the lower drawing of Fig. 2.4(c). This is made more explicit by writing

$$U(t) = D\left(\frac{\eta\Omega}{\epsilon}\left(e^{i\epsilon t} - 1\right)S_y\right)\exp\left[i\frac{\left(\eta\Omega S_y\right)^2}{\epsilon}\left(t - \frac{\sin\epsilon t}{\epsilon}\right)\right]. \tag{2.48}$$

The accumulated phase factor $e^{i\Phi}$ when the state is $|\pm y\rangle_1|\pm y\rangle_2$ ($S_y = \pm 2$) is given by

$$\Phi = 2\pi(2\eta\Omega/\epsilon)^2, \tag{2.49}$$

which is the geometric phase drawn in Fig. 2.4(c). With a proper choice of Ω and ϵ, one achieves one type of a two-qubit gate called the Mølmer-Sørensen gate. We have shown this phonon-mediated gate in detail to compare it with the magnon-mediated gate discussed in Chapter 5.

2.3.2 Magnetic dipole-dipole interaction

In NV center platforms, a straightforward way to implement two-qubit gates is the use of magnetic dipole-dipole interaction. This interaction also leads to remarkable demonstrations of two qubit gates between a central NV center electron spin and surrounding nuclear spins. Here we restrict our discussion to the NV-NV two-qubit gates. For two NV centers coupled with magnetic dipole interaction, the system Hamiltonian is given by

$$\mathcal{H} = \sum_{i=1,2} \mathcal{H}_{\mathrm{NV}}^{(i)} + \vec{S}_{\mathrm{NV1}} \cdot \overleftrightarrow{A} \cdot \vec{S}_{\mathrm{NV2}}, \tag{2.50}$$

$$\overleftrightarrow{A} = \frac{\mu_0}{4\pi} \frac{I - 3\hat{r}_{12} \otimes \hat{r}_{12}}{r^3}, \tag{2.51}$$

where $\mathcal{H}_{\mathrm{NV}}^{(i)}$ is the NV Hamiltonian provided in Eq. (2.1), $i = 1, 2$ labels the NVs, $\vec{S}_{\mathrm{NV}i}$ is the spin operator of the NVi ($i = 1, 2$), $\overleftrightarrow{A}$ is the magnetic dipole-dipole interaction tensor, $\hat{r}_{12}$ is the displacement vector between the two NVs, and r is the distance between the two NVs. Clearly, this magnetic dipole-dipole interaction is always on, so we need a clever way to cancel the gate, instead of turning on the gate. To make it more explicit, we consider the case where the two NV center's main symmetry axis directions are different, $\hat{n}$ and $\hat{n}'$, and the magnetic field is small such that the ground (first excited) state is $|g\rangle_1 \approx |\vec{S}_{\mathrm{NV1}} \cdot \hat{n} = 0\rangle$ ($|e\rangle_1 \approx |\vec{S}_{\mathrm{NV1}} \cdot \hat{n} = -1\rangle$) for NV1 and $|g\rangle_2 \approx |\vec{S}_{\mathrm{NV2}} \cdot \hat{n}' = 0\rangle$ ($|e\rangle_2 \approx |\vec{S}_{\mathrm{NV2}} \cdot \hat{n}' = -1\rangle$) for NV2. In this situation, the two NV centers have different resonant frequencies $\omega_{\mathrm{NV}}^{(1)}$ and $\omega_{\mathrm{NV}}^{(2)}$ for the transitions $|g\rangle_1 \leftrightarrow |e\rangle_1$ and $|g\rangle_2 \leftrightarrow |e\rangle_2$, respectively. Dropping fast oscillating terms and a constant term, the Hamiltonian in the subspace of our interest becomes

$$\mathcal{H} = \sum_{i=1,2} \omega_{\mathrm{NV}}^{(i)} |e\rangle_i \langle e| + A_{nn'} |e\rangle_1 \langle e| \otimes |e\rangle_2 \langle e|, \tag{2.52}$$

$$A_{nn'} = \frac{\mu_0 \gamma^2}{4\pi} \frac{\hat{n} \cdot (I - 3\hat{r}_{12} \bigotimes \hat{r}_{12}) \cdot \hat{n}'}{r^3}. \tag{2.53}$$

Its energy scale ϵ_{dip} is characterized by the following

$$\epsilon_{\text{dip}}/\hbar = \frac{\mu_0(\hbar\gamma)^2}{4\pi\hbar r^3} \approx (2\pi \times 0.0519 \text{ Hz}) \times \left(\frac{1\ \mu\text{m}}{r}\right)^3, \tag{2.54}$$

$$\approx (2\pi \times 1.924 \text{ kHz}) \times \left(\frac{30 \text{ nm}}{r}\right)^3, \tag{2.55}$$

where we explicitly write the Dirac constant $\hbar$ here. Considering the coherence times of NV centers, for the dipole-dipole interaction to be strong enough, the distance between two NVs need to be tens of nanometers.

Although Eq. (2.52) represents controlled-R_z type interaction, to perform two-qubit gates, one needs a dynamical decoupling sequence to turn off the interaction at will. Furthermore, when multiple qubits exist in the system, it is nontrivial to dynamically decouple all spins except for a desired pair of qubits for the two-qubit gate. This is done in a NV-center-nuclear-spin system remarkably well. However, in the following we illustrate how the controlled-phase gate is performed between the two NV centers with dynamical decoupling, for simplicity. Replacing $\omega_{\text{NV}}^{(i)} + \langle A_{nn'} \rangle \to \omega_{\text{NV}}^{(i)}$ and in the interaction picture, the two-qubit dynamics is governed by

$$\mathcal{H} = \frac{A}{2}\sigma_z^{(1)}\sigma_z^{(2)}, \tag{2.56}$$

where $A = A_{nn'}/2$. The dynamical decoupling can be applied without turning off this interaction, as shown in Fig. 2.5. This is made explicit by writing the time evolution operator:

$$U(t) = \exp\left[-i\frac{A}{2}\sigma_z^{(1)}\sigma_z^{(2)}t\right]. \tag{2.57}$$

Due to the relation $X_1X_2\mathcal{H}X_1X_2 = \mathcal{H}$ for the Hamiltonian provided in Eq. (2.56), where X_i is the X-gate for the NVi, we have the following property:

$$X_1X_2U(t/2)X_1X_2U(t/2) = U(t). \tag{2.58}$$

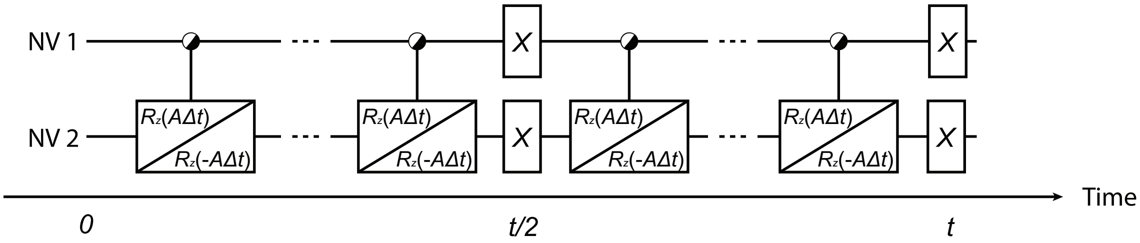

Figure 2.5: Illustration of two NV centers under a dynamical decoupling (Hahn-echo) sequence, where the two NV centers are interacting with a magnetic dipole-dipole interaction.

Note that in Fig. 2.5, we identify $|e\rangle = |0\rangle$ and $|g\rangle = |1\rangle$ for the representation of the controlled gates. We use half-open (half-filled) circles for the conditional operation of $|0\rangle$ ($|1\rangle$) (based on the quantum computing convention of σ_z, this choice of $|0\rangle$ and $|1\rangle$ is appropriate, though it may be confusing as it can be opposite to physics convention). We also note that, if the second qubit's π-pulse (X gate) is turned off, the interaction is cancelled:

$$X_1 U(t/2) X_1 U(t/2) = I. \tag{2.59}$$

Even in the current simple situation, Eqs. (2.58) and (2.59) already suggest that by choosing an appropriate dynamical decoupling sequence, one can turn on and off the controlled-phase gate at will. Therefore, the only challenge to make this scheme scalable is the weak strength of the magnetic dipole-dipole interaction that limit the NV-NV distance to be within tens of nanometers.

2.3.3 Promoting Bell-state preparation to two-qubit gates

An alternative approach of two-qubit gate is the scheme based on the quantum communication technique with single-photon detection. NV center are known to host excellent spin-photon interface. Using single photon detection, we can probabilistically create Bell state. The spin-photon entanglement is expressed by the evolution of

$$\left(\sqrt{1-p}|g\rangle_1 + \sqrt{p}|e\rangle_1\right)|0\rangle \to \left(\sqrt{1-p}|g\rangle_1 + \sqrt{p}|e\rangle_1 a_1^\dagger\right)|0\rangle, \tag{2.60}$$

$$\left(\sqrt{1-p}|g\rangle_2 + \sqrt{p}|e\rangle_2\right)|0\rangle \to \left(\sqrt{1-p}|g\rangle_2 + \sqrt{p}|e\rangle_2 a_2^\dagger\right)|0\rangle, \tag{2.61}$$

where p is the probability of being in the excited state for each NVs, $a_i^\dagger$ is the creation operator of a photon at the NVi's position ($i = 1, 2$), and $|0\rangle$ is the vacuum state of photons. These photons are guided into a beam splitter, and they become:

$$a_1^\dagger \to \frac{d_1^\dagger + d_2^\dagger}{\sqrt{2}}, \tag{2.62}$$

$$a_2^\dagger \to \frac{d_1^\dagger - d_2^\dagger}{\sqrt{2}}, \tag{2.63}$$

where $d_1^\dagger$ ($d_2^\dagger$) is the photon creation operator at the first (second) detector position. Combining Eqs (2.60)-(2.63), we obtain

$$\begin{aligned}
&\left(\sqrt{1-p}|g\rangle_1 + \sqrt{p}|e\rangle_1\right)\left(\sqrt{1-p}|g\rangle_2 + \sqrt{p}|e\rangle_2\right)|0\rangle,\\
\to &\left[(1-p)|g\rangle_1|g\rangle_2 + \sqrt{p(1-p)}\left(\frac{|e\rangle_1|g\rangle_2 + |g\rangle_1|e\rangle_2}{\sqrt{2}}\right)d_1^\dagger\right.\\
&\left.+\sqrt{p(1-p)}\left(\frac{|e\rangle_1|g\rangle_2 - |g\rangle_1|e\rangle_2}{\sqrt{2}}\right)d_2^\dagger + p|e\rangle_1|e\rangle_2\left(\frac{d_1^\dagger d_1^\dagger + d_2^\dagger d_2^\dagger}{2}\right)\right]|0\rangle.
\end{aligned} \tag{2.64}$$

This means that, upon the detection of only one photon in the detector, the wavefunction will collapse to either $(|e\rangle_1|g\rangle_2 + |g\rangle_1|e\rangle_2)/\sqrt{2}$ or $(|e\rangle_1|g\rangle_2 - |g\rangle_1|e\rangle_2)/\sqrt{2}$ depending on which detector observed the single photon. In this way, the NV-NV entanglement has been demonstrated over long distances on the order of meter to kilometers scale.

The Bell state creation can be promoted to a two-qubit gate of nearby quantum memories if we have (I) a two-qubit gate between the NV and the quantum memory, (II) single shot readout of the NV state, and (III) single qubit gate on the quantum memory based on the measurement outcome. To illustrate this, we assume the NV centers are entangled in the

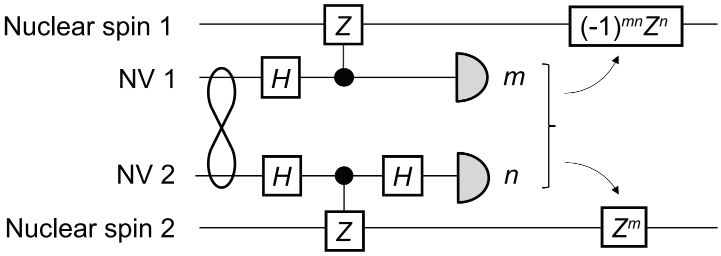

Figure 2.6: Quantum circuit representing how to promote the Bell-state generation into two-qubit gates. Two NV centers are entangled with the detection of a single photon detection. After two-qubit gate operations at each nodes, NV center's spin state are read out, and based on the measurement out come single-qubit gates are applied to the nuclear spin quantum memory, forming a controlled-Z gate between two nuclear spins.

form

$$|\psi_B\rangle_e = \frac{|00\rangle_e + |11\rangle_e}{\sqrt{2}}, \tag{2.65}$$

after an appropriate gate on the NVs and with appropriate identification of $|0\rangle$ and $|1\rangle$ states of the NV centers. The subscript e indicates the electron spin. We write the nearby nuclear quantum memory's quantum state as $|\mu\rangle_{n1}$ and $|\nu\rangle_{n2}$, where $n1$ and $n2$ indicate the nuclear spin label for the NV position 1 and 2, respectively, which we call as the communication nodes. Controlled-Z gate between the two nuclear spin memory can be performed by taking advantage of these entangled NV center electron spins by:

(i) Apply $H_e(CZ)$ (Hadamard on the electron spin) on the node 1,

(ii) Apply $H_e(CZ)H_e\,(= \mathrm{C}_n\mathrm{NOT}_e)$ on the node 2,

(iii) Apply appropriate single-qubit gates based on the detection,

where the Hadamard gate is defined as

$$H = \frac{1}{\sqrt{2}}[|0\rangle\ |1\rangle] \begin{bmatrix} 1 & 1 \\ 1 & -1 \end{bmatrix} \begin{bmatrix} \langle 0| \\ \langle 1| \end{bmatrix}. \tag{2.66}$$

The quantum circuit representing these steps are shown in Fig. 2.6. Applying the gates (i) and (ii) to the electron-nuclear spin state $|\psi_{\rm B}\rangle_e\,|\mu\rangle_{n1}|\nu\rangle_{n2}$ with $\mu,\nu=0,1$ results in

$$U\,|\psi_B\rangle_e\,|\mu\rangle_{n1}|\nu\rangle_{n2} = \frac{1}{2}\sum_{nm}\exp\left[i\pi\delta_{\mu,(m\oplus 1)}\delta_{v,(n\oplus 1)}\right]|mn\rangle_e|\mu\rangle_{n1}|\nu\rangle_{n2}, \tag{2.67}$$

$$U = [H_e(CZ)]_1\,(\mathrm{C}_n\mathrm{NOT}_e)_2\,, \tag{2.68}$$

where $\oplus$ indicates the addition modulo two. This is gate operation is made more explicit by writing:

$$U\,|\psi_B\rangle_e\,|0\rangle_{n1}|0\rangle_{n2} = \frac{1}{2}[+|00\rangle+|01\rangle+|10\rangle-|11\rangle]_e|0\rangle_{n1}|0\rangle_{n2}, \tag{2.69}$$

$$U\,|\psi_B\rangle_e\,|0\rangle_{n1}|1\rangle_{n2} = \frac{1}{2}[+|00\rangle+|01\rangle-|10\rangle+|11\rangle]_e|0\rangle_{n1}|1\rangle_{n2}, \tag{2.70}$$

$$U\,|\psi_B\rangle_e\,|1\rangle_{n1}|0\rangle_{n2} = \frac{1}{2}[+|00\rangle-|01\rangle+|10\rangle+|11\rangle]_e|1\rangle_{n1}|0\rangle_{n2}, \tag{2.71}$$

$$U\,|\psi_B\rangle_e\,|1\rangle_{n1}|1\rangle_{n2} = \frac{1}{2}[-|00\rangle+|01\rangle+|10\rangle+|11\rangle]_e|1\rangle_{n1}|1\rangle_{n2}. \tag{2.72}$$

As described in (iii), based on the measurement outcome m (n) of the first (second) electron spin, we can apply the following correction gate $U_{\rm corr}^{(m,n)}$ to the nuclear spins:

$$U_{\rm corr}^{(m,n)} = (-1)^{mn}Z_1^nZ_2^m. \tag{2.73}$$

Then we obtain the CZ gate because

$$U_{\rm corr}^{(m,n)}\exp\left[i\pi\delta_{\mu,(m\oplus 1)}\delta_{\nu,(n\oplus 1)}\right]|\mu\rangle_n|\nu\rangle_n = \exp\left[i\pi\delta_{\mu,1}\delta_{\nu,1}\right]|\mu\rangle_n|\nu\rangle_n. \tag{2.74}$$

Combining Eqs. (2.67), (2.74), and the single-shot detections of the two electron spin states, two-qubit gate between the two nuclear spins are realized at long distances. This is more efficient than teleporting the quantum state from the node 1 to the node 2, applying a two-qubit gate at the node 2, and teleporting back the state from the node 2 to the node 1.

Chapter 3

Quantum Mechanics: Boson-mediated interaction of qubits

In this chapter, we review multiple derivations of virtual boson mediated qubit interactions, including the self-interaction and the two-qubit interaction. Typically, we have the following total Hamiltonian of the interacting system under the rotating-wave approximation

$$\mathcal{H} = \omega_s \sum_{i=\text{qubit label}} |e\rangle_i\langle e| + \sum_{j=\text{boson label}} \omega_j b_j^\dagger b_j + \sum_{i,j} \left(g_j^{(i)} b_j \sigma_+^{(i)} + \text{H.c.} \right), \tag{3.1}$$

where ω_s is the qubit frequency, $|g\rangle_i$ ($|e\rangle_i$) is the ground (excited) state of the qubit labeled by i, ω_j is the boson frequency with label j, $b_j^\dagger$ (b_j) is the boson creation (annihilation) operator with the commutation relation $[b_{j_1}, b_{j_2}^\dagger] = \delta_{j_1 j_2}$, $g_j^{(i)}$ is the qubit-boson coupling constant, and $\sigma_+^{(i)} = |e\rangle_i\langle g|$. For example, when the boson has a continuum of three-dimensional modes with momentum/wave-vector label $\mathbf{k}$, we can replace

$$\sum_j \to V \int \frac{d\mathbf{k}}{(2\pi)^3}; \quad \sqrt{V} b_j \to b_{\mathbf{k}}; \quad \sqrt{V} g_j^{(i)} \to g_{\mathbf{k}}^{(i)}, \tag{3.2}$$

with the commutation relation $[b_{\mathbf{k}_1}, b^\dagger_{\mathbf{k}_2}] = (2\pi)^3\delta(\mathbf{k}_1 - \mathbf{k}_2)$, where V is the volume of the real space where the Fourier transform is performed. Then the full Hamiltonian [Eq. (3.1)] turns into

$$\mathcal{H} = \omega_s \sum_{i=\text{ qubit label}} |e\rangle_i\langle e| + \int \frac{d\mathbf{k}}{(2\pi)^3}\omega_{\mathbf{k}} b^\dagger_{\mathbf{k}} b_{\mathbf{k}} + \sum_i \int \frac{d\mathbf{k}}{(2\pi)^3}(g^{(i)}_{\mathbf{k}} b_{\mathbf{k}}\sigma^{(i)}_+ + \text{H. c.}). \tag{3.3}$$

In the following sections, we will consider

1. Exactly diagonalizable situation (Jaynes-Cummings model),
2. Schrieffer-Wolff transformation,
3. Diagrammatic approach,
4. Lindblad master equation under Born-Markov approximation,

for one-qubit and two-qubit cases.

3.1 Single qubit case (self-interaction and decay dissipation)

3.1.1 Exactly diagonalizable situation (Jaynes-Cummings model)

Firstly, we consider the one-qubit and one boson case, which is diagonalizable. We encounter the self-interaction of the qubit mediated by the boson. The reason for the terminology "self-interaction" should be understood in the Feynman-diagrammatic sense (Sec. 3.1.3). In this case, the total Hamiltonian reads:

$$\mathcal{H} = \omega_s|e\rangle\langle e| + \omega_b b^\dagger b + g\left(b\sigma_+ + b^\dagger\sigma_-\right), \tag{3.4}$$

where we have applied the gauge transformation $b \to be^{i\theta}$ $\left(b^\dagger \to b^\dagger e^{-i\theta}\right)$ such that the coupling g is real and positive, and ω_b is the boson frequency. As this commutes with the total excitation number operator $N = |e\rangle\langle e| + b^\dagger b$, i.e., $[\mathcal{H}, N] = 0$, we can block diagonalize the Hamiltonian with the projector P_n onto the subspace of the eigenspace of N with eigenvalue n. As the subspace onto which P_n projects is spanned by $\{|g, n\rangle, |e, n-1\rangle\}$ (for $n \geq 1$), we obtain:

$$\begin{aligned}
\mathcal{H} &= \sum_{n\geq 1} [|e, n-1\rangle \quad |g, n\rangle] \begin{bmatrix} \omega_s + (n-1)\omega_b & \sqrt{n}g \\ \sqrt{n}g & n\omega_b \end{bmatrix} \begin{bmatrix} \langle e, n-1| \\ \langle g, n| \end{bmatrix}, \\
&= \sum_{n\geq 1} [|e, n-1\rangle \quad |g, n\rangle] \\
&\quad \times \left(\left(n\omega_b + \frac{\omega_s - \omega_b}{2} \right) I + \left(\left(\omega_s - \omega_b \right) /2 \right) \tau_z + \sqrt{n} g \tau_x \right) \begin{bmatrix} \langle e, n-1| \\ \langle g, n| \end{bmatrix}, \qquad (3.5)
\end{aligned}$$

where I is the 2×2 identity matrix, $|g, n\rangle$ ($|e, n\rangle$) is the state with ground (excited) state qubit and n bosons, and $\{\tau_x, \tau_y, \tau_z\}$ are Pauli matrices. The eigenenergies of this Hamiltonian are 0 (for $|g, 0\rangle$) and $\epsilon_{n,\pm}$ with

$$\begin{aligned}
\epsilon_{n,\pm} &= (n-1)\omega_b + \frac{\omega_s + \omega_b}{2} \pm \operatorname{sgn}\left(\omega_s - \omega_b \right) \sqrt{\left[\left(\omega_s - \omega_b \right) /2 \right]^2 + n g^2}, \\
&\approx (n-1)\omega_b + \frac{\omega_s + \omega_b}{2} \pm \left[\frac{\omega_s - \omega_b}{2} + \frac{n g^2}{\omega_s - \omega_b} \right], \qquad (3.6)
\end{aligned}$$

where in the second line we assume $\sqrt{n}g \ll |\omega_b - \omega_s|/2$ and the existance of $\operatorname{sgn}(\omega_s - \omega_b)$ in the first line is merely for the sign convention of the definition. Writing the energies of the states $|e, n\rangle$ and $|g, n\rangle$ in the absence of the coupling g as $E^0_{|e,n\rangle} = (n-1)\omega_b + \omega_s$ and $E^0_{|g,n\rangle} = n\omega_b$, respectively, the two energies $\epsilon_{n,\pm}$ in Eq. (3.6) can be written as

$$\epsilon_{n,+} \approx E^0_{|e,n-1\rangle} + \frac{(n-1)g^2}{\omega_s - \omega_b} + \frac{g^2}{\omega_s - \omega_b}, \qquad (3.7)$$

$$\epsilon_{n,-} \approx E^0_{|g,n\rangle} - \frac{n g^2}{\omega_S - \omega_b}. \qquad (3.8)$$

In fact, the first one [Eq. (3.7)] has the eigenstate approximately equal to $|e, n-1\rangle$ and the second one [Eq. (3.8)] has the eigenstate approximately equal to $|g, n\rangle$. Therefore, we find that, for the weak coupling condition $\sqrt{n}g \ll |\omega_s - \omega_b|/2$, the eigenenergies are modified due to the coupling g as

$$\begin{aligned} E^0_{|e,n\rangle} &\rightarrow E^0_{|e,n\rangle} + \Sigma_{\text{Stark}} + \Sigma_{\text{Lamb}} \,, \\ E^0_{|g,n\rangle} &\rightarrow E^0_{|g,n\rangle} - \Sigma_{\text{Stark}} \,, \end{aligned} \tag{3.9}$$

where we define the Lamb shift Σ_{Lamb} and the Stark shift Σ_{Stark} as follows:

$$\Sigma_{\text{Lamb}} \equiv \frac{g^2}{\omega_s - \omega_b}, \tag{3.10}$$

$$\Sigma_{\text{Stark}} \equiv \frac{ng^2}{\omega_s - \omega_b}. \tag{3.11}$$

The Lamb shift Σ_{Lamb} is due to the self-interaction of the qubit mediated by the boson (Sec. 3.1.3). The Stark shift term Σ_{Stark} can be understood as the frequency modulation due to the alternating-current (a.c.) stark effect caused by n bosons, i.e., n bosons drive the qubit with a far detuned condition. More specifically, if we prapare a coherent state $|\beta\rangle$ of the boson at time $t = 0$ such that $b|\beta\rangle = \beta|\beta\rangle$ with real positive β, and if we ignore the back action to the boson from the qubit, we obtain

$$\langle \mathcal{H}(t) \rangle = \langle \beta | \mathcal{H}(t) | \beta \rangle = \omega_s |e\rangle\langle e| + \Omega \left(\sigma_+ e^{-i\omega_b t} + \sigma_- e^{+i\omega_b t} \right), \tag{3.12}$$

in the interaction picture of the bosons, where we define $g\beta = \Omega$. In the rotating frame [i.e., $|\psi(t)\rangle_R = U(r)|\psi(t)\rangle$ with $U(t) = \exp(i\omega_b t |e\rangle\langle e|)$], this Hamiltonian transforms into

$$\langle \mathcal{H}(t) \rangle_R = U(t) \left[\langle \mathcal{H}(t) \rangle - i\partial_t \right] U^\dagger(t) = (\omega_s - \omega_b) |e\rangle\langle e| + \Omega (\sigma_+ + \sigma_-) \,. \tag{3.13}$$

Its eigenenergies $\tilde{\epsilon}^{(R)}_{n,\pm}$ are [the subscript (R) stands for the rotating frame] given by

$$\begin{aligned}\tilde{\epsilon}^{(R)}_{n,\pm} &= \frac{\omega_s - \omega_b}{2} \pm \operatorname{sgn}(\omega_s - \omega_b)\sqrt{\left(\frac{\omega_s - \omega_b}{2}\right)^2 + \Omega^2}, \\ &\approx \tilde{\epsilon}^{(R)}_{n,\pm}(\Omega = 0) \pm \frac{\langle n \rangle g^2}{\omega_s - \omega_b}, \end{aligned} \tag{3.14}$$

where $\tilde{\epsilon}^{(R)}_{n,+}(\Omega = 0) = \omega_s - \omega_b$ and $\tilde{\epsilon}^{(R)}_{n,-}(\Omega = 0) = 0$ are the eigenenergies in the absence of the drive $\Omega = 0$, and in the second line we approximate the first line assuming the large detuning $\Omega \ll \omega_s - \omega_b|/2$ and use $\Omega = g\beta$ with the mean boson number $\langle n \rangle = |\beta|^2$. Comparing Eq. (3.14) with Eqs. (3.11) and (3.9), it makes sense to call the terms $\pm ng^2/(\omega_s - \omega_b)$ as the Stark shift.

3.1.2 Schrieffer-Wolff transformation

When there are multiple boson modes, one may need to apply some approximations to obtain the Stark shift and the Lamb shift. One way to obtain them is to use the second-order perturbation, but in this section we take another approach using the unitary transformation called the Schrieffer-Wolff transformation. Schrieffer-Wolff transformation is used, for example, to derive the phonon-mediated electron-electron interaction Hamiltonian in the study of the superconductivity [55]. The strength of this transformation is that we obtain the effective Hamiltonian of the system, in contrast to the second-order perturbation case where we only obtain the energy shifts (and the changes in states), which is less convenient. Additionally, when truncating higher-order terms in the expansion of the Schrieffer-Wolff transformation, this approach leads to the same result as that in the second order perturbation.

The Schrieffer-Wolff transformation is the unitary transformation of the full Hamiltonian $\mathcal{H} = H_0 + V$, where H_0 is the unperturbed Hamiltonian and V is the perturbation, of the form:

$$\mathcal{H}' = e^S \mathcal{H} e^{-S} = \mathcal{H} + [S, \mathcal{H}] + \frac{1}{2}[S, [S, \mathcal{H}]] + \cdots, \tag{3.15}$$

$$[H_0, S] = V, \tag{3.16}$$

where we use the Baker-Campbell-Hausdorff (BCH) formula to obtain the series in Eq. (3.15). Dropping higher-order terms of order $O(V^3)$, we obtain

$$\mathcal{H}' \approx H_0 + H_{\text{eff}} \quad ; H_{\text{eff}} = \frac{1}{2}[S, V], \tag{3.17}$$

where H_{eff} is the effective Hamiltonian. To solve for the operator S satisfying Eq. (3.16), it is convenient to use the interaction picture $\mathcal{O}_I(t) = e^{iH_0 t}\mathcal{O}e^{-iH_0 t}$. Then the condition Eq. (3.16) turns into

$$-i\partial_t S_I(t) = V_I(t). \tag{3.18}$$

Assuming that the interaction is adiabatically turned on and off from $t = -\infty$ and $t = \infty$, as is typiucally done in the quantum field theory and many-body condensed matter physics [56, 57], we obtain by integrating from $-\infty$ to t:

$$S_I(t) = i \int_{-\infty}^{t} d\tau V_I(\tau). \tag{3.19}$$

Therefore, the operator S reads

$$S = S_I(t = 0) = i \int_{-\infty}^{0} d\tau V_I(\tau), \tag{3.20}$$

and the effective Hamiltonian becomes

$$H_{\text{eff}} = \frac{i}{2} \int_{-\infty}^{0} dt \left[V_I(t), V_I(0)\right]. \tag{3.21}$$

Note that this takes the form of the advanced Green's function [58], except for the presence of the boson bath expectation $\langle \cdots \rangle = \mathrm{Tr}_B[\cdots R_0]$ with the boson density matrix R_0:

$$iG^A_{BA}(t) = -\theta(-t) \left\langle [B_I(t), A_I(0)] \right\rangle, \tag{3.22}$$

$$G^A_{BA}[\omega] = \int_{-\infty}^{\infty} dt G^A_{BA}(t) e^{i\omega t}, \tag{3.23}$$

where $\theta(t)$ is the Heaviside step function. In our case of one qubit coupled to multi-mode bosons, we can identify:

$$\mathcal{H} = H_0 + V, \tag{3.24}$$

$$H_0 = \omega_s |e\rangle\langle e| + \sum_j \omega_j b_j^\dagger b_j, \tag{3.25}$$

$$V = \sum_j g_j b_j \sigma_+ + g_j^* b_j^\dagger \sigma_-. \tag{3.26}$$

From Eq. (3.19), the operator S appearing in the Schrieffer-Solff transformation in the interaction picture reads

$$\begin{aligned} S_I(t) &= i \int_{-\infty}^{t} d\tau \left(\sum_j g_j b_j \sigma_+ e^{-i(\omega_j - \omega_s)\tau} + \text{ H. c} \right), \\ &= \sum_j \frac{g_j b_j \sigma_+ e^{-i(\omega_j - \omega_s)t}}{\omega_s - \omega_j + i\eta} - \text{ H.c. }, \end{aligned} \tag{3.27}$$

where $\eta \to +0$. Assuming the case with no on-resonant bosons $\omega_j \neq \omega_s$, we obtain

$$S = S_I(0) = \sum_j \frac{g_j b_j \sigma_+}{\omega_s - \omega_j} - \text{ H.c.} \tag{3.28}$$

We can directly compute and confirm that Eq. (3.16) is satisfied for this choice of S. Then the effective Hamiltonian can be computed as

$$\begin{aligned}
H_{\text{eff}} &= \frac{i\int_{-\infty}^{0} dt\left[B_-(t), B_+(0)\right]e^{i\omega_s t} + \text{H.c.}}{2}\sigma_+\sigma_- + \frac{i\int_{-\infty}^{0} dt B_+(0)B_-(t)e^{i\omega_s t} + \text{H.c.}}{2}\left[\sigma_+, \sigma_-\right], \\
&= \Sigma_{\text{Lamb}}|e\rangle\langle e| + \sum_{j_1 j_2}\frac{g_{j_2}^* g_{j_1} b_{j_2}^\dagger b_{j_1}}{2}\left(\frac{1}{\omega_s - \omega_{j_1}} + \frac{1}{\omega_s - \omega_{j_2}}\right)\sigma_z, \qquad (3.29)
\end{aligned}$$

where we define the noise operators $B_\pm$ for notational simplicity:

$$B_- \equiv \sum_j g_j b_j; \quad B_+ = \left(B_-\right)^\dagger, \qquad (3.30)$$

such that $V = B_-\sigma_+ + B_+\sigma_-$. Operators with a time argument are in the interaction picture. The second term and the first term of Eq. (3.29) are the Stark shift and the Lamb shift, respectively, with the definition

$$\Sigma_{\text{Lamb}} = \sum_j \frac{\left|g_j\right|^2}{\omega_s - \omega_j}. \qquad (3.31)$$

Importantly, the Lamb shift can be thought of as the real part of the advanced Green's function [see the first line of Eq. (3.29)]:

$$\begin{aligned}
\Sigma_{\text{Lamb}} &= \text{Re}\left[G^A_{B_-B_+}\left[\omega_S\right]\right], \qquad (3.32) \\
G^A_{B_-B_+}\left[\omega_s\right] &= i\int_{-\infty}^{0} dt\left\langle\left[B_-(t), B_+(0)\right]\right\rangle e^{i\omega_s t}, \\
&= i\int_{-\infty}^{0} dt\left[B_-(t), B_+(0)\right]e^{i\omega_s t}, \qquad (3.33)
\end{aligned}$$

where we use the fact that $[B_-(t), B_+(0)]$ is not an operator. We can relate this to the response functions, or the retarded Green's function [58]:

$$iG^R_{BA}(t) = \theta(t)\left\langle [B_I(t), A_I(0)] \right\rangle, \tag{3.34}$$

$$G^R_{BA}[\omega] = \int_{-\infty}^{\infty} dt G^R_{BA}(t) e^{i\omega t}. \tag{3.35}$$

If $\langle [B_I(t), A_I(0)] \rangle = \langle [B_I(0), A_I(-t)] \rangle$ is satisfied, which is true for the stationary bath states or for the current situation with $B_I(t) = B_-(t)$ and $A_I(t) = B_+(t)$, we have the following relationship between the retarded and the advanced Green's function

$$\left(G^A_{BA}[\omega]\right)^* = G^R_{A^\dagger B^\dagger}[\omega], \tag{3.36}$$

$$\left(G^A_{BA}[\omega]\right)^* = G^R_{BA}[\omega]; \quad \text{for } B = A^\dagger. \tag{3.37}$$

Therefore, in terms of the retarded Green's function and the response function defined by

$$\chi_{BA}(t) = -G^R_{BA}(t); \quad \chi_{BA}[\omega] = -G^R_{BA}[\omega], \tag{3.38}$$

the lamb-shift term in the current setting can be written as

$$\Sigma_{\text{Lamb}} = \text{Re}[G^R_{B_-B_+}[\omega_s]] = -\text{Re}\left[\chi_{B_-B_+}[\omega_s]\right], \tag{3.39}$$

and the effective Hamiltonian reads

$$H_{\text{eff}} = -\text{Re}\left[\chi_{B_-B_+}[\omega_s]\right] |e\rangle\langle e| + \sum_{j_1 j_2} \frac{g^*_{j_2} g_{j_1} b^\dagger_{j_2} b_{j_1}}{2} \left(\frac{1}{\omega_s - \omega_{j_1}} + \frac{1}{\omega_s - \omega_{j_2}}\right) \sigma_z. \tag{3.40}$$

This confirms that the Lamb shift term is due to the self-response of the qubit mediated by the bosons. Note that the minus sign in front of the retarded Green's function in Eq. (3.38) is chosen such that the linear response due to an external force $f(t)$ acting on the system via the interaction Hamiltonian $H_{\text{int}} = -f(t)A$ results in the response of the observable B

following $\langle \delta B(t) \rangle = \int_{-\infty}^{\infty} d\tau \chi_{BA}(t-\tau) f(\tau)$, where $\langle \delta B(t) \rangle = \langle B(t) \rangle - \langle B \rangle_{\mathrm{eq}}$ is the deviation from the value without the external force (equilibrium value).

3.1.3 Diagrammatic approach

To understand the self-response (Lamb shift term) of the qubit graphically, it is convenient to borrow the language of Feynman diagrams. In this section, we show that the Lamb shift term can be understood as the self-energy (self-interaction) of the qubit mediated by the boson. The formalism provided in this section is merely for the graphical visualization.

As Feynman diagrams in many-body theories are typically performed in the second-quantized language [56–58], it is convenient to write our Hamiltonian in terms of the qubit creation and annihilation operators, too. In the single mode case, we start from

$$\mathcal{H} = H_0 + V, \tag{3.41}$$

$$H_0 = \omega_s c_e^\dagger c_e + \omega_b b^\dagger b, \tag{3.42}$$

$$V = g\left(b c_e^\dagger c_g + b^\dagger c_g^\dagger c_e\right), \tag{3.43}$$

where $c_e^\dagger$ (c_e) and $c_g^\dagger$ (c_g) are excited state and ground state creation (annihilation) operators. As the qubit operator always appear in a pair such as $c_g^\dagger c_e$, it does not matter if we regard them as fermion or boson operators. We also note that although the above Hamiltonian take into account only one mode, it is straightforward to include multiple modes. Using this single mode case, we will verify that the result is consistent with that we obtained in Sec. 3.1.1. We employ the simplest zero-temperature formalism, i.e., the case where there is no excitations initially. The matrix element $\langle f, 0 | U(t) | i, 0 \rangle$ of the time-evolution operator $U(t) = \exp[-i\mathcal{H}t]$ is, where $i, f \in \{e, g\}$,

$$\langle f, 0 | U(t) | i, 0 \rangle = \left\langle 0 \left| c_f U(t) c_i^\dagger \right| 0 \right\rangle. \tag{3.44}$$

Here, $|0\rangle$ is the vacuum state of the free Hamiltonian ($b|0\rangle = c_e|0\rangle = c_g|0\rangle = 0$). As this free vacuum state also satisfies $V|0\rangle = 0$, we don't need to distinguish the free vacuum (the ground state of H_0) and the interacting vacuum (the ground state of $\mathcal{H} = H_0 + V$), which we typically need to pay attention to [56, 59, 60]. Using the Heisenberg picture operator $\mathcal{O}_{\rm H}(t) = U^\dagger(t)\mathcal{O}U(t)$, Eq. (3.44) becomes

$$\langle f, 0|U(t)|i, 0\rangle = \left\langle 0 \left| c_{f,\rm H}(t) c^\dagger_{i,\rm H}(0) \right| 0 \right\rangle, \tag{3.45}$$

where we use $U(t)|0\rangle = |0\rangle$ as $\mathcal{H}|0\rangle = 0$. For $t > 0$, we obtain

$$\langle f, 0|U(t > 0)|i, 0\rangle = \left\langle 0 \left| \mathcal{T} c_{f,\rm H}(t) c^\dagger_{i,\rm H}(0) \right| 0 \right\rangle = \left\langle \mathcal{T} c_f(t) c^\dagger_i(0) \right\rangle\Big|_{\rm Heis}, \tag{3.46}$$

where $\mathcal{T}$ represents the time-ordering. Using the Gell-Mann-Low formula [56, 59, 60], we obtain

$$\begin{aligned} \left\langle \mathcal{T} c_f(t) c^\dagger_i(0) \right\rangle\Big|_{\rm Heis} &= \frac{\left\langle 0 \left| T c_{f,I}(t) c^\dagger_{i,I}(0) S(\infty) \right| 0 \right\rangle}{\langle 0|S(\infty)|0\rangle}, & (3.47) \\ S(\infty) &= \mathcal{T} \exp\left[-i \int_{-\infty}^{\infty} dt \mathcal{H}_I(t) \right]. & (3.48) \end{aligned}$$

This expression allows to use the standard linked-cluster theorem [56, 59, 60] in the evaluation of the matrix element of the time-evolution operator. Now, we define the following propagators:

$$\left\langle \mathcal{T} c_e(t) c^\dagger_e(0) \right\rangle\Big|_{\rm Heis} = i\mathcal{F}(t), \tag{3.49}$$

$$\left\langle 0 \left| \mathcal{T} c_{g,I}(t) c^\dagger_{g,I}(0) \right| 0 \right\rangle = i\mathcal{G}_0(t); \quad \mathcal{G}_0(\omega) = (\omega + i\eta)^{-1}, \tag{3.50}$$

$$\left\langle 0 \left| \mathcal{T} c_{e,I}(t) c^\dagger_{e,I}(0) \right| 0 \right\rangle = i\mathcal{F}_0(t); \quad \mathcal{F}_0(\omega) = (\omega - \omega_s + i\eta)^{-1}, \tag{3.51}$$

$$\left\langle 0 \left| \mathcal{T} b_I(t) b^\dagger_I(0) \right| 0 \right\rangle = i\mathcal{D}_0(t); \quad \mathcal{D}_0(\omega) = (\omega - \omega_b + i\eta)^{-1}, \tag{3.52}$$

where $\mathcal{F}$ is the dressed excited qubit propagator, $\mathcal{G}_0$ is the free ground state qubit propagator,

$\mathcal{F}_0$ is the free excited state qubit propagator, and $\mathcal{D}_0$ is the free boson propagator. Using the linked-cluster theorem, we obtain the following Dyson equation

$$\mathcal{F}(\omega) = \mathcal{F}_0(\omega) + \mathcal{F}_0(\omega)\Sigma(\omega)\mathcal{F}(\omega), \tag{3.53}$$

where $\Sigma(\omega)$ is the self-energy

$$\Sigma(\omega) = ig^2 \int \frac{d\omega_1}{2\pi}\mathcal{D}_0\left(\omega - \omega_1\right)\mathcal{G}_0(\omega_1) =$$

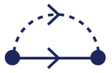

$$= \frac{g^2}{\omega - \omega_b + i\eta}. \tag{3.54}$$

Here, the solid line represents the ground state qubit $\mathcal{G}_0$ and the dashed curve represents the boson $\mathcal{D}_0$. For small coupling g, the dressed excited state qubit propagator approximately becomes

$$\mathcal{F}(\omega) = \frac{1}{\mathcal{F}_0^{-1}(\omega) - \Sigma(\omega)} \approx \mathcal{F}_{\approx}(\omega) = \frac{1}{\omega - \left(\omega_s + \Sigma\left(\omega_s\right)\right) + i\eta}, \tag{3.55}$$

where in the middle line we approximated $\Sigma(\omega) \approx \Sigma(\omega_s)$ as the energy $\omega = \omega_s$ provides the most relevant contribution. The self-energy evaluated at the qubit energy ω_s reads

$$\Sigma\left(\omega_s\right) = \frac{g^2}{\omega_s - \omega_b + i\eta} = \Sigma_{\text{Lamb}}, \tag{3.56}$$

which indicates that the Lamb shift is the self-energy. The definition of the Lamb shift here [Eq. (3.56)] is consistent with Eq. (3.10), and from Eq. (3.55) we confirm that the excited state qubit energy is modified from ω_s to $\omega_s + \Sigma(\omega_s)$. From the graphical representation in Eq. (3.54), we find that the Lamb shift can be regarded as the self-energy (self-interaction) due to the emission and reabsorption of a boson. Note that if we don't approximate $\Sigma(\omega) \approx \Sigma(\omega_s)$, we obtain two poles in $\mathcal{F}(\omega)$. In fact, we can obtain the exact time evolution $\langle e, 0|U(t)|e, 0\rangle$ from $\mathcal{F}(\omega)$.

When we have multiple boson modes, the self-energy becomes

$$\Sigma(\omega_s) = \sum_j \frac{\left|g_j\right|^2}{\omega_s - \omega_j + i\eta} = \Sigma_{\text{Lamb}} = -\text{Re}[\chi_{B_- B_+}, [\omega_s]], \tag{3.57}$$

which is consistent with the result in Sec. 3.1.2. By considering the continuum of boson modes labeled by the wave vector $\mathbf{k}$, we further obtain the real-space illustration of the emission and reabsorption of the boson modes. To this end, we consider the following system Hamiltonian:

$$\begin{aligned} \mathcal{H} &= H_0 + V, && (3.58) \\ H_0 &= \omega_s c_e^\dagger c_e + \int \frac{d\mathbf{k}}{(2\pi)^3} \omega_{\mathbf{k}} b_{\mathbf{k}}^\dagger b_{\mathbf{k}}, && (3.59) \\ V &= \int \frac{d\mathbf{k}}{(2\pi)^3} \left(g_{\mathbf{k}} b_{\mathbf{k}} e^{+i\mathbf{k}\cdot\mathbf{r}_{\text{q}}} c_e^\dagger c_g + g_{\mathbf{k}}^* b_{\mathbf{k}}^\dagger e^{-i\mathbf{k}\cdot\mathbf{r}_{\text{q}}} c_g^\dagger c_e \right), \\ &= \int d\mathbf{r} \left(g\left(\mathbf{r}_{\text{q}} - \mathbf{r}\right) b(\mathbf{r}) c_e^\dagger c_g + g^*\left(\mathbf{r}_{\text{q}} - \mathbf{r}\right) b^\dagger(\mathbf{r}) c_g^\dagger c_e \right), && (3.60) \end{aligned}$$

where $\mathbf{r}_{\text{q}}$ is the qubit position and $g(\mathbf{r})$ is the Fourier transform of $g_{\mathbf{k}}$. The self-interaction in real space reads

$$\Sigma\left(\tau_2 - \tau_1\right) =$$

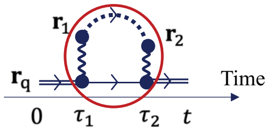

$$= i \int d\tau_2 d\tau_1 \int d\mathbf{r}_2 d\mathbf{r}_1 g\left(\mathbf{r}_{\text{q}} - \mathbf{r}_2\right) g^*\left(\mathbf{r}_{\text{q}} - \mathbf{r}_1\right) \mathcal{D}_0\left(\mathbf{r}_2 - \mathbf{r}_1, \tau_2 - \tau_1\right) \mathcal{G}_0\left(\tau_2 - \tau_1\right), \tag{3.61}$$

where the double line represents the excited state qubit $\mathcal{F}_0$. Clearly, this diagram shows the process where the boson is created at time τ_1 at position $\mathbf{r}_1$ while changing the qubit state ($|e\rangle \to |g\rangle$), and at time τ_2 the qubit reabsorbs ($|g\rangle \to |e\rangle$) the boson at position $\mathbf{r}_2$.

3.1.4 Lindblad master equation under Born-Markov approximation

Lastly for the single-qubit case, we derive the self-interaction term of the qubit mediated by boson modes in the Lindblad master equation formalism under the Born-Markov approximation [61]. This also allows to derive the decay dissipation of the qubit due to the boson emission and absorption at finite temperatures. Our starting point is the equation of motion of the qubit reduced density operator ρ for the system initially described by the total Hamiltonian $\mathcal{H} = H_0 + H_B + V$, where H_0 is the qubit Hamiltonian, H_B is the bath Hamiltonian, and V is the perturbative qubit-bath interaction Hamiltonian. Under the Born-Markov approximation with a stationary bath density operator R_0, i.e., $[H_B, R_0] = 0$, and assuming that the mean effect of the bath on the qubit is zero $\langle V \rangle = 0$, where $\langle \cdots \rangle = \mathrm{Tr}_B[\cdots R_0]$ is the bath expectation and $\mathrm{Tr}_B[\cdots]$ represents the partial trace of the bath states, we obtain [62]:

$$\frac{d}{dt}\rho(t) = -i\left[H_0, \rho\right] - \int_{-\infty}^{0} dt' \, \mathrm{Tr}_B \left[V(0), \left[V\left(t'\right), \rho(t) R_0\right]\right], \tag{3.62}$$

where $V(t)$ is in the interaction picture. Note that the double commutator part can be decomposed into the Hermitian-like and the non-Hermitian-like terms using the identity for Hermitian operators A, B, and C:

$$[A, [B, C]] = i\left[\frac{i}{2}[B, A], C\right] - \left(ACB + BCA - \frac{1}{2}\{AB, C\} - \frac{1}{2}\{BA, C\}\right), \tag{3.63}$$

where $A = V(0)$, $B = V(t')$, and $C = \rho(t)R_0$ in our setting. The first term is Hermitian-like and the second term is non-Hermitian-like. Using the above identity, we obtain

$$\frac{d}{dt}\rho(t) = -i\left[H_0 + H_{\text{eff}}, \rho\right] + \mathcal{N}[\rho(t)], \tag{3.64}$$

$$H_{\text{eff}} = \frac{i}{2}\int_{-\infty}^{0} dt' \left\langle \left[V\left(t'\right), V(0)\right]\right\rangle, \tag{3.65}$$

$$\mathcal{N}[\rho(t)] = \int_{-\infty}^{0} dt' \, \text{Tr}_B \left[V(0)\rho R_0 V\left(t'\right) - \frac{1}{2}\left\{V\left(t'\right)V(0), \rho R_0\right\}\right] + \text{H.c}, \tag{3.66}$$

where H_{eff} is the effective Hamiltonian and $\mathcal{N}[\rho(t)]$ is the non-Hermitian term. We find that the effective Hamiltonian H_{eff} provided in Eq. (3.65) takes almost the same form as that we obtained in Sec. 3.1.2, expect that the above effective Hamiltonian involves the bath expectation. In our case of one qubit coupled to multi-mode bosons, we can identify:

$$\mathcal{H} = H_0 + H_B + V, \tag{3.67}$$

$$H_0 = \omega_s |e\rangle\langle e|, \tag{3.68}$$

$$H_B = \sum_j \omega_j b_j^\dagger b_j, \tag{3.69}$$

$$V = B_-\sigma_+ + B_+\sigma_-; \quad B_- = \sum_j g_j b_j; \quad B_+ = (B_-)^\dagger. \tag{3.70}$$

Taking the boson density operator R_0 to be in their thermal state $R_0 = Z^{-1}\exp[-\beta H_B]$, where $\beta = 1/k_{\text{B}}T$ is the inverse temperature and $Z = \text{Tr}_B[\exp(-\beta H_B)]$ is the partition function, the effective Hamiltonian becomes

$$H_{\text{eff}} = \Sigma_{\text{Lamb}}|e\rangle\langle e| + \Sigma_{\text{Stark}}\sigma_z, \tag{3.71}$$

$$\Sigma_{\text{Lamb}} = \sum_j \mathcal{P}\frac{\left|g_j\right|^2}{\omega_s - \omega_j} = -\,\text{Re}\left[\chi_{B_-B_+}\left[\omega_s\right]\right], \tag{3.72}$$

$$\Sigma_{\text{Stark}} = \sum_j \mathcal{P}\frac{\left|g_j\right|^2 n_B(\omega_j)}{\omega_s - \omega_j}, \tag{3.73}$$

where $n_B(\omega) = [\exp(\beta\omega) - 1]^{-1}$ is the bose distribution. We note that although it is not discussed in Sec. 3.1.2, when there is on-resonant continuum of boson, the Lamb-shift term acquires the Cauchy's principal-value integral $\mathcal{P}$. The consideration of the presence of on-resonant boson continuum is important here as we would also like to derive the decay dissipation in this section and the on-resonant bosons are the source of the decay dissipation. Using the stationary condition of the boson bath and assuming $\langle B_-(t)B_-(0)\rangle = \langle B_+(t)B_+(0)\rangle = 0$ which is valid in our case (or applying the secular approximation), the non-Hermitian term turns into the following form:

$$\mathcal{N}[\rho(t)] = iG^{>}_{B_-B_+}[\omega_s]\,\mathcal{L}[\sigma_-]\,\rho + iG^{<}_{B_-B_+}[\omega_s]\,\mathcal{L}[\sigma_+]\,\rho, \tag{3.74}$$

$$\mathcal{L}[\mathcal{O}]\rho \equiv \mathcal{O}\rho\mathcal{O}^\dagger - \frac{1}{2}\left\{\mathcal{O}^\dagger\mathcal{O}, \rho\right\}, \tag{3.75}$$

where we define the greater and the lesser Green's functions [58]:

$$iG^{>}_{BA}(t) = \langle B(t)A(0)\rangle; \quad G^{>}_{BA}[\omega] = \int_{-\infty}^{\infty} dt G^{>}_{BA}(t)e^{i\omega t}, \tag{3.76}$$

$$iG^{<}_{BA}(t) = \langle A(0)B(t)\rangle; \quad G^{<}_{BA}[\omega] = \int_{-\infty}^{\infty} dt G^{<}_{BA}(t)e^{i\omega t}. \tag{3.77}$$

We note that $iG^{>}_{B_-B_+}[\omega_s]$ and $iG^{<}_{B_-B_+}[\omega_s]$ are real as we have $iG^{<}_{BA}[\omega], iG^{>}_{BA}[\omega] \in \mathbb{R}$ for $B = A^\dagger$. More explicitly, they are written as

$$iG^{>}_{B_-B_+}[\omega_s] = (n_B(\omega_s) + 1)\sum_j |g_j|^2\, 2\pi\delta(\omega_s - \omega_j), \tag{3.78}$$

$$iG^{<}_{B_-B_+}[\omega_s] = n_B(\omega_s)\sum_j |g_j|^2\, 2\pi\delta(\omega_s - \omega_j). \tag{3.79}$$

The T_1 decay rate [i.e., the decay rate of the population in the form $\langle\sigma_z(t)\rangle/\langle\sigma_z(0)\rangle = \exp(-t/T_1)$] reads

$$1/T_1 = iG^{>}_{B_-B_+}[\omega_s] + iG^{<}_{B_-B_+}[\omega_s] = iG^{K}_{B_-B_+}[\omega_s], \tag{3.80}$$

where we define the Keldysh Green's function [58]:

$$iG^K_{BA}(t) = iG^>_{BA}(t) + iG^<_{BA}(t) = \langle \{B(t), A(0)\} \rangle, \tag{3.81}$$

$$G^K_{BA}[\omega] = \int_{-\infty}^{\infty} dt G^K_{BA}(t) e^{i\omega t}. \tag{3.82}$$

Importantly, at thermal equilibrium the T_1 decay rate and the Lamb shift are related by the fluctuation-dissipation relation and the Kramers-Kronig relation. From the fluctuation-dissipation relation (Sec. 3.1.4), at thermal equilibrium of the boson bath, we obtain

$$iG^K_{BA}[\omega] = A_{BA}[\omega] \coth[\beta\omega/2], \tag{3.83}$$

where $A_{BA}[\omega]$ is the spectral function defined by [58]:

$$A_{BA}(t) = iG^>_{BA}(t) - iG^<_{BA}(t) = iG^R_{BA}(t) - iG^A_{BA}(t) = \langle [B(t), A(0)] \rangle, \tag{3.84}$$

$$A_{BA}[\omega] = \int_{-\infty}^{\infty} dt A_{BA}(t) e^{i\omega t}. \tag{3.85}$$

Remembering the relation Eq. (3.37), the spectral function is proportional to the imaginary part of the retarded Green's function when $A = B^\dagger$:

$$A_{BA}[\omega] = -2\,\mathrm{Im}\left[G^R_{BA}[\omega]\right], \text{ for } B = A^\dagger. \tag{3.86}$$

Combining Eqs. (3.86), (3.83), (3.80), and (3.38), we obtain the relation between the T_1 decay rate and the imaginary part of the susceptibility $\chi_{B_-B_+}[\omega_s]$:

$$1/T_1 = iG^K_{B_-B_+}[\omega_s] = A_{B_-B_+}[\omega_S] \coth[\beta\omega_s/2] = 2\,\mathrm{Im}\left[\chi_{B_-B_+}[\omega_s]\right] \coth[\beta\omega_s/2]. \tag{3.87}$$

This should be seen in contrast to the self-enrgy (self-interaction) or the Lamb shift term derived in Eq. (3.72), which is the real part of the susceptibility. These real part and imaginary part of the susceptibility are related by the Kramers-Kronig relation (Sec. 3.1.4):

$$\mathrm{Re}\left[\chi_{B_-B_+}[\omega]\right] = -\mathcal{P}\int_{-\infty}^{\infty}\frac{d\omega'}{\pi}\frac{\mathrm{Im}\left[\chi_{B_-B_+}\left[\omega'\right]\right]}{\omega-\omega'}, \tag{3.88}$$

$$\mathrm{Im}\left[\chi_{B_-B_+}[\omega]\right] = +\mathcal{P}\int_{-\infty}^{\infty}\frac{d\omega'}{\pi}\frac{\mathrm{Re}\left[\chi_{B_-B_+}\left[\omega'\right]\right]}{\omega-\omega'}. \tag{3.89}$$

Therefore, if we have access to the frequency dependence of the longitudinal decay rate T_1, i.e., $T_1 = T_1[\omega]$, we obtain using Eqs. (3.72), (3.88), and (3.87):

$$\mathrm{Re}\left[\chi_{B_-B_+}\left[\omega_s\right]\right] = -\Sigma_{\mathrm{Lamb}} = -\mathcal{P}\int_{-\infty}^{\infty}\frac{d\omega'}{\pi}\frac{1}{\omega_s-\omega'}\cdot\frac{1/T_1\left[\omega'\right]}{2\coth\left[\beta\omega'/2\right]}. \tag{3.90}$$

This equation clarifies the relation between the self-energy (Σ_{Lamb}) and the decay dissipation (T_1).

Fluctuation-dissipation relation

In this section, we show the fluctuation-dissipation relation. Although it is a well-known relation [58], as we are considering the case where operators A and B appearing in the Green's functions $G^{>}_{BA}$ and $G^{<}_{BA}$ are not Hermitian, it is instructive to show and verify the relation here. We assume $[H, \mu N] = 0$ [Note: we drop the subscript of H_B and write it as H because we only consider the boson Hilbert space] and $Ae^{\beta\mu N} = e^{\beta\mu(N-1)}A$ (satisfied when $[N, A] = A$), where N is the number operator (in our case, $N = \sum_j b_j^\dagger b_j$), μ is the chemical potential (note that μ can be zero and in that case $[H, \mu N] = 0$ and $Ae^{\beta\mu N} = e^{\beta\mu(N-1)}A$ always hold), and A is the operator appears in the Green's functions $G^{>}_{BA}$ and $G^{<}_{BA}$. Then, in the time domain, the greater and the lesser Green's function are related by:

$$\begin{aligned}
iG^{>}_{BA}(t) &= Z^{-1}\operatorname{Tr}\left[e^{-\beta(H-\mu N)}B(t)A\right] = Z^{-1}\operatorname{Tr}\left[e^{-\beta(H-\mu N)}e^{+iHt}Be^{-iHt}A\right], \\
&= Z^{-1}\operatorname{Tr}\left[e^{\beta\mu N}e^{+iH(t+i\beta)}Be^{-iH(t+i\beta)}e^{-\beta H}A\right] = Z^{-1}\operatorname{Tr}\left[e^{\beta\mu N}B(t+i\beta)e^{-\beta H}A\right], \\
&= Z^{-1}\operatorname{Tr}\left[e^{-\beta H}Ae^{\beta\mu N}B(t+i\beta)\right] = Z^{-1}\operatorname{Tr}\left[e^{-\beta H}e^{\beta\mu(N-1)}AB(t+i\beta)\right], \\
&= e^{-\beta\mu}Z^{-1}\operatorname{Tr}\left[e^{-\beta(H-\mu N)}AB(t+i\beta)\right] = e^{-\beta\mu}iG^{<}_{BA}(t+i\beta), \qquad (3.91)
\end{aligned}$$

where $Z = \operatorname{Tr}[e^{\beta(H-\mu N)}]$ is the partition function. In the frequency domain, this becomes

$$\begin{aligned}
G^{>}_{BA}[\omega] &= e^{-\beta\mu}\int_{-\infty}^{\infty} dt e^{i\omega t}G^{<}_{BA}(t+i\beta) = e^{-\beta\mu}\int_{-\infty+i\beta}^{\infty+i\beta} dt' e^{i\omega(t'-i\beta)}G^{<}_{BA}\left(t'\right), \\
&= e^{\beta(\omega-\mu)}\int_{-\infty+i\beta}^{\infty+i\beta} dt' e^{i\omega t'}G^{<}_{BA}\left(t'\right) = e^{\beta(\omega-\mu)}\int_{-\infty}^{\infty} dt' e^{i\omega t'}G^{<}_{BA}\left(t'\right), \\
&= e^{\beta(\omega-\mu)}G^{<}_{BA}[\omega]. \qquad (3.92)
\end{aligned}$$

This is called the detailed balance or the detailed balancing condition [58]. Using this condition, we obtain the fluctuation-dissipation relation:

$$\begin{aligned}
iG^{K}_{BA}[\omega] &= i\left(G^{>}_{BA}[\omega] + G^{<}_{BA}[\omega]\right) = \frac{i\left(G^{>}_{BA}[\omega] + G^{<}_{BA}[\omega]\right)}{i\left(G^{>}_{BA}[\omega] - G^{<}_{BA}[\omega]\right)}A_{BA}[\omega], \\
&= A_{BA}[\omega]\coth[\beta(\omega-\mu)/2]. \qquad (3.93)
\end{aligned}$$

When we use this relation in Eq. (3.83), we assume that the chemical potential is zero $\mu = 0$.

Kramers-Kronig relation

In this section, we show the Kramers-Kronig relation. Although it is a well-known relation, as we are considering the case where operators A and B appearing in the susceptibility χ_{BA} are not Hermitian, it is instructive to show and verify the relation here. From the definition of $\chi_{BA}(t)$, we can write

$$\chi_{BA}(t) = i\theta(t) A_{BA}(t). \tag{3.94}$$

Its Fourier transform is given by

$$\theta[\omega] = \frac{i}{\omega + i\eta}. \tag{3.95}$$

Using the convolution theorem, we obtain

$$\chi_{BA}[\omega] = i \int_{-\infty}^{\infty} \frac{d\omega'}{2\pi} \theta\left[\omega - \omega'\right] A_{BA}\left[\omega'\right] = - \int_{-\infty}^{\infty} \frac{d\omega'}{2\pi} \frac{A_{BA}\left[\omega'\right]}{\omega - \omega' + i\eta}. \tag{3.96}$$

Using the Plemelj formula $1/(\omega + i\eta) = \mathcal{P}/\omega - i\pi\delta(\omega)$, we obtain

$$\chi_{BA}[\omega] = \chi'_{BA}[\omega] + i\chi''_{BA}[\omega], \tag{3.97}$$

where we define the first part ($\chi'_{BA}[\omega]$) and the second part ($\chi''_{BA}[\omega]$) as

$$\chi'_{BA}[\omega] \equiv -\frac{G^R_{BA}[\omega] + G^A_{BA}[\omega]}{2} = -\mathcal{P} \int_{-\infty}^{\infty} \frac{d\omega'}{2\pi} \frac{A_{BA}\left[\omega'\right]}{\omega - \omega'}, \tag{3.98}$$

$$\chi''_{BA}[\omega] \equiv -\frac{G^R_{BA}[\omega] - G^A_{BA}[\omega]}{2i} = \frac{A_{BA}[\omega]}{2}. \tag{3.99}$$

We note that the first part and the second part are not necessarily the real part and the imaginary part, although we show they become the real and the imaginary parts under a certain condition. For these susceptibilities, we have the following Kramers-Kronig relation:

$$\chi'_{BA}[\omega] = -\mathcal{P} \int_{-\infty}^{\infty} \frac{d\omega'}{\pi} \frac{\chi''_{BA}\left[\omega'\right]}{\omega - \omega'}, \tag{3.100}$$

$$\chi''_{BA}[\omega] = +\mathcal{P} \int_{-\infty}^{\infty} \frac{d\omega'}{\pi} \frac{\chi'_{BA}\left[\omega'\right]}{\omega - \omega'}. \tag{3.101}$$

Furthermore, the first and the second parts become the real and the imaginary parts when $B = A^\dagger$, i.e.,

$$\left.\begin{aligned} \chi'_{BA}[\omega] &= \mathrm{Re}\left[\chi_{BA}[\omega]\right] \\ \chi''_{BA}[\omega] &= \mathrm{Im}\left[\chi_{BA}[\omega]\right] \end{aligned}\right\} \mathrm{For} B = A^\dagger. \tag{3.102}$$

In Eqs. (3.88) and (3.89), we use the fact that $B = B_- = (B_+)^\dagger = A^\dagger$ is satisfied in the Green's functions, and hence the Kramers-Kronig relation simply connects the real part and the imaginary part of the susceptibility $\chi_{B_-B_+}[\omega]$.

3.2 Two qubits case (qubit-qubit interaction)

Next, we consider the case where there are two qubits coupled to the boson modes. In this case, we can derive the qubit-qubit interaction mediated by the boson. Importantly, we show that the qubit-qubit interaction equals to the self-interaction (Lamb shift) term when the separation of the two qubits are zero.

3.2.1 Exactly diagonalizable situation (Jaynes-Cummings model)

In this section, we consider the case where there are two qubits coupled to a common single boson mode. After an appropriate gauge transformation on the qubits by $U = \exp[-i(\theta_1\sigma_z^{(1)} + \theta_2\sigma_z^{(2)})]$ and $\mathcal{H} \to U^\dagger \mathcal{H} U$ for appropriate $\theta_1, \theta_2 \in \mathbb{R}$, we obtain the following full Hamiltonian

$$\mathcal{H} = H_0 + V, \tag{3.103}$$

$$H_0 = \omega_s \left(|e\rangle_1\langle e| + |e\rangle_2\langle e|\right) + \omega_b b^\dagger b, \tag{3.104}$$

$$V = g\left(b\left[\sigma_+^{(1)} + \sigma_+^{(2)}\right] + b^\dagger\left[\sigma_-^{(1)} + \sigma_-^{(2)}\right]\right), \tag{3.105}$$

for real and positive coupling g. Here, we assume that the two qubits have the same frequency. Then, in the same way as in the single qubit case (Sec. 3.1.1), the total number of excitation $N = |e\rangle_1\langle e| + |e\rangle_2\langle e| + b^\dagger b$ commutes with the above total Hamiltonian, i.e., $[N, \mathcal{H}] = 0$. Furthermore, the above Hamiltonian commutes with the projector onto the dark state $P_D \equiv |D\rangle\langle D|$ with $|D\rangle = (|e_1g_2\rangle - |g_1e_2\rangle)/\sqrt{2}$, as $|D\rangle$ is the eigenstate: $\mathcal{H}|D\rangle = \omega_s|D\rangle$. The state $|D\rangle$ is called the dark state as the boson system does not see this qubit subspace, which is indicated by $V|D\rangle = 0$. The subspace of the vectors orthogonal to $|D\rangle$ is spanned by $\{|g_1g_2\rangle, |B\rangle, |e_1e_2\rangle\}$ with the bright state $|B\rangle = (|e_1g_2\rangle + |g_1e_2\rangle)/\sqrt{2}$, so if we write the projector onto this subspace as $P_{\perp D}$, we obtain

$$\begin{aligned}
\mathcal{H} &= [|B;0\rangle \quad |g_1g_2;1\rangle] \begin{bmatrix} \omega_s & \sqrt{2}g \\ \sqrt{2}g & \omega_b \end{bmatrix} \begin{bmatrix} \langle B;0| \\ \langle g_1g_2;1| \end{bmatrix} + \omega_s|D\rangle\langle D|, \\
&\quad + \sum_{n\geq 2} P_{\perp D}P_n\mathcal{H}P_nP_{\perp D}.
\end{aligned} \tag{3.106}$$

Here, the number after the semicolon in the bra/ket notation is the number of boson excitations. We also note that $|g_1g_2;0\rangle$ is the eigenstate with zero energy $\mathcal{H}|g_1g_2;0\rangle = 0$. The last term of Eq. (3.106) can be written in the 3×3 matrix form with three basis vectors $\{|g_1g_2;n\rangle, |B;n-1\rangle, |e_1e_2;n-2\rangle\}$. The first term of Eq. (3.106) can be diagonalized in the same way as in Sec. 3.1.1, and we obtain the following eigenenergies

$$\begin{aligned}
\epsilon_\pm &= \frac{\omega_s+\omega_b}{2} \pm \mathrm{sgn}\,(\omega_s-\omega_b)\sqrt{((\omega_s-\omega_b)/2)^2 + 2g^2}, \\
&\approx \frac{\omega_s+\omega_b}{2} \pm \left[\frac{\omega_s-\omega_b}{2} + \frac{2g^2}{\omega_s-\omega_b}\right],
\end{aligned} \tag{3.107}$$

where we assume $2g^2 \ll |\omega_s-\omega_b|/2$ in the second line. In fact, the eigenstate associated with ϵ_+ is approximately equal to $|B;0\rangle$ in the small copuling g limit. Writing the energy of the zero-boson bright state $|B;0\rangle$ in the absence the coupling g as $E^0_{|B;0\rangle} = \omega_s$, we observe that the energies are modified by the coupling g following

$$E^0_{|B;0\rangle} \to \epsilon_+ \approx E^0_{|B;0\rangle} + \frac{2g^2}{\omega_S - \omega_b}. \tag{3.108}$$

In contrast, the dark state energy $E^0_{|D;0\rangle} = \omega_s$ and the energy $E^0_{|g_1 g_2;0\rangle}$ of the state $|g_1 g_2; 0\rangle$ are unchanged by adding the coupling g:

$$\begin{aligned} E^0_{|D;0\rangle} &\to E^0_{|D;0\rangle}, &(3.109)\\ E^0_{|g_1 g_2;0\rangle} &\to E^0_{|g_1 g_2;0\rangle}. &(3.110) \end{aligned}$$

This is the manifestation of the following effective Hamiltonian at low boson occupation (low temperature):

$$\begin{aligned} H_{\text{eff}} &= \frac{g^2}{\omega_S - \omega_b} \left(\sigma_+^{(1)} + \sigma_+^{(2)}\right) \left(\sigma_-^{(1)} + \sigma_-^{(2)}\right), \\ &= \Sigma_{\text{Lamb}} \left(|e\rangle_1 \langle e| + |e\rangle_2 \langle e|\right) - g_{\text{eff}} \left(\sigma_+^{(1)} \sigma_-^{(2)} + \sigma_-^{(1)} \sigma_+^{(2)}\right), \qquad (3.111) \end{aligned}$$

where the Lamb shift Σ_{Lamb} and the effective qubit-qubit coupling strength g_{eff} are given by

$$\begin{aligned} \Sigma_{\text{Lamb}} &\equiv \frac{g^2}{\omega_s - \omega_b}, &(3.112)\\ g_{\text{eff}} &\equiv -\frac{g^2}{\omega_s - \omega_b}. &(3.113) \end{aligned}$$

This is confirmed by considering the projection of H_{eff} onto the subspace with lower than one excitations by applying the projector $P_{n\leq 1}$:

$$\begin{aligned} P_{n\leq 1}H_{\text{eff}}P_{n\leq 1} &= \Sigma_{\text{Lamb}}\left(|e_1g_2\rangle\langle e_1g_2| + |g_1e_2\rangle\langle g_1e_2|\right) - g_{\text{eff}}\left(\sigma_+^{(1)}\sigma_-^{(2)} + \sigma_-^{(1)}\sigma_+^{(2)}\right), \\ &= \frac{g^2}{\omega_s-\omega_b}\left(|e_1g_2\rangle + |g_1e_2\rangle\right)\left(\langle e_1g_2| + \langle g_1e_2|\right), \\ &= \frac{2g^2}{\omega_s-\omega_b}|B\rangle\langle B|. \end{aligned} \tag{3.114}$$

Note that the minus sign in front of the effective coupling g_{eff} is simply due to the sign convention of this dissertation. This effective coupling g_{eff} between the two qubits are mediated by the boson, which is visually clarified in Sec. 3.2.3. Interestingly, the Lamb shift term Σ_{Lamb} and the effective coupling g_{eff} in the single-mode boson case share the same coefficient $g^2/(\omega_s-\omega_b)$ (up to sign), which is because the qubit-qubit interaction is due to the similar process as in the Lamb shift case: the first qubit flips and emits a single boson, and then the second qubit absorbs the boson emitted by the first qubit. This is also visually explained in Sec. 3.2.3.

The qubit-qubit effective coupling g_{eff} results in the interaction of the two qubits in the form of the oscillation between the states $|e_1g_2;0\rangle$ and $|g_1e_2;0\rangle$. More explicitly, the matrix element of the time evolution operator $U(t) = \exp[-i(H_0 + H_{\text{eff}})t]$ with $H_0 = \omega_s\left(|e\rangle_1\langle e| + |e\rangle_2\langle e|\right) + \omega_b b^\dagger b$ is given by

$$\langle g_1e_2;0|U(t)|e_1g_2;0\rangle = e^{-i(\omega_{\text{s}}+\Sigma_{\text{Lamb}})t} \times i\sin\left[g_{\text{eff}}t\right]. \tag{3.115}$$

This expression will be used to verify the result we obtain in the diagrammatic approach in Sec. 3.2.3.

3.2.2 Schrieffer-Wolff transformation

The effective Hamiltonian describing the boson-mediated interaction can be derived from the Schrieffer-Wolff transformation in the same way as we derived the Lamb shift term in Sec. 3.1.2. To this end, we consider the following total Hamiltonian with two qubits coupled to multi-mode bosons

$$\mathcal{H} = H_0 + V, \tag{3.116}$$

$$H_0 = \omega_s \left(|e\rangle_1 \langle e| + |e\rangle_2 \langle e| \right) + \sum_j \omega_j b_j^\dagger b_j, \tag{3.117}$$

$$V = \sum_{i=1,2} B_-^{(i)} \sigma_+^{(i)} + B_+^{(i)} \sigma_-^{(i)}; \quad B_-^{(i)} = \sum_j g_j^{(i)} b_j; \quad B_+^{(i)} = \left(B_-^{(i)} \right)^\dagger . \tag{3.118}$$

Following the procedure provided in Sec. 3.1.2, the operator S in the Schrieffer-Wolff transformation ($\mathcal{H} \to e^S \mathcal{H} e^{-S}$) can be the following:

$$S = \sum_{i,j} \frac{g_j^{(i)} b_j \sigma_+^{(i)}}{\omega_s - \omega_j} - \text{H.c.} \tag{3.119}$$

Under this transformation, the effective Hamiltonian Eq. (3.21) becomes, in analogy to Eq. (3.29),

$$\begin{aligned} H_{\text{eff}} &= \sum_{i_1, i_2} \frac{i \int_{-\infty}^0 dt \left[B_-^{(i_1)}(t), B_+^{(i_2)}(0) \right] e^{i\omega_s t} + (\text{ H. c. } \& \; i_1 \leftrightarrow \text{i}_2)}{2} \sigma_+^{(i_1)} \sigma_-^{(i_2)} \\ &\quad + \sum_i \frac{i \int_{-\infty}^0 dt B_+^{(i)}(0) B_-^{(i)}(t) e^{i\omega_s t} + \text{H. c.}}{2} \left[\sigma_+^{(i)}, \sigma_-^{(i)} \right], \\ &= -\left(g_{\text{eff}} \sigma_+^{(1)} \sigma_-^{(2)} + g_{\text{eff}}^* \sigma_-^{(1)} \sigma_+^{(2)} \right) \\ &\quad + \sum_i \left(\Sigma_{\text{Lamb}}^{(i)} |e\rangle_i \langle e| + \sum_{j_1 j_2} \frac{g_{j_2}^{(i)*} g_{j_1}^{(i)} b_{j_2}^\dagger b_{j_1}}{2} \left[\frac{1}{\omega_s - \omega_{j_1}} + \frac{1}{\omega_s - \omega_{j_2}} \right] \sigma_z^{(i)} \right). \end{aligned} \tag{3.120}$$

Here, the Lamb shift for the qubit i and the qubit-qubit effective coupling strength g_{eff} are given by [see the first line of Eq. (3.120)]

$$\Sigma^{(i)}_{\text{Lamb}} = -\frac{\chi^*_{B_-^{(i)} B_+^{(i)}}\left[\omega_s\right] + \chi_{B_-^{(i)} B_+^{(i)}}\left[\omega_s\right]}{2} = -\,\mathrm{Re}\left[\chi_{B_-^{(i)} B_+^{(i)}}\left[\omega_s\right]\right] = \sum_i \frac{\left|g_j^{(i)}\right|^2}{\omega_s - \omega_j}, \tag{3.121}$$

$$g_{\text{eff}} = \frac{\chi^*_{B_-^{(2)} B_+^{(1)}}\left[\omega_s\right] + \chi_{B_-^{(1)} B_+^{(2)}}\left[\omega_s\right]}{2} = \chi'_{B_-^{(1)} B_+^{(2)}}\left[\omega_s\right] = -\sum_j \frac{g_j^{(2)*} g_j^{(1)}}{\omega_s - \omega_j}, \tag{3.122}$$

where $\chi_{BA}[\omega]$ is the susceptibility that we define in Eq. (3.38). Note that the primed susceptibility $\chi'_{BA}[\omega]$ appearing in the second equation is not the real part, but the first part we define in Eq. (3.98). We observe from the last line of Eq. (3.120) that there are two distinct parts in this effective Hamiltonian. One of them is the term inside the first parentheses, which describes the effective qubit-qubit interaction. The other is the terms inside the second parentheses, which is essentially the same as the single-qubit result provided in Eq. (3.29). From the expression of the effective qubit-qubit interaction Eq. (3.122), we find that this effective coupling is the average of the two response functions: (i) the response of the process where the qubit 2 emits a boson and then the boson influences the qubit 1, and the complex conjugation of (ii) the response of the process where the qubit 1 emits the boson and then the boson influences the qubit 2. This expression Eq. (3.122) in terms of the response functions ($\chi[\omega_s]$) could be used to simulate the effective coupling g_{eff} from a classical simulation of the dynamics of the boson system. Interestingly, we find by comparing Eqs. (3.121) and (3.122) that the Lamb shift $\Sigma^{(i)}_{\text{Lamb}}$ and the effective coupling constant g_{eff} take a similar form. Therefore, when two qubits' coupling constants to the boson modes are the same, i.e., $B_\pm^{(1)} = B_\pm^{(2)} \equiv B_\pm$, which occurs for example when the two qubits are on top of each other, the effective qubit-qubit coupling equals to the Lamb shift and hence the real part of the self-response (up to sign). This is made more explicit by writing

$$g_{\text{eff}}\left|_{B_{\pm}^{(1)}=B_{\pm}^{(2)}}\right. = -\Sigma_{\text{Lamb}}^{(1)} = -\Sigma_{\text{Lamb}}^{(2)} = \text{Re}\left[\chi_{B_-B_+}\left[\omega_S\right]\right], \tag{3.123}$$

or, when the coupling $g_j^{(i)}$ to the boson modes depend only on the qubit position $\mathbf{r}_{\text{q}(i)}$, we obtain

$$g_{\text{eff}}\left|_{\mathbf{r}_{\text{q}(1)}\to\mathbf{r}_{\text{q}(2)}}\right. \to \text{Re}\left[\chi_{B_-B_+}\left[\omega_S\right]\right]. \tag{3.124}$$

3.2.3 Diagrammatic approach

To obtain the graphical intuition about the boson-mediated qubit-qubit interaction, in this section we use the Feynman diagrams and show that the qubit-qubit effective interaction is due to the exchange of a (virtual) boson. To check the consistency of the result obtained from this diagrammatic approach with that we obtained in Sec. 3.2.1, we consider the single-mode boson case, although it is straightforward to extend this approach to multi-mode boson case. The total Hamiltonian in the second quantization language is given by

$$\mathcal{H} = H_0 + V, \tag{3.125}$$

$$H_0 = \omega_s\left(c_{e1}^{\dagger}c_{e1} + c_{e2}^{\dagger}c_{e2}\right) + \omega_b b^{\dagger}b, \tag{3.126}$$

$$V = \sum_{i=1,2} g\left(bc_{ei}^{\dagger}c_{gi} + b^{\dagger}c_{gi}^{\dagger}c_{ei}\right). \tag{3.127}$$

We focus on the matrix element $\langle g_1e_2;0|U(t)|e_1g_2;0\rangle$ of the time-evolution operator $U(t) = \exp[-i\mathcal{H}t]$, and we define the two-body-like Green's function $\mathfrak{G}(t)$ as

$$\mathfrak{G}(t) = (-i)^2\left\langle Tc_{g1}(t)c_{e2}(t)c_{e1}^{\dagger}(0)c_{g2}^{\dagger}(0)\right\rangle\Big|_{\text{Heis}}, \tag{3.128}$$

$$\mathfrak{G}[\omega] = \int_{-\infty}^{\infty} dt e^{i\omega t}\mathfrak{G}(t), \tag{3.129}$$

such that the time evolution for $t > 0$ is given by

$$\langle g_1 e_2; 0|U(t)|e_1 g_2; 0\rangle = i^2 \mathfrak{G}(t). \tag{3.130}$$

From the diagrammatic analysis, we obtain the frequency domain Green's function $\mathfrak{G}[\omega]$ as

$$\mathfrak{G}[\omega] \quad =$$

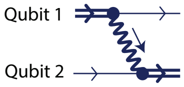

$$= \int \frac{dp}{2\pi}\frac{dq}{2\pi} \left[\mathcal{G}_0(\omega-q)\mathcal{F}(q)\cdot i\langle \omega-q, q|t|\omega-p, p\rangle \cdot \mathcal{F}(\omega-p)\mathcal{G}_0(p)\right], \tag{3.131}$$

where $\mathcal{G}_0(\omega)$ and $\mathcal{F}(\omega)$ are the ground-state propagator (thin line) and the dressed excited-state propagator (bold double line), respectively, which are defined in Sec. 3.1.3, and $\langle \omega - q, q|t|\omega - p, p\rangle$ is the T-matrix (drawn by the bold wiggly line). From the diagrammatic analysis, we obtain the following Dyson equation for the T-matrix:

$$\begin{aligned}\langle \omega-q, q|t|\omega-p, p\rangle = \quad & g^2\mathcal{D}_0(q-p) \\ & + g^4 i^2 \int \frac{d\alpha d\beta}{(2\pi)^2}\mathcal{D}_0(\alpha-p)\mathcal{G}_0(\omega-\alpha)\mathcal{F}(\alpha) \\ & \qquad \times\mathcal{D}_0(\alpha-\beta)\mathcal{F}(\omega-\beta)G_0(\beta) \\ & \qquad \times\langle \omega-q, q|t|\omega-\beta, \beta\rangle. \end{aligned} \tag{3.132}$$

While solving the above integral equation directly is possible and we will obtain the correct time evolution, here we instead provide an approximate approach with $\mathcal{F}(\omega) \approx \mathcal{F}_{\approx}(\omega)$ [i.e., approximating the dressed excited-state propagator to the approximate dressed-excited state propagator. See Eq. (3.55)] and $\mathcal{D}_0(\omega) \approx \mathcal{D}_0(\omega_s)$, which is valid for small coupling g. Then, the T-matrix becomes

$$\langle \omega-q, q|t|\omega-p, p\rangle \;=\; g_{\text{eff}} + \cdots = \frac{g_{\text{eff}}}{1-\left[\omega-(\omega_s+\Sigma_{\text{Lamb}})+i\epsilon\right]^{-2} g_{\text{eff}}^2}, \tag{3.133}$$

$$g_{\text{eff}} \;=\; g^2\mathcal{D}_0(\omega_s), \tag{3.134}$$

where Σ_{Lamb} is the Lamb shift (self-energy) we define in Sec. 3.2.1. We find that the effective coupling g_{eff} is the boson propagator multiplied by the qubit-boson coupling. Substituting Eq. (3.133) into Eq. (3.131), we obtain

$$\mathfrak{G}[\omega] \approx \int \frac{dp}{2\pi}\frac{dq}{2\pi}\left[\mathcal{G}_0(\omega-q)\mathcal{F}_{\approx}(q)\cdot i\frac{g_{\mathrm{eff}}}{1-(\omega-(\omega_s+\Sigma_{\mathrm{Lamb}})+i\epsilon)^{-2}\,g_{\mathrm{eff}}^2}\cdot\mathcal{F}_{\approx}(\omega-p)\mathcal{G}_0(p)\right]. \tag{3.135}$$

Performing the inverse Fourier transformation, we obtain the time evolution that is consistent with Sec. 3.2.1:

$$\langle g_1 e_2; 0|U(t)|e_1 g_2; 0\rangle = i^2\mathfrak{G}(t) \approx e^{-i(\omega_{\mathrm{s}}+\Sigma_{\mathrm{Lamb}})t}\times i\sin\left[g_{\mathrm{eff}}t\right]. \tag{3.136}$$

The argument provided so far, especially the diagram drawn in Eq. (3.131) and the expression of the effective coupling in terms of the propagator Eq. (3.134), clarifies that the effective qubit-qubit coupling is due to the exchange of a boson between the two qubits. Sometimes, as the wiggly line in Eq. (3.131) is an intermediate process appearing in the perturbation and the there is no on-resonant ("on-shell" in some quantum field theory literatures [57]) boson, this boson is called a virtual ("off-shell") boson. In conclusion, we can phrase that the effective qubit-qubit coupling is due to the exchange of a virtual boson.

3.2.4 Lindblad master equation under Born-Markov approximation

Lastly, for completeness we show the two-qubit case of the derivation of the effective time evolution of the qubit density matrix ρ in the Lindblad master equation formalism. We take the initial total Hamiltonian to be that of the two qubits coupled to multi-mode boson bath:

$$\mathcal{H} = H_0 + H_B + V, \tag{3.137}$$

$$H_0 = \omega_s \left(|e\rangle_1 \langle e| + |e\rangle_2 \langle e| \right), \tag{3.138}$$

$$H_B = \sum_j \omega_j b_j^\dagger b_j, \tag{3.139}$$

$$V = \sum_i B_-^{(i)} \sigma_+^{(i)} + B_+^{(i)} \sigma_-^{(i)}; \quad B_-^{(i)} \equiv \sum_j g_j^{(i)} b_j; \quad B_+^{(i)} = \left(B_-^{(i)} \right)^\dagger. \tag{3.140}$$

In the same way as in Sec. 3.1.4, under the Born-Markov approximation and for the thermal boson bath which is stationary, and assuming $\langle B_-^{(i_1)}(t) B_-^{(i_2)}(0) \rangle = \langle B_+^{(i_1)}(t) B_+^{(i_2)}(0) \rangle = 0$ which is valid in our case (or applying the secular approximation), we obtain the equation of motion for the reduced qubit density operator ρ as

$$\frac{d}{dt}\rho(t) = -i \left[H_0 + H_{\text{eff}}, \rho \right] + \mathcal{N}[\rho(t)], \tag{3.141}$$

$$H_{\text{eff}} = -\left(g_{\text{eff}} \sigma_+^{(1)} \sigma_-^{(2)} + g_{\text{eff}}^* \sigma_-^{(1)} \sigma_+^{(2)} \right) + \sum_i \left(\Sigma_{\text{Lamb}}^{(i)} |e\rangle_i \langle e| + \Sigma_{\text{Stark}}^{(i)} \sigma_z^{(i)} \right), \tag{3.142}$$

$$\begin{aligned} \mathcal{N}[\rho(t)] = & \sum_{i_1, i_2} i G^<_{B_-^{(i_1)} B_+^{(i_2)}} [\omega_s] \, \mathcal{L}\left[\sigma_+^{(i_1)}, \sigma_+^{(i_2)} \right] \rho \\ & + \sum_{i_1, i_2} i G^>_{B_-^{(i_1)} B_+^{(i_2)}} [\omega_s] \, \mathcal{L}\left[\sigma_-^{(i_2)}, \sigma_-^{(i_1)} \right] \rho, \end{aligned} \tag{3.143}$$

where the the Lamb shfit $\Sigma_{\text{Lamb}}^{(i)}$ and the effective coupling g_{eff} are provided in Eqs. (3.121) and (3.122), and the Stark shift is given by

$$\Sigma_{\text{Stark}}^{(i)} \equiv \sum_j \frac{\left| g_j^{(i)} \right|^2 n_B(\omega_j)}{\omega_s - \omega_j}. \tag{3.144}$$

We also defined the two-argument Lindblad operator

$$\mathcal{L}[X, Y]\rho \equiv X \rho Y^\dagger - \frac{1}{2} \left\{ Y^\dagger X, \rho \right\}, \tag{3.145}$$

such that when the two arguments are the same, it reduces to the standard Lindblad operator $\mathcal{L}[X,X]=\mathcal{L}[X]$. The greater and the lesser Green's function in Eq. (3.143) can be explicitly written as

$$iG^{>}_{B_-^{(i_1)}B_+^{(i_2)}}[\omega_s]=\left(n_B\left(\omega_s\right)+1\right)\sum_j g_j^{(i_2)*}g_j^{(i_1)}2\pi\delta\left(\omega_s-\omega_j\right), \tag{3.146}$$

$$iG^{<}_{B_-^{(i_1)}B_+^{(i_2)}}[\omega_s]=n_B\left(\omega_s\right)\sum_j g_j^{(i_2)*}g_j^{(i_1)}2\pi\delta\left(\omega_s-\omega_j\right). \tag{3.147}$$

We note in Eq. (3.143) that the terms in the summation with $i_1=i_2$ are essentially the same as what we obtained in the single qubit case [Eq. (3.74)]:

$$\mathcal{N}[\rho(t)]|_{i_1=i_2}=\sum_i\left(iG^{<}_{B_-^{(i)}B_+^{(i)}}[\omega_s]\,\mathcal{L}\left[\sigma_+^{(i)}\right]\rho+iG^{>}_{B_-^{(i)}B_+^{(i)}}[\omega_s]\,\mathcal{L}\left[\sigma_-^{(i)}\right]\rho\right). \tag{3.148}$$

However, there are also additional terms in Eq. (3.143), such as the terms with $\mathcal{L}[\sigma_-^{(1)},\sigma_-^{(2)}]$. We call these as correlated decay dissipation terms, as they are related to operators such as $\mathcal{L}[\sigma_-^{(1)}+\sigma_-^{(2)}]$. For example,

$$\mathcal{L}\left[\sigma_-^{(1)}+\sigma_-^{(2)}\right]=\mathcal{L}\left[\sigma_-^{(1)}\right]+\mathcal{L}\left[\sigma_-^{(2)}\right]+\mathcal{L}\left[\sigma_-^{(1)},\sigma_-^{(2)}\right]+\mathcal{L}\left[\sigma_-^{(2)},\sigma_-^{(1)}\right]. \tag{3.149}$$

Noticing that $\mathcal{L}[\sigma_-^{(1)}+\sigma_-^{(2)}]$ describes the decay process of $|e_1e_2\rangle\to(|g_1e_1\rangle+|e_1g_2\rangle)/\sqrt{2}$, it makes sense to call its effect as the correlated decay dissipation.

Interestingly, the time scale of the correlated decay process are related to the qubit-qubit interaction via the fluctuation-dissipation and the Kramers-Kronig relation, which can be shown through a similar argument as that provided in Sec. 3.1.4 where the T1 decay rate is related to the Lamb shift. We define the rate of the correlated decay process as

$$1/T_1^{(\mathrm{corr})}=iG^{>}_{B_-^{(1)}B_+^{(2)}}[\omega_s]+iG^{<}_{B_-^{(1)}B_+^{(2)}}[\omega_s]=iG^{K}_{B_-^{(1)}B_+^{(2)}}[\omega_s], \tag{3.150}$$

where $G^K_{B^{(1)}_- B^{(2)}_+}[\omega_s]$ is the Keldysh Green's function defined in Eq. (3.81). Using the fluctuation-dissipation relation [Eq. (3.93) with zero chemical potential $\mu = 0$] and the definition of the second part of the susceptibility [Eq. (3.99)], we obtain in analogy to Eq. (3.87) the following:

$$\begin{aligned} 1/T_1^{(\mathrm{corr})} &= iG^K_{B^{(1)}_- B^{(2)}_+}[\omega_s] = A_{B^{(1)}_- B^{(2)}_+}[\omega_s]\cosh[\beta\omega_s/2], \\ &= 2\chi''_{B^{(1)}_- B^{(2)}_+}[\omega_s]\cosh[\beta\omega_s/2]. \end{aligned} \tag{3.151}$$

Therefore, the correlated decay rate $1/T_1^{(\mathrm{corr})}$ is proportional to the second part (not imaginary part) of the susceptibility, which should be seen in contrast to the effective qubit-qubit coupling g_{eff} provided in Eq. (3.122), which is the first part of the susceptibility. Using the Kramers-Kronig relation shown in Eq. (3.100), we obtain the relation between them with the assumption that we have access to the frequency dependence $T_1^{(\mathrm{corr})} = T_1^{(\mathrm{corr})}[\omega]$:

$$g_{\mathrm{eff}} = \chi'_{B^{(1)}_- B^{(2)}_+}[\omega_s] = -\mathcal{P}\int_{-\infty}^{\infty} \frac{d\omega'}{\pi}\frac{1}{\omega_s - \omega'}\cdot\frac{1/T_1^{(\mathrm{corr})}[\omega']}{2\coth[\beta\omega'/2]}. \tag{3.152}$$

This equation clearly shows the connection of the correlated decay rates and the effective qubit-qubit interaction in analogy to Eq. (3.90).

3.3 Quantum-mechanical derivation of magnetic dipole-dipole interaction of spin qubits mediated by photons

In this section, we derive photon-mediated magnetic dipole-dipole interaction between two spins as an example of the boson-mediated qubit-qubit interaction. We follow the argument provided in Ref. [63] with the use of the effective Hamiltonian derived in our previous sections [see Eqs. (3.21) and (3.65)], and we obtain the conventional result where the interaction scales as $\propto r_{21}^{-3}$ with the qubit-qubit distance r_{21}. We start from the following total Hamiltonian for two spin-1/2 systems (qubits) coupled to the magnetic field that is quantized using the Coulomb gauge:

$$\mathcal{H} = H_0 + H_{\text{EM}} + V, \tag{3.153}$$

$$H_0 = \omega_{s,1}|e\rangle_1\langle e| + \omega_{s,2}|e\rangle_2\langle e|, \tag{3.154}$$

$$H_{\text{EM}} = \sum_{\mathbf{k},\sigma} \omega_{|\mathbf{k}|} b^\dagger_{\mathbf{k}\sigma} b_{\mathbf{k}\sigma}; \quad \omega_{|\mathbf{k}|} = c|\mathbf{k}|, \tag{3.155}$$

$$V = -\boldsymbol{\mu}_1 \cdot \mathbf{B}\left(\mathbf{x}_1\right) - \boldsymbol{\mu}_2 \cdot \mathbf{B}\left(\mathbf{x}_2\right), \tag{3.156}$$

where $\omega_{s,i}$ is the qubit frequency labeled by $i = 1, 2$, H_{EM} is the electromagnetic field Hamiltonian, c is the speed of light, $\sigma = 1, 2$ labels the photon linear polarization, $\mathbf{x}_i$ is the position of the qubit i, and $\boldsymbol{\mu}_i$ is the magnetic dipole operator for the spin i:

$$\boldsymbol{\mu}_i = \frac{(-1)g\mu_{\text{B}}}{2}\sigma^{(i)} = \frac{(-1)g\mu_{\text{B}}}{2}\left(\hat{\epsilon}_-^{(i)}\sigma_+^{(i)} + \hat{\epsilon}_+^{(i)}\sigma_-^{(i)} + \hat{z}^{(i)}\sigma_z^{(i)}\right), \tag{3.157}$$

$$\hat{\epsilon}_\pm^{(i)} \equiv \hat{x}^{(i)} \pm i\hat{y}^{(i)}. \tag{3.158}$$

Here, g is the g-factor of the spin, μ_{B} is the Bohr magneton, the unit vector $\hat{z}_i$ is parallel to the quantization direction of the qubit spin i, and the non-normalized complex vectors $\{\hat{\epsilon}_-^{(i)}, \hat{\epsilon}_+^{(i)}\}$ are orthogonal to $\hat{z}^{(i)}$. The magnetic field operator $\mathbf{B}(\mathbf{x})$ is written in terms of the photon creation and annihilation operators ($b^\dagger_{\mathbf{k}\sigma}$ and $b_{\mathbf{k}\sigma}$) as

$$\mathbf{B}(\mathbf{x}) = i\sum_{\mathbf{k},\sigma} Z_{|\mathbf{k}|}(\hat{k} \times \vec{e}_{\mathbf{k}\sigma})\left(b_{\mathbf{k}\sigma}e^{i\mathbf{k}\cdot\mathbf{x}} - b^\dagger_{\mathbf{k}\sigma}e^{-i\mathbf{k}\cdot\mathbf{x}}\right), \tag{3.159}$$

$$Z_{|\mathbf{k}|} \equiv \sqrt{\frac{\mu_0\omega_{|\mathbf{k}|}}{2V}}, \tag{3.160}$$

where V is the volume of the real space where the Fourier transform is performed and $\vec{e}_{\mathbf{k}\sigma}$ is the polarization vector (unit vector of the linear polarization σ). As counter-rotating terms such as $b_{\mathbf{k}\sigma}\sigma_-^{(i)}$ turn out to also contribute to the qubit-qubit interaction, we do not apply the rotating-wave approximation. This is implied by the fact that the coupling $Z_{|\mathbf{k}|}$ becomes larger with higher energies $\omega_{|\mathbf{k}|}$, which competes with the detuning $\omega_{|\mathbf{k}|} - \omega_{s,i}$ appearing in the denominator when computing the effective interaction. From Eqs. (3.21) or (3.65), the effective Hamiltonian of the two-qubit system becomes

$$\begin{aligned} H_{\text{eff}} &= \frac{i}{2}\int_{-\infty}^{0} dt' \left[V\left(t'\right), V(0)\right], \\ &= \frac{i}{2}\int_{-\infty}^{0} dt' \sum_{i_1,i_2} \left[\boldsymbol{\mu}_{i_1}\left(t'\right)\cdot \mathbf{B}\left(\mathbf{x}_{i_1}, t'\right), \boldsymbol{\mu}_{i_2}\cdot \mathbf{B}\left(\mathbf{x}_{i_2}\right)\right]. \end{aligned} \tag{3.161}$$

The above expression includes both the self-interaction part and the qubit-qubit interaction part. As we care about the qubit-qubit interaction, we do not treat the possible divergence of the self-interaction and we focus on the following qubit-qubit interaction part:

$$H_{\text{eff}}^{\text{qubit}-\text{qubit}} = \frac{i\int_{-\infty}^{0} dt' \left[\boldsymbol{\mu}_1\left(t'\right)\cdot \mathbf{B}\left(\mathbf{x}_1, t'\right), \boldsymbol{\mu}_2\cdot \mathbf{B}\left(\mathbf{x}_2\right)\right] + (1 \leftrightarrow 2)}{2}. \tag{3.162}$$

As the time-evolution of $\boldsymbol{\mu}_i(t)$ appears only in the form of the phase evolution $e^{i\theta t}$ for some real number θ, i.e.,

$$\boldsymbol{\mu}_i(t) = \frac{(-1)g\mu_B}{2}\left(\hat{\epsilon}_-^{(i)}\sigma_+^{(i)}e^{+i\omega_{s,i}t} + \hat{\epsilon}_+^{(i)}\sigma_-^{(i)}e^{-i\omega_{s,i}t} + \hat{z}^{(i)}\sigma_z^{(i)}\right), \tag{3.163}$$

we only need to evaluate the following frequency domain Green's function:

$$\begin{aligned} \overleftrightarrow{G}_{\mathbf{B}(\mathbf{x}_1)\mathbf{B}(\mathbf{x}_2)}[\omega] &\equiv i\int_{-\infty}^{0} dt' \left[\mathbf{B}\left(\mathbf{x}_1, t'\right), \mathbf{B}\left(\mathbf{x}_2\right)\right] e^{i\omega t}, \\ &= -\overleftrightarrow{\chi}_{\mathbf{B}(\mathbf{x}_2)\mathbf{B}(\mathbf{x}_1)}[-\omega], \end{aligned} \tag{3.164}$$

where its tensor elements need to be appropriately chosen. In the second equality, we use the following relation valid when $[B(t), A(0)] = [B(0), A(-t)]$, which is satisfied in our current setting or for stationary states in general,

$$G^{A}_{BA}[\omega] = G^{R}_{AB}[-\omega], \tag{3.165}$$

and we also use the definition of the susceptibility in terms of the retarded Green's function [Eq. (3.38)]. Then, Eq. (3.162) turns into the following form:

$$H_{\text{eff}}^{\text{qubit}-\text{qubit}} = -\frac{\boldsymbol{\mu}_2 \cdot \overleftrightarrow{\chi}_{\mathbf{B}(\mathrm{x}_2)\mathbf{B}(\mathrm{x}_1)} \left[\omega = 0, \pm\omega_{s,1}\right] \cdot \boldsymbol{\mu}_1 + (1 \leftrightarrow 2)}{2}, \tag{3.166}$$

where the frequency argument of the susceptibility $\overleftrightarrow{\chi}_{\mathbf{B}(\mathbf{x}_2)\mathbf{B}(\mathbf{x}_1)}[\omega]$ needs to be appropriately chosen when performing the dot product with $\boldsymbol{\mu}_1$. For example in the first term, $\omega = +\omega_{s,1}$ ($\omega = -\omega_{s,1}$) needs to be chosen when it is multiplied by $\sigma_-^{(1)}$ ($\sigma_+^{(1)}$) and $\omega = 0$ when $\sigma_z^{(1)}$. Now, the response function to be evaluated is

$$\begin{aligned} &\overleftrightarrow{\chi}_{\mathbf{B}(\mathbf{x}_2)\mathbf{B}(\mathbf{x}_1)}(t) = i\theta(t)\left[\mathbf{B}\left(\mathbf{x}_2, t\right), \mathbf{B}\left(\mathbf{x}_1\right)\right], \\ &= i\theta(t)\sum_{\mathbf{k},\sigma}\frac{\mu_0\omega_k}{2V}\left(e^{i\mathbf{k}\cdot(\mathbf{x}_2-\mathbf{x}_1)-i\omega_k t} - e^{-i\mathbf{k}\cdot(\mathbf{x}_2-\mathbf{x}_1)+i\omega_k t}\right)(\hat{k}\times\vec{e}_{\mathbf{k}\sigma})\otimes(\hat{k}\times\vec{e}_{\mathbf{k}\sigma}). \end{aligned} \tag{3.167}$$

In the frequency domain, we obtain

$$\begin{aligned} \overleftrightarrow{\chi}_{\mathbf{B}(\mathbf{x}_2)\mathbf{B}(\mathbf{x}_1)}[\omega] &= \sum_{\mathbf{k},\sigma}\frac{\mu_0\omega_k}{2V}\left(-\frac{e^{i\mathbf{k}\cdot(\mathbf{x}_2-\mathbf{x}_1)}}{\omega-\omega_k+i\eta} + \frac{e^{-i\mathbf{k}\cdot(\mathbf{x}_2-\mathbf{x}_1)}}{\omega+\omega_k+i\eta}\right)(\hat{k}\times\vec{e}_{\mathbf{k}\sigma})\otimes(\hat{k}\times\vec{e}_{\mathbf{k}\sigma}), \\ &= \int\frac{d\mathbf{k}}{(2\pi)^3}\frac{\mu_0\omega_k}{2}\left(-\frac{e^{i\mathbf{k}\cdot(\mathbf{x}_2-\mathbf{x}_1)}}{\omega-\omega_k+i\eta} + \frac{e^{-i\mathbf{k}\cdot(\mathbf{x}_2-\mathbf{x}_1)}}{\omega+\omega_k+i\eta}\right)(I-\hat{\Omega}\otimes\hat{\Omega}). \end{aligned} \tag{3.168}$$

Here, in the second line we replace the sum over $\mathbf{k}$ into the integral and use $\sum_\sigma(\hat{k}\times\vec{e}_{\mathbf{k}\sigma})\otimes(\hat{k}\times\vec{e}_{\mathbf{k}\sigma}) = \hat{I} - \hat{\Omega}\otimes\hat{\Omega}$, where $\hat{\Omega} = \hat{k} = \mathbf{k}/|\mathbf{k}|$ is the unit vector in the direction of $\mathbf{k}$. We change this notation to make it explicit that the unit vector $\hat{\Omega}$ is independent of the radial component of the wave vector $k = |\mathbf{k}|$. Writing the integral over $\mathbf{k}$ into the angular part

$\int d\Omega = \int d\cos\theta d\phi$ [θ is the angle between $\mathbf{k}$ and $\mathbf{x}_2 - \mathbf{x}_1$] and the radial part $\int_0^\infty dk$, we obtain after combining the two terms in Eq. (3.168) by changing the variable $k \to -k$ for the second term:

$$\begin{aligned} \overleftrightarrow{\chi}_{\mathbf{B}(\mathbf{x}_2)\mathbf{B}(\mathbf{x}_1)}[\omega] &= \int_{-\infty}^{\infty} \frac{dkk^2}{(2\pi)^3} \frac{\mu_0 ck}{2} \cdot \frac{-1}{\omega - ck + i\eta} \int d\Omega (I - \widehat{\Omega} \otimes \widehat{\Omega}) e^{ik|\mathbf{x}_2 - \mathbf{x}_1| \cos\theta}, \\ &= \frac{\mu_0}{4\pi} \cdot \frac{1}{|\mathbf{x}_2 - \mathbf{x}_1|^3} \int_{-\infty}^{\infty} \frac{d\xi}{\pi} \frac{\xi^3}{\xi - \xi_\omega - i\eta} \int \frac{d\Omega}{4\pi} (I - \widehat{\Omega} \otimes \widehat{\Omega}) e^{i\xi \cos\theta}, \end{aligned} \tag{3.169}$$

where in the second line we changed the integration variable $\xi = k|\mathbf{x}_2 - \mathbf{x}_1|$ and ξ_ω is the phase that electromagnetic waves with (angular) frequency ω will accumulate after the propagation of a distance $|\mathbf{x}_2 - \mathbf{x}_1|$:

$$\xi_\omega = \omega |\mathbf{x}_2 - \mathbf{x}_1| / c. \tag{3.170}$$

After a direct evaluation of the integrals with a regulator for oscillating non-convergent integrals, we obtain

$$\begin{aligned} &\overleftrightarrow{\chi}_{\mathbf{B}(\mathbf{x}_2)\mathbf{B}(\mathbf{x}_1)}[\omega] \\ &= -\frac{\mu_0}{4\pi} \frac{1}{|\mathbf{x}_2 - \mathbf{x}_1|^3} \left[(\cos\xi_\omega + \xi_\omega \sin\xi_\omega) \left(\hat{I} - 3\hat{r}_{21} \otimes \hat{r}_{21} \right) - \xi_\omega^2 \cos\xi_\omega \left(\hat{I} - \hat{r}_{21} \otimes \hat{r}_{21} \right) \right], \\ &\quad + \frac{\mu_0}{4\pi} \frac{1}{|\mathbf{x}_2 - \mathbf{x}_1|^3} i \left[f(\xi_\omega) \hat{I} + g(\xi_\omega) \hat{r}_{21} \otimes \hat{r}_{21} \right], \end{aligned} \tag{3.171}$$

$$f(\xi) = \xi^2 \sin\xi + \xi \cos\xi - \sin\xi, \tag{3.172}$$

$$g(\xi) = -\xi^2 \sin\xi - 3\xi \cos\xi + 3\sin\xi, \tag{3.173}$$

where $\hat{r}_{21} = (\mathbf{x}_2 - \mathbf{x}_1)/|\mathbf{x}_2 - \mathbf{x}_1|$ is the unit vector along the direction $\mathbf{x}_2 - \mathbf{x}_1$. Note that Eq. (3.171) may have a sign mismatch with Ref. [63], but it is consistent with Ref. [64]. When the spin-spin distance is much smaller than the wavelength of the photon with qubit frequency $\omega_{s,i}$, we have $\xi_\omega \ll 1$ and the susceptibility becomes

$$\overleftrightarrow{\chi}_{\mathbf{B}(\mathbf{x}_2)\mathbf{B}(\mathbf{x}_1)}[\omega] = -\frac{\mu_0}{4\pi}\frac{1}{|\mathbf{x}_2 - \mathbf{x}_1|^3}\left[\left(\hat{I} - 3\hat{r}_{21}\otimes\hat{r}_{21}\right) + \mathcal{O}\left(\xi_\omega^2\right)\right]. \tag{3.174}$$

This reduces to the standard magnetic dipole-dipole interaction between the spins:

$$H_{\text{eff}}^{\text{qubit}-\text{qubit}} \approx \frac{\mu_0}{4\pi}\frac{\boldsymbol{\mu}_2\cdot\left(\hat{I} - 3\hat{r}_{21}\otimes\hat{r}_{21}\right)\cdot\boldsymbol{\mu}_1}{|\mathbf{x}_2 - \mathbf{x}_1|^3}, \tag{3.175}$$

indicating that the magnetic dipole-dipole interaction between spins can be thought of as a consequence of the exchange of virtual photons, which completes the discussion in this chapter.

Chapter 4

All-optical cryogenic thermometry based on NV centers in nanodiamonds

4.1 Introduction

In this chapter, we show that temperature sensing based on nitrogen-vacancy (NV) center ensembles in diamond have great applicability in studying the nontrivial emergent thermal effects in yttrium-iron-garnet (YIG). Especially, we provide a new platform with NV centers as temperature sensors to study the spin caloritronic effects in YIG such as the spin Seebeck effect [65–69], where local temperature variation plays a central role. The spin Seebeck effect is a phenomenon where a spin current is generated as a consequence of a temperature gradient in a magnetic material. While the NV centers are widely known as an excellent magnetic field sensor, their thermometry has been a focus only recently. Additionally, the NV center's sensing stability across a wide range of temperatures [70] and magnetic fields makes it suitable for studying these spin caloritronic effects, as they need to be studied as a function of temperature and magnetic field [66]. With a recently developed array of nanodiamonds (NDs) embedded within a portable polydimethylsiloxane (PDMS) sheet [71], we can scan local temperature variations of the YIG substrate without disturbing its temperature profile.

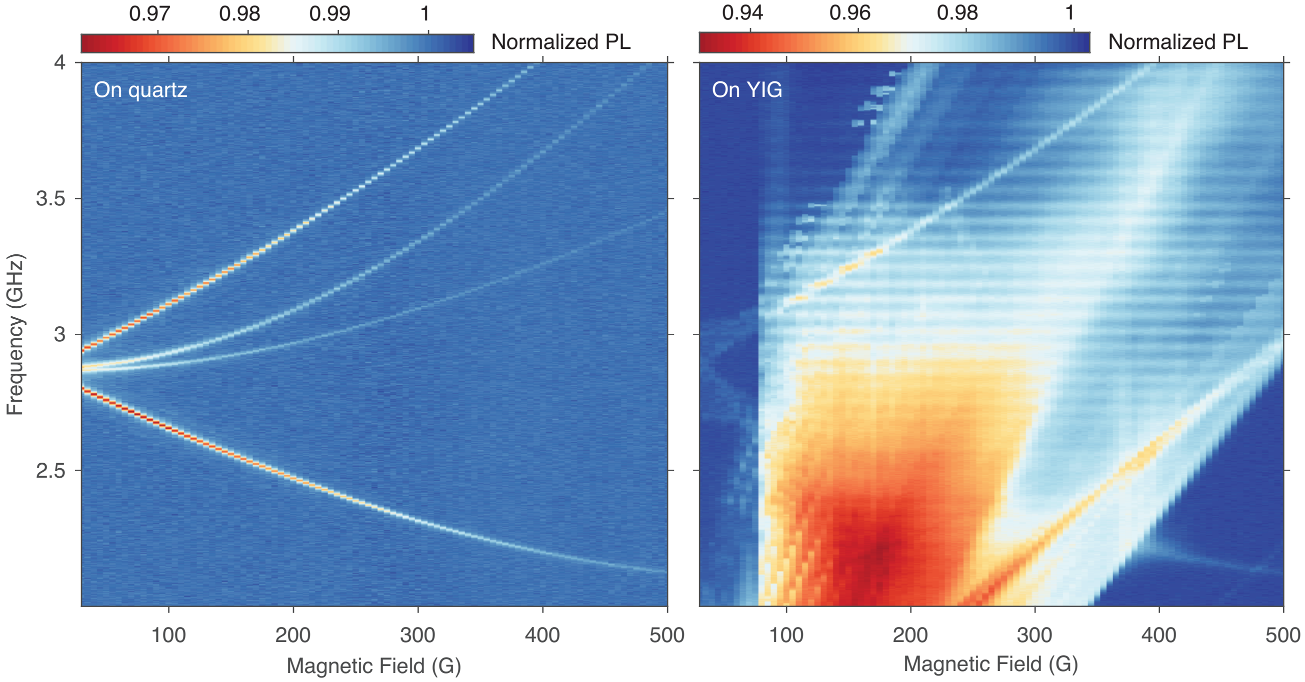

Figure 4.1: (a) ODMR of an ensemble of NV centers in a bulk diamond created by nitrogen implantation, where the diamond is placed on a quartz substrate and the NV layer is facing the quartz. (b) ODMR of the same diamond sample as described in (a), where the diamond is placed on an YIG substrate and the NV layer is facing the YIG. The magnetic field is applied in plane of the quartz or the YIG substrate, which is along the (110) direction of the diamond crystal.

We avoid the need to interface bulk diamond with the YIG substrate, which would provide and additional path for heat transfer.

There are, however, a few obstacles for NV thermometry on YIG [65–69]. One is the magnetic noise caused by the YIG substrates, which can destroy the NV center's microwave resonances. In Fig. 4.1, we show the optically detected magnetic resonance (ODMR) image of a shallow ensemble of NV centers made by nitrogen implantation in a bulk diamond as a function of the external magnetic field and the applied microwave frequency with [See (b)] and without [See (a)] the YIG substrate. Clearly, the sharp resonances visible in Fig. 4.1(a) are overwhelmed by an additional large signal in Fig. 4.1(b), which is due to the magnetic noise caused by the spin-wave resonances in YIG [72]. This poses a technical challenge of performing the standard thermometry technique with NV center's spin transitions driven

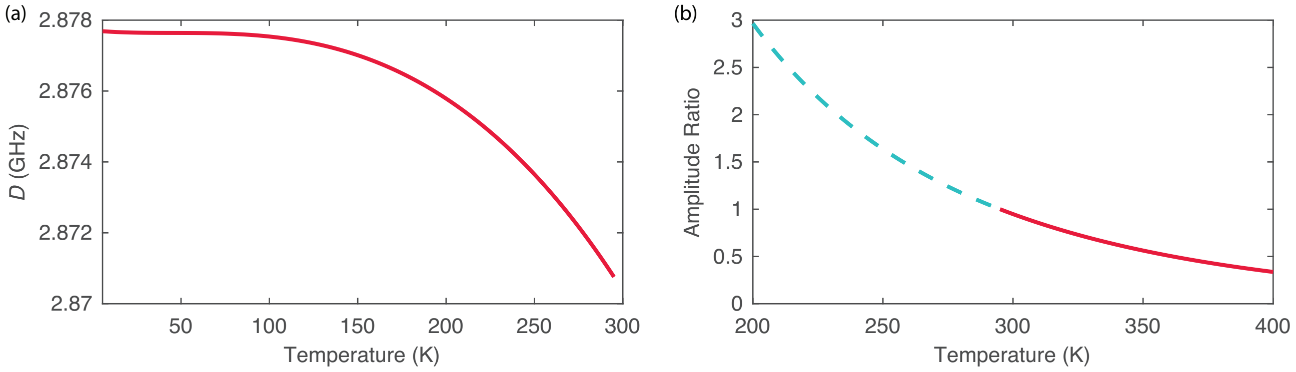

Figure 4.2: (a) Schematic of the temperature dependence of the zero-field splitting D. The curve is drawn from the fit parameters provided in [73]. (b) Schematic of the temperature dependence of the zero-phonon-line (ZPL) amplitude ratio drawn with the equation provided in [74]. The solid curve is drawn for the temperature range provided in [74], while the dashed curve is the extrapolation to lower temperatures.

by microwaves, and adds a concern of microwave heating in the YIG substrate. Another obstacle of the NV-center-based thermometry is the difficulty of using the conventional thermometry techniques based on the shift in the zero-field splitting D at low temperatures, whose study is largely confined to room temperature (and above) applications. As shown in Fig. 4.2(a), the temperature dependence of the zero-field splitting D is weaker at cryogenic temperatures, as the shift is due to lattice contraction. This weaker dependency leads to lower temperature sensitivity at lower temperatures. As the study of the spin Seebeck effect is typically performed from room temperature (and above) down to cryogenic temperatures (100 K and below), it is favorable for the temperature sensor to be able to scan the temperature variations at cryogenic temperatures in addition to room remperature.

Here we use an alternative approach that does not require microwaves, ratiometric all-optical thermometry [74–80]. This technique makes use of the temperature dependence of the zero-phonon-line amplitude ratio with respect to the phonon sideband fluorescence. This method only requires a spectrometer (in addition to a laser) and does not use microwaves. As shown in Fig. 4.2(b), the extrapolation of the model equation provided in [74] is expected to show stronger dependence at lower temperature [See the dashed curve], in contrast to the zero-field splitting [Fig. 4.2(a)]. Using this technique, we demonstrate that it may be utilized to liquid nitrogen temperatures without deterioration of the sensitivity. The use of an array of NDs on a polydimethylsiloxane (PDMS) sheet [71] combined with all-optical thermometry completely removes configurational restrictions needed for microwave applications, offering a versatile device capable of probing a wide variety of solid-state systems over tens of microns with an adjustable spatial resolution on the order of a few microns. This makes all-optical thermometry suitable for probing and imaging a variety of condensed matter systems, and may have advantages over conventional NV-center thermometry techniques depending on the required thermal or spatial resolutions as well as the potential microwave response of the target system.

4.1.1 Extrapolation of the temperature dependence of all-optical thermometry

Reference [74] provides a model that explains the temperature dependence of the zero-phonon line (ZPL) amplitude ratio under temperature range 295 K$\leq T \leq$ 400 K. The ZPL spectrum is fit by a sum of the Lorenzian function and an exponential function with the coefficient A and B, respectively. More specifically, the χ^2 minimization scheme is used:

$$\chi^2 = \sum_n \left(N_n - B\mathrm{e}^{bn} - \frac{A\Gamma^2}{\Gamma^2 + (n - n_0)^2} \right)^2 , \tag{4.1}$$

where N_n is the number of photons detected in nth spectral bin divided by the integral intensity of the spectrum in the experimental spectral window (from 610 to 660 nm), Γ is the linewidth, n_0 is the center of the Lorenzian spectrum, and b represents the slope of hte exponential. In the model provided in [74], the ratio A is proportional to the Debye-Waller factor (DWF) divided by a ZPL linewith Γ, as the Zero-phonon-line total photon emission is proportional to $\propto A\Gamma$. The linewidth Γ is taken to be proportional to $\propto T^2$, and the temperature dependence of the DWF is taken to be

$$(\mathrm{DWF}) = \exp\left[-S\left(1+\frac{2}{3}\pi^2\left(\frac{T}{T_D}\right)^2\right)\right], \tag{4.2}$$

where S is the electron-phonon coupling parameter (Huang-Rhys factor) and T_D is the Debye temperature. Its derivation is shown later. Then the temperature dependence of the ratio A is given by

$$A = \alpha T^{-2} \exp\left(-\gamma T^2\right), \tag{4.3}$$

resulting in the temperature response

$$\left|\frac{dA}{dT}\right| = 2T\left(T^{-2}+\gamma\right)A, \tag{4.4}$$

where α and γ are temperature independent constants, and γ is related to the (temperature independent) electron-phonon coupling parameter S and the Debye temperature T_D via $\gamma = 2\pi^2 S/(3T_D^2)$. We note that the DWF is defined as the ratio of the integral ZPL intensity to the total PL. From this expression, the temperature response is expected to be larger at lower temperatures, which potentially gives rise to a higher temperature sensitivity at lower temperatures though it also depends on the uncertainty of the measurement of the ratio A. The uncertainty σ_A is given by

$$\sigma_A = \frac{f(r)A}{\sqrt{C_{\mathrm{ZPL}}\Delta t}}, \tag{4.5}$$

$$f(r) = \sqrt{c_1 + c_2 r + c_3\sqrt{r^2+r}}, \tag{4.6}$$

where $[c_1, c_2, c_3] = [3, 3, 1]$, $r = B/A$, C_{ZPL} is the ZPL counts rate, and Δt is the measurement time. From Eq. (4.5), the temperature sensitivity, or the noise floor, becomes

$$\eta \equiv \sigma_A \sqrt{\Delta t} |dT/dA| = \frac{T f(r)}{2\left(1 + \gamma T^2\right)\sqrt{C_{\text{ZPL}}}}. \tag{4.7}$$

Assuming for simplicity that the temperature dependence of the total PL is negligible, we obtain

$$C_{\text{ZPL}} = C_{\text{tot}} (\text{DWF})|_{T=0} \exp\left(-\gamma T^2\right), \tag{4.8}$$

where C_{tot} is the total PL counts rate and $(\text{DWF})|_{T=0}$ is the DWF at absolute zero temperature. From Eqs. (4.7) and (4.8), we obtain

$$\eta = \frac{T f(r)}{2\left(1 + \gamma T^2\right)\sqrt{C_{\text{tot}}\ (\text{DWF})|_{T=0}}} \exp\left(\frac{1}{2}\gamma T^2\right). \tag{4.9}$$

As the temperature decreases, the background factor $r = B/A$ decreases as the phonon-side-band emission under the ZPL Lorenzian becomes smaller, which is not shown in [74] but is confirmed in a regime 85 K$\leq T \leq$ 300 K in this work. Then we obtain $d\eta/dT > 0$, demonstrating an improved sensitivity at lower temperatures (note that the smaller η gives the better sensitivity), at least in a regime 300 K$\leq T \leq$ 400 K where the model is confirmed.

4.1.2 Derivation of the temperature dependence of the Debye-Waller factor

The temperature dependence of the Debye-Waller factor [Eq. (4.2)] is initially used to explain the temperature dependence of the fraction of the ZPL emission with respect to the total fluorescence in the color centers in Alkali metal halide [81]. Its derivation is as follows. We consider an electron dipole transition coupled to a phonon mode labeled by i with mode frequency ω_i, under the Born-Oppenheimer approximation [55] and a linear coupling.

The ground state and the excited state potentials, i.e., the potential for the lattice when the electron is in the ground state and the excited state, are given by $V_g^i(q)$ and $V_e^i(q)$, respectively, with

$$V_g^i(q) = \frac{1}{2} m\omega_i^2 q^2, \tag{4.10}$$

$$\begin{aligned} V_e^i(q) &= E_{eg} + a_i \hbar\omega_i \left(q/x_{0,i}\right) + \frac{1}{2} m\omega_i^2 q^2, \\ &= E_{eg} + \frac{1}{2} m\omega_i^2 \left(q + a_i x_{0,i}\right)^2 - \frac{a_i^2}{2}\hbar\omega_i, \end{aligned} \tag{4.11}$$

where $x_{0,i} \equiv (\hbar/m\omega_i)^{1/2}$, q is the lattice coordinate, m is the lattice atom mass, a_i is the linear coupling constant, and E_g and E_e are the ground state and the excited state electron energies, respectively. From Eq. (4.11), it is clear that the equilibrium position of the lattice displacement is shifted from 0 to $-a_i x_{x,i}$ by going from the electron ground state to electron excited state, which is due to the change in the electron distribution. By energy relaxation from $q = 0$ to $q = -a_i x_{0,i}$ position in the excited state, the system earns the following relaxation energy:

$$E_R^i = \frac{a_i^2}{2}\hbar\omega_i. \tag{4.12}$$

In this situation, the lattice wave function for the ground state $|\chi_\alpha^{g,i}\rangle$ (for α phonons) and the excited state $|\chi_\beta^{e,i}\rangle$ (for β phonons) are given by

$$\left|\chi_\alpha^{g,i}\right\rangle = \int dq \left[\frac{(m\omega_i/\hbar)^{1/2}}{\pi^{1/2} 2^\alpha \alpha!}\right]^{1/2} e^{-\frac{1}{2}\rho_i^2} H_\alpha\left(\rho_i\right)|q\rangle, \tag{4.13}$$

$$\left|\chi_\beta^{e,i}\right\rangle = T\left(-a_i x_{0,i}\right)\left|\chi_\beta^{g,i}\right\rangle, \tag{4.14}$$

where H_α is the Hermite polynomial, $\rho_i = q/x_{0,i}$ is the dimensionless latice coordinate, and $T(\Delta x) = \exp[-ip\Delta x/\hbar]$ is the the translation operator with the momentum operator $p = -i\hbar\partial_q$. From the Fermi's golden rule, transition rates under optical excitation are proportional to the wave-function overlap:

$$\text{(Transition rate)} \propto \left| \left\langle \chi_{\beta}^{e,i} \mid \chi_{\alpha}^{g,i} \right\rangle \right|^2 . \tag{4.15}$$

Especially at finite temperatures, the fraction $P_k^{(i)}$ of the dipole transition involving the emission of k phonons into this mode i is given by

$$\begin{aligned} P_k^{(i)} &= \sum_{\alpha} p_{\alpha}^{(i)} \left| \left\langle \chi_{\alpha+k}^{e,i} \mid \chi_{\alpha}^{g,i} \right\rangle \right|^2 , & (4.16) \\ p_{\alpha}^{(i)} &= \frac{e^{-\hbar\omega_i \alpha / k_B T}}{\sum_{\alpha} e^{-\hbar\omega_i \alpha / k_B T}}, & (4.17) \end{aligned}$$

where T is the temperature. Note that it satisfies the normalization:

$$\begin{aligned} \sum_k P_k^{(i)} &= \sum_{\alpha} p_{\alpha}^{(i)} \left\langle \chi_{\alpha}^{g,i} \middle| \left(\sum_k \left| \chi_{\alpha+k}^{e,i} \right\rangle \left\langle \chi_{\alpha+k}^{e,i} \right| \right) \middle| \chi_{\alpha}^{g} \right\rangle , \\ &= \sum_{\alpha} p_{\alpha}^{(i)} \left\langle \chi_{\alpha}^{g,i} \mid \chi_{\alpha}^{g,i} \right\rangle , \\ &= \sum_{\alpha} p_{\alpha}^{(i)} = 1. & (4.18) \end{aligned}$$

To evaluate Eq. (4.16), it is useful to notice [82]:

$$\left\langle \chi_{\alpha}^{g,i} \mid \chi_{\beta}^{e,i} \right\rangle = e^{-a_i^2/4} \left[\frac{\alpha!}{\beta!} \right]^{1/2} \left(-\frac{a_i}{2^{1/2}} \right)^{\beta-\alpha} L_{\alpha}^{\beta-\alpha} \left(\frac{a_i^2}{2} \right) , \tag{4.19}$$

where L_n^m is the Laguerre polynomials. Therefore, the fraction $P_k^{(i)}$ is evaluated as

$$\begin{aligned}
P_k^{(i)} &= \sum_\alpha p_\alpha^{(i)} \left| \left\langle \chi_{\alpha+k}^{e,i} \mid \chi_\alpha^{g,i} \right\rangle \right|^2, \\
&= \frac{1}{\sum_\alpha e^{-\hbar\omega_i \alpha / k_B T}} \sum_\alpha e^{-\hbar\omega_i \alpha / k_B T} \left| \left\langle \chi_{\alpha+k}^{e,i} \mid \chi_\alpha^{g,i} \right\rangle \right|^2, \\
&= \frac{1}{\sum_\alpha e^{-\hbar\omega_i \alpha / k_B T}} \sum_\alpha e^{-\hbar\omega_i \alpha / k_B T} e^{-a^2/2} \frac{\alpha!}{(\alpha+k)!} \left(\frac{a_i^2}{2} \right)^K L_\alpha^k \left(\frac{a_i^2}{2} \right) L_\alpha^k \left(\frac{a_i^2}{2} \right), \\
&= \frac{1}{\sum_\alpha e^{-\hbar\omega_i \alpha / k_B T}} e^{-a_i^2/2} y_i^k \sum_\alpha L_\alpha^k (y_i) L_\alpha^k (y_i) t_i^\alpha \alpha! / \Gamma(\alpha + k + 1), \qquad (4.20)
\end{aligned}$$

where in the last line we define $t_i = e^{-\hbar\omega_i / k_B T}$ and $y_i = a_i^2/2$. According to [82], there is the following formula:

$$\begin{aligned}
&\sum_{n=0}^{\infty} L_n^m(x) L_n^m(y) t^n n! / \Gamma(m+n+1) \\
&= \frac{(xyt)^{-m/2}}{1-t} \exp\left[-\frac{(x+y)t}{1-t} \right] I_m \left(\frac{2(xyt)^{1/2}}{1-t} \right), \qquad (4.21)
\end{aligned}$$

where I_m is the Bessel function of the first kind with the imaginary argument. Using this formula, we obtain:

$$\begin{aligned}
P_k^{(i)} &= \frac{1}{\sum_\alpha e^{-\hbar\omega_i \alpha / k_B T}} e^{-a_i^2/2} y_i^k \left[\frac{\left(y_i^2 t_i\right)^{-k/2}}{1-t_i} \exp\left[-\frac{2 y_i t_i}{1-t_i} \right] I_k \left(\frac{2\left(y_i^2 t_i\right)^{1/2}}{1-t_i} \right) \right], \\
&= e^{-a_i^2/2} t_i^{-k/2} \exp\left[-\frac{2 y_i t_i}{1-t_i} \right] I_k \left(\frac{2 y_i t_i^{1/2}}{1-t} \right), \\
&= \exp\left[\frac{m\hbar\omega_i}{2k_B T} \right] \exp\left[-\frac{a_i^2}{2} \coth \hbar\omega_i / 2k_B T \right] I_k \left(\frac{a_i^2}{2} \operatorname{csch} \hbar\omega_i / 2k_B T \right). \qquad (4.22)
\end{aligned}$$

Defining the parameter $S_i = a_i^2/2$, we obtain

$$P_m^{(i)} = \exp\left[\frac{m\hbar\omega_i}{2k_B T} \right] \exp\left[-S_i \coth \hbar\omega_i / 2k_B T \right] I_m \left(S_i \operatorname{csch} \hbar\omega_i / 2k_B T \right). \qquad (4.23)$$

To get a sense of the so-called Huang-Rhys factor S_i, let's take the zero temperature limit $T \to 0$. Under this limit, we obtain

$$\begin{aligned}
P_m^{(i)} &\approx \exp\left[\frac{m\hbar\omega_i}{2k_BT}\right]\exp\left[-S_i\right] I_m\left[2S_i\left(\exp\left[\frac{m\hbar\omega_i}{2k_BT}\right]\right)^{-1}\right], \\
&\approx \exp\left[\frac{m\hbar\omega_i}{2k_BT}\right]\exp\left[-S_i\right]\left(\frac{1}{2}2S_i\left(\exp\left[\frac{m\hbar\omega_i}{2k_BT}\right]\right)^{-1}\right)^m \cdot \frac{1}{\Gamma(m+1)}, \\
&= \frac{e^{-S_i}S_i^m}{m!}, \qquad (4.24)
\end{aligned}$$

where we use the series expansion of I_α:

$$I_\alpha(u) = \left(\frac{1}{2}u\right)^\alpha \sum_{n=0}^{\infty} \frac{\left(\frac{1}{4}u^2\right)^n}{n!\Gamma(\alpha+n+1)}. \qquad (4.25)$$

From Eq. (4.24), we observe that the emitted phonon distribution is the Poisson distribution, and the mean number of the emitted phonons from the mode i is the Huang-Rhys factor S_i. When multiple phonon modes are taken into account, as the sum of Poisson distribution variable is also Poisson distribution, the emitted phonon distribution P_m and the number of emitted phonons S are given by

$$\begin{aligned}
P_m &\equiv \prod_{i|\sum_i m_i = m} P_{m_i}^{(i)} = \frac{e^{-S}S^m}{m!}, \qquad (4.26) \\
S &\equiv \sum_i S_i = \int d\omega \rho(\omega) s(\omega), \qquad (4.27)
\end{aligned}$$

where in the second equality of Eq. (4.27), we define

$$s\left(\omega_i\right) \equiv VS_i; \quad \rho(\omega) = \text{ phonon density of states }, \qquad (4.28)$$

by assuming that the factor S_i depends only on the phonon energy. Now we go back to the finite temperature case and consider the ZPL. The zero-phonon emission probability from the phonon mode i is the $k = 0$ case of the probability $P_k^{(i)}$, and it is given by [See Eq. (4.23)]:

$$\begin{aligned} P_0^{(i)} &= \exp\left[-S_i \coth \hbar\omega_i/2k_BT\right] I_0\left[S_i \operatorname{csch} \hbar\omega_i/2k_BT\right], \\ &\approx \exp\left[-S_i \coth \hbar\omega_i/2k_BT\right]. \end{aligned} \tag{4.29}$$

Here, we use $I_0(z) \approx 1 + z^2/4$ and also use the fact that $S_i \sim S/N$ is small, where N is the number of phonon modes which is big. The zero-phonon line is the emission when all the modes produces zero phonons, so its probability is

$$\begin{aligned} P_0 &= \prod_p P_0^{(i)} = \exp\left[-\sum_i S_i \coth \hbar\omega_i/2k_BT\right], \\ &= \exp\left[-\int d\omega \rho(\omega) s(\omega) \coth \hbar\omega/2k_BT\right], \\ &= \exp\left[-S\left(1 + \frac{2\int d\omega\rho(\omega)s(\omega)n_B(\omega)}{\int d\omega\rho(\omega)s(\omega)}\right)\right], \end{aligned} \tag{4.30}$$

where $n_B(\omega) = (\exp(\hbar\omega/k_BT) - 1)^{-1}$ is the bose distribution. To perform this integral, we need to know the dependency of $s(\omega)$ on ω. To this end, instead of making a_i constant, we make $E_R^i = a_i^2\hbar\omega_i/2 = S_i\hbar\omega_i$ constant [See Eq. (4.12)], such that $s(\omega) = VS_i = VE_R^i/(\hbar\omega_i) \sim VE_R/(\hbar\omega_i N) \propto \omega_i^{-1}$, where $E_R \sim NE_R^i$ is the total relaxation energy. Then, together with the phonon density of states $\rho(\omega) \propto \omega^2$, we obtain

$$\begin{aligned} \frac{2\int d\omega\rho(\omega)s(\omega)n_B(\omega)}{\int d\omega\rho(\omega)s(\omega)} &= \frac{4}{\omega_D^2}\int_0^{\omega_D} d\omega \frac{\omega}{e^{\hbar\omega/k_BT} - 1}, \\ &= 4\left(\frac{T}{T_D}\right)^2 \int_0^{T_D/T} \frac{x\,dx}{e^x - 1} \approx \frac{2}{3}\pi^2\left(\frac{T}{\Theta_D}\right)^2, \end{aligned} \tag{4.31}$$

where ω_D is the Debye frequency, $T_D = \hbar\omega_D/k_B$ is the Debye temperature, and in the last line we assume $T_D/T \gg 1$. Combining Eqs. (4.30) and (4.31), we successfully obtain

$$(\mathrm{DWF}) = P_0 = \exp\left[-S\left(1 + \frac{2}{3}\pi^2\left(\frac{T}{T_D}\right)^2\right)\right]. \tag{4.32}$$

4.2 Cryogenic all-optical thermometry setup

In this and the following sections, we extend the all-optical thermometry technique based on the NV$^-$ centers in NDs from room temperature to liquid nitrogen temperatures, 85 K $\leq$ T $\leq$ 300 K, and demonstrate its application on a ferromagnetic insulator (yttrium iron garnet, YIG) substrate. We initially demonstrate that a laser-pulse sequence to control the NV centers' charge states improves the sensitivity of the all-optical thermometer by approximately a factor of $\sqrt{3}$. Next, we systematically study the temperature dependence of the sensitivity, demonstrating that it improves at cryogenic temperatures. Finally, we apply this all-optical cryogenic thermometry technique at $T = 170$ K to measure the surface temperature profile of a YIG slab in contact with a resistive heater, with the array of NDs embedded on the surface of a flexible PDMS sheet. The observed temperature gradient over a range of tens of micrometers confirms the applicability of the technique on the YIG substrate, indicating that it provides a tool for studying local thermal properties of a wide variety of substrates over a broad range of temperatures.

Throughout this study, we define the NV$^-$ centers' zero phonon line (ZPL) amplitude ratio (A) as the ratio of the ZPL intensity with respect to an average photoluminescence (PL) intensity in a spectral range around the ZPL. We focus on the temperature (T) dependence of A. As schematically drawn in Fig. 4.3, the experiment is conducted on an array of NDs containing ensembles of NV$^-$ centers measured with a confocal microscope using a high numerical aperture objective (NA = 0.9). The laser power (with wavelength 532-nm and 594-nm), for all the experiments in this study, is fixed at 200 μW to reduce the heating below 0.5 K due to the YIG absorption [83]. An array of NDs embedded into the flexible PDMS sheet is placed on top of the surface of a 3.05-μm-thick YIG film grown on a 500-μm-thick gadolinium gallium garnet (GGG) substrate (MTI Corp.). The diameter of the spot with NDs in the PDMS sheet, which is defined by our microfabrication technique, is 1000 nm. For local heating, a Ti/Au (thickness: 8nm/200nm) resistive heater is patterned directly on the YIG film using a lithographic process. The bottom of the GGG substrate is affixed to a

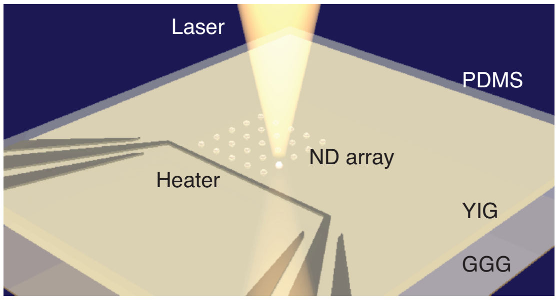

Figure 4.3: Schematic drawing of an array of nanodiamonds (NDs) on a 3.05-μm-thick YIG film grown on a GGG substrate. YIG film is patterned with a resistive heater (central wire has a width of 5 μm and a length of 200 μm) and NDs embedded onto the surface of a flexible PDMS sheet are attached on top of the YIG.

copper thermal sink within a flow cryostat. With PID control, the base temperature of the sample is stabilized within ± 0.3 K throughout the experiment. The temperature accuracy is confirmed to be ± 0.5 K using a calibration thermocouple right next to the sample position, while the chamber thermocouple is positioned a few centimeters away from the sample. Both characterization (Sec. 4.3 and 4.4) and application (Sec. 4.5) of the thermometry are conducted on the same device with a YIG substrate for consistency.

In Fig. 4.4(a), we show a two-dimensional PL scan of an individual spot in the array of NDs under continuous 594-nm excitation, with a horizontal linecut through the maximum shown in Fig. 4.4(b). Due to the spectral selectivity, the 594-nm light does not excite the neutrally-charged NV-center (NV^0) [84, 85], which has been used to improve the spectral contrast of the ZPL of NV^- photoluminescence. Each spot in the array contains tens of NDs, where each ND contains hundreds of NV centers (Adamas Technology, NV-ND-100 nm, 3 ppm NV density). Therefore, there are approximately 3000 NV centers in each spot. When we apply pulsed laser sequences as shown in Fig. 4.4(c), interestingly (though not unexpectedly), the PL is enhanced by a factor of ≈ 3, improving the temperature sensitivity by a factor of $\approx \sqrt{3}$ [See further discussion below].

In Fig. 4.5, we show the enhancement of the PL at different spots in the array, where Fig. 4.5(a) is identical to Fig. 4.4(b). Each PL peak is fit by a sum of a Gaussian function and a constant, where the amplitudes of the Gaussian functions are extracted from the fits. The

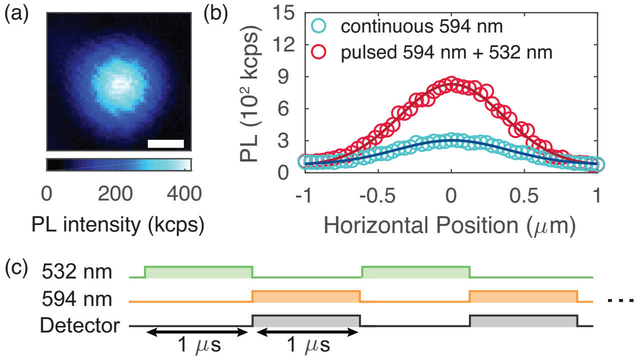

Figure 4.4: (a) Fast stirring mirror (FSM) scanned two-dimensional photoluminescence (PL) image of NV centers in NDs collected under continuous 594-nm excitation. The measurement is conducted at $T = 170$ K. Scale bar, 0.5 μm. (b) One-dimensional scan of PL intensity profiles of NV centers under two different excitation pulse sequences. (c) Schematic of the pulse sequences of a 532-nm laser (NV^- charge state initialization), a 594-nm laser (NV^- detection) and a detector.

enhancement in the amplitudes due to the pulse sequences is observed, where the enhancement factors are approximately 3.1, 2.4, and 3.4 for Figs. 4.5(a), (b), and (c), respectively. Though the factor depends on the spots, enhancements by approximately a factor of three are observed. The enhancement is due to the increased NV^- population under the pulsed laser sequence as compared to the continuous 594 nm illumination [86–88]: while the 594-nm excitation preferentially converts NV^- into NV^0, the 532-nm excitation preferentially converts NV^0 back to NV^-. It has been reported that the illumination of a continuous wave 532 nm (594 nm) laser results in a 75% (10%) steady state NV^- occupancy [86]. The time scale of the charge-state conversion depends on the laser power [86, 89], and recall that the powers of the two lasers in our study are both set to 200 μW. This leads to an estimate that the relaxation time of the charge-state conversion is larger than 2 μs [89]. Since the charge state conversion rate is slower than our pulse repetition rate (note that our pump-probe frequency is limited by the gating rate of the intensifier of the CCD camera, which is 500 kHz), we can estimate that the average NV^- population under the pump-probe sequence is between 75% and 10%. Assuming the charge initialization rates for both lasers are approximately equal, we estimate that the NV^- population is at $\approx 40\%$. This would lead to a ≈ 4 enhancement in signal, which is consistent with the experimental observation.

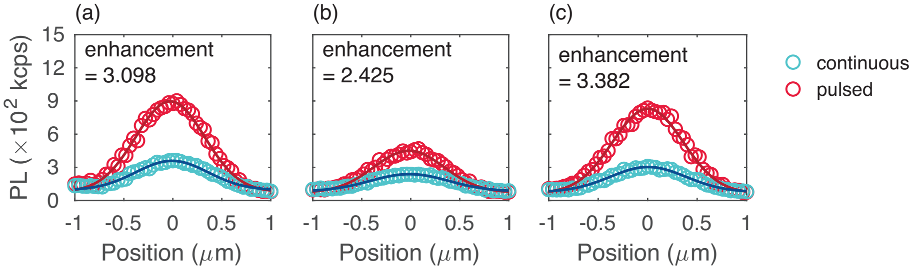

Figure 4.5: One-dimensional PL scan of three different ND spots (a), (b), and (c), where (a) is identical to Fig. 4.4(b). The enhancement of the PL due to the pulse sequence shown in Fig. 4.4(c) is shown.

Since the sensitivity of the all-optical thermometer is limited by a shot noise, a higher PL count rate by roughly a factor of three results in a higher sensitivity of temperatures by approximately a factor of $\sqrt{3}$. However, note that the pulse sequences also reduce the fraction of the measurement time in the total scanning time. While it improves the physical sensitivity η of temperatures, it may result in worse practical sensitivity $\eta_{\text{practical}}$ if the enhancement factor is less than two, as the pulse sequence Fig. 4.4(c) introduces an inactive time of the sensing. We observe, however, improved sensitivity with the pulse sequences not only because the enhancement is larger than two but also because it reduces the noise due to the CCD dark counts and the background counts. Here we note that physical sensitivity η is defined as the minimum temperature difference that can be resolved by a given amount of NV-center-measurement time, while the practical sensitivity $\eta_{\text{practical}}$ is the minimum temperature difference that can be resolved by a given total time including the time necessary for charge state preparation, background measurement, control of the equipment, and feedback control to focus on the target spot.

In the following measurements, we send the PL to a spectrometer and gate a single-photon sensitive CCD camera in the spectrometer triggered by the pulse sequences. Every spectral measurement is followed by a background measurement taken off the ND and the background counts are subtracted.

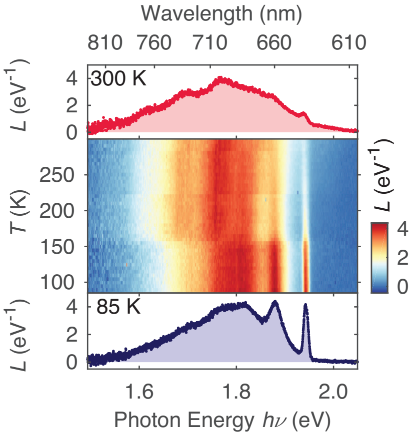

Figure 4.6: Temperature evolution of NV centers' PL spectrum $L(h\nu)$ between 85 K and 300 K. The areas under the spectra are normalized to one. Discontinuities at $T \approx 230$ K and $T \approx 150$ K are associated with the PDMS's phase transitions. Top (bottom) graph shows the spectrum at 300 K (85 K).

4.3 Cryogenic all-optical thermometry characterization

Figure 4.6 shows the PL spectra $L(h\nu)$ of the NV centers in NDs in the range 85 K $\leq T \leq$ 300 K. Monotonic change in the spectra is observed except near $T \approx 230$ K and $T \approx 150$ K, which are due to the melting point [90] and the glass transition point [91] of the PDMS, respectively. Since the PL spectrum is normalized such that the integral PL spectral intensity is unity, these transitions suggest that there is a redistribution of the PL spectral intensity. These effects may be due to a change in strain inside the NDs on the PDMS sheet or a change in the wavelength-dependence of the index of reflection and the transmission efficiency, though we have not examined these scenarios in detail. In Fig. 4.7, we show the spectra obtained from NDs without the PDMS sheet, which are scattered on a quartz substrate and contain hundreds of NDs under a focused laser spot. The spectra are measured at T=85 K, 110 K, 150 K, 200 K, 250 K, and 300 K. As the sharp changes in the PL spectrum near $T \approx 230$ K and $T \approx 150$ K in Fig. 4.6 are absent in this condition, the features near $T \approx 230$ K and $T \approx 150$ K in Fig. 4.6 are the artifact of the presence of the PDMS sheet. We note that the PDMS sheet does not appear to change the thermometry property of NV centers in NDs except PL count rates, as we use a smaller spectral range for

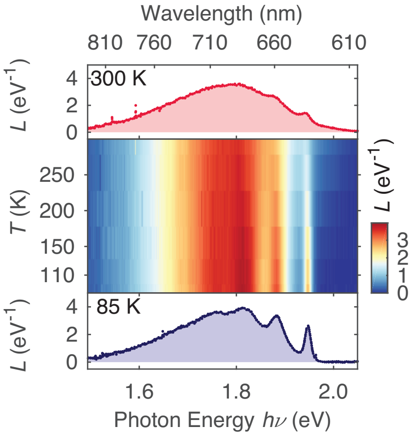

Figure 4.7: Temperature evolution of NV centers' PL spectrum $L(h\nu)$ between 85 K and 300 K for NDs on a quartz substrate, where hundreds of NDs existed under a laser-focused spot. The spectra are measured at T=85 K, 110 K, 150 K, 200 K, 250 K, and 300 K. The areas under the spectra are normalized to one. Top (bottom) graph shows the spectrum at 300 K (85 K).

the normalization in the following temperature sensing scheme.

In this study, we focus on the ZPL peak at ≈ 1.94 eV(637 nm) and the spectral range around the ZPL: from 605 nm to 660 nm, which we define as $\mathcal{R}$[9]. As shown in the inset of Fig. 4.8(a), we fit the relative spectrum by a sum of a squared-Lorentzian function and an exponential function:

$$\begin{aligned} &L(h\nu)/\langle L\rangle_{\mathcal{R}} \\ &= A\frac{1}{\left[w^2+(h\nu-h\nu_{\mathrm{ZPL}})^2\right]^2}+B\exp\left[-\frac{h\left(\nu-\nu_{\mathrm{ZPL}}\right)}{k_{\mathrm{B}}\Theta}\right], \end{aligned} \tag{4.33}$$

where k_{B} is the Boltzmann constant, h is the Plank constant, $\langle L\rangle_{\mathcal{R}}$ is the average PL intensity in $\mathcal{R}$ and $\{A, B, \Theta, w, \nu_{\mathrm{ZPL}}\}$ are fitting parameters [92]. A squared-Lorentzian function instead of a Lorentzian function is used for better fits at cryogenic temperatures [93]. Figure 4.8(a) shows the temperature evolution of the ZPL amplitude ratio A, which are used as the indicator of the temperature, and the temperature response dA/dT of the amplitude ratio. The solid and dotted curves are derived from the two fits of the reduced Debye-Waller

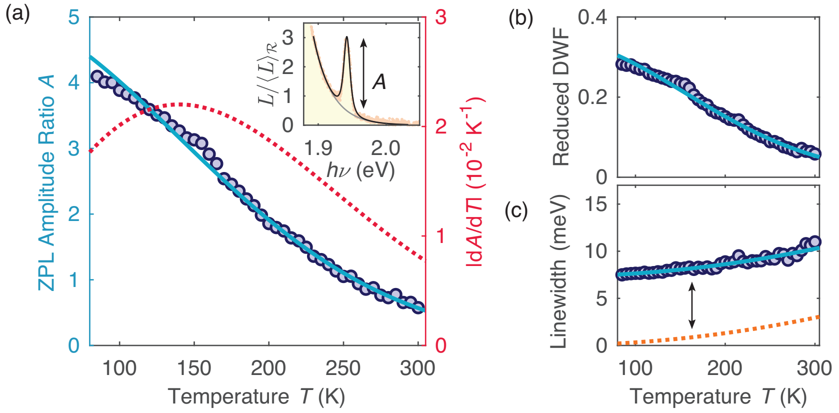

Figure 4.8: (a) Temperature dependence of the ZPL amplitude ratio A (left axis) and its temperature response $|dA/dT|$ (right axis). The solid blue curve and the dotted red curve are derived from the fits as shown in (b) and (c). Inset shows the fit of the ZPL spectrum at $T = 170$ K. (b) Reduced DWF as a function of T. A Gaussian-functional fit is shown. (c) ZPL linewidth as a function of T. The solid blue fit is the second-order polynomial $a + bT^2$ and the dotted orange curve shows bT^2.

factor (DWF) and the ZPL linewidth shown in Figs. 4.8(b) and (c). In this work, the reduced DWF [$(\mathrm{DWF})_{\mathcal{R}}$] is defined as the ratio of the ZPL counts, which corresponds to the area under the squared-Lorentzian fit, to the total PL counts in $\mathcal{R}$. We fit the temperature dependence of $(\mathrm{DFW})_{\mathcal{R}}$ with a Gaussian function

$$(\mathrm{DFW})_{\mathcal{R}} = \alpha \exp\left(-\gamma T^2\right), \tag{4.34}$$

where α and γ are the fitting parameters with γ related to the electron-phonon coupling, S, and the Debye temperature, T_{D}, by a relation $\gamma = 2\pi^2 S/3T_{\mathrm{D}}^2$ [75, 81]. In this experiment, we obtain $\gamma = (218\ \mathrm{K})^{-2}$, which corresponds to $T_{\mathrm{D}}/S = 560$ K. Though the value of T_{D}/S is almost half of that reported in Ref. [8], the difference is associated with the different size and number of NDs as well as the different NV density used in this study. The temperature dependence of the ZPL linewidth, w, is fit by a second-order polynomial $w = a + bT^2$.

To support that the presence of the PDMS sheet does not largely affect the thermometry property of NDs, in Fig. 4.9 we show the temperature dependence of the ZPL amplitude ratio and its response without the PDMS sheet. From the fit of $(\mathrm{DFW})_{\mathcal{R}}$, we obtain $\gamma =$

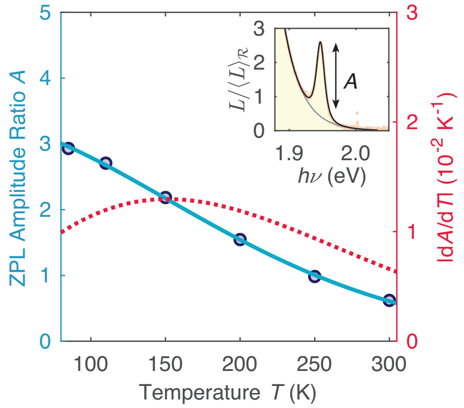

Figure 4.9: Temperature dependence of the ZPL amplitude ratio A (left axis) and its temperature response $|dA/dT|$ (right axis). The analysis is performed in the same way as in Fig. 4.8.

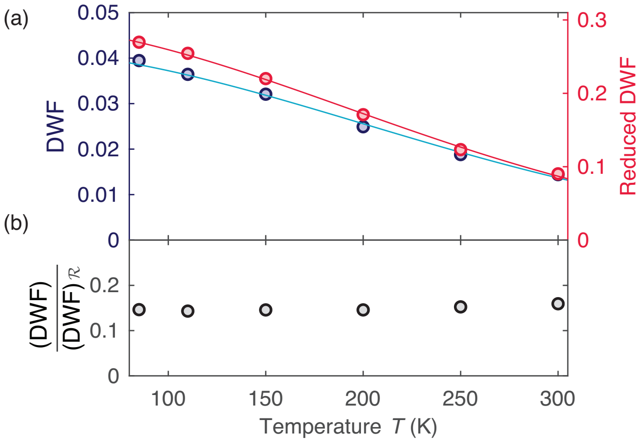

Figure 4.10: (a) Temperature dependencies of the Debye-Waller factor (DWF) (left axis) and the reduced Debye-Waller factor $(\mathrm{DFW})_{\mathcal{R}}$ (right axis) measured on NDs without the PDMS. (b) Temperature dependence of the ratio $(\mathrm{DFW})/(\mathrm{DFW})_{\mathcal{R}}$, which equals to the fraction of the integrated PL in the range $\mathcal{R}$ to the total PL.

$(283\text{ K})^{-2}$, which stays within 25% from the value $\gamma = (218\text{ K})^{-2}$ of the NDs embedded in the PDMS array, showing that the presence of the PDMS sheet does not change the main result in this report.

When performing the fit of the reduced Debye-Waller factor with Eq. (4.34), there is an implicit assumption that the temperature dependence of $(\mathrm{DFW})_{\mathcal{R}}$ is approximately that of (DFW) (See Eq. 4.32). In Fig. 4.10, we compare the Debye-Waller factor [(DFW)] and the reduced Debye-Waller factor $[(\mathrm{DFW})_{\mathcal{R}}]$ using NDs without the PDMS. Fig. 4.10 shows almost constant ratio $(\mathrm{DFW})/(\mathrm{DFW})_{\mathcal{R}}$ over the temperature range $85\text{ K} \leq T \leq 300\text{ K}$, confirming this assumption.

Now, let's go back to the discussion of Fig. 4.8. As the spectrum shown in Fig. 4.8(a), which is used for the fit, is firstly divided by the mean PL intensity in the range $\mathcal{R} = \left\{hv \mid hc(660\ \text{nm})^{-1} \leq hv \leq hc(605\ \text{nm})^{-1}\right\}$:

$$\langle L\rangle_{\mathcal{R}} = \frac{1}{\Delta\mathcal{R}}\int_{\nu_{\mathrm{i}}}^{\nu_{\mathrm{f}}} L(h\nu)hd\nu, \tag{4.35}$$

where $\nu_{\mathrm{i}} = c(660\ \text{nm})^{-1}$, $\nu_{\mathrm{f}} = c(605\ \text{nm})^{-1}$, and $\Delta\mathcal{R} = h(\nu_{\mathrm{f}} - \nu_{\mathrm{i}})$, we can write the reduced Debye-Waller factor as

$$(\mathrm{DWF})_{\mathcal{R}} = \frac{(\pi/2)Aw}{\Delta\mathcal{R}}, \tag{4.36}$$

with the fit parameters A and w. Therefore, we obtain the amplitude ratio (A) through the equation

$$A = \frac{2\alpha\exp\left(-\gamma T^2\right)\Delta\mathcal{R}}{\pi\left(a + bT^2\right)}, \tag{4.37}$$

where $\Delta\mathcal{R}$ is the size of the spectral range $\mathcal{R}$. Importantly, as shown in the dashed curve in Fig. 4.8(a), the temperature response $|dA/dT|$ increases at low temperatures, which leads to the sensitivity improvement. In the above fitting model, this is captured by the derivative:

$$\left|\frac{dA}{dT}\right| = 2T\left(\frac{b}{a + bT^2} + \gamma\right)A. \tag{4.38}$$

Under a simplifying assumption $a \gg bT^2$, the this response is maximized at $T \approx 1/\sqrt{2\gamma} \approx$ 154 K, which is consistent with the experimental observation. This temperature $T \approx$150 K coincidentally corresponds to the glass transition temperature of the PDMS, though does not appear to be related to it based on the measurements done without the PDMS sheet [See Fig. 4.9]. On the other hand, under the condition $a \ll bT^2$, we reproduce Eq. (4.4), which let us expect a monotonic improvement in the sensitivity at lower temperature from the extrapolation of the observation in the regime 295 K $\leq T \leq$ 400 K (See Sec. 4.1.1). We note that the enhancement dA/dT is limited by the existence of the constant offset (a) in the linewidth $w = a + bT^2$, which is due to the spectral resolution of the spectrometer that accounts for ≈50% of the linewidth and an inhomogeneous broadening caused by crystal strain variations both between different NDs and within the individual commercial NDs used in this study. These limitations could be overcome by optimizing the spectral resolution and introducing engineered nanoparticles [94], leading to an enhanced temperature response at cryogenic temperatures.

4.3.1 Spectrometer information and background measurement

As it turns out that the constant offset (a) in the linewidth $w = a + bT^2$ plays a major role in the temperature sensitivity, in this section we describe the spectrometer information and how the background is subtracted in the measurement. For the spectral measurement, we use a spectrometer with a single-photon sensitive CCD camera (Acton SP-2750, Princeton Instrument, 300 gr/mm with 750 nm blaze; iStar 334T, Andor). To maximize the PL count rate, we widely opened the slit in the spectrometer, which results in a worse wavelength resolution. Each spectral measurement is followed by an off-spot background measurement with the same measurement duration. This not only deteriorates the practical sensitivity $\eta_{\text{practical}}$, but also adds additional noise to the physical sensitivity η due to the background counts in the CCD camera. However, this factor is taken into account in the calculation of the noise model, where CCD camera's dark-current shot noise also contributes in addition to the ZPL photon shot noise, in the next section.

The resolution of the spectrometer is quantified in the following way. We scan the spectrum of the narrow line laser with 594 nm, and the full width at half maximum (FWHM) is approximately 3.5 nm. Since there are ≈60 pixels in this 3.5 nm range, we can say that the measured spectrum $L(\lambda)$ is the convolution of the NV-center associated distribution $f(\lambda)$

and the broadening due to the measurement $g(\lambda)$. Then the ZPL linewidth w can be written as

$$w^2 = \mathrm{Var}_1(\lambda) + \mathrm{Var}_2(\lambda), \tag{4.39}$$

where $\mathrm{Var}_1(\lambda)$ and $\mathrm{Var}_2(\lambda)$ are the variance associated with the discribution $g(\lambda)$ and $f(\lambda)$, respectively. Note that I ignore the case where the distribution $f(\lambda)$ cannot define the variance, for example the Lorenzian distribution. To quantify the NV-center associated linewidth component, we fit the data of the 594-nm narrow line laser with a function

$$\propto \exp\left[-\left|\frac{\lambda-\lambda_c}{b}\right|^a\right], \tag{4.40}$$

and the best fit is obtained with parameters $a = 5.07$ and $b = 1.99$. This results in (FWHM) = 3.7 nm (11 meV) and (Standard Deviation) = 1.13 nm (3.5 meV). We identify this standard deviation as the wavelength resolution which poses a lower bound for the ZPL linewidth measurenment.

4.4 Characterization of the temperature noise floor

To fully characterize the sensitivity

$$\eta = \sigma_A\sqrt{\Delta t}\,|dA/dT|^{-1}, \tag{4.41}$$

where Δt is the integration time, in Fig. 4.11 we show the uncertainty σ_A as a function of temperature. At each temperature T, PL spectrum measurements with measurement time $\Delta t = 2.5$ s are repeated one hundred times (Fig. 4.11(a)). Then, we calculate the standard deviation σ_A for each data set and show its temperature dependence in Fig. 4.11(b). To quantitatively compare the results at different temperatures, σ_A is rescaled by a factor

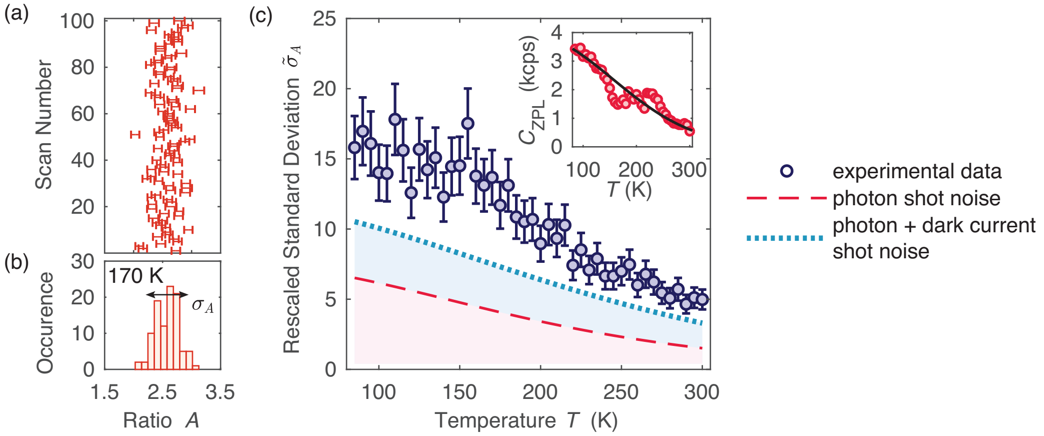

Figure 4.11: (a) ZPL amplitude ratio scanned over 100 times at $T = 170$ K. A single scan consists of a PL integration time of $\Delta t = 2.5$ s. (b) Histogram built from the measurements in (a). The standard deviation σ_A is depicted. (c) Rescaled standard deviation $\tilde{\sigma}_A = \sigma_A\sqrt{C_{\mathrm{ZPL}}\Delta t}$ as a function of T, where C_{ZPL} is the ZPL counts rate. The dashed red curve and the dotted blue curve are lower bounds under two different models as defined in the main text. Inset shows C_{ZPL} as a function of T. Solid black curve shows a one-parameter (a_1) fit of the ZPL counts rate $C_{\mathrm{ZPL}}(T) = a_1(\mathrm{DWF})_{\mathcal{R}}^{(T)}$, where $(\mathrm{DWF})_{\mathcal{R}}^{(T)}$ is the solid curve shown in Fig. 4.8(b).

$\sqrt{C_{\mathrm{ZPL}}\Delta t}$ to account for the variation in the number of detected photons, i.e.,

$$\tilde{\sigma}_A = \sigma_A\sqrt{C_{\mathrm{ZPL}}\Delta t}, \tag{4.42}$$

where C_{ZPL} is the ZPL count rate shown in the inset of Fig. 4.8(a). The black curve in the inset shows a one-parameter (a_1) fit of the ZPL count rate

$$C_{\mathrm{ZPL}} = a_1(\mathrm{DWF})_{\mathrm{R}}^{(T)}, \tag{4.43}$$

where $(\mathrm{DWF})_{\mathrm{R}}^{(T)}$ is the curve we obtain in Fig. 4.8(b). This is validated under the assumption that the temperature dependence of C_{ZPL} is dominated by that of the reduced DWF.

We show in the dotted and dashed curves in Fig. 4.11(c) the lower bounds for the rescaled standard deviation $\tilde{\sigma}_A$ under different models. The dashed curve is the lower bound when the noise is coming only from the photon shot noise of the ZPL and the phonon sideband under the ZPL, while the dotted curve shows the lower bound when the CCD camera's dark-current shot noise also contributes to the uncertainty σ_A. In a model where photon counts under the ZPL peak add noise to the fit of the ZPL [95], the rescaled standard deviation is given by

$$\tilde{\sigma}_A = \sigma_A \sqrt{C_{\mathrm{ZPL}} \Delta t} = g(y) A, \tag{4.44}$$

$$g(y) = \sqrt{c_1 + c_2 y + c_3 \sqrt{y^2 + y}}, \tag{4.45}$$

with $[c_1, c_2, c_3] = [2.00, 1.98, 0.763]$ based on the procedure explained in the following. The function $g(y)$ is different from the case when using a Lorentzian function for the ZPL fit [See [74] and Eq. (4.6)]. In Fig. 4.11(c), the dashed curve is drawn by setting $y = B/A$, while the dotted curve is drawn by setting $y = B/A + 2c_{\mathrm{dark}}/(\overline{\langle L \rangle_{\mathcal{R}}} A h \delta\nu)$, where the temperature dependence of B/A is fit by an exponential function as shown in Fig. 4.16, $\delta\nu$ is the frequency range corresponding to one line of vertically binned pixels of the two-dimensional CCD image, $\overline{\langle L \rangle_{\mathcal{R}}} \equiv (1/N) \sum_{i=1}^{N} \langle L \rangle_{\mathcal{R}}^{(T_i)}$ represents the average of $\langle L \rangle_{\mathcal{R}}$ over the temperatures $T_i = \{85, 90, \cdots, 300\mathrm{K}\}$ with maximum label $i = N$, and c_{dark} is the counts due to the CCD's dark current whose average value is cancelled by the background measurement subtraction while it adds noise to the spectrum. The dotted curve explains the experimentally observed standard deviation $\tilde{\sigma}_A$ and the residual would be associated with the background counts from the surroundings of NDs such as the PDMS sheet. The noise due to c_{dark} is non-negligible because the PL is spread over thousands of pixels in the CCD camera in the spectrometer.

To derive the function $g(y)$, we apply the theory given in Ref. [95] to the case with

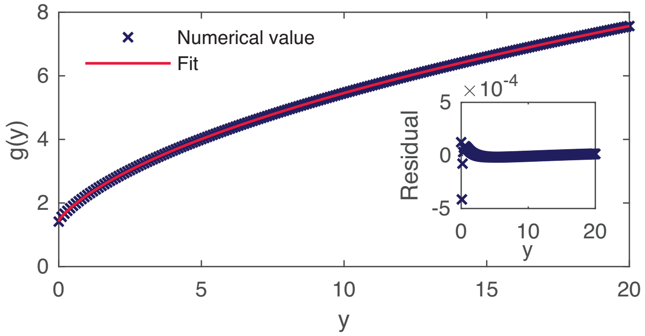

Figure 4.12: Numerical evaluation of the function $g(y)$ and the fit. Inset shows the residuals.

squared-Lorentzian function, which gives

$$g(y) = \sqrt{\frac{f_2(y)}{f_1(y)f_2(y) - (f_3(y))^2} \frac{\sqrt{\pi}\Gamma\left(\beta - \frac{1}{2}\right)}{\Gamma(\beta)}}, \tag{4.46}$$

$$f_1(y) = \int_{-\infty}^{\infty} dx \left(\frac{\left(x^2+1\right)^\beta}{y\left(x^2+1\right)^\beta + 1} \right) \left(\frac{1}{\left(x^2+1\right)^\beta} \right)^2, \tag{4.47}$$

$$f_2(y) = \int_{-\infty}^{\infty} dx \left(\frac{\left(x^2+1\right)^\beta}{y\left(x^2+1\right)^\beta + 1} \right) \left(\frac{x^2}{\left(x^2+1\right)^{\beta+1}} \right)^2, \tag{4.48}$$

$$f_3(y) = \int_{-\infty}^{\infty} dx \left(\frac{\left(x^2+1\right)^\beta}{y\left(x^2+1\right)^\beta + 1} \right) \left(\frac{x^2}{\left(x^2+1\right)^{\beta+1}} \right), \tag{4.49}$$

where $\beta = 2$ and $\Gamma(x)$ is the Gamma function. Instead of evaluating them analytically, we compute them numerically and fit the function $g(y)$ by a form $\sqrt{c_1 + c_2 y + c_3\sqrt{y^2+y}}$ in analogy to Eq. (4.6) and the fit is shown in Fig. 4.12, where $[c_1, c_2, c_3]$ are the fitting parameters. The function is well fit by $[c_1, c_2, c_3] = [2.00, 1.98, 0.763]$.

Combining the temperature dependencies of $\tilde{\sigma}_A$ and $|dA/dT|$ as shown in Figs. 4.8(a) and 4.11(c), we show in Fig. 4.13 the rescaled sensitivity as a function of temperature, where the rescaled sensitivity is defined as

$$\tilde{\eta} = \eta\sqrt{C_{\text{ZPL}}} = \sigma_A\sqrt{C_{\text{ZPL}}\Delta t}\,|dA/dT|^{-1} = \tilde{\sigma}_A\,|dA/dT|^{-1}. \tag{4.50}$$

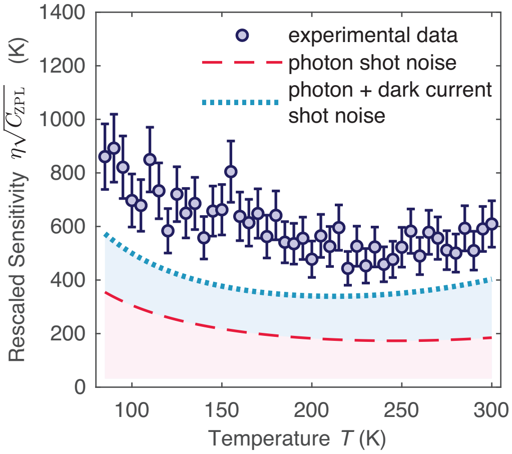

Figure 4.13: Rescaled temperature sensitivity $\tilde{\eta} = \eta\sqrt{C_{\text{ZPL}}}$ as a function of temperature T. The dashed red and the dotted blue curves identify the lower bounds for the sensitivity.

This rescaled sensitivity is the metric of the minimum temperature difference that can be resolved by a single ZPL photon detection. The curve in Fig. 4.13 can be modeled by the combination of Eqs. (4.38) and (4.44), leading to

$$\tilde{\eta} = \eta\sqrt{C_{\text{ZPL}}} = \tilde{\sigma}_A \left|dA/dT\right|^{-1} = \frac{g(y)}{2T\left(\frac{b}{a+bT^2} + \gamma\right)}. \tag{4.51}$$

Based on this equation, we expect a low temperature behavior (at $a \gg bT^2$) of $\tilde{\eta} = \eta\sqrt{C_{\text{ZPL}}} \sim 1/T$, which is consistent with the experimental observation shown in Fig. 4.13.

Finally, in Fig. 4.14 we show the temperature evolution of the sensitivity. Importantly, the sensitivity improves at cryogenic temperatures in contrast to other NV-based thermometry techniques[96–101]. This observation is modeled by the combination of Eqs. (4.8) and (4.51), resulting in

$$\eta = \frac{g(y)}{2T\left(\frac{b}{a+bT^2} + \gamma\right)\sqrt{C_{\text{tot}}(\text{DWF})|_{T=0}}} \exp\left(\frac{1}{2}\gamma T^2\right), \tag{4.52}$$

where C_{tot} is the total PL count rate [102–104]. For example, under a simplifying assumption

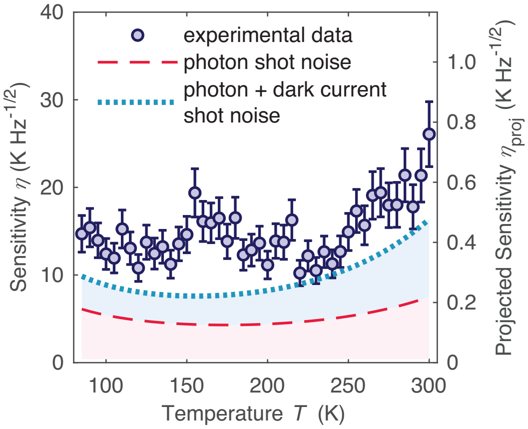

Figure 4.14: Temperature sensitivity η as a function of temperature T. The dashed red and the dotted blue curves identify the lower bounds for the sensitivity. The spike near 160 K arises from the dip in the experimental data of C_{ZPL} as shown in the inset of Fig. 4.11(c). Right axis shows a projected sensitivity η_{proj} under the assumption of a higher detection rate of the PL as explained in the main text.

$a \gg bT^2$, $\gamma \gg b/a$, and $g(y) \approx g(0) \approx \sqrt{2}$, we obtain

$$\eta \simeq \frac{1}{T\gamma\sqrt{2C_{\mathrm{tot}}\,(\mathrm{DWF})|_{T=0}}} \exp\left(\frac{1}{2}\gamma T^2\right), \tag{4.53}$$

which takes a minimum at $T = 1/\sqrt{\gamma} = 218$ K. This approximation corresponds to the case where we only consider the temperature evolution of the DWF, and it approximately explains the highest temperature sensitivity near $T \approx 200$ K in the experimental observation. We also note that Fig. 4.14 shows non-negligible effects of the PDMS sheet. This is mainly due to the temperature dependence of the absolute ZPL counts rate shown in the inset of Fig. 4.11(c), which is largely affected by the optical transparency of the PDMS sheet that modifies the PL collection efficiency of our setup. Temperature dependence of the rescaled sensitivity shown in Fig. 4.13 supports this statement, since there are no observable dips/peaks in the figure. While the inset of Fig. 4.11(c) and Fig. 4.14 are affected by the existence of the PDMS sheet, the general tendency of these figures are expected to be due to the NV-center's intrinsic properties, since the temperature dependence of the total PL of NV centers are reported to be negligible or non-increasing with temperature increase [102–104], leading to the decrease of the ZPL counts rate with temperature increase, due to the Debye-Waller factor.

We note that the sensitivity calculated in this study at $T = 300$ K does not reach the level of the sensitivity provided in the previous report on all-optical thermometry at room temperature [74]; however, taking into account detection efficiency differences, our result is fully consistent with the finding in [74]. In our experiment, the ZPL count rates are orders of magnitude smaller than those measured in the former study, where the ZPL counts rate from a single ND containing 100 NV centers is observed to be $C_{\text{ZPL},1}^{(295\text{ K})} = 900$ kcps at $T = 295$ K [74], in contrast to our measurement of $C_{\text{ZPL},2}^{(295\text{ K})} = 0.76$ kcps at $T = 295$ K. To compare our result with the previous study, we define a projected sensitivity [75]

$$\eta_{\text{proj}} = \sqrt{C_{\text{ZPL},2}^{(295\text{ K})} / C_{\text{ZPL},1}^{(295\text{ K})}}\,\eta, \tag{4.54}$$

and it is shown in the right axis of the Fig. 4.14. Though the projected sensitivity merely gives a rough estimate of a sensitivity given a higher detection efficiency of the PL, it also shows our result is consistent with the previous report [74]. To further improve the sensitivity at low temperatures, one could increase the ZPL count rate by improving the detection efficiency and utilizing brighter NDs that contain more NV^- centers. For example, if we can improve the detection efficiency up to the level of that reported in [80], we would achieve $\times\sqrt{100}$ improvement in sensitivity under similar laser powers. While the total internal reflection inside the PDMS sheet reduces the detection efficiency by approximately a factor of three, it does not fully explain the detection efficiency differences. A more detailed analysis of the photon losses in our setup needs to be performed as some contributions are still not identified. Alternatively, using a larger diamond particle with 1 μm diameter and 10 ppm NV density [74], the sensitivity could be improved by a factor of $\approx \sqrt{300}$, with a minor loss in spatial resolution. We do not explore the effect below liquid nitrogen temperatures as Eq. 4.52 predicts that the sensitivity becomes monotonically worse.

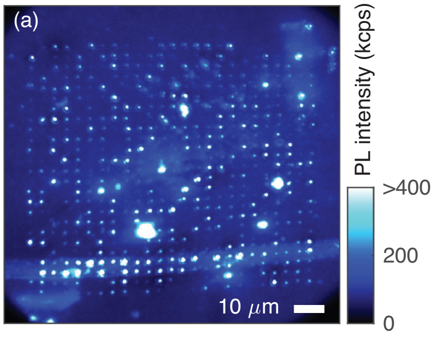

Figure 4.15: (a) Spatial PL scan of NV centers in NDs in the array. Temperature measurements are performed in the circled ND spots shown in (b).

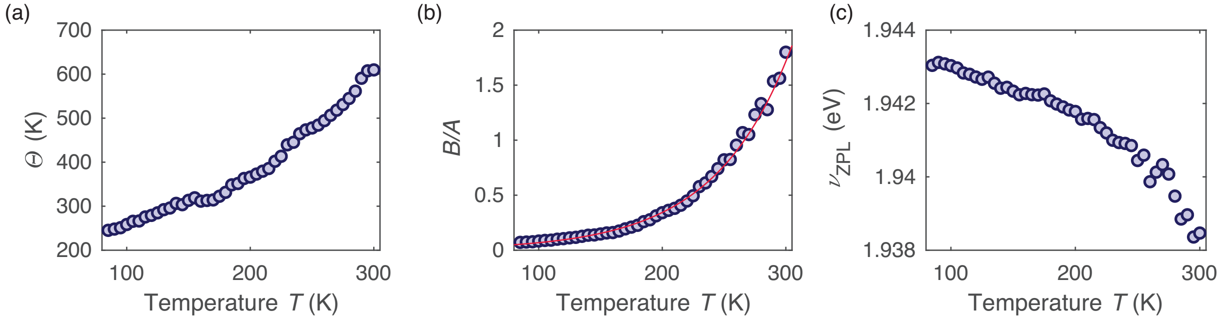

Figure 4.16: Temeperature T dependencies of the fit parameters (a) Θ, (b) B/A, and (c) ν_{ZPL}. In (b), the ratio B/A are fit by an exponential function, and shown with a solid red curve.

4.5 Surface temperature imaging of a YIG film

To demonstrate the applicability of the all-optical thermometer, we apply an 80-mA current to the resistive heater to generate a temperature gradient in the YIG and measure the spatial temperature variation of the YIG surface using an array of NDs, as illustrated in Fig. 4.3. Since the YIG has spin-wave resonances at microwave frequencies near $\mathcal{D}$ [72, 105, 106], this measurement confirms that the all-optical thermometry technique can be used independently of substrate materials where microwave control is problematic. The experiment is conducted at 170 K, which is above the glass transition temperature of the PDMS and the proximity of the NDs on the YIG surface is ensured. Figure 4.15(a) shows a two-dimensional spatial scan of the PL from the array of NDs used in this study. We use 24 spots in the array to construct the temperature profile, which are approximately evenly distributed and bright without spatial broadenings as shown in 4.15(b). The YIG substrate is magnetized to an in-plane direction of the YIG film by applying a DC magnetic field before the temperature measurements. For each temperature measurement in the following, the PL is collected in total for 500 s.

For sensing the YIG temperature gradient, temperature dependencies of $\{B, \Theta, w, \nu_{\mathrm{ZPL}}\}$ in addition to A are utilized for calculating the local temperature. In Fig. 4.16, we show the temperature dependence of Θ, B/A, and ν_{ZPL}. The parameter Θ represents the slope of the exponential function in the fit of the phonon sideband. The value is different from the true temperature by a factor of order one, which is called Urbach's rule and similar dependencies are observed in many other materials [92]. We note that the temperature dependence of this exponential tail can potentially be used as a temperature sensor below the liquid nitrogen temperatures for future applications.

For the calibration of the temperature sensors, we initially select 31 spots in the array which are approximately evenly distributed and bright enough to give higher sensitivity to reduce the measurement time. As the total calibration and measurement time is limited due to our flow cryostat, majority of the spots are excluded before the calibration. We also exclude spots which have spatial broadenings to avoid possible degrading of the crystalline quality or imperfect contact to the YIG substrate. Each of these 31 spots undergoes a calibration. In the temperature calibration, we conduct multiple scans of the spectrum at $T = 170$ K and $T = 180$ K by changing the base temperatures of the flow cryostat. The average value and the variance of the fitting coefficients $\{A, B, \Theta, w, \nu_{\mathrm{ZPL}}\}$ are extracted, and then we calculate the linear dependence to convert the value of $\{A, B, \Theta, w, \nu_{\mathrm{ZPL}}\}$ into temperatures. In the following, only 24 measurement spots with error < 2.5 K are shown to avoid the artifact due to the interpolation of the measurement spots, while the error distribution among the total 31 spots is 1.8 ± 1.5 K. Note that this error accounts for both the inaccuracy due to the calibration and the sensitivity. The variation of errors in each spot is associated with the use of different sized nanoparticles along with the number of NDs

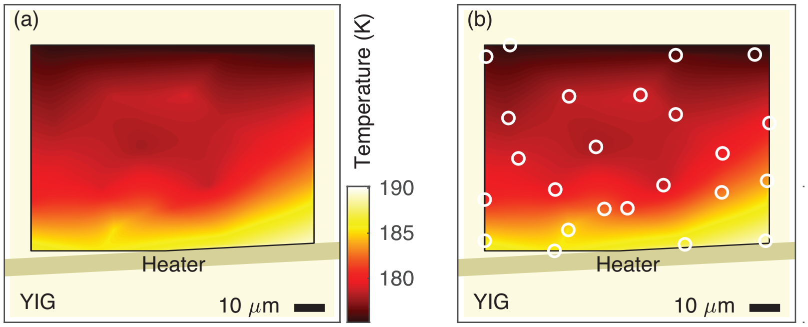

Figure 4.17: (a) Two-dimensional temperature imaging of the YIG surface using NV centers in the array of NDs embedded on the surface of the PDMS sheet measured by the all-optical thermometry technique. An 80-mA current is applied to the resistive heater. The base temperature is set to $T = 170$ K. The measurements are performed in the circled ND spots shown in (b), and temperatures around the scanned spots are smoothly interpolated or extrapolated.

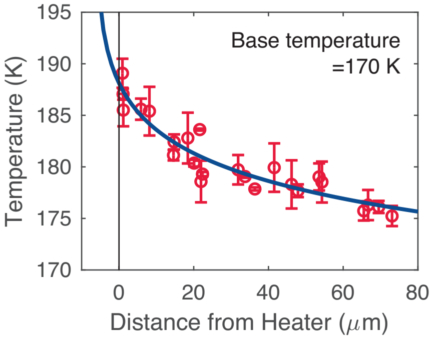

Figure 4.18: YIG surface temperature as a function of the distance from the resistive heater. Fit with a logarithmic function is shown.

per spot, which may be equalized by using a single diamond microparticle with standardized size after centrifugation. The temperature dependencies of the parameters $\{B, \Theta, w, \nu_{\mathrm{ZPL}}\}$ in addition to A are used for temperature estimation by taking the weighted average. After taking temperature measurements, the temperatures around the scanned spots are smoothly interpolated or extrapolated.

Figure 4.17 shows the resulting temperature profile of the YIG surface, where we observe a temperature decay on the order of tens-of-microns from the heat source. The temperature of each spot as a function of the distance from the heater is shown in Fig. 4.18. Note that the error accounts for both the inaccuracy due to the calibration and the sensitivity. The distribution of the errors is associated with the use of different sized nanoparticles along with the number of NDs per spot, which may be equalized by using a single diamond microparticle with standardized size after centrifugation. The data fits well to the Green's function to the 2D Poisson equation which is logarithmic, i.e.,

$$T(x) = -\xi \log(x - \zeta), \tag{4.55}$$

where $x - \zeta$ is the distance from the resistive heater and $\{\xi, \zeta\}$ are fitting parameters. This shows that the temperature field in the YIG approximately follows the steady state diffusion equation with a single heat carrier. We note that the Poisson equation is not accurate in YIG because there are two kinds of heat carriers, phonons and magnons. A deviation from the Poisson equation is expected near the heat source within a length scale of a magnon-phonon thermalization, which is much smaller than a few micrometers [67, 69, 83]. More specifically, the temperature profile follows [83]

$$\left(\kappa_m \kappa_p \nabla^4 - g\left(\kappa_m + \kappa_p\right)\nabla^2\right) T_p = -\left(\kappa_m \nabla^2 - g\right) Q_p + g Q_m, \tag{4.56}$$

instead of the Poisson equation, where κ_m (κ_p) is the magnon (phonon) thermal conductivity, g is the magnon-phonon coupling, the subscript of T_p indicates the phonon (lattice) temperature which NV centers sense, and Q_m (Q_p) is the power densities of external heating absorbed by magnons (phonons). Here we ignore, for simplicity, the spatial derivatives of the thermal conductivities, κ_m and κ_p. It is shown in [83], however, that Eq. (4.56) can be approximated to the Poisson equation in a regime where the phononic temperature gradient is dominant over the gradient of the magnon-phonon temperature difference. The observed logarithmic behavior of the phononic temperature profile supports this approximation and that the steady-state phononic temperature profile is not largely disturbed by magnons in YIG. For further study of the temperature profile of the YIG film, higher temperature sensitivity is required. In our experiment, we do not observe a deviation from the Poisson equation due to the limitation of the temperature resolution ≈ 1 K and the spatial resolution

$\approx 1\mu$m. We also note that in the field of spin-caloritronics, lock-in infrared thermography techniques have recently been used to investigate thermo-spin or magneto-thermoelectric effects at room temperature [107–109]. The spatial and temperature resolutions of those methods are ≈ 10 μm and ≈ 0.1 mK, respectively. While the temperature sensitivity currently achievable with our method is not comparable to the ones used in the study of the emergent spin-caloritronics effects, such as the spin Peltier effect, the better spatial resolution may enable crucial investigation of the details of these systems in the future.

4.6 Conclusion

We demonstrate and characterize an all-optical thermometry technique based on NV^- center ensembles in NDs. The technique can be deployed from room temperature to liquid nitrogen temperatures, with a sensitivity that increases with decreasing temperature. The PL intensity of NV^- centers is enhanced by implementing pulse sequences to convert the NV center's charge states, i.e., NV^0 into NV^-, leading to a higher temperature sensitivity by approximately a factor of $\sqrt{3}$. Systematic noise analysis reveals that the sensitivity is limited by the shot noise and the inhomogeneous broadening of the ZPL linewidth. This suggests a pathway for further sensitivity improvements by improving the PL detection efficiency and introducing engineered NDs with high brightness and homogeneous crystal strains. Taking advantage of an array of NDs embedded in a flexible and portable PDMS sheet, we show the utility of the all-optical thermometer at $T = 170$ K by measuring the surface temperature profile of a YIG slab with a temperature gradient applied by a resistive heater. This all-optical thermometry technique along with the versatility of the ND membrane array provides a microwave-free, minimally invasive, and cryogenically compatible way of measuring local temperatures within a variety of substrate materials.

Chapter 5

Opportunities for long-range magnon-mediated entanglement of spin qubits via on- and off-resonant coupling

5.1 Introduction

In this chapter, we theoretically show that the hybrid quantum system of NV centers and YIG is a promising solid-state platform to enable long-distance NV-NV two-qubit gates. As entanglement and quantum coherence are at the core of quantum information technologies, NV centers with long spin-coherence time can serve as promising qubit platforms. Additionally, NV centers' excellent quantum state control and the ability to initialize and readout the spin state optically [51, 54, 110–114] have made them a suitable testbed for quantum applications. Although there are remarkable applications of NV centers in the areas of quantum sensing and quantum communication [22, 38–41, 115–122], quantum computation using NV centers remains challenging due to the difficulty of engineering useful long-distance gates, i.e., over an optically resolvable distance on the order of micrometers [123–128] which entangle qubits faster than decoherence rates, as the magnetic dipole-dipole interaction between two NV centers is weak for such long distances. Once this long-distance two-NV gate is established, however, NV centers will be a scalable platform of quantum computation enabled by their nanoscale localization and on-chip integratability [129].

Several potential solutions to this challenge have recently been proposed by making use of boson modes as an information mediator [22, 39, 40, 43, 117, 118, 130–133]. While photon-mediated NV-NV entanglement has been experimentally demonstrated over a meter and a kilometer length scales [22, 39, 40, 117, 118], based on indistinguishable single photon detection, its extension to two-qubit gates is still challenging due to its slow entangling rate as a result of its low success probability. (Note that being able to produce an entangled state at long distances and having long-distance two-qubit gates are different. Although the latter leads to the former, there are additional requirements to promote the former to the latter.) It has been proposed, however, that the long-distance entangled-state preparation can be promoted into two-qubit gates by harnessing such entangled NV-center pair generation under both single-shot readout and local gates based on the measurement outcome [43]. This is possible when NV centers have access to quantum memories in the decoherence-free subspace [134], which survive during the multiple entangling attempts of NV centers that cause decoherence [39–41, 43, 122]. Alternatively, as a different approach of trying to extend NV-NV interaction on a wafer without needing single boson detection and with faster gate operations, hybrid quantum systems have been extensively studied where NV centers interface other bosonic systems [130–133]. In a carbon-nanotube-NV-center hybrid system [131], for example, it has been proposed to couple NV centers and phonon modes in a suspended carbon nanotube by injecting an electric current through the nanotube.

To this end, hybrid quantum systems of NV centers and magnons in ferromagnets (or ferrimagnets) such as YIG have emerged and attracted attention as another highly promising platform to extend such NV-NV interaction [135–145]. In this system, NV-center spins are

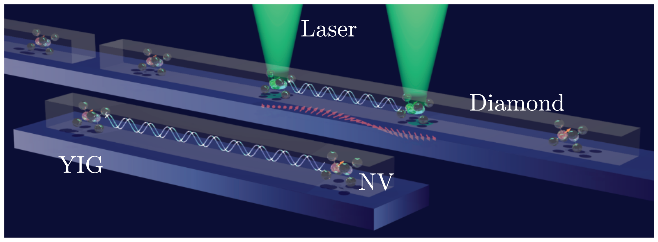

Figure 5.1: Schematic of NV centers in diamond placed on top of an infinitely long magnon waveguide and a finite length magnetic bar made of YIG.

intrinsically (differently from the carbon-nanotube platform case described above) coupled to magnon modes through their dynamical fringe magnetic fields. NV-NV entanglement has been investigated theoretically by taking advantage of virtual-magnon exchange in one-dimensional spin chains [135] or transduction of energy quanta in ferromagnetic discs [140], and this has stimulated a variety of experiments on the NV-magnon hybrid system [72, 105, 106, 146, 147]. Nonetheless, optimal device geometries and gate protocols suitable for entangling separated NV centers have yet to be explored. Additionally, several important practical aspects and entangling schemes of these systems have not been fully addressed theoretically, e.g., realistic ferromagnetic structures, relevant magnetic interactions [148–150], finite temperatures, and possible entanglement protocols.

In this work, we present a practical and realistic hybrid quantum system composed of NV centers and a YIG material to engineer NV-NV entanglement over micron length scales via on- and off-resonant magnon excitations at low temperatures ($T \lesssim 150$ mK). Building on our review of the off-resonant protocol in Chapter 3, this chapter provides a more in-depth study on both the off-resonant protocol and the on-resonant protocol, which utilizes the so called "on-shell" magnons. The entanglement protocol in this study is based on the strong coupling of NV spins to the magnon modes in yttrium-iron-garnet (YIG) nanodevices. We obtain strong NV-magnon interactions (i.e., high cooperativity) and high entangling gate to decoherence ratio (GDR), under realistic YIG structures and geometries and we accurately take into account both dipole and exchange interactions, in both an infinitely long YIG waveguide and a finite length YIG bar structure (see Fig. 5.1). Especially for the latter, we obtain for two NV centers separated by more than 2 μm the NV-magnon cooperativity as large as $\mathcal{C} \gtrsim 10^4$ for on-resonance conditions and NV-NV GDR $\approx 10^3$ under off-resonant magnon excitations. This leads to a usefully-fast entangling gate (relative to the qubit decoherence rate of NV centers) at optically resolvable NV-NV separations. Our results are obtained with the use of a Hamiltonian formalism [151, 152], where we show semi-analytical expressions for the coupling in terms of the relevant experimental and geometrical quantities. Finally, as another major focus in this work, we explore and compare the calculated entanglement quality of both on-resonant transduction and off-resonant virtual-magnon exchange entangling gate protocols. We use fidelity, negativity, and the degrees of the Bell-inequality violation for the evaluation of the entanglement quality. We achieve this comparison by the Lindblad master equation simulations which take into account two NV centers and a magnon mode near the resonance condition at finite temperatures. Notably, our results show that although the off-resonant protocols are robust at temperatures up to $T \approx 150$ mK due to the absence of magnon occupation decay, the transduction protocol can outperform it due to its faster gate operations at lower temperatures when the magnon damping parameter is sufficiently small $\alpha \lesssim (\Delta\omega/\omega_\mu)(1/4g_\mu T_2^*)[\pi/(\pi-1)]$. Here, ω_μ is magnon frequency, T_2^* is NV center coherence time, $\Delta\omega$ is the NV-magnon detuning frequency, and g_μ is the NV-spin-magnon-mode coupling. Our calculations and analysis will guide future experiments that aim to engineer on-chip long-distance entangling gates between multiple NV centers mediated by magnons in ferromagnetic nanostructures including waveguide and bar structures.

In the remainder of this chapter, we begin in Sec. 5.2 with the description of the Hamiltonian formalism for the dipole-exchange magnons coupled to NV centers. In Sec. 5.3 we compute the full properties of magnons in a YIG waveguide interacting with NV centers using this Hamiltonian formalism. We obtain the NV-NV coupling strength, the entanglement rate (ER), and the gate to decoherence ratio (GDR) under the off-resonant condition, where the NV frequency is detuned from the magnon band frequencies to avoid direct occupation of magnon modes. Similarly, in Sec. 5.4 we calculate the properties of magnons in a finite length YIG bar. We evaluate NV-magnon on-resonant coupling strength and its cooperativity in addition to the NV-NV coupling strength under the off-resonant condition. For the latter, we provide the entanglement rate (ER) and the gate to decoherence ratio (GDR). Finally, in Sec. 5.5 we compare the transduction and virtual-magnon-exchange protocols in terms of the generated entanglement quality under different system parameters and physical conditions.

5.2 Hamiltonian formalism of dipole-exchange magnons and NV-magnon interaction

In this section, we outline the Hamiltonian formalism of dipole-exchange magnons coupled to NV centers. This formalism provides a complete and accurate treatment of both magnetic dipole and quantum exchange interactions between the spins in YIG waveguides and bars with finite cross section. This treatment is crucial in our study, as the NV centers have eigenfrequencies typically on the order of gigahertz, which interact with the so-called dipole-exchange magnons in ferromagnets [148]. Using simpler magnon dispersion relations considering only the exchange interaction, as in Ref. [135], leads to an overestimation of the NV-magnon coupling though it provides a crude estimate. As illustrated in Fig. 5.1, we consider hybrid quantum devices where NV centers are placed on top of the YIG structures. While multiple NV centers can be placed on top of the infinitely long YIG waveguide in a scalable fashion as shown in Fig. 5.1, in the following calculations we only focus on coupling two NV centers for convenience. The total Hamiltonian of our hybrid system is written as $\mathcal{H} = \mathcal{H}_{\text{NV}} + \mathcal{H}_{\text{m}} + \mathcal{H}_{\text{int}}$, where $\mathcal{H}_{\text{NV}}$ is the NV Hamiltonian, $\mathcal{H}_{\text{m}}$ is the magnon Hamiltonian, and $\mathcal{H}_{\text{int}}$ is the interaction Hamiltonian,

$$\mathcal{H}_{\text{NV}} = \sum_{i=1,2} D_{\text{NV}} \left(\hat{n}_{\text{NV}} \cdot \mathbf{S}_{\text{NV}_i}\right)^2 + \gamma\mu_0 \mathbf{S}_{\text{NV}_i} \cdot \mathbf{H}_{\text{ext}}, \tag{5.1}$$

$$\begin{aligned}\mathcal{H}_{\text{m}} = & -\mu_0 \int d\mathbf{r}\mathbf{H}_{\text{ext}} \cdot \mathbf{M}(\mathbf{r}) + \frac{\mu_0}{2} \int d\mathbf{r}\alpha_{\text{ex}}(\mathbf{r})\nabla\mathbf{M} : \nabla\mathbf{M} \\ & + \frac{\mu_0}{2} \int d\mathbf{r}d\mathbf{r}'(\nabla \cdot \mathbf{M}(\mathbf{r}))G\left(\mathbf{r}-\mathbf{r}'\right)\left(\nabla' \cdot \mathbf{M}\left(\mathbf{r}'\right)\right),\end{aligned} \tag{5.2}$$

$$\mathcal{H}_{\text{int}} = \sum_{i=1,2} \gamma\mu_0 \mathbf{S}_{\text{NV}_i} \cdot \nabla \int d\mathbf{r}' G\left(\mathbf{r}-\mathbf{r}'\right) \nabla' \cdot \mathbf{M}\left(\mathbf{r}'\right)\Big|_{\mathbf{r}=\mathbf{r}_i}. \tag{5.3}$$

Here, $D_{\text{NV}} = 2\pi \times 2.877$ GHz is the zero-field splitting of the NV center, $\hat{n}_{\text{NV}}$ is the unit vector along the NV main symmetry axis, $\mathbf{S}_{\text{NV}_i}$ is the spin-1 operator of the NV center labeled by $i \in \{1, 2\}$, $\gamma = 2\pi \times 28$ MHz/mT is the absolute value of the electron gyromagnetic ratio, μ_0 is the vacuum permeability, $\mathbf{H}_{\text{ext}}$ is the external magnetic field, $\mathbf{M}(\mathbf{r})$ is the magnetization with the constraint $|\mathbf{M}(\mathbf{r})| = M_s(\mathbf{r}) = M_s\mathcal{F}(\mathbf{r})$, $M_s = 245.8$ mT$/\mu_0$ is the YIG saturation magnetization, $\mathcal{F}(\mathbf{r}) = 1$ (0) inside (outside) the ferromagnetic structure, $\alpha_{\text{ex}}(\mathbf{r}) = \alpha_{\text{ex}}\mathcal{F}(\mathbf{r})$, $\alpha_{\text{ex}} = \lambda_{\text{ex}}^2 = D_{\text{ex}}/\gamma\mu_0 M_s$ is the exchange-length squared, $D_{\text{ex}} = 5.39 \times 10^{-2}\ \gamma$ mT μm^2 is the YIG exchange constant, the double-dot product is defined as $\nabla\mathbf{M} : \nabla\mathbf{M} = \partial_a M_b \partial^a M^b$ (summation over indices appearing twice are suppressed as usual), $\mathbf{r}_i$ is the position of NV$_i$, $G(\mathbf{r} - \mathbf{r}') = 1/4\pi|\mathbf{r} - \mathbf{r}'|$ is the Green's function, and we set $\hbar = 1$ in the following. We note that the first term in Eq. (5.2) is the Zeeman energy, the second term is the exchange energy, and the third term is the magnetic dipole energy. Inclusion of both the second and the third term in Eq. (5.2) results in the dipole-exchange magnons in ferromagnets.

We note that the interaction Hamiltonian $\mathcal{H}_{\text{int}}$ in Eq. (5.3) can also be understood in

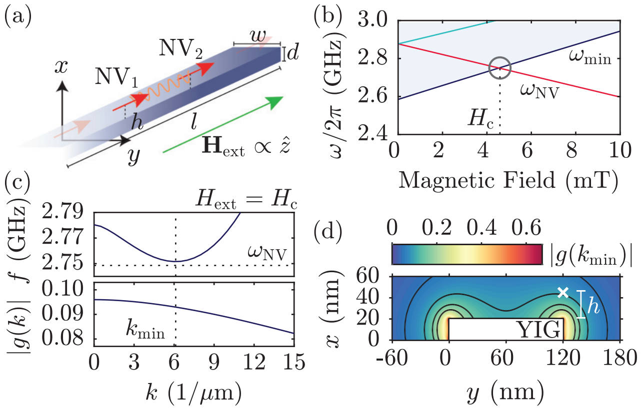

Figure 5.2: (a) Schematic and coordinates of NV centers placed on top of an infinitely long YIG waveguide. External magnetic field $\mathbf{H}_{\rm ext}$ is applied along $\hat{z}$ direction. (b) NV center's transition frequencies and magnon spectrum as a function of external field $H_{\rm ext}$ for $d = 20$ nm and $w = 120$ nm. Shaded area represents continuum of magnon modes. The lowest magnon frequency $\omega_{\rm min}$ and the NV transition frequency $\omega_{\rm NV}$ of $|g\rangle \leftrightarrow |e\rangle$ are detuned by $\Delta f = 3$ MHz at $H_{\rm ext} = H_{\rm c}$. (c) Dispersion relation $f(k) = \omega_{k,(0,0)}/2\pi$ of magnons and the dimensionless coupling $g(k) = g(\boldsymbol{\rho}, k)$ between magnons and the NV center at $H_{\rm ext} = H_{\rm c}$. The NV center is positioned at $\boldsymbol{\rho} = x\hat{x} + y\hat{y} = (d+h)\hat{x} + w\hat{y}$ with $h = 25$ nm [see the white cross mark in (d)]. The minimum frequency $\omega_{\rm min}$ and its respective wavenumber $k_{\rm min}$ are shown. (d) Spatial density plot of the dimensionless coupling $g(k_{\rm min})$ at $H_{\rm ext} = H_{\rm c}$ with contours at $|g(k_{\rm min})| = 0.05, 0.1, 0.15$ and 0.2.

terms of the dipolar tensor $\hat{D}(\mathbf{r}-\mathbf{r}')$:

$$\mathcal{H}_{\rm int} = \sum_{i=1,2} \gamma\mu_0 \mathbf{S}_{{\rm NV}_i} \cdot \int d\mathbf{r}' \widehat{D}\left(\mathbf{r}-\mathbf{r}'\right) \cdot \mathbf{M}\left(\mathbf{r}'\right)\Big|_{\mathbf{r}=\mathbf{r}_i}, \tag{5.4}$$

$$\begin{aligned}\hat{D}(\mathbf{r}-\mathbf{r}') &= -(\nabla \otimes \nabla')G(\mathbf{r}-\mathbf{r}') \\ &= \frac{1}{4\pi}\left(\frac{3}{|\mathbf{r}-\mathbf{r}'|^5}\left(\mathbf{r}-\mathbf{r}'\right)\otimes\left(\mathbf{r}-\mathbf{r}'\right) - \frac{1}{|\mathbf{r}-\mathbf{r}'|^3}\right), \text{when } \mathbf{r} \neq \mathbf{r}',\end{aligned} \tag{5.5}$$

where the second form of Eq. (5.5) is the conventional expression of magnetic dipole-dipole interaction between two magnetic dipoles.

5.3 Infinitely long ferromagnetic waveguide

In this section, we consider the case of an infinitely long YIG waveguide with thickness, width, and length given by d, w, and $l(\rightarrow \infty)$, respectively. The external magnetic field is applied along the YIG waveguide, $\mathbf{H}_{\text{ext}} = H_{\text{ext}}\hat{z}$, and the two NV centers are positioned at height h from its top surface [see illustration in Fig. 5.2(a)]. The equilibrium magnetization is $\mathbf{M}_0(\mathbf{r}) = M_s\hat{z}\mathcal{F}(\mathbf{r})$, for which its contribution in the interaction Hamiltonian Eq. (5.3) vanishes. [Although in principle we need to obtain the equilibrium magnetization from the energy minimization of $\mathcal{H}_{\text{m}}$, in the infinitely long waveguide case $\mathbf{M}(\mathbf{r}) = M_{\text{s}}(\mathbf{r})\hat{z}$ holds as the field is applied along the direction where demagnetization factor is zero. In the finite length magnetic bar case which we consider in later sections, this is still approximately correct as in our setting the length l is much larger than both the width w and the thickness d.] This can be understood as the source (”monopole”) of the demagnetization field is the divergence of the magnetization, $\nabla\mathbf{M}_0(\mathbf{r})$, which exist at infinitely far away in the current geometry and the contribution vanishes. We note that this vanishing static field from the equilibrium magnetization is important as the zeroth-order contribution of the NV-YIG interaction is the static demagnetization field, which it is easy to forget when computing the NV-magnon interaction. The choice of this current geometry in this section is due to this simplicity of not having the zeroth-order contribution. The NV main symmetry axis is set to be parallel to the external magnetic field, $\hat{n}_{\text{NV}} = \hat{z}$, for geometrical simplicity. We further define the deviation from the equilibrium magnetization

$$\delta\mathbf{M}(\mathbf{r}) = \mathbf{M}(\mathbf{r}) - \mathbf{M}_0(\mathbf{r}) \approx \mathbf{m}(\mathbf{r}) - [|\mathbf{m}(\mathbf{r})|^2/2M_s(\mathbf{r})]\hat{z}, \tag{5.6}$$

where $\mathbf{m}(\mathbf{r}) = m_x(\mathbf{r})\hat{x} + m_y(\mathbf{r})\hat{y}$ is a small two-dimensional magnetization deviation. The linearized magnetization dynamics [153] are governed by the Hamiltonian equation of motion for

$$m^-(\mathbf{r}) = [2\gamma M_s(\mathbf{r})]^{1/2} a(\mathbf{r}), \tag{5.7}$$

$$m^+(\mathbf{r}) = [2\gamma M_s(\mathbf{r})]^{1/2} a^*(\mathbf{r}), \tag{5.8}$$

using the magnon Hamiltonian $\mathcal{H}_{\rm m}$ up to quadratic order in the complex canonical variables $a(\mathbf{r})$ and $a^*(\mathbf{r})$, where we have performed the Holstein-Primakoff approximation [149] and $m^{\pm}(\mathbf{r}) = m_x(\mathbf{r}) \pm i m_y(\mathbf{r})$.

We note that the choice of $m^- \propto a$ and $m^+ \propto a^\dagger$, which may be opposite to some literatures, is made such that the Hamiltonian equation of motion repreduces the the Landau-Lifshitz-Gilbert (LLG) equation (without dissipation). More concretely, following the Holstein-Primakoff transformation:

$$M_-(\mathbf{r}) = \sqrt{2\gamma M_{\rm s}(\mathbf{r})}a(\mathbf{r})f\left(a^*(\mathbf{r})a(\mathbf{r})\right), \tag{5.9}$$

$$M_+(\mathbf{r}) = \sqrt{2\gamma M_{\rm s}(\mathbf{r})}a^*(\mathbf{r})f\left(a^*(\mathbf{r})a(\mathbf{r})\right), \tag{5.10}$$

$$M_z(\mathbf{r}) = M_{\rm s}(\mathbf{r}) - \gamma a^*(\mathbf{r})a(\mathbf{r}), \tag{5.11}$$

where $M_\pm = M_x \pm iM_y$, $M_z = \sqrt{M_{\rm s}^2 - M_x^2 - M_y^2}$, and $f(x) = \sqrt{1 - \gamma x/(2M_{\rm s}(\mathbf{r}))}$, we can reproduce the LLG equation. Here, $a(\mathbf{r})$ and $a^*(\mathbf{r})$ are the complex canonical variables satisfying $\partial_t a(\mathbf{r}) = -i\delta\mathcal{H}/\delta a^*(\mathbf{r})$ and $\partial_t a^*(\mathbf{r}) = +i\delta\mathcal{H}/\delta a(\mathbf{r})$. The relation between $a(\mathbf{r})$, $a^*(\mathbf{r})$ and $M_-(\mathbf{r})$, $M_+(\mathbf{r})$ is carefully chosen such that it satisfies the dissipationless LLG equation $\partial_t \mathbf{M} = -\gamma\mu_0 \mathbf{M} \times \mathbf{H}_{\rm eff}$. This is also consistent with the standard sign convention of the time evolution of the creation/annihilation operators $a \leftrightarrow \hat{a} \propto e^{-i\omega t}$ and $a^* \leftrightarrow \hat{a}^\dagger \propto e^{+i\omega t}$. Note that we use $\gamma > 0$ as the absolute value of the electron gyromagnetic ratio, so the electron gyromagnetic ratio is $-\gamma$. The Hamiltonian equation of motion gives

$$\partial_t M_x = -\gamma M_z \frac{\delta\mathcal{H}}{\delta M_y}; \quad \partial_t M_y = +\gamma M_z \frac{\delta\mathcal{H}}{\delta M_x}, \tag{5.12}$$

and writing $\mathcal{H}[M_x, M_y] = \mathcal{W}[M_x, M_y, M_z(M_x, M_y)]$ with $M_z(M_x, M_y) = \sqrt{M_{\rm s}^2 - M_x^2 - M_y^2}$, we obtain

$$\partial_t M_x = \gamma \left[M_y \frac{\delta \mathcal{W}}{\delta M_z} - M_z \frac{\delta \mathcal{W}}{\delta M_y} \right],$$
$$\partial_t M_y = \gamma \left[M_z \frac{\delta \mathcal{W}}{\delta M_x} - M_x \frac{\delta \mathcal{W}}{\delta M_z} \right]. \tag{5.13}$$

As the effective field is obtained by $\mu_0 \mathbf{H}_{\text{eff}} = -\delta \mathcal{W} / \delta \mathbf{M}$, the dissipationless LLG equation $\partial_t \mathbf{M} = -\gamma \mu_0 \mathbf{M} \times \mathbf{H}_{\text{eff}}$ is successfully derived. By approximating $f(x) \approx 1$, Eqs. (5.9)-(5.11) turns into Eq. (5.6) with a correct identification of the complex canonical variables Eqs. (5.7) and (5.8).

5.3.1 Simplification of the magnon Hamiltonian

In the following calculation, we simplify the magnon Hamiltonian $\mathcal{H}_{\text{m}}$. We write $\mathcal{H}_{\text{m}} = \mathcal{H}_{\text{Z}} + \mathcal{H}_{\text{ex}} + \mathcal{H}_{\text{dip}}$, where $\mathcal{H}_{\text{Z}}$ is the Zeeman Hamiltonian, $\mathcal{H}_{\text{ex}}$ is the exchange Hamiltonian, and $\mathcal{H}_{\text{dip}}$ is the magnetic dipole Hamiltonian given by

$$\mathcal{H}_{\text{Z}} = -\mu_0 \int d\mathbf{r} \mathbf{H}_{\text{ext}} \cdot \mathbf{M}(\mathbf{r}), \tag{5.14}$$
$$\mathcal{H}_{\text{ex}} = \frac{\mu_0}{2} \int d\mathbf{r} \alpha_{\text{ex}}(\mathbf{r}) \nabla \mathbf{M}(\mathbf{r}) : \nabla \mathbf{M}(\mathbf{r}), \tag{5.15}$$
$$\mathcal{H}_{\text{dip}} = \frac{\mu_0}{2} \int d\mathbf{r} d\mathbf{r}' (\nabla \cdot \mathbf{M}(\mathbf{r})) G\left(\mathbf{r} - \mathbf{r}'\right) \left(\nabla' \cdot \mathbf{M}\left(\mathbf{r}'\right)\right), \tag{5.16}$$

where the double-dot product is defined as $\nabla \mathbf{M} : \nabla \mathbf{M} = \partial_a M_b \partial^a M^b$. Firstly, we simplify the Zeeman Hamiltonian and the dipole Hamiltonian. Using $\mathbf{M}(\mathbf{r}) = \mathbf{M}_0(\mathbf{r}) + \delta \mathbf{M}(\mathbf{r})$, we

obtain

$$
\begin{aligned}
\mathcal{H}_{\mathrm{Z}} &= -\mu_0 \int d\mathbf{r} \mathbf{H}_{\mathrm{ext}} \cdot \delta\mathbf{M}(\mathbf{r}) + \text{const.}, && (5.17) \\
\mathcal{H}_{\mathrm{dip}} &= \mathcal{H}_{\mathrm{dem}} + \mathcal{H}_{\mathrm{dip(2)}} + \text{const.}, && (5.18) \\
\mathcal{H}_{\mathrm{dem}} &= -\mu_0 \int d\mathbf{r} \mathbf{H}_{\mathrm{d}}(\mathbf{r}) \cdot \delta\mathbf{M}(\mathbf{r}), && (5.19) \\
\mathcal{H}_{\mathrm{dip(2)}} &= \frac{\mu_0}{2} \int d\mathbf{r} d\mathbf{r}' (\nabla \cdot \delta\mathbf{M}(\mathbf{r})) G\left(\mathbf{r} - \mathbf{r}'\right) \left(\nabla' \cdot \delta\mathbf{M}\left(\mathbf{r}'\right)\right). && (5.20)
\end{aligned}
$$

Here, $\mathcal{H}_{\mathrm{dem}}$ is the demagnetization field Hamiltonian, $\mathcal{H}_{\mathrm{dip(2)}}$ is the dipole Hamiltonian that is second order in $\delta\mathbf{M}$, and $\mathbf{H}_{\mathrm{d}}(\mathbf{r})$ is the demagnetization field defined by

$$
\mathbf{H}_{\mathrm{d}}(\mathbf{r}) = \nabla \int d\mathbf{r}' G\left(\mathbf{r} - \mathbf{r}'\right) \left(\nabla' \cdot \mathbf{M}_0\left(\mathbf{r}'\right)\right). \tag{5.21}
$$

For the infinitely long waveguide, we have $\mathbf{H}_{\mathrm{d}}(\mathbf{r}) = 0$. For the finite length magnetic bar structure which we consider in later sections, we approximate $\mathbf{H}_{\mathrm{d}}(\mathbf{r}) \approx H_{\mathrm{d}}^{z}(\mathbf{r})\hat{z}$ as the z-component is dominant compared to the x and y components. Therefore, we obtain

$$
\mathcal{H}_{\mathrm{dem}} \approx -\mu_0 \int d\mathbf{r} H_{\mathrm{d}}^{z}(\mathbf{r}) \delta M_z(\mathbf{r}). \tag{5.22}
$$

Up to the quadratic order in $\mathbf{m}(\mathbf{r})$, we obtain

$$
\begin{aligned}
\mathcal{H}_{\mathrm{Z}} &\approx \mu_0 H_{\mathrm{ext}} \int d\mathbf{r} \frac{\mathbf{m}^2(\mathbf{r})}{2M_{\mathrm{s}}(\mathbf{r})} + \text{const.}, && (5.23) \\
\mathcal{H}_{\mathrm{dem}} &\approx \mu_0 \int d\mathbf{r} H_{\mathrm{d}}^{z}(\mathbf{r}) \frac{\mathbf{m}^2(\mathbf{r})}{2M_{\mathrm{s}}(\mathbf{r})}, && (5.24) \\
\mathcal{H}_{\mathrm{dip(2)}} &\approx \frac{\mu_0}{2} \int d\mathbf{r} d\mathbf{r}' (\nabla \cdot \mathbf{m}(\mathbf{r})) G\left(\mathbf{r} - \mathbf{r}'\right) \left(\nabla' \cdot \mathbf{m}\left(\mathbf{r}'\right)\right). && (5.25)
\end{aligned}
$$

Using $M_{\mathrm{s}}(\mathbf{r}) = M_{\mathrm{s}}\mathcal{F}(\mathbf{r})$ and writing $\mathbf{m}(\mathbf{r}) = \vec{\mathcal{M}}(\mathbf{r})\mathcal{F}(\mathbf{r})$, we obtain

$$\mathcal{H}_{\mathrm{Z}} \approx \mu_0 H_{\mathrm{ext}} \int d\mathbf{r}\mathcal{F}(\mathbf{r})\frac{\vec{\mathcal{M}}^2(\mathbf{r})}{2M_{\mathrm{s}}} + \mathrm{const.}, \tag{5.26}$$

$$\mathcal{H}_{\mathrm{dem}} \approx \mu_0 \int d\mathbf{r}\mathcal{F}(\mathbf{r})H_{\mathrm{d}}^z(\mathbf{r})\frac{\vec{\mathcal{M}}^2(\mathbf{r})}{2M_{\mathrm{s}}}, \tag{5.27}$$

$$\mathcal{H}_{\mathrm{dip(2)}} \approx \frac{\mu_0}{2} \int d\mathbf{r}d\mathbf{r}'(\nabla \cdot \vec{\mathcal{M}}(\mathbf{r})\mathcal{F}(\mathbf{r}))G\left(\mathbf{r}-\mathbf{r}'\right)\left(\nabla' \cdot \vec{\mathcal{M}}\left(\mathbf{r}'\right)\mathcal{F}\left(\mathbf{r}'\right)\right). \tag{5.28}$$

Similarly, the exchange Hamiltonian can be written, using $\mathbf{M}(\mathbf{r}) = \mathbf{M}_0(\mathbf{r}) + \delta\mathbf{M}(\mathbf{r})$, as

$$\mathcal{H}_{\mathrm{ex}} = -\mu_0 \int d\mathbf{r}\delta\mathbf{M}(\mathbf{r}) \cdot \partial_\mu \left[\alpha_{\mathrm{ex}}(\mathbf{r})\partial^\mu \mathbf{M}_0(\mathbf{r})\right] - \frac{\mu_0}{2}\int d\mathbf{r}\delta\mathbf{M}(\mathbf{r}) \cdot \partial_\mu \left[\alpha_{\mathrm{ex}}(\mathbf{r})\partial^\mu \delta\mathbf{M}(\mathbf{r})\right] + \mathrm{const.} \tag{5.29}$$

Up to the quadratic order in $\mathbf{m}(\mathbf{r})$, the above equation becomes

$$\mathcal{H}_{\mathrm{ex}} \approx \frac{\mu_0}{2}\int d\mathbf{r}\frac{\mathbf{m}^2(\mathbf{r})}{M_{\mathrm{s}}(\mathbf{r})}\partial_\mu \left[\alpha_{\mathrm{ex}}(\mathbf{r})\partial^\mu M_{\mathrm{s}}(\mathbf{r})\right] - \frac{\mu_0}{2}\int d\mathbf{r}\mathbf{m}(\mathbf{r}) \cdot \partial_\mu \left[\alpha_{\mathrm{ex}}(\mathbf{r})\partial^\mu \mathbf{m}(\mathbf{r})\right] + \mathrm{const.} \tag{5.30}$$

Using $M_{\mathrm{s}}(\mathbf{r}) = M_{\mathrm{s}}\mathcal{F}(\mathbf{r})$, $\alpha_{\mathrm{ex}}(\mathbf{r}) = \alpha_{\mathrm{ex}}\mathcal{F}(\mathbf{r})$, and writing $\mathbf{m}(\mathbf{r}) = \vec{\mathcal{M}}(\mathbf{r})\mathcal{F}(\mathbf{r})$, we obtain

$$\begin{aligned}\mathcal{H}_{\mathrm{ex}} &\approx \frac{\mu_0\alpha_{\mathrm{ex}}}{2}\int d\mathbf{r}\mathcal{F}^3(\mathbf{r})\nabla\vec{\mathcal{M}}(\mathbf{r}) : \nabla\vec{\mathcal{M}}(\mathbf{r}) + \mathrm{const.},\\ &= -\frac{\mu_0\alpha_{\mathrm{ex}}}{2}\int d\mathbf{r}\left(\mathcal{F}^3(\mathbf{r})\vec{\mathcal{M}}(\mathbf{r}) \cdot \nabla^2\vec{\mathcal{M}}(\mathbf{r}) + \left[\partial_\mu\mathcal{F}^3(\mathbf{r})\right]\vec{\mathcal{M}}(\mathbf{r}) \cdot \partial^\mu\vec{\mathcal{M}}(\mathbf{r})\right) + \ \mathrm{const.},\end{aligned} \tag{5.31}$$

where the double-dot product is $\nabla\vec{\mathcal{M}} : \nabla\vec{\mathcal{M}} = \partial_a\mathcal{M}_b\partial^a\mathcal{M}^b$. Note that the term $\partial_\mu\mathcal{F}^3(\mathbf{r})$ in the second equation gives a delta-functional contribution peaked at the ferromagnet's boundary. Using the totally-free surface spin condition, $\partial_\mu\vec{\mathcal{M}} = \vec{0}$ on the ferromagnet's boundary, we obtain

$$\mathcal{H}_{\mathrm{ex}} \approx -\frac{\mu_0 \alpha_{\mathrm{ex}}}{2} \int d\mathbf{r} \mathcal{F}^3(\mathbf{r}) \vec{\mathcal{M}}(\mathbf{r}) \cdot \nabla^2 \vec{\mathcal{M}}(\mathbf{r}) + \mathrm{const.} \tag{5.32}$$

Combining equations (5.26), (5.27), (5.28), and (5.32), we obtain

$$\begin{aligned}\mathcal{H}_{\mathrm{m}} \approx \mu_0 \int d\mathbf{r} \mathcal{F}(\mathbf{r})(H_{\mathrm{ext}} + H_{\mathrm{d}}^z(\mathbf{r})) \frac{\vec{\mathcal{M}}^2(\mathbf{r})}{2M_{\mathrm{s}}} - \frac{\mu_0 \alpha_{\mathrm{ex}}}{2} \int d\mathbf{r} \mathcal{F}^3(\mathbf{r}) \vec{\mathcal{M}}(\mathbf{r}) \cdot \nabla^2 \vec{\mathcal{M}}(\mathbf{r}) \\ + \frac{\mu_0}{2} \int d\mathbf{r} d\mathbf{r}' (\nabla \cdot \vec{\mathcal{M}}(\mathbf{r}) \mathcal{F}(\mathbf{r})) G\left(\mathbf{r} - \mathbf{r}'\right) \left(\nabla' \cdot \vec{\mathcal{M}}\left(\mathbf{r}'\right) \mathcal{F}\left(\mathbf{r}'\right)\right),\end{aligned} \tag{5.33}$$

where we dropped the constant shift in energy.

5.3.2 Diagonalization of the magnon Hamiltonian

To obtain the magnon dynamics and the magnon spatial profiles for the infinitely long ferromagnetic waveguide ($l \to \infty$), we diagonalize the magnon Hamiltonian Eq. (5.33) by expanding $\vec{\mathcal{M}}(\mathbf{r})$ as

$$\vec{\mathcal{M}}(\mathbf{r}) = \int \frac{dk}{2\pi} e^{-ikz} \sum_{nm} \psi_n^X(x) \psi_m^Y(y) \sqrt{2\gamma M_{\mathrm{s}}} \frac{1}{2} \left[a_{k,(n,m)}^* \ a_{-k,(n,m)} \right] \begin{bmatrix} \widehat{e}_- \\ \widehat{e}_+ \end{bmatrix}, \tag{5.34}$$

$$\psi_n^X(x) = \sqrt{\frac{2}{\left(1+\delta_{n,0}\right) d}} \cos\left(\kappa_n^X x\right), \tag{5.35}$$

$$\psi_m^Y(y) = \sqrt{\frac{2}{\left(1+\delta_{m,0}\right) w}} \cos\left(\kappa_m^Y y\right), \tag{5.36}$$

where $\kappa_n^X = n\pi/d$, $\kappa_m^Y = m\pi/w$, $n, m = 0, 1, \cdots$, $\widehat{e}_\pm = \hat{x} \pm i\hat{y}$, and $a_{k,(n,m)}$ is the complex canonical variable in the new basis. Note that we have $\mathbf{m}(\mathbf{r}) = \vec{\mathcal{M}}(\mathbf{r})\mathcal{F}(\mathbf{r})$ and in the current geometry $\mathcal{F}(\mathbf{r}) = \mathcal{F}^X(x)\mathcal{F}^Y(y)$, where $\mathcal{F}^X(x) = \Theta(x)\Theta(d-x)$, $\mathcal{F}^Y(y) = \Theta(y)\Theta(w-y)$, and Θ is the Heaviside step function. Recalling $M_{\mathrm{s}}(\mathbf{r}) = M_{\mathrm{s}}\mathcal{F}(\mathbf{r})$ and using Eqs. (5.7) and

(5.8), the above expansion corresponds to the following:

$$a(\mathbf{r}) = \int \frac{dk}{2\pi} e^{ikz} \sum_{nm} f_n^X(x) f_m^Y(y) a_{k,(n,m)}, \tag{5.37}$$

$$a^*(\mathbf{r}) = \int \frac{dk}{2\pi} e^{-ikz} \sum_{nm} f_n^X(x) f_m^Y(y) a^*_{k,(n,m)}, \tag{5.38}$$

$$f_n^X(x) = \sqrt{\frac{2\mathcal{F}^X(x)}{\left(1+\delta_{n,0}\right) d}} \cos\left(\kappa_n^X x\right), \tag{5.39}$$

$$f_m^Y(y) = \sqrt{\frac{2\mathcal{F}^Y(y)}{\left(1+\delta_{m,0}\right) w}} \cos\left(\kappa_m^Y y\right). \tag{5.40}$$

After simplification, the magnon Hamiltonian Eq. (5.33) becomes,

$$\begin{aligned}\mathcal{H}_\mathrm{m} = \frac{1}{2} \int \frac{dk}{2\pi} \sum_{\substack{n_1 m_1 \\ n_2 m_2}} & \left[a^*_{k,(n_1,m_1)} \ a_{-k,(n_1,m_1)} \right] \\ & \times \left[\begin{array}{cc} A_{k,(n_1 m_1)(n_2 m_2)} & B_{k,(n_1 m_1)(n_2 m_2)} \\ B^*_{k,(n_1 m_1)(n_2 m_2)} & A^*_{k,(n_1 m_1)(n_2 m_2)} \end{array} \right] \left[\begin{array}{c} a_{k,(n_2,m_2)} \\ a^*_{-k,(n_2,m_2)} \end{array} \right], \end{aligned} \tag{5.41}$$

with

$$A_{k,(n_1 m_1)(n_2 m_2)} = \Delta_{k,(n_1 m_1)} \delta_{(n_1 m_1)(n_2 m_2)} + \omega_M H^{00}_{k,(n_1 m_1)(n_2 m_2)}, \tag{5.42}$$

$$B_{k,(n_1 m_1)(n_2 m_2)} = \omega_M H^{01}_{k,(n_1 m_1)(n_2 m_2)}, \tag{5.43}$$

$$\Delta_{k,(nm)} = \omega_H + D_\mathrm{ex} K^2_{k,(nm)}, \tag{5.44}$$

where $\omega_M = \gamma\mu_0 M_\mathrm{s}$, $\omega_H = \gamma\mu_0 H_\mathrm{ext}$, $K^2_{k,(nm)} = k^2 + \left(\kappa^X_n\right)^2 + \left(\kappa^Y_m\right)^2$, $D_\mathrm{ex} = \alpha_\mathrm{ex}\omega_M$, and

$$\begin{aligned} &H^{00}_{k,(n_1m_1)(n_2m_2)} \\ &= \frac{1}{2}\left(H^{XX}_{k,(n_1m_1)(n_2m_2)} + H^{YY}_{k,(n_1m_1)(n_2m_2)} + i\left(H^{XY}_{k,(n_1m_1)(n_2m_2)} - H^{YX}_{k,(n_1m_1)(n_2m_2)}\right)\right), \end{aligned} \tag{5.45}$$

$$\begin{aligned} &H^{01}_{k,(n_1m_1)(n_2m_2)} \\ &= \frac{1}{2}\left(H^{XX}_{k,(n_1m_1)(n_2m_2)} - H^{YY}_{k,(n_1m_1)(n_2m_2)} - i\left(H^{XY}_{k,(n_1m_1)(n_2m_2)} + H^{YX}_{k,(n_1m_1)(n_2m_2)}\right)\right). \end{aligned} \tag{5.46}$$

Here, $H^{XX}_{k,(n_1m_1)(n_2m_2)}$, $H^{XY}_{k,(n_1m_1)(n_2m_2)}$, $H^{YX}_{k,(n_1m_1)(n_2m_2)}$, and $H^{YY}_{k,(n_1m_1)(n_2m_2)}$ are given by

$$H^{XX}_{k,(n_1m_1)(n_2m_2)} = \int d\boldsymbol{\rho}_1 d\boldsymbol{\rho}_2 (\partial_{x_1}\varphi^{XY}_{n_1m_1}(\boldsymbol{\rho}_1))\frac{K_0(|k(\boldsymbol{\rho}_1-\boldsymbol{\rho}_2)|)}{2\pi}(\partial_{x_2}\varphi^{XY}_{n_2m_2}(\boldsymbol{\rho}_2)), \tag{5.47}$$

$$H^{XY}_{k,(n_1m_1)(n_2m_2)} = \int d\boldsymbol{\rho}_1 d\boldsymbol{\rho}_2 (\partial_{x_1}\varphi^{XY}_{n_1m_1}(\boldsymbol{\rho}_1))\frac{K_0(|k(\boldsymbol{\rho}_1-\boldsymbol{\rho}_2)|)}{2\pi}(\partial_{y_2}\varphi^{XY}_{n_2m_2}(\boldsymbol{\rho}_2)), \tag{5.48}$$

$$H^{YX}_{k,(n_1m_1)(n_2m_2)} = \int d\boldsymbol{\rho}_1 d\boldsymbol{\rho}_2 (\partial_{y_1}\varphi^{XY}_{n_1m_1}(\boldsymbol{\rho}_1))\frac{K_0(|k(\boldsymbol{\rho}_1-\boldsymbol{\rho}_2)|)}{2\pi}(\partial_{x_2}\varphi^{XY}_{n_2m_2}(\boldsymbol{\rho}_2), \tag{5.49}$$

$$H^{YY}_{k,(n_1m_1)(n_2m_2)} = \int d\boldsymbol{\rho}_1 d\boldsymbol{\rho}_2 (\partial_{y_1}\varphi^{XY}_{n_1m_1}(\boldsymbol{\rho}_1))\frac{K_0(|k(\boldsymbol{\rho}_1-\boldsymbol{\rho}_2)|)}{2\pi}(\partial_{y_2}\varphi^{XY}_{n_2m_2}(\boldsymbol{\rho}_2)), \tag{5.50}$$

where K_α is the modified Bessel function of the second kind, $\boldsymbol{\rho} = x\hat{x} + y\hat{y}$, and $\varphi^{XY}_{nm}(\boldsymbol{\rho}) = \mathcal{F}^X(x)\mathcal{F}^Y(y)\psi^X_n(x)\psi^Y_m(y)$. Note that we have relations $A_{k,(n_1m_1)(n_2m_2)} = \left(A_{k,(n_2m_2)(n_1m_1)}\right)^*$ and $B_{k,(n_1m_1)(n_2m_2)} = B_{k,(n_2m_2)(n_1m_1)}$.

As we consider the case where the thickness d and the width w are small such that the exchange energy difference $D_\mathrm{ex}K^2_{k,(n_1m_1)} - D_\mathrm{ex}K^2_{k,(n_2m_2)}$ [with $(n_1, m_1) \neq (n_2, m_2)$] is large as compared to the off-diagonal components [elements of $A_{k,(n_1m_1)(n_2m_2)}$ or $B_{k,(n_1,m_1)(n_2m_2)}$

with $(n_1 m_1) \neq (n_2, m_2)$] of the Hamiltonian, we apply the block-diagonal approximation [148]. Note that we can go beyond the block-diagonal approximation with the procedure using a paraunitary matrix presented in Ref. [151]. Under this block-diagonal approximation, we obtain

$$\mathcal{H}_{\mathrm{m}} = \frac{1}{2}\int \frac{dk}{2\pi}\sum_{nm}\left[a^*_{k,(n,m)}\ a_{-k,(n,m)}\right]\begin{bmatrix} A_{k,(n,m)} & B_{k,(n,m)} \\ B^*_{k,(n,m)} & A_{k,(n,m)} \end{bmatrix}\begin{bmatrix} a_{k,(n,m)} \\ a^*_{-k,(n,m)} \end{bmatrix}, \tag{5.51}$$

$$A_{k,(n,m)} = A_{k,(nm)(nm)}; \quad B_{k,(n,m)} = B_{k,(nm)(nm)}. \tag{5.52}$$

The Hamiltonian above can be diagonalized by the standard 2×2 Bogoliubov transformation:

$$\beta_{k,(n,m)} = \lambda_{k,(n,m)} a_{k,(n,m)} + \mu_{k,(n,m)} a^*_{-k,(n,m)}, \tag{5.53}$$

$$\beta^*_{-k,(n,m)} = \mu^*_{k,(n,m)} a_{k,(n,m)} + \lambda_{k,(n,m)} a^*_{-k,(n,m)}, \tag{5.54}$$

$$\lambda_{k,(n,m)} = \sqrt{\frac{A_{k,(n,m)} + \omega_{k,(n,m)}}{2\omega_{k,(n,m)}}}; \quad \mu_{k,(n,m)} = \frac{B_{k,(n,m)}}{\left|B_{k,(n,m)}\right|}\sqrt{\frac{A_{k,(n,m)} - \omega_{k,(n,m)}}{2\omega_{k,(n,m)}}}, \tag{5.55}$$

$$\omega_{k,(n,m)} = \sqrt{A^2_{k,(n,m)} - \left|B_{k,(n,m)}\right|^2}, \tag{5.56}$$

and we obtain

$$\mathcal{H}_{\mathrm{m}} = \sum_{nm}\int \frac{dk}{2\pi}\omega_{k,(n,m)}\beta^*_{k,(n,m)}\beta_{k,(n,m)}. \tag{5.57}$$

Now we limit our discussion to the subspace with $(n, m) = (0, 0)$ that gives the lowest energy magnon band, for which magnetization dynamics is uniform across x-y plane in the ferromagnet. After promoting the classical complex canonical variables to the quantum creation and annihilation operators via $\beta_{k,(0,0)} \to \sqrt{\hbar}\hat{\beta}_{k,(0,0)}$ and $\beta^*_{k,(0,0)} \to \sqrt{\hbar}\hat{\beta}^\dagger_{k,(0,0)}$, we

obtain

$$\mathcal{H}_{\mathrm{m}} = \int \frac{dk}{2\pi} \hbar\omega_{k,(0,0)} \beta^{\dagger}_{k,(0,0)} \beta_{k,(0,0)}. \tag{5.58}$$

Here, $\hbar\omega_{k,(00)}$ is the magnon energy and $\beta_{k,(00)}$ is the normal mode magnon annihilation operator satisfying $[\beta_{k,(00)}, \beta^{\dagger}_{k',(00)}] = 2\pi\delta(k-k')$. For calculating the dispersion relation in Fig. 5.2(c), we numerically evaluate Eqs. (5.47)-(5.50). In the subspace with $(n,m) = (0,0)$, $\psi^X_n(x)$ and $\psi^Y_m(y)$ are constant functions, so the derivatives only act on $\mathcal{F}^X(x)$ and $\mathcal{F}^Y(y)$, resulting in the surface integrals and the evaluation is simpler. Beyond the diagonal approximation $(n_1, m_1) = (n_2, m_2)$ made for Eq. (5.41), we can diagonalize the full Hamiltonian via the Bogoliubov transformation with the paraunitary matrix [151] after a truncation of large wavenumber modes, which is used in the magnetic bar calculations later sections.

In Fig. 5.2(b) we plot the NV center's transition frequencies and magnon mode frequencies as a function of the external magnetic field H_{ext}, where we have assumed $(d, w) =$ (20 nm, 120 nm) for the waveguide dimensions [154]. As we take the limit where the length of the YIG waveguide is infinity ($l \to \infty$), the magnon mode frequencies form a continuum with its minimum denoted as ω_{min}. At field $H_{\mathrm{ext}} = H_c$, the NV center's lower transition frequency ω_{NV} is detuned from the magnon dispersion minimum ω_{min} by $\Delta\omega = \omega_{\mathrm{min}} - \omega_{\mathrm{NV}} = 2\pi\Delta f = 2\pi \times 3$ MHz, which become important when computing the NV-NV effective coupling in the next section.

5.3.3 NV-magnon coupling

The coupling strength between magnons and NV centers is obtained by applying the same Bogoliubov transformation in the interaction Hamiltonian Eq. (5.3). Up to the quadratic order in $\mathbf{m}(\mathbf{r})$, we obtain

$$\mathcal{H}_{\text{int}} = \sum_{i=1,2} \gamma\mu_0 \mathbf{S}_{\text{NV}_i} \cdot \left[\mathbf{H}_{\text{d}}(\mathbf{r}) + \nabla \int d\mathbf{r}' G\left(\mathbf{r}-\mathbf{r}'\right) \left(\nabla' \cdot \vec{\mathcal{M}}\left(\mathbf{r}'\right) \mathcal{F}\left(\mathbf{r}'\right) - \frac{\partial'_z \mathcal{F}\left(\mathbf{r}'\right) \vec{\mathcal{M}}^2\left(\mathbf{r}'\right)}{2M_{\text{s}}} \right) \right] \Bigg|_{\mathbf{r}=\mathbf{r}_i} . \tag{5.59}$$

In the infinitely long waveguide case, we have $\mathbf{H}_{\text{d}}(\mathbf{r}) = 0$. Up to the lowest order (linear order) in $\mathbf{m}(\mathbf{r})$, we obtain

$$\mathcal{H}_{\text{int}} = \sum_{i=1,2} \gamma\mu_0 \mathbf{S}_{\text{NV}_i} \cdot \mathbf{h}(\mathbf{r})\big|_{\mathbf{r}=\mathbf{r}_i} , \tag{5.60}$$

$$\mathbf{h}(\mathbf{r}) = \nabla \int d\mathbf{r}' G\left(\mathbf{r}-\mathbf{r}'\right) \left(\nabla' \cdot \vec{\mathcal{M}}\left(\mathbf{r}'\right) \mathcal{F}\left(\mathbf{r}'\right) \right) . \tag{5.61}$$

As the NV axis is set $\hat{n}_{\text{NV}} = \hat{z}$, the rotating-wave term comes from the perpendicular contribution $\mathbf{h}_{\perp}(\mathbf{r}) = h_x(\mathbf{r})\hat{x} + h_y(\mathbf{r})\hat{y}$. Using the Bogoliubov transformation (5.55), we obtain

$$\mu_0\gamma\mathbf{h}_{\perp}(\mathbf{r}) = \frac{\sqrt{2\omega_M\omega_d}}{\sqrt{w/d^2}} \frac{1}{4} \sum_{nm} \int \frac{dk}{2\pi} e^{ikz} [\widehat{e}_+ \; \widehat{e}_-] \begin{bmatrix} \Gamma^{-,+}_{k,nm} & \Gamma^{-,-}_{k,nm} \\ \Gamma^{+,+}_{k,nm} & \Gamma^{+,-}_{k,nm} \end{bmatrix} \times \begin{bmatrix} \lambda_{k,(n,m)} & -\mu_{k,(n,m)} \\ -\mu^*_{k,(n,m)} & \lambda_{k,(n,m)} \end{bmatrix} \begin{bmatrix} \beta_{k,(n,m)} \\ \beta^{\dagger}_{-k,(n,m)} \end{bmatrix} , \tag{5.62}$$

where $\omega_d = \mu_0(\hbar\gamma)^2/(\hbar d^3)$ and

$$\Gamma^{-,+}_{k,nm} = \left(\Gamma^{XX}_{k,nm} + \Gamma^{YY}_{k,nm} + i\left(\Gamma^{XY}_{k,nm} - \Gamma^{YX}_{k,nm}\right)\right), \tag{5.63}$$

$$\Gamma^{-,-}_{k,nm} = \left(\Gamma^{XX}_{k,nm} - \Gamma^{YY}_{k,nm} - i\left(\Gamma^{XY}_{k,nm} + \Gamma^{YX}_{k,nm}\right)\right), \tag{5.64}$$

$$\Gamma^{+,+}_{k,nm} = \left(\Gamma^{XX}_{k,nm} - \Gamma^{YY}_{k,nm} + i\left(\Gamma^{XY}_{k,nm} + \Gamma^{YX}_{k,nm}\right)\right), \tag{5.65}$$

$$\Gamma^{+,-}_{k,nm} = \left(\Gamma^{XX}_{k,nm} + \Gamma^{YY}_{k,nm} - i\left(\Gamma^{XY}_{k,nm} - \Gamma^{YX}_{k,nm}\right)\right). \tag{5.66}$$

Here, $\Gamma^{XX}_{k,nm}$, $\Gamma^{XY}_{k,nm}$, $\Gamma^{YX}_{k,nm}$, and $\Gamma^{YY}_{k,nm}$ are functions of $\boldsymbol{\rho}$, and they are given by

$$\Gamma^{XX}_{k,nm} = -\int d\boldsymbol{\rho}'|k|\left(\widehat{\boldsymbol{\rho}-\boldsymbol{\rho}'}\right)_x \frac{K_1\left(\left|k\left(\boldsymbol{\rho}-\boldsymbol{\rho}'\right)\right|\right)}{2\pi}\partial'_x\tilde{\varphi}^{XY}_{nm}(\boldsymbol{\rho}'), \tag{5.67}$$

$$\Gamma^{XY}_{k,nm} = -\int d\boldsymbol{\rho}'|k|\left(\widehat{\boldsymbol{\rho}-\boldsymbol{\rho}'}\right)_x \frac{K_1\left(\left|k\left(\boldsymbol{\rho}-\boldsymbol{\rho}'\right)\right|\right)}{2\pi}\partial'_y\tilde{\varphi}^{XY}_{nm}(\boldsymbol{\rho}'), \tag{5.68}$$

$$\Gamma^{YX}_{k,nm} = -\int d\boldsymbol{\rho}'|k|\left(\widehat{\boldsymbol{\rho}-\boldsymbol{\rho}'}\right)_y \frac{K_1\left(\left|k\left(\boldsymbol{\rho}-\boldsymbol{\rho}'\right)\right|\right)}{2\pi}\partial'_x\tilde{\varphi}^{XY}_{nm}(\boldsymbol{\rho}'), \tag{5.69}$$

$$\Gamma^{YY}_{k,nm} = -\int d\boldsymbol{\rho}'|k|\left(\widehat{\boldsymbol{\rho}-\boldsymbol{\rho}'}\right)_y \frac{K_1\left(\left|k\left(\boldsymbol{\rho}-\boldsymbol{\rho}'\right)\right|\right)}{2\pi}\partial'_y\tilde{\varphi}^{XY}_{nm}(\boldsymbol{\rho}'), \tag{5.70}$$

where $\tilde{\varphi}^{XY}_{nm} = \sqrt{dw}\varphi^{XY}_{nm}$ is a dimensionless function and $\widehat{\boldsymbol{\rho}-\boldsymbol{\rho}'} = (\boldsymbol{\rho}-\boldsymbol{\rho}')/|\boldsymbol{\rho}-\boldsymbol{\rho}'|$. We consider the external field range $\gamma H_{\text{ext}} < D_{\text{NV}}$, where NV center's ground state is $|g\rangle = |S_z = 0\rangle$ and the first excited state is $|e\rangle = |S_z = -\hbar\rangle$. In the NV center's subspace spanned by $\{|g\rangle, |e\rangle\}$, we can write

$$\mathcal{H}_{\text{NV}} = \sum_{i=1,2} \frac{\hbar\omega_{\text{NV}}}{2}\sigma^z_{\text{NV}_i}, \tag{5.71}$$

where $\omega_{\text{NV}} = D_{\text{NV}} - \gamma H_{\text{ext}}$, $\sigma^z_{\text{NV}} = |e\rangle\langle e| - |g\rangle\langle g|$, and we drop a constant shift in energy. We also have $S^+_{\text{NV}} = \sqrt{2}\hbar\sigma^-_{\text{NV}}$ and $S^-_{\text{NV}} = \sqrt{2}\hbar\sigma^+_{\text{NV}}$, where $\sigma^+_{\text{NV}} = |e\rangle\langle g|$, and $\sigma^-_{\text{NV}} = |g\rangle\langle e|$. Under the rotating wave approximation, we obtain

$$\mathcal{H}_{\text{int}} \approx \hbar \sum_{i=1,2} \frac{\sqrt{\omega_M\omega_d}}{\sqrt{w/d^2}} \sum_{nm} \int \frac{dk}{2\pi}\, \frac{1}{2}\left(\Gamma^{+,+}_{k,nm}\lambda_{k,(n,m)} - \Gamma^{+,-}_{k,nm}\mu^*_{k,(n,m)}\right)\Big|_{\boldsymbol{\rho}=\boldsymbol{\rho}_i} \sigma^+_{\text{NV}_i}\beta_{k,(n,m)}e^{ikz_i} + \text{H.c.}. \tag{5.72}$$

Limiting our discussion to the subspace with $(n, m) = (0, 0)$, which shows the uniform magnetization precession across the YIG waveguide's cross section and gives the lowest energy magnon band, we obtain

$$\mathcal{H}_{\text{int}} = \hbar \frac{\sqrt{\omega_M \omega_d}}{\sqrt{w/d^2}} \sum_{i=1,2} \int \frac{dk}{2\pi} g(\boldsymbol{\rho}_i, k) \sigma^{+}_{\text{NV}_i} \beta_{k,(0,0)} e^{ikz_i} + \text{H.c.}, \tag{5.73}$$

$$g(\boldsymbol{\rho}_i, k) = \left(\left(\Gamma^{+,+}_{k,nm}/2 \right) \lambda_{k,(n,m)} - \left(\Gamma^{+,-}_{k,nm}/2 \right) \mu^{*}_{k,(n,m)} \right) \Big|_{\boldsymbol{\rho}=\boldsymbol{\rho}_i} . \tag{5.74}$$

Here, $g(\boldsymbol{\rho}_i, k)$ is the dimensionless coupling. To calculate the spatial distribution of the dimensionless coupling, we evaluate Eqs. (5.67)-(5.70) numerically.

5.3.4 Effective NV-NV Hamiltonian

The NV-NV interaction mediated by magnons can be calculated via the Schrieffer-Wolff transformation [155], $\mathcal{H} \to D\mathcal{H}D^{\dagger}$ with $D = \exp\left(S - S^{\dagger}\right)$ (as discussed in Chapter 3). Here, Eqs. (5.58), (5.71), and (5.73) are used in $\mathcal{H} = \mathcal{H}_0 + \mathcal{H}_{\text{int}}$ with $\mathcal{H}_0 = \mathcal{H}_{\text{NV}} + \mathcal{H}_{\text{m}}$. We pick

$$S = \frac{\sqrt{\omega_M \omega_d}}{\sqrt{w/d^2}} \sum_{i=1,2} \int \frac{dk}{2\pi} \frac{g(\boldsymbol{\rho}_i, k) \sigma^{+}_{\text{NV}_i} \beta_{k,(0,0)} e^{ikz_i}}{\omega_{\text{NV}} - \omega_{k,(0,0)}}, \tag{5.75}$$

such that $[S - S^{\dagger}, \mathcal{H}_0] = -\mathcal{H}_{\text{int}}$. Noting that we can write $S - S^{\dagger} = (i/\hbar) \int_{-\infty}^{0} d\tau \mathcal{H}_{\text{int}}(\tau)$, where $\mathcal{H}_{\text{int}}(\tau)$ is the interaction Hamiltonian in the interaction picture, we obtain the following effective Hamiltonian

$$\mathcal{H}_{\text{eff}} = \frac{1}{2}[S - S^{\dagger}, \mathcal{H}_{\text{int}}] = \frac{i}{2\hbar} \int_{-\infty}^{0} d\tau [\mathcal{H}_{\text{int}}(\tau), \mathcal{H}_{\text{int}}], \tag{5.76}$$

which is related to the linear response theory. This effective Hamiltonian includes the Lamb shift, the Stark shift, and the NV-NV interaction. The NV-NV interaction contribution is,

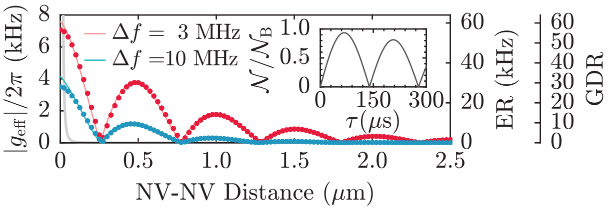

Figure 5.3: Effective NV-NV coupling strength $g_{\rm eff}$ [Eq. (5.78)] as a function of the NV-NV distance under $\Delta f = 3$ MHz and $\Delta f = 10$ MHz. The gray curve shows the coupling due to the direct magnetic dipole-dipole interaction between NV centers. The entanglement rate and the gate to decoherence ratio are shown on the right axis for $T_2^* = 1$ ms. Inset shows the time τ evolution of the entanglement negativity at $T = 0$ from the initial state $|g\rangle_1|e\rangle_2$ scaled by the Bell state negativity $\mathcal{N}_{\rm B}$.

assuming $\boldsymbol{\rho}_1 = \boldsymbol{\rho}_2$ and writing $g(k) = g(\boldsymbol{\rho}_i, k)$,

$$\mathcal{H}_{\rm eff}^{\rm NV-NV} = -\hbar\left(g_{\rm eff}\sigma_{{\rm NV}_1}^{+}\sigma_{{\rm NV}_2}^{-} + {\rm H.c.}\right), \tag{5.77}$$

$$g_{\rm eff} = \frac{\omega_M\omega_d}{w/d^2}\int\frac{dk}{2\pi}|g(k)|^2\frac{\exp\left[ik\left(z_1 - z_2\right)\right]}{\omega_{k,(0,0)} - \omega_{\rm NV}}. \tag{5.78}$$

Here, $g_{\rm eff}$ is the effective NV-NV coupling strength.

Figure 5.2(c) shows the magnon dispersion relation near $\omega_{\rm min}$ and the wavenumber dependence of the dimensionless coupling strength $g(k)$ at $H_{\rm ext} = H_{\rm c}$, $\boldsymbol{\rho}_i = (d+h)\hat{x} + w\hat{y}$, and $h = 25$ nm [see the cross marker in Fig. 5.2(d)]. The coupling strength also depends on the spatial position of the NV center relative to the YIG waveguide, which is shown in Fig. 5.2(d). As the dynamical fringe magnetic field generated by a single magnon is confined near the YIG device, the coupling strength is larger if the NV center is positioned near the YIG waveguide.

Under the off-resonant condition shown in Fig. 5.2(c), the NV centers on top of the YIG waveguide interact to each other via the exchange of virtual magnons. In Fig. 5.3, we plot the effective NV-NV coupling strength $g_{\rm eff}$ [Eq. (5.78)] as a function of the NV-NV distance $\delta z = |z_1 - z_2|$ for both $\Delta f = 3$ MHz and $\Delta f = 10$ MHz cases represented by the red and blue dots, respectively. The coupling decays rapidly with detuning, which allows the entangling interaction to be switched off by increasing the external magnetic field from $H_{\rm ext} = H_c$ by

≈ 0.1 mT. We show that the calculated coupling strength is well explained by the analytical formula

$$g_{\rm eff} \approx \frac{\omega_M \omega_{\bar{d}}}{\Delta\omega} |g(k_{\rm min})|^2 \cos(k_{\rm min}\delta z) e^{-\delta z/\xi_0} \tag{5.79}$$

as shown by the solid red and blue curves in Fig. 5.3, where $\xi_0 = \sqrt{D_{\rm ex}/\Delta\omega}$ is the spin correlation length and $\omega_{\bar{d}} = \mu_0 \gamma^2/(\xi_0 w d)$. The entangling gate rate ER $= 4g_{\rm eff}/\pi$ [the inverse of the time required for the $\sqrt{i\rm SWAP}$ gate, $\tau_{\sqrt{i\rm SWAP}} = \pi/(4|g_{\rm eff}|)$, under the interaction Hamiltonian (5.77)] and the gate to decoherence ratio GDR $= 4g_{\rm eff}T_2^*/\pi$ are shown on the right axis, where a coherence time $T_2^* = 1$ ms of the NV center is used [54]. As we obtain GDR > 10 for 1 μm separated NV centers, we predict a useful and practical entangling gate.

The approximate analytic expression of $g_{\rm eff}$ can be obtained in the following way. We first expand the dispersion $\omega_{k,(0,0)}$ around the two energy minimum at $k = \pm k_{\rm min}$ and approximate $g(k) \approx g(k_{\rm min})$. Secondly, we also approximate the curvature to be exchange dominated, i.e., $\omega_{l,(0,0)} \approx \omega_{k_{\rm min},(0,0)} + D_{\rm ex}(k \mp k_{\rm min})^2$. Then we obtain, after writing $\Delta\omega = \omega_{k_{\rm min},(0,0)} - \omega_{\rm NV}$,

$$\begin{aligned} g_{\rm eff} &\approx \frac{\omega_M \omega_d}{w/d^2} \left|g\left(k_{\rm min}\right)\right|^2 \left(\int_{-\infty}^{\infty} \frac{dk}{2\pi} \frac{\exp\left[ik\left(z_1 - z_2\right)\right]}{D_{\rm ex}\left(k - k_{\rm min}\right)^2 + \Delta\omega} + \int_{-\infty}^{\infty} \frac{dk}{2\pi} \frac{\exp\left[ik\left(z_1 - z_2\right)\right]}{D_{\rm ex}\left(k + k_{\rm min}\right)^2 + \Delta\omega} \right), \\ &= \frac{\omega_M \omega_{\bar{d}}}{\Delta\omega} \left|g\left(k_{\rm min}\right)\right|^2 \cos\left(k_{\rm min}\delta z\right) \exp\left[\delta z/\xi_0\right], \end{aligned} \tag{5.80}$$

where $\xi_0 = \sqrt{D_{\rm ex}/\Delta\omega}$, $\delta z = |z_1 - z_2|$ and $\omega_{\bar{d}} = \mu_0(\gamma\hbar)^2/(\hbar d w \xi_0)$. Note that the circle dots in Fig. 5.3 are obtained by the numerical evaluation of Eq. (5.78), while the solid curves are obtained from the analytical expression (5.80), thus showing the great agreement between them.

To show that this system can manipulate the NV-NV entanglement, we perform a simulation using the Lindblad master equation. In the inset of Fig. 5.3 we plot the entanglement negativity [156] $\mathcal{N}$ at $T = 0$ as a function of the NV-NV interaction time after the preparation of the initial spin state in $|g\rangle_1|e\rangle_2$, where the negativity is normalized by the Bell state's negativity $\mathcal{N}_{\mathrm{B}}$. As we obtain $\mathcal{N} > 0$, we clearly demonstrate that the NV centers are entangled. If multiple NV centers are placed on top of the YIG waveguide (see Fig. 5.1), neighboring two-NV gates can thus be performed by locally changing the external magnetic field around the two NV centers to shift their transition frequencies relative to the minimum magnon mode frequency in the range $\Delta\omega > 0$. Alternatively, local electric field [157] or strain [158] can be used to shift NV centers' transition frequencies to avoid applying a local magnetic field at the underlying YIG location, the effect of which is discussed in Appendix of Ref. [2].

To evaluate how good the perturbation is, we consider one NV case and recall the wave function modification in the first order perturbation

$$|n^{(1)}\rangle = \frac{1}{E_n^{(0)} - \mathcal{H}_0}\mathcal{H}_{\mathrm{int}}|n^0\rangle = \sum_{k(\neq n)} \frac{\langle k^{(0)}|\mathcal{H}_{\mathrm{int}}|n^{(0)}\rangle}{E_n^{(0)} - E_k^{(0)}}|k^{(0)}\rangle, \tag{5.81}$$

where $|n^{(0)}\rangle$ and $E_n^{(0)}$ are the unperturbed eigenstate and eigenenergy. The fraction of the finite magnon-number state contribution in the original ground state $|n^{(0)}\rangle = |g\rangle|0\rangle_{\mathrm{m}}$ is, where $|0\rangle_{\mathrm{m}}$ is the magnon vacuum,

$$\left\| \left| n^{(1)} \right\rangle \right\|^2 = \sum_{k(\neq n)} \left| \frac{\left\langle k^{(0)}|\mathcal{H}_{\mathrm{int}}|n^{(0)} \right\rangle}{E_n^{(0)} - E_k^{(0)}} \right|^2 = \frac{\omega_M \omega_d}{w/d^2} \int \frac{dk}{2\pi} \frac{|g(k)|^2}{(\omega_{k,(0,0)} - \omega_{\mathrm{NV}})^2}. \tag{5.82}$$

Under the geometry presented in the red curve in Fig. 5.3, we obtain $\||n^{(1)}\rangle\|^2 \approx 10^{-3} \ll 1$, which indicates the perturbation theory is valid.

To estimate the corresponding cooperativity of the red solid curve in Fig. 5.3, we assume the waveguide has a length l as in [137]. By discretizing the integral $\int dk$ using the periodic boundary condition and rescaling the creation/annihilation operators via $\bar{\beta}_{k,(0,0)} = \beta_{k,(0,0)}/\sqrt{l}$ to have a correct commutation relation for the discretized modes, $[\bar{\beta}_{k,(0,0)}, \tilde{\beta}^{\dagger}_{k',(0,0)}] =$

$\delta_{k,k'}$, the interaction Hamiltonian becomes

$$\mathcal{H}_{\text{int}} = \sum_{i=1,2} \sum_{k} \hbar \bar{g}(k) \sigma^{+}_{\text{NV}_i} \bar{\beta}_{k,(0,0)} e^{ikz_i} + \text{H.c.}, \tag{5.83}$$

$$\bar{g}(k) = \frac{\sqrt{\omega_M \omega_d}}{\sqrt{lw/d^2}} g(k). \tag{5.84}$$

As we are mostly using magnons with $|k| \approx k_{\text{min}}$ in the virtual-magnon mediated NV-NV coupling, it is reasonable to calculate the equivalent cooperativity with $\bar{g} = \bar{g}(k_{\text{min}})$:

$$\mathcal{C}_{\text{eq}} = \frac{\bar{g}^2}{\alpha \omega_{\text{min}} / T_2^*}. \tag{5.85}$$

Under the geometry presented in the red curve in Fig. 5.3, and using the NV center's coherence time [54] $T_2^* = 1$ ms and the Gilbert damping parameter of YIG [159] $\alpha = 10^{-5}$, we obtain $\bar{g} \approx 130$ kHz and $\mathcal{C}_{\text{eq}} \approx 3700$.

In Fig. 5.4 we plot the NV-NV entanglement rate and the gate to decoherence ratio as a function of the waveguide thickness d for different waveguide dimensions and NV centers' heights h. We assume a fixed NV-NV distance of 1 μm, $(x_i, y_i) = (d + h, w)$, and $\Delta\omega = 2\pi \times 3$ MHz. The red (blue) solid curve shows the waveguide thickness d dependence of the ER and the GDR under the fixed aspect ratio $w/d = 6$ at $h = 25$ nm (5 nm), and the red (blue) dashed curve shows the dependence where the waveguide width is kept constant with $w = 120$ nm at $h = 25$ nm (5 nm). From these graphs we see that in order to make the entangling gate faster, one can either have the NV center closer to the YIG waveguide (diminishing h) or make the waveguide's cross-sectional area smaller. As for placing NV centers in proximity to the YIG waveguide, we note the common challenge of making high coherence NV centers near the diamond surface due to the surface noise known in the area of NV-based quantum sensing [160].

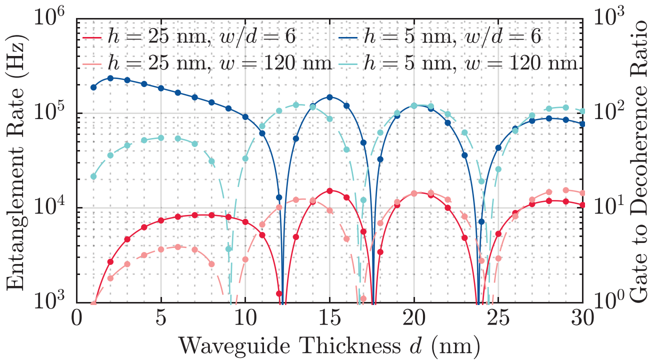

Figure 5.4: The entanglement rate ($4g_{\text{eff}}/\pi$) and the gate to decoherence ratio (GDR=$4g_{\text{eff}}T_2^*/\pi$) between two NV centers separated by 1 μm as a function of the waveguide thickness d. NV centers are placed on the YIG waveguide as drawn in Figs. 2(a) and 2(d). Red curves and blue curves are calculated for $h = 25$ nm and 5 nm, respectively. Solid curves and dashed curves are calculated for a fixed aspect ratio w/d and width w of the waveguide, respectively. Sharp dips correspond to the nodes in the oscillation of g_{eff} as shown in Fig. 5.3. Calculation is performed for detuning $\Delta\omega/2\pi = 3$ MHz.

5.4 Finite length ferromagnetic bar

In this section, we show that the strength of the NV-magnon coupling can be strongly enhanced by confining the magnon's mode volume to a finite length ferromagnetic bar. The system allows us to control the NV levels to be on- and off-resonant to the magnon levels as the magnon mode frequencies are discretized for this case. Here, the interaction Hamiltonian Eq. (5.3) can be transformed into the form of the Jaynes-Cummings model [140, 161], and the entangling gate protocols used in quantum optics or circuit quantum electrodynamics (circuit QEDs) can now be implemented in our hybrid quantum system [29, 162, 163].

We first obtain the NV-magnon interaction Hamiltonian for a finite length YIG bar using a similar procedure shown in Sec. 5.3. For that, we first take the equilibrium magnetization to be $\mathbf{M}_0 = M_s\mathcal{F}(\mathbf{r})\hat{z}$ and approximate the x, y component of the resulting static demagnetization field in Eq. (5.2) to be negligible compared to its z component. Although there is also a finite static demagnetization field contribution in the interaction Hamiltonian Eq. (5.3), we verified that its value is small under the geometry parameters and NV center positions we consider.

5.4.1 Diagonalization of the magnon Hamiltonian

To diagonalize the magnon Hamiltonian Eq. (5.33), we expand the canonical variables as

$$a(\mathbf{r}) = \sum_{nmp} f_n^X(x) f_m^Y(y) f_p^Z(z) a_{(nmp)}, \tag{5.86}$$

$$a^*(\mathbf{r}) = \sum_{nmp} f_n^X(x) f_m^Y(y) f_p^Z(z) a_{(nmp)}^*, \tag{5.87}$$

$$f_p^Z(z) = \sqrt{\mathcal{F}^Z(z)}\psi_p^Z(z), \tag{5.88}$$

$$\psi_p^Z(z) = \sqrt{\frac{2}{\left(1+\delta_{p,0}\right)l}} \cos\left(\kappa_p^z z\right), \tag{5.89}$$

where $\kappa_p^Z = p\pi/l$, $p = 0, 1, \cdots$, and $\mathcal{F}^Z(z) = \Theta(z)\Theta(l-z)$. Note that we have $\mathcal{F}(\mathbf{r}) = \mathcal{F}^X(x)\mathcal{F}^Y(y)\mathcal{F}^Z(z)$. After simplification and writing $\mu = (nmp)$, the magnon Hamiltonian Eq. (5.33) with corresponding parameters become

$$\mathcal{H}_{\mathrm{m}} = \frac{\omega_M}{2} \sum_{\mu_1\mu_2} \left[a_{\mu_1}^* \; a_{\mu_1}\right] \begin{bmatrix} A_{\mu_1\mu_2} & B_{\mu_1\mu_2} \\ B_{\mu_1\mu_2}^* & A_{\mu_1\mu_2}^* \end{bmatrix} \begin{bmatrix} a_{\mu_2} \\ a_{\mu_2}^* \end{bmatrix}, \tag{5.90}$$

$$A_{\mu_1\mu_2} = \widetilde{\Delta}_{\mu_1}\delta_{\mu_1\mu_2} - \mathcal{N}_{\mu_1\mu_2} + H_{\mu_1\mu_2}^{00}, \tag{5.91}$$

$$B_{\mu_1\mu_2} = H_{\mu_1\mu_2}^{01}, \tag{5.92}$$

$$\widetilde{\Delta}_{(nmp)} = (\omega_H + D_{\mathrm{ex}} K_{(nmp)}^2)/\omega_M, \tag{5.93}$$

$$\mathcal{N}_{\mu_1\mu_2} = -\int d\mathbf{r} \tilde{H}_{\mathrm{d}}^z(\mathbf{r}) f_{\mu_1}^{XYZ}(\mathbf{r}) f_{\mu_2}^{XYZ}(\mathbf{r}), \tag{5.94}$$

where $K_{(nmp)}^2 = \left(\kappa_n^X\right)^2 + \left(\kappa_m^Y\right)^2 + \left(\kappa_p^Z\right)^2$, $f_\mu^{XYZ}(\mathbf{r}) = f_n^X(x) f_m^Y(y) f_p^Z(z)$, $\tilde{H}_{\mathrm{d}}^z(\mathbf{r})$ is a dimensionless demagnetization field

$$\widetilde{H}_{\mathrm{d}}^z(\mathbf{r}) = \frac{H_{\mathrm{d}}^z(\mathbf{r})}{M_s} = \frac{1}{M_s}\partial_z \int d\mathbf{r}' G\left(\mathbf{r}-\mathbf{r}'\right)\left(\nabla' \cdot \mathbf{M}_0\left(\mathbf{r}'\right)\right), \tag{5.95}$$

and $H^{00}_{\mu_1\mu_2}$ and $H^{01}_{\mu_1\mu_2}$ are given by

$$H^{00}_{\mu_1\mu_2} = \frac{1}{2}\left(H^{XX}_{\mu_1\mu_2} + H^{YY}_{\mu_1\mu_2} + i\left(H^{XY}_{\mu_1\mu_2} - H^{YX}_{\mu_1\mu_2}\right)\right), \tag{5.96}$$

$$H^{01}_{\mu_1\mu_2} = \frac{1}{2}\left(H^{XX}_{\mu_1\mu_2} - H^{YY}_{\mu_1\mu_2} - i\left(H^{XY}_{\mu_1\mu_2} + H^{YX}_{\mu_1\mu_2}\right)\right). \tag{5.97}$$

Here, $H^{XX}_{\mu_1\mu_2}$, $H^{XY}_{\mu_1\mu_2}$, $H^{YX}_{\mu_1\mu_2}$, and $H^{YY}_{\mu_1\mu_2}$ are given by

$$H^{XX}_{\mu_1\mu_2} = \int d\mathbf{r}_1 d\mathbf{r}_2 \left(\partial_{x_1}\varphi^{XYZ}_{\mu_1}(\mathbf{r}_1)\right) G(\mathbf{r}_1 - \mathbf{r}_2) \left(\partial_{x_2}\varphi^{XYZ}_{\mu_2}(\mathbf{r}_2)\right), \tag{5.98}$$

$$H^{XY}_{\mu_1\mu_2} = \int d\mathbf{r}_1 d\mathbf{r}_2 \left(\partial_{x_1}\varphi^{XYZ}_{\mu_1}(\mathbf{r}_1)\right) G(\mathbf{r}_1 - \mathbf{r}_2) \left(\partial_{y_2}\varphi^{XYZ}_{\mu_2}(\mathbf{r}_2)\right), \tag{5.99}$$

$$H^{YX}_{\mu_1\mu_2} = \int d\mathbf{r}_1 d\mathbf{r}_2 \left(\partial_{y_1}\varphi^{XYZ}_{\mu_1}(\mathbf{r}_1)\right) G(\mathbf{r}_1 - \mathbf{r}_2) \left(\partial_{x_2}\varphi^{XYZ}_{\mu_2}(\mathbf{r}_2)\right), \tag{5.100}$$

$$H^{YY}_{\mu_1\mu_2} = \int d\mathbf{r}_1 d\mathbf{r}_2 \left(\partial_{y_1}\varphi^{XYZ}_{\mu_1}(\mathbf{r}_1)\right) G(\mathbf{r}_1 - \mathbf{r}_2) \left(\partial_{y_2}\varphi^{XYZ}_{\mu_2}(\mathbf{r}_2)\right), \tag{5.101}$$

where $\varphi^{XYZ}_{nmp}(\mathbf{r}) = \mathcal{F}(\mathbf{r})\psi^X_n(x)\psi^Y_m(y)\psi^Z_p(z)$. Note that we have relations $A_{\mu_1\mu_2} = A^*_{\mu_2\mu_1}$ and $B_{\mu_1\mu_2} = B_{\mu_2\mu_1}$.

Finally, the Hamiltonian Eq. (5.90) can be written in the matrix form

$$\mathcal{H}_\mathrm{m} = \frac{\omega_M}{2}\left[\boldsymbol{\alpha}^* \ \boldsymbol{\alpha}\right] \hat{\mathbf{H}} \begin{bmatrix} \boldsymbol{\alpha} \\ \boldsymbol{\alpha}^* \end{bmatrix}, \tag{5.102}$$

where $\boldsymbol{\alpha} = [a_{\mu_0} \ a_{\mu_1} \ \cdots]$, $\boldsymbol{\alpha}^* = [a^*_{\mu_0} \ a^*_{\mu_1} \ \cdots]$, and we transpose $\boldsymbol{\alpha}$ or $\boldsymbol{\alpha}^*$ if necessary. No confusion is expected for the column or row vectors for $\boldsymbol{\alpha}$ and $\boldsymbol{\alpha}^\dagger$ as in Refs. [151] and [153]. This Hamiltonian matrix can be diagonalized by the paraunitary matrix [151] $\mathbf{T}$ via

$$\begin{bmatrix} \boldsymbol{\alpha} \\ \boldsymbol{\alpha}^* \end{bmatrix} = \mathbf{T} \begin{bmatrix} \boldsymbol{\beta} \\ \boldsymbol{\beta}^* \end{bmatrix}, \tag{5.103}$$

$$\mathcal{H}_\mathrm{m} = \frac{\omega_M}{2}\left[\boldsymbol{\beta}^* \ \boldsymbol{\beta}\right] \begin{bmatrix} \mathbf{E} & \mathbf{O} \\ \mathbf{O} & \mathbf{E} \end{bmatrix} \begin{bmatrix} \boldsymbol{\beta} \\ \boldsymbol{\beta}^* \end{bmatrix}, \tag{5.104}$$

where, $\boldsymbol{\beta} = [\beta_{\mu_0} \ \beta_{\mu_1} \ \cdots]$ and $\boldsymbol{\beta}^* = [\beta^*_{\mu_0} \ \beta^*_{\mu_1} \ \cdots]$ are normal mode magnon complex canonical variables, and $\omega_M \mathbf{E} = \mathrm{diag}[\omega_{\mu_0}, \omega_{\mu_1}, \cdots]$ is a diagonal matrix whose entries are magnon eigenfrequencies with increasing energy order $0 \leq \omega_{\mu_0} \leq \omega_{\mu_1} \leq \cdots$. The paraunitary matrix $\mathbf{T}$ satisfies

$$\mathbf{T}^\dagger \boldsymbol{\sigma}_3 \mathbf{T} = \boldsymbol{\sigma}_3, \tag{5.105}$$

$$\boldsymbol{\sigma}_3 = \mathrm{diag}[+1, +1, \cdots, +1, -1, -1, \cdots, -1]. \tag{5.106}$$

Based on Ref. [151], one can find the paraunitary matrix $\mathbf{T}$ using a method based on the Cholesky decomposition. The outline of the method is shown in the following.

1. Firstly, we decompose $\hat{\mathbf{H}}$ into a product of an upper triangle matrix $\mathbf{K}$ and its Hermitian conjugate using the Cholesky decomposition

$$\hat{\mathbf{H}} = \mathbf{K}^\dagger \mathbf{K}. \tag{5.107}$$

2. Next, we define a new Hermitian matrix $\mathbf{W} = \mathbf{K}\boldsymbol{\sigma}_3\mathbf{K}^\dagger$ and diagonalize this matrix with a unitary matrix $\mathbf{U}$:

$$\mathbf{U}^\dagger \mathbf{W} \mathbf{U} = \begin{bmatrix} \mathbf{E} & \mathbf{O} \\ \mathbf{O} & -\mathbf{E} \end{bmatrix}. \tag{5.108}$$

   Note that one can find $\mathbf{U}$ such that the right-hand side becomes the desired form, which is shown in Ref. [151].

3. Lastly, we define the following matrix $\widetilde{\mathbf{T}}$:

$$\widetilde{\mathbf{T}} = \mathbf{K}^{-1}\mathbf{U} \begin{bmatrix} \mathbf{E}^{1/2} & \mathbf{O} \\ \mathbf{O} & -\mathbf{E}^{1/2} \end{bmatrix} = \begin{bmatrix} \widetilde{\mathbf{T}}^{pp} & \widetilde{\mathbf{T}}^{pn} \\ \widetilde{\mathbf{T}}^{np} & \widetilde{\mathbf{T}}^{nn} \end{bmatrix}. \tag{5.109}$$

Then the desired paraunitary matrix is

$$\mathbf{T} = \begin{bmatrix} \mathbf{T}^{pp} & \mathbf{T}^{pn} \\ \mathbf{T}^{np} & \mathbf{T}^{nn} \end{bmatrix} = \begin{bmatrix} \widetilde{\mathbf{T}}^{pp} & \left(\widetilde{\mathbf{T}}^{np}\right)^* \\ \widetilde{\mathbf{T}}^{np} & \left(\widetilde{\mathbf{T}}^{pp}\right)^* \end{bmatrix}. \tag{5.110}$$

To obtain the eigenfrequencies of the magnons for the finite magnetic bar case, we restrict our discussion for $(n, m) = (0, 0)$ (magnon mode that is uniform across the x-y plane, as we consider the case with $d, w \ll l$) and consider $p = 0, 1, \cdots, N$, where $p = N$ is the highest z-directional wavenumber to be taken into account and we truncated the sum. We set $\mu_0 = (000)$, $\mu_1 = (001)$, $\cdots$, $\mu_N = (00N)$. After the above Bogoliubov transformation with the paraunitary matrix, we obtain

$$\mathcal{H}_{\mathrm{m}} = \sum_{p=0,1,\cdots} \omega_{(00p)} \beta^*_{(00p)} \beta_{(00p)}, \tag{5.111}$$

with corresponding transformation given by

$$\begin{bmatrix} a_{(000)} \\ a_{(001)} \\ \vdots \\ a_{(00N)} \end{bmatrix} = \mathbf{T}^{pp} \begin{bmatrix} \beta_{(000)} \\ \beta_{(001)} \\ \vdots \\ \beta_{(00N)} \end{bmatrix} + \mathbf{T}^{pn} \begin{bmatrix} \beta^*_{(000)} \\ \beta^*_{(001)} \\ \vdots \\ \beta^*_{(00N)} \end{bmatrix}, \tag{5.112}$$

$$\begin{bmatrix} a^*_{(000)} \\ a^*_{(001)} \\ \vdots \\ a^*_{(00N)} \end{bmatrix} = (\mathbf{T}^{pn})^* \begin{bmatrix} \beta_{(000)} \\ \beta_{(001)} \\ \vdots \\ \beta_{(00N)} \end{bmatrix} + (\mathbf{T}^{pp})^* \begin{bmatrix} \beta^*_{(000)} \\ \beta^*_{(001)} \\ \vdots \\ \beta^*_{(00N)} \end{bmatrix}. \tag{5.113}$$

To calculate the magnon eigenfrequencies, we evaluate numerically Eqs. (5.94), (5.95) and

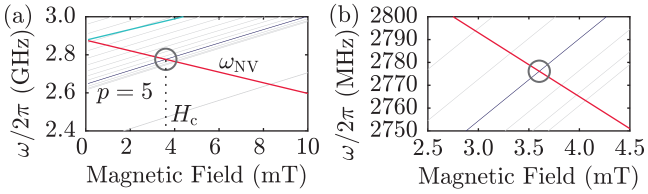

Figure 5.5: (a) NV center's transition frequencies and magnon spectrum as a function of external field $H_{\rm ext}$ for $(d, w, l) = (5\ {\rm nm}, 30\ {\rm nm}, 3\ \mu{\rm m})$. The dark gray and red lines represent frequencies $\omega_{(00,p=5)}$ and $\omega_{\rm NV}$, respectively. (b) Zoom-in of the crossing region between $\omega_{(005)}$ and $\omega_{\rm NV}$.

(5.98)-(5.101). After promoting $\beta_\mu \to \sqrt{\hbar}\hat{\beta}_\mu$ and $\beta^*_\mu \to \sqrt{\hbar}\hat{\beta}^\dagger_\mu$, we obtain

$$\mathcal{H}_{\rm m} = \sum_{p=0,1,\cdots} \hbar\omega_{(00p)}\beta^\dagger_{(00p)}\beta_{(00p)}, \tag{5.114}$$

which is the goal of this section. In Fig. 5.5(a) we plot the external magnetic field $H_{\rm ext}$ dependence of the discretized magnon mode frequencies of a YIG bar with dimensions $(d, w, l) = (5\ {\rm nm}, 30\ {\rm nm}, 3\ \mu{\rm m})$. The neighboring magnon mode frequencies are separated from each other by over $2\pi \times 10$ MHz for modes with $p \geq 5$, as shown in Fig. 5.5(b). At field $H_{\rm ext} = H_{\rm c}$, the NV center's transition frequency $\omega_{\rm NV}$ and the magnon mode frequency $\omega_{(005)}$ are on-resonant.

5.4.2 NV-magnon coupling

The coupling strength between magnons and NV centers is obtained by applying the same Bogoliubov transformation with the paraunitary matrix $\mathbf{T}$ [Eq. (5.59)]. Although the demagnetization field $\mathbf{H}_{\rm d}$ contribution in (5.59) is not negligible when NV centers are placed near the two edges of the ferromagnetic bar, we verify it is small in the calculations for Figs. 5.6(b) and 5.7. In the same way as in Sec. 5.3, the perpendicular component of the fringing field $\mathbf{h}_\perp$ is given by

$$\gamma\mu_0\mathbf{h}_\perp(\mathbf{r}) = \sqrt{2\omega_M\omega_{dwl}}\frac{1}{4}[\widehat{e}_+\ \widehat{e}_-]\begin{bmatrix}\left[\Gamma^{-,+}_{\mu_0}\cdots\Gamma^{-,+}_{\mu_N}\right] & \left[\Gamma^{-,-}_{\mu_0}\cdots\Gamma^{-,-}_{\mu_N}\right] \\ \left[\Gamma^{+,+}_{\mu_0}\cdots\Gamma^{+,+}_{\mu_N}\right] & \left[\Gamma^{+,-}_{\mu_0}\cdots\Gamma^{+,-}_{\mu_N}\right]\end{bmatrix} \times \begin{bmatrix}\mathbf{T}^{pp} & \mathbf{T}^{pn}\\ \mathbf{T}^{np} & \mathbf{T}^{nn}\end{bmatrix}\begin{bmatrix}\boldsymbol{\beta}\\ \boldsymbol{\beta}^\dagger\end{bmatrix}, \tag{5.115}$$

where $\omega_{dwl} = \mu_0(\gamma\hbar)^2/(\hbar wld)$ and

$$\Gamma^{-,+}_{\mu} = \left(\Gamma^{XX}_{\mu} + \Gamma^{YY}_{\mu} + i\left(\Gamma^{XY}_{\mu} - \Gamma^{YX}_{\mu}\right)\right), \tag{5.116}$$

$$\Gamma^{-,-}_{\mu} = \left(\Gamma^{XX}_{\mu} - \Gamma^{YY}_{\mu} - i\left(\Gamma^{XY}_{\mu} + \Gamma^{YX}_{\mu}\right)\right), \tag{5.117}$$

$$\Gamma^{+,+}_{\mu} = \left(\Gamma^{XX}_{\mu} - \Gamma^{YY}_{\mu} + i\left(\Gamma^{XY}_{\mu} + \Gamma^{YX}_{\mu}\right)\right), \tag{5.118}$$

$$\Gamma^{+,-}_{\mu} = \left(\Gamma^{XX}_{\mu} + \Gamma^{YY}_{\mu} - i\left(\Gamma^{XY}_{\mu} - \Gamma^{YX}_{\mu}\right)\right). \tag{5.119}$$

Here Γ^{XX}_{μ}, Γ^{XY}_{μ}, Γ^{YX}_{μ}, and Γ^{YY}_{μ} are functions of $\mathbf{r}$, and they are given by

$$\Gamma^{XX}_{\mu} = \int d\mathbf{r}'\frac{-\left(\mathbf{r}-\mathbf{r}'\right)_x}{4\pi\left|\mathbf{r}-\mathbf{r}'\right|^3}\partial'_x\tilde{\varphi}^{XYZ}_{\mu}\left(\mathbf{r}'\right), \tag{5.120}$$

$$\Gamma^{XY}_{\mu} = \int d\mathbf{r}'\frac{-\left(\mathbf{r}-\mathbf{r}'\right)_x}{4\pi\left|\mathbf{r}-\mathbf{r}'\right|^3}\partial'_y\tilde{\varphi}^{XYZ}_{\mu}\left(\mathbf{r}'\right), \tag{5.121}$$

$$\Gamma^{YX}_{\mu} = \int d\mathbf{r}'\frac{-\left(\mathbf{r}-\mathbf{r}'\right)_y}{4\pi\left|\mathbf{r}-\mathbf{r}'\right|^3}\partial'_x\tilde{\varphi}^{XYZ}_{\mu}\left(\mathbf{r}'\right), \tag{5.122}$$

$$\Gamma^{YY}_{\mu} = \int d\mathbf{r}'\frac{-\left(\mathbf{r}-\mathbf{r}'\right)_y}{4\pi\left|\mathbf{r}-\mathbf{r}'\right|^3}\partial'_y\tilde{\varphi}^{XYZ}_{\mu}\left(\mathbf{r}'\right), \tag{5.123}$$

where $\tilde{\varphi}^{XYZ}_{\mu} = \sqrt{wld}\varphi^{XYZ}_{\mu}$ is a dimensionless function.

In the same way as in Sec. 5.3, under the rotating-wave approximation, we obtain the

NV-magnon interaction Hamiltonian in the form of the Jaynes-Cummings model

$$\mathcal{H}_{\text{int}} = \sum_{i=1,2}\sum_{\mu=(00p)} \hbar g_\mu(\mathbf{r}_i)\sigma^+_{\mathrm{NV}_i}\beta_\mu + \text{H.c.} \tag{5.124}$$

$$\begin{aligned} g_{(00p)}(\mathbf{r}_i) = {} & \sqrt{\omega_M\omega_{dwl}} \times \\ & \sum_{q=0,1,\cdots,N}\left[\left(\Gamma^{+,+}_{(00q)}/2\right)[\mathbf{T}^{pp}]_{qp} + \left(\Gamma^{+,-}_{(00q)}/2\right)[\mathbf{T}^{np}]_{qp}\right]\Big|_{\mathbf{r}=\mathbf{r}_i}, \end{aligned} \tag{5.125}$$

To calculate the spatial distribution of the dimensionless coupling, we evaluate numerically Eqs. (5.120)-(5.123).

5.4.3 Effective NV-NV Hamiltonian

When we introduce a detuning between the target mode frequency $\omega_{(00p)}$ and the NV frequency ω_{NV}, we obtain an effective Hamiltonian in the same way as in Sec. I. Now the total Hamiltonian $\mathcal{H} = \mathcal{H}_0 + \mathcal{H}_{\text{int}}$ with $\mathcal{H}_0 = \mathcal{H}_{\mathrm{NV}} + \mathcal{H}_{\mathrm{m}}$ is given by Eqs. (5.71), (5.114), and (5.124). For the the Schrieffer-Wolff transformation, we choose

$$S = \sum_{\substack{i=1,2\\ \mu=(00p)}} \frac{g_\mu\left(\mathbf{r}_i\right)\sigma^+_{\mathrm{NV}_i}\beta_\mu}{\omega_{\mathrm{NV}_i} - \omega_\mu}, \tag{5.126}$$

in the same way as in Eq. (5.75). Following Eq. (5.76), we obtain

$$\begin{aligned} \mathcal{H}_{\text{eff}} \;=\; & \hbar\sum_{i,\mu}\frac{\left|g_\mu\left(\mathbf{r}_i\right)\right|^2}{\omega_{\mathrm{NV}} - \omega_\mu}\left(|e\rangle_i\langle e| + \sigma^z_{\mathrm{NV}_i}\beta^\dagger_\mu\beta_\mu\right) \\ & +\frac{\hbar}{2}\sum_{i,\mu\neq v}\left(\frac{g_\mu\left(\mathbf{r}_i\right)g^*_v\left(\mathbf{r}_i\right)}{\omega_{\mathrm{NV}} - \omega_\mu}\sigma^z_{\mathrm{NV}_i}\beta^\dagger_v\beta_\mu + \text{H.c.}\right) \\ & +\hbar\sum_{\mu}\left(\frac{g_\mu\left(\mathbf{r}_1\right)g^*_\mu\left(\mathbf{r}_2\right)}{\omega_{\mathrm{NV}} - \omega_\mu}\sigma^+_{\mathrm{NV}_1}\sigma^-_{\mathrm{NV}_2} + \text{H.c.}\right), \end{aligned} \tag{5.127}$$

where the first right hand side term is the Lamb shift and the Stark shift, respectively. The interaction Hamiltonian between the two NV centers is given by the last right hand side term.

If we detune the NV frequency from the mode frequency for $\mu = (00p)$ by $\omega_{\mathrm{NV}} = \omega_{(00p)} - \Delta\omega$ and if we only consider the effect from the mode $\mu = (00p)$, we obtain

$$\mathcal{H}_{\mathrm{eff}}^{\mathrm{NV-NV}} = -\hbar\left(g_{\mathrm{eff}}\sigma_{\mathrm{NV}_1}^{+}\sigma_{\mathrm{NV}_2}^{-} + \mathrm{H.c.}\right), \tag{5.128}$$

$$g_{\mathrm{eff}} = g_{(00p)}\left(\mathbf{r}_1\right) g_{(00p)}^{*}\left(\mathbf{r}_2\right)/\Delta\omega. \tag{5.129}$$

We plot in Fig. 5.6(a) the spatial distribution of the NV-magnon coupling strength $g_{(005)}$ at $H_{\mathrm{ext}} = H_{\mathrm{c}}$ for a fixed NV center height $h = 5$ nm [see Fig. 5.2(a)], and obtain $g_{(005)} \approx 2\pi \times 0.5$ MHz depending on the NV center positions. With the Gilbert damping parameter of YIG $\alpha = 10^{-5}$ [159] and the coherence time of NV centers $T_2^* = 1$ ms [54], we show on the right axis of Fig. 5.6(a) the corresponding single magnon μ-mode cooperativity[130, 133]

$$\mathcal{C}_{\mu} = \frac{|g_{\mu}(\mathbf{r})|^2}{\alpha\omega_{\mu}/T_2^*} \tag{5.130}$$

which is a dimensionless measure of the coupling. We find $\mathcal{C}_{(005)} \gtrsim 10^4$ over a wide range of NV center positions, achieving the strong coupling regime for our hybrid quantum system. Our calculations enable us to optimize both the coupling strength and the cooperativity in order to increase NV-NV entanglement efficiency in our system.

In Fig. 5.6(b), we use Eq. (5.129) focusing on the magnon mode with $p = 5$ and plot the effective coupling strength g_{eff}, entangling rate (ER), and GDR. Here, the two NV centers are placed at $\mathbf{r}_1 = (d+h)\hat{x} + w\hat{y} + (400\text{ nm})\hat{z}$ [see a cross mark in Fig. 5.6(a)] and $\mathbf{r}_2 = \mathbf{r}_1 + \delta z\hat{z}$, where δz is the NV-NV distance along the bar length. The detuning is set to $\Delta\omega = \omega_{(005)} - \omega_{\mathrm{NV}} = 2\pi \times 3$MHz, which could be produced by electric field [157], strain [158] or magnetic field deviation from $H_{\mathrm{ext}} = H_c$. Surprisingly, useful entangling gates for 2.2 μm separated NV centers with $g_{\mathrm{eff}} = 2\pi \times 90$ kHz and GDR > 700 are predicted for this YIG bar system. This makes experiments more accessible in terms of the independent optical initialization and the readout of NV centers than the waveguide case. In contrast to Sec. 5.3, where we have a translationally invariant infinitely long waveguide, here

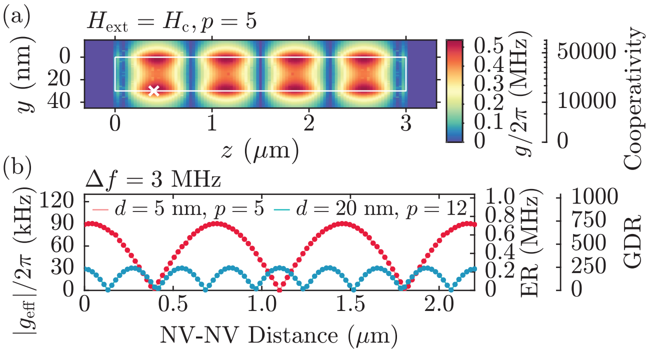

Figure 5.6: (a) Spatial plot of the coupling strength $g = g_{(005)}$ at $H_{\rm ext} = H_{\rm c}$ and $h = 5$ nm. The white rectangle delimits the bar dimension, and the white cross mark represent the position of NV$_1$ referred in (b). The corresponding cooperativity $\mathcal{C}_{(005)}$ is shown on the right axis. (b) Effective NV-NV coupling strength $g_{\rm eff}$ between two NV centers as a function of the NV-NV distance, where NV$_1$ and NV$_2$ are placed at $\mathbf{r}_1 = (d+h)\hat{x} + w\hat{y} + (400\text{ nm})\hat{z}$ and $\mathbf{r}_2 = \mathbf{r}_1 + \delta z\hat{z}$, respectively. The red (blue) curve is calculated for $(d,p) = (5\text{ nm}, 5)$ $[(d,p) = (20\text{ nm}, 12)]$. The entanglement gate rate (ER) and the gate to decoherence ratio (GDR) are shown on the right axis. In both cases aspect ratio is $w/d = 6$, length of the magnetic bar is $l = 3$ μm, and detuning is $\Delta f = \Delta\omega/2\pi = (\omega_{(00p)} - \omega_{\rm NV})/2\pi = 3$ MHz.

the position of the NV center along z-direction plays a major role in the coupling strength.

We also show these quantities for a less challenging to fabricate YIG geometry with $(d, w, l, h) = (20\text{ nm}, 120\text{ nm}, 3\ \mu\text{m}, 5\text{ nm})$. The result is plotted as a blue curve in Fig. 5.6(b), for which we obtain GDR > 100 for the 2.2 μm separated NV centers. This result clarifies the significance of using the YIG bar structures to entangle two NV centers separated by a few micrometers. Moreover, the discretized magnon mode frequencies allows for controlling the NV center frequencies to be on-resonant to one of the magnon mode frequencies, which enables the entanglement of two NV centers via the transduction of energy quanta that we discuss in the next section. We also comment that it would be possible to control the NV-magnon coupling strength via parametric driving of the discretized magnon modes as studied in the cavity quantum electrodynamics [164] (see Appendix of Ref. [2]).

5.5 Transduction and virtual-magnon exchange protocols

In this section, we explore and compare two entanglement schemes for our hybrid quantum system, on-resonant transduction and off-resonant ("off-shell") virtual-magnon exchange. As illustrated in the left schematic of Fig. 5.7(a), Entanglement generation via the transduction protocol is simulated by controlling the NV center frequencies independently. For this case, the NV spins are initially prepared in the state tensor product of the ground state and the excited state $|g\rangle_1|e\rangle_2$. We first shift the frequency ω_{NV_2} on-resonant to the μ-magnon mode frequency ω_μ for a certain variable time τ_{var} while ω_{NV_1} is detuned from ω_μ by a large amount $\delta\omega = 2\pi \times 5$ MHz. Second, we swap the NV_1 spin state and the magnon state by matching $\omega_{\mathrm{NV}_1} = \omega_\mu$ for the swap gate time τ_{SWAP} during which the second qubit frequency ω_{NV_2} is detuned from ω_μ by the detuning $\delta\omega$. The total interaction time in this protocol is $\tau_{\mathrm{int}} = \tau_{\mathrm{var}} + \tau_{\mathrm{SWAP}}$, and it is varied by the variable interaction time τ_{var}. By applying a local magnetic field, electric field [157], or strain [158], the control of the NV centers' transition frequencies can be performed. An alternative possibility of controlling the transition frequencies would be to use a periodic modulation of the external magnetic field [165, 166] (see Appendix of Ref. [2]). In contrast, in the virtual-magnon ("off-shell") exchange protocol, as shown in the right schematic of Fig. 5.7(a), the NV centers' frequencies are both detuned from the μ-magnon mode frequency by $\Delta\omega = \omega_\mu - \omega_{\mathrm{NV}_{1,2}} = 2\pi \times 3$ MHz. We prepare the NV centers' spin state in $|g\rangle_1|e\rangle_2$, and the whole system evolves over the interaction time τ_{int}.

Using the Lindblad master equation [61, 130, 167], we simulate the time evolution of our hybrid quantum system for both protocols at a finite temperature T considering two NV

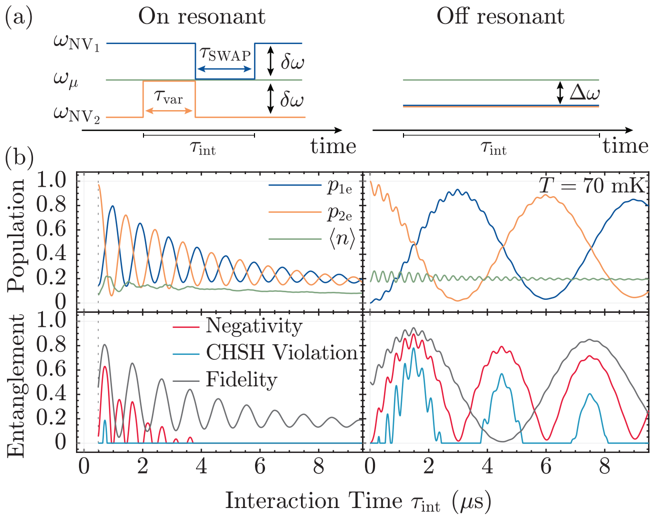

Figure 5.7: (a) Schematic gate sequence of on-resonant transduction (left) and off-resonant virtual-magnon exchange (right) entanglement protocols. (b) Comparison of the two protocols at $T = 70$ mK. The top two figures show NV center's excited state population p_{ie} ($i = 1, 2$) and magnon population $\langle n \rangle = \langle \hat{n}_\mu \rangle$ [$\mu = (005)$] as a function of the total system interaction time at the end of the gate operations. NV centers are separated by ad distance 2.2 μm on top of the YIG bar as shown in Fig. 5.6(a). For the transduction protocol, as illustrated in the inset, NV center frequencies are modulated where lines represent the frequencies of NV centers or the magnon mode. The bottom two figures show entanglement measures [entanglement negativity, the degree of the Bell inequality violation, and the fidelity] as a function of the interaction time. The red, sky blue, and gray curves are the negativity divided by the Bell-state's negativity, the degree of the Bell inequality violation where the inequality is violated if the curve is above zero, and the fidelity to the target pure entangled states, respectively.

centers and a near resonant magnon mode μ,

$$\begin{aligned} \dot{\rho} = \quad & -i[\mathcal{H}(t), \rho] + 2\kappa \left(1 + \bar{n}_{\mathrm{m}}^{\mathrm{th}}\right) \mathcal{D}[a]\rho \\ & + 2\kappa \bar{n}_{\mathrm{m}}^{\mathrm{th}} \mathcal{D}\left[a^\dagger\right]\rho + \frac{\gamma_2}{2} \sum_{i=1,2} \mathcal{D}\left[\sigma^z_{\mathrm{NV}_i}\right]\rho, \end{aligned} \tag{5.131}$$

where $\mathcal{D}[\mathcal{O}]\rho = \mathcal{O}\rho\mathcal{O}^\dagger - \frac{1}{2}(\mathcal{O}^\dagger\mathcal{O}\rho + \rho\mathcal{O}^\dagger\mathcal{O})$, $\kappa = \alpha\omega_\mu$, $\gamma_2 = 1/T_2^*$, $a = \beta_\mu$, $a^\dagger = \beta_\mu^\dagger$, $\bar{n}_{\mathrm{m}}^{\mathrm{th}} = (\exp[\omega_\mu/k_{\mathrm{B}}T] - 1)^{-1}$ is the thermal magnon population, k_{B} is the Boltzmann constant, T is temperature, and ρ is the system density operator. Here, the parameter of the magnon damping $\kappa = \alpha\omega_\mu$ is based on the dissipation/loss term in the Landau-Lifshitz-Gilbert equation $\partial_t \mathbf{M}|_{\mathrm{diss}} = (\alpha/M_{\mathrm{s}})\mathbf{M} \times \partial_t \mathbf{M}$, which results in $\partial_t \beta_\mu|_{\mathrm{diss}} \approx -\alpha\omega_\mu\beta_\mu$ under the assumption $\partial\omega_\mu/\partial H_{\text{ext}} \approx \mu_0\gamma$, which is verified by Fig. 5.5(b) (see Appendix of Ref. [2]). In the total Hamiltonian $\mathcal{H}(t)$, for computational accessibility, we only take into account the magnon mode with $\mu = (005)$, as this mode produces the dominant contribution in the NV-NV interaction in addition to the magnon induced decoherence of NV centers in both protocols. We assume the NV center's longitudinal decay rate to be zero in the simulation as it is much smaller than the transverse decoherence rate [51]. The two NV centers are separated by 2.2 μm along the YIG bar length with the position $\mathbf{r}_1 = (d+h)\hat{x}+w\hat{y}+(400\text{ nm})\hat{z}$ and $\mathbf{r}_2 = \mathbf{r}_1 + (l-800\text{ nm})\hat{z}$. We use the homogeneous Gilbert damping parameter $\alpha = 10^{-5}$ of YIG [159] and the NV center coherence time $T_2^* = 1$ ms [54].

We plot the NV centers' excited state population p_{ie} $(i = 1, 2)$ and the magnon population $\langle n\rangle = \langle \hat{n}_\mu\rangle$ $[\mu = (005)]$ at the end of the transduction (on resonant) and the virtual-magnon exchange (off resonant) protocols as a function of the total system interaction time τ_{int} at $T =$ 70 mK in the upper two panels of Fig. 5.7(b). In the lower two panels, we show three different entanglement measures [entanglement negativity normalized by the Bell-state's negativity, the degree of the Bell inequality violation, and the fidelity to the target pure entangled states, which are given by the red, sky blue, and gray curves, respectively] as a function of the interacting time τ_{int} for each protocol. The resulting entanglement are detected by $\mathcal{N} > 0$, and one expects to observe the violation of the Clauser-Horne-Shimony-Holt (CHSH) form of Bell inequality if CHSH Violation > 0 [168, 169] (see Appendix of Ref. [2]).

We first find, in Fig. 5.7(b), that the transduction protocol is faster in completing the gate as compared to the virtual-magnon exchange protocol. This can be understood as the NV-magnon on-resonant coupling rate $g_\mu \approx 2\pi \times 0.5$ MHz is larger than the off-resonant NV-NV coupling rate $g_{\text{eff}} \approx 2\pi \times 90$ kHz. On the other hand, from the figure it is observed that the virtual-magnon exchange protocol results in larger amplitude oscillations in the NV centers' excited state populations [See the blue and orange curves] and higher fidelity under the parameters and the temperature used in the simulation. This is due to a combination of two factors: First, the virtual-magnon exchange protocol creates magnons only virtually (with magnon population suppressed by $g_\mu/\Delta\omega$ due to the energy mismatch), which make them approximately insensitive to the magnon damping parameter. Secondly, the magnon damping rate $\alpha\omega_\mu$ is larger than the NV center's decoherence rate $1/T_2^*$, which means there is more loss of information if a real magnon is excited. Nonetheless, we predict in both protocols entangled states can be manipulated and the violation of the Bell inequality will be observed.

To further compare the two entanglement protocols and get deeper intuition, we perform simulations under multiple temperatures and have observed that the virtual-magnon-exchange protocol is more robust at higher temperatures up to ≈ 150 mK (see Appendix of Ref. [2]). We show that both protocols do not produce useful entanglement for higher temeprature $T \gtrsim 150$ mK due to the NV centers' dephasing originating from magnon number fluctuations of modes with $\mu \neq (005)$. We also evaluate the decay contribution due to these magnon modes and verify that this is negligible for temperatures $T \leq 150$ mK for both upper and lower transitions of NV centers (see Appendix of Ref. [2]). Interestingly, the on-resonant transduction protocol improves more drastically at lower temperatures than the virtual-magnon exchange protocol. We find based on the zero temperature analysis the following inequality for which the transduction protocol performs better (see Appendix of Ref. [2]):

$$\alpha \lesssim \frac{\Delta\omega/g_\mu}{4(1-1/\pi)}\frac{1}{\omega_\mu T_2^*}. \tag{5.132}$$

The transduction protocol is shown to outperform the virtual-magnon exchange protocol for the parameters used in this section (with $\Delta\omega = 2\pi \times 3$ MHz) if $\alpha \lesssim 10^{-7}$ is achieved. In Appendix of Ref.[2] we further analyze the parameter conditions for which protocol outperforms. We also calculate an average gate fidelity $\bar{F}$ [170] as a square-root-of-iSWAP gate for the off-resonance protocol to show that it can directly lead to two-qubit gates, and we obtain $\bar{F} \approx 0.88$ at $T = 70$ mK (see Appendix of Ref. [2]).

We note that for keeping the system at low temperatures $T \lesssim 150$ mK, the laser illumination and microwave irradiation on the system for the initialization, manipulation, and readout of NV centers may cause unwanted heating of the system. Although YIG has been studied under irradiation of microwaves in superconducting qubit platforms [171] and color centers have been studied under the illuminations of lasers in dilution refrigerator temperatures $T < 100$ mK [172–175], it is still important to minimize the average microwave irradiation and laser illumination power on the system to achieve the required low temperatures.

Additionally, we note that the small Gilbert damping parameter $\alpha = 10^{-5}$ used in the current study can be optimistic for small YIG structures, as this value is obtained from a bulk YIG sample [159]. One of this cause is the nontrivial magnetic behavior of the gadolinium-gallium-garnet (GGG) substrates at millikelvin temperatures [YIG is typically grown on the GGG substrate [176]]. This would be mitigated by employing a free-standing structure [177]. Another cause is the impurity relaxation in the YIG material [178]. However, with recent advances in magnonics research, the damping of thin YIG films can be improved considerably, for example, with techniques based on a recrystallization of amorphous YIG into single crystals [179]. In addition, we obtain a high cooperativity condition $\mathcal{C} \approx 500$ even with the larger Gilbert damping parameter $\alpha = 10^{-3}$, which can be calculated from Fig. 5.6(a). Simulations with $\alpha = 10^{-3}$ is shown in the Appendix of Ref. [2], and we find that the entanglement can still be produced at $T = 70$ mK for the off-resonant protocol, although we find further optimization on the detuning frequency is needed to improve the quality of the entanglement. This is to avoid the overlap of the NV centers' transition frequencies with the now broader (due to larger Gilbert damping) linewidth of the magnon mode resonance (see Appendix of Ref. [2]).

5.6 Conclusion

We show that hybrid quantum systems consisting of NV centers in diamond and magnons in ferromagnetic bar and waveguide structures are promising platforms for the quantum information processing. With the Hamiltonian formalism of the dipole-exchange magnons, we calculate that the useful two-NV entangling gates over 1-2 μm NV-NV separations at finite temperatures can be achieved. We explore the on-resonant transduction and off-resonant virtual-magnon exchange protocols of entanglement generation and compare them under realistic experimental conditions with the Lindblad master equation. Although the transduction protocol is faster in gate operation, with the typical Gilbert damping parameter of YIG, the virtual-magnon exchange protocol results in higher fidelity. We obtain at $T = 70$ mK entangled state's fidelity $F \approx 0.81$ and $F \approx 0.95$ for the on-resonant and off-resonant protocols, respectively. The virtual-magnon exchange protocol is found to be robust against thermal magnon fluctuations, but the transduction protocol outperforms it close to zero temperature for $\alpha\omega_\mu T_2^* \lesssim (\Delta\omega/g_\mu)/[4(1-1/\pi)]$. Calculations presented in this study could serve as a theoretical support to find optimal device geometries and entangling gate protocols in future experiments that aim to entangle spatially separated NV centers using magnon modes in ferromagnets.

Chapter 6

Surface-magnon mediated self-interaction of spin qubits in diamond revealed by longitudinal relaxometry

6.1 Introduction

In this chapter, we experimentally quantify a self-interaction (or the Lamb shift) of NV centers in diamond mediated by the nearby surface spin waves in a YIG slab. Using the fluctuation-dissipation relation and the Kramers-Kronig relation, we estimate the real part of the self interaction (susceptibility) from longitudinal (T_1) relaxometry measurements of an ensemble of NV centers in a NV-YIG hybrid quantum system, where a diamond membrane that hosts NV centers near the surface is placed on top of a YIG slab. This real part of the susceptibility is crucial for quantifying the expected magnon-mediated NV-NV interaction in the hybrid quantum system, as the virtual-magnon-mediated NV-NV interaction equals to the real part of the self-susceptibility, or the Lamb shift, when the distance between the two NV centers are close enough (as compared to the inverse of the standard deviation of the wavenumber of magnons that are virtually excited). The model provided in the theoretical study in Chapter 5 is used for the simulation of the T_1 relaxation rates of the NV centers placed on top of the YIG material, and we find that the model accurately captures both the quantitative and qualitative feature of the surface magnon induced enhancement of the NV center's T_1 decay rates. Although the expected NV-NV interaction strength in our system is small ($|g_{\mathrm{eff}}|/2\pi \lesssim 2$ Hz) as we use a non-structured YIG film with 3 μm thickness, the procedure used in this work can be applied to future characterizations of the NV-magnon and the NV-NV interaction strength placed on top of YIG nanodevices, such as YIG bar and waveguide structures, which can enhance the coupling strength, as suggested in Ref. [2].

Susceptibilities of quantum many-body systems to external perturbations are fundamental physical quantities for characterizing the system's dynamical responses [56, 60, 180]. When the perturbations are triggered by quantum-mechanical objects such as spins, these susceptibilities lead to spin-spin interactions as well as self responses, providing effective quantum dynamics of the hybrid quantum system. Importantly, the susceptibilities are related to the noise spectrum of the system via the fluctuation-dissipation relation (FDR) [181], allowing us to analyze the system's response features from the noise spectroscopy of the system. These susceptibilities and noise spectrum are of particular interest when characterizing the hybrid quantum architectures. Their interaction is critical but may not be straightforward to measure, while it can be easily estimated via the FDR.

NV centers in diamond coupled to magnons in ferrimagnets are among such hybrid quantum systems where the quantification of the coupling strength is of great interest. This is due to theoretical predictions that the system may enable on-chip long-distance NV-NV entanglement [2, 135, 140]. While these proposals suggest to use magnonic nanodevices, the quantification of the NV-magnon coupling strength have been elusive so far even in experimentally more accessible ferromagnetic films or slabs. This is because of the continuum nature of the magnon modes of the system, making it difficult to quantify the coupling strength in the unit of energy. In this work, we show that a magnon-mediated self-susceptibility is a useful metric to experimentally quantify the NV-magnon coupling strength of the system indirectly, as it can also be used for discrete mode cases and provides direct insight into the expected magnon-mediated NV-NV interaction strength.

The experimental studies of these NV-magnon hybrid systems in the past have been two fold. On the one hand, NV centers are used as a sensor to probe equilibrium magnetic noise properties generated by magnons in thin magnetic films (on the order of tens of nanometers) with the longitudinal relaxometry approach [105, 106, 142, 146]. On the other hand, non-equilibrium or coherent spin waves (magnons) are generated using a microstripline transducer, which either causes the incoherent magnetic noise at the NV center position [146, 182] or allows coherent driving of the NV center's Rabi oscillation [72, 146, 183]. For the latter approach, surface spin waves in a micron-thick YIG film are shown to be able of to drive NV centers exceptionally efficiently [72, 183], which lead to expect the existence of a large coupling between the NV ceneters and the surface spin waves. However, as shown in the theoretical study Ref. [138] and its reformulation provided in Appendix A of this dissertation, the efficient driving of the NV centers with the surface spin wave is the product of both the NV-magnon coupling and the magnon-transducer coupling. This makes it nontrivial to deconvolve the intrinsic NV-magnon coupling strength of the system, which is a key point for estimating the magnon-mediated NV-NV interaction for a given ferromagnetic geometries. Therefore, it is desirable to experimentally quantify or characterize the coupling strength in a given structure in practice.

6.2 Experimental setup

To avoid the difficulty of extracting the NV-surface-magnon coupling strength, here we use the longitudinal relaxometry approach to probe noise spectrum due to magnons in the micron-thick YIG film to quantify the intrinsic coupling between the surface magnons and

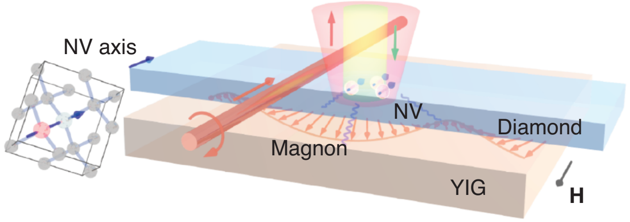

Figure 6.1: Schematic of NV centers in a diamond membrane placed on top of a YIG film. A copper wire is suspended above the structure to drive NV center's spin transitions. The crystalline orientation of the diamond is shown in the left drawing. External magnetic field is applied parallel to the YIG and the diamond surface.

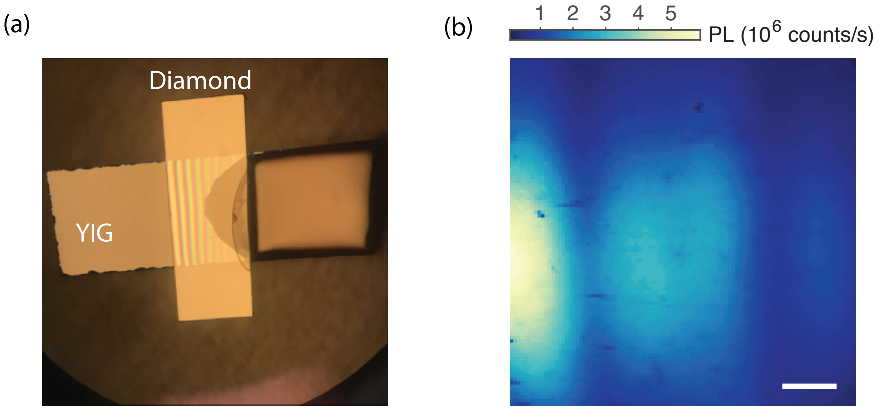

Figure 6.2: (a) Microscope image of a diamond membrane on top of an YIG film. (b) FSM image of the ensemble of NV centers placed on top of the YIG film. The left (right) optical interference node corresponds to 266 nm (532 nm) distance between the bottom surface of the diamond membrane and the YIG top surface. Scale bar: 20 μm.

NV centers. As shown in Fig. 6.1, we use a diamond membrane with an NV axis parallel to the diamond surface and place it on top of the 3-μm-thick YIG slab, which allows us to apply a magnetic field parallel to both the NV axis and the in-plane direction of the YIG slab. The NV centers are created by the nitrogen irradiation at an average depth of ≈ 7.7 nm from the diamond surface (See Appendix B). In this geometry, both NV center's quantization axis and the equilibrium magnetization of YIG are along the external magnetic field direction, and this in-plane magnetic field configuration has been known to host surface magnon modes in the YIG film [149, 150]. This highly symmetric orientation of spins (of both NV and YIG) and the magnetic field is optimal for studying the magnetostatic surface spin waves in the YIG film with NV centers, as their propagation property is strongly dependent on the propagation direction relative to the external magnetic field and the polarization of the

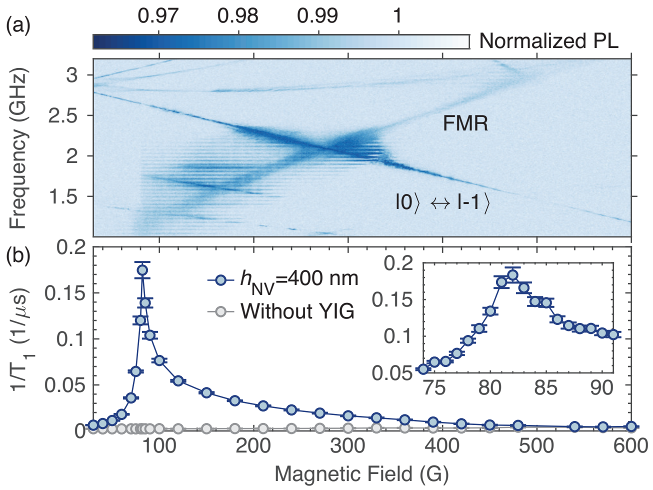

Figure 6.3: (a) Two-dimensional ODMR image of the NV centers on top of the YIG film at room temperature. The transition $|S_z = 0\rangle \leftrightarrow |S_z = -1\rangle$ and the ferromagnetic resonance (FMR) of YIG is labeled. PL is normalized by the measurement without the microwaves. NV centers are ≈ 7.7 nm deep from the diamond surface and 400 nm from the YIG surface, which is measured by the optical interference pattern. (b) T_1 relaxation rate as a function of the magnetic field, where the blue curve is for NVs on the YIG at 400-nm height and the gray curve is a controlled measurement taken off the YIG for the same diamond membrane. Inset shows the finer scan near 82 G.

magnetic noise caused by the surface magnons is strongest in this geometry (See Appendix A). All the measurements are performed at room temperature.

In Fig. 6.3(a), we show a microscope image of the diamond membrane placed on top of the YIG film. The lateral dimension of the YIG is 3 mm × 1 mm and the thickness is 3 μm. The diamond membrane has the lateral dimension of 2 mm × 0.72 mm and the thickness is 0.1 mm. The side that the NV centers are implanted are facing down (YIG side).

6.3 T_1 relaxation rate of NV centers placed on top of a YIG slab

In Fig. 6.3(a), we show a two-dimensional image of the optically detected magnetic resonance (ODMR) scanned for the ensemble of NV centers located 400 nm from the YIG surface. As we apply the magnetic field along the NV center's main symmetry axis, we observe the

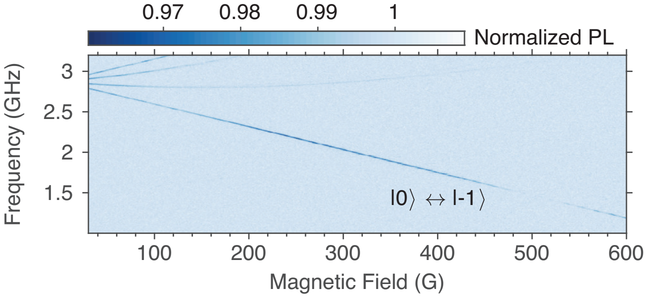

Figure 6.4: Two-dimensional ODMR image of the NV centers without the YIG film. The transition $|S_z = 0\rangle \leftrightarrow |S_z = -1\rangle$ is labeled. PL is normalized by the measurement without the microwaves.

transition $|S_z = 0\rangle \leftrightarrow |S_z = -1\rangle$ as a stright line in the normalized PL, and we also observe the signature of the ferromagnetic resonance (FMR) of the YIG due to its associated magnetic noise. We perform the T_1 relaxometry measurement on this lower transition of the NV center $|S_z = 0\rangle \leftrightarrow |S_z = -1\rangle$, and the T_1 relaxation rate [of form $\langle\sigma_z(t)\rangle/\langle\sigma_z(t = 0)\rangle = \exp(-t/T_1)$ with $\sigma_z = |S_z = -1\rangle\langle S_z = -1| - |S_z = 0\rangle\langle S_z = 0|$] as a function of the magnetic field is shown in Fig. 6.3(b). We find a sharp peak near ≈ 80 G, and the inset of Fig. 6.3(b) shows the finer scan near this peak. For the T_1 measurement, we firstly initialize the NV-center's spin to the state $|S_z = 0\rangle$ by the illumination of a 532-nm laser with a confocal microscopy and then measure the PL of the NV centers after a variable wait time with and without applying a microwave pulse (duration of which is in the range 120-220 ns) to exchange the population of $|S_z = 0\rangle$ and $|S_z = -1\rangle$. The difference of the PL with and without the microwave pulse is fit by the exponential function. As a control, we also show the T_1 relaxation rate of NVs without the YIG by looking at a different position of the same diamond membrane in the same setup under which the YIG film is absent, confirming that the enhanced T_1 relaxation rate is due to the presence of the YIG material. We also show the ODMR without the YIG film in Fig. 6.4.

6.4 Simulated T_1 decay rates enhanced by surface magnons

To uncover the origin of the sharp peak in the T_1 relaxation rate shown in Fig. 6.3(b), we perform a simulation of the noise spectrum and the resulting T_1 relaxation rate of the NV center located at 400-nm high from the YIG surface, and the result is shown in Fig. 6.5(a). Here, the simulation is performed by the full diagonalization of the magnon matrix originating from the total Hamiltonian $\mathcal{H}$ for the magnetically coupled dipole-exchange magnons and an NV center defined by (in the same way as in Chapter 5 and in Ref. [2]):

$$\mathcal{H} = \mathcal{H}_{\mathrm{NV}} + \mathcal{H}_{\mathrm{m}} + \mathcal{H}_{\mathrm{int}}, \tag{6.1}$$

$$\mathcal{H}_{\mathrm{NV}} = D_{\mathrm{NV}} \left(\hat{n}_{\mathrm{NV}} \cdot \mathbf{S}_{\mathrm{NV}}\right)^2 + \gamma\mu_0 \mathbf{S}_{\mathrm{NV}} \cdot \mathbf{H}_{\mathrm{ext}}, \tag{6.2}$$

$$\begin{aligned}\mathcal{H}_{\mathrm{m}} = &-\mu_0 \int d\mathbf{r}\mathbf{H}_{\mathrm{ext}} \cdot \mathbf{M}(\mathbf{r}) + \frac{\mu_0}{2} \int d\mathbf{r}\alpha_{\mathrm{ex}}(\mathbf{r}) \nabla\mathbf{M} : \nabla\mathbf{M} \\ &+\frac{\mu_0}{2} \int d\mathbf{r}d\mathbf{r}'(\nabla \cdot \mathbf{M}(\mathbf{r}))G\left(\mathbf{r} - \mathbf{r}'\right)\left(\nabla' \cdot \mathbf{M}\left(\mathbf{r}'\right)\right),\end{aligned} \tag{6.3}$$

$$\mathcal{H}_{\mathrm{int}} = \gamma\mu_0 \mathbf{S}_{\mathrm{NV}} \cdot \nabla \int d\mathbf{r}' G\left(\mathbf{r} - \mathbf{r}'\right) \nabla' \cdot \mathbf{M}\left(\mathbf{r}'\right)\Big|_{\mathbf{r}=\mathbf{r}_{\mathrm{NV}}}, \tag{6.4}$$

where $\mathcal{H}_{\mathrm{NV}}$ is the NV Hamiltonian, $\mathcal{H}_{\mathrm{m}}$ is the magnon Hamiltonian, $\mathcal{H}_{\mathrm{int}}$ is the interaction Hamiltonian, $D_{\mathrm{NV}} = 2\pi \times 2.87$ GHz is the zero-field splitting of the NV center, $\hat{n}_{\mathrm{NV}}$ is the unit vector along the NV main symmetry axis, $\mathbf{S}_{\mathrm{NV}}$ is the spin-1 operator of the NV center, $\gamma = 2\pi \times 2.8$ MHz/G is the absolute value of the electron gyromagnetic ratio, μ_0 is the vacuum permeability, $\mathbf{H}_{\mathrm{ext}}$ is the external magnetic field (we sometimes write it as simply $\mathbf{H}$ when there is no confusion), $\mathbf{M}(\mathbf{r})$ is the magnetization with the constraint $|\mathbf{M}(\mathbf{r})| = M_s(\mathbf{r}) = M_s\mathcal{F}(\mathbf{r})$, M_s is the YIG saturation magnetization, $\mathcal{F}(\mathbf{r}) = 1$ (0) inside (outside) the ferromagnetic structure, $\alpha_{\mathrm{ex}}(\mathbf{r}) = \alpha_{\mathrm{ex}}\mathcal{F}(\mathbf{r})$, $\alpha_{\mathrm{ex}} = \lambda_{\mathrm{ex}}^2 = D_{\mathrm{ex}}/\gamma\mu_0 M_s$ is the exchange-length squared, $D_{\mathrm{ex}} = 5.39 \times 10^{-3}\ \gamma$ G μm^2 is the YIG exchange constant, the double-dot product is defined as $\nabla\mathbf{M} : \nabla\mathbf{M} = \partial_a M_b \partial^a M^b$ (summation over indices appearing twice are suppressed as usual), $\mathbf{r}_i$ is the position of NV$_i$, $G(\mathbf{r} - \mathbf{r}') = 1/4\pi|\mathbf{r} - \mathbf{r}'|$ is the Green's function, and we set $\hbar = 1$ in the following. After expressing the Hamiltonian in a Fourier form with in-plane wave vector $\mathbf{k}$, we expand the thickness-directional wave functions with totally-free surface spin condition and truncate the higher-order modes, resulting in the paraunitary diagonalization of $2N \times 2N$ matrices for each wave vectors. In the simulation, we included approximately $N \approx 50$ thickness modes which are enough to simulate magnons with frequency $\lesssim 5$ GHz. This results in

$$\mathcal{H}_m = \sum_{n=1}^{N} \int \frac{d\mathbf{k}}{(2\pi)^2} \omega_{n,\mathbf{k}} \beta^\dagger_{n,\mathbf{k}} \beta_{n,\mathbf{k}}, \tag{6.5}$$

$$\mathcal{H}_{\text{int}} = \sum_{n=1}^{N} \int \frac{d\mathbf{k}}{(2\pi)^2} g_{n,\mathbf{k}} \beta_{n,\mathbf{k}} e^{i\mathbf{k}\cdot\mathbf{r}_{\text{NV}}} \sigma_+ + \text{H.c.}, \tag{6.6}$$

where we use the rotating wave approximation for the second line with the definition $\sigma_- = |S_z = 0\rangle\langle S_z = -1|$. The NV-magnon coupling $g_{n,\mathbf{k}}$ are numerically evaluated with the paraunitary matrix. The T_1 relaxation rate is evaluated by the numerical integration of

$$1/T_1 = (2n_{\text{B}}(\omega_{\text{NV}}) + 1) \sum_{n=1}^{N} \int \frac{d\mathbf{k}}{(2\pi)^2} |g_{n,\mathbf{k}}|^2 2\pi\delta(\omega_{n,\mathbf{k}} - \omega_{\text{NV}}), \tag{6.7}$$

where $\omega_{\text{NV}} = D_{\text{NV}} - \gamma H_0$ is the lower transition frequency of the NV center [transition frequency of $|S_z = 0\rangle \leftrightarrow |S_z = -1\rangle$] and $n_{\text{B}}(\omega) = [\exp(\beta\omega) - 1]^{-1}$ is the Bose distribution with the inverse temperature β. For the numerical evaluation of Eq. (6.7), we replaced the delta function with a Lorentzian with a small linewidth.

We note that the expression Eq. (6.7) does not look identical to the one used in other literatures such as Ref. [142], though the difference seems to be minor. To derive Eq. (6.7), we assume the thermal occupation of magnons, i.e., the partition function Z is given by $Z = \text{Tr}[-\beta\mathcal{H}_m]$ with the quadratic magnon Hamiltonian $\mathcal{H}_m$ following the statistical physics. On the other hand, in Ref. [142], the thermal motion of the magnetization are driven by white noise magnetic fields in the Landau-Lifshitz-Gilbert (LLG) equation, which is done in micromagnetic simulations, too. These approaches are approximately the same but not identical when Bogoliubov transformation is taken into account, though it appears that the difference is minor. In the following, we illustrate the difference in two approaches by considering the case of a single boson mode with frequency ω_b driven by a white noise, with and without the squeezed interaction, which is equivalent to the Bogoliubov transformation, using the complex canonical variables a and a^*. When there is no squeezed interaction, the classical Hamiltonian is given by

$$\mathcal{H} = \omega_b a^* a + \left(a^* + a\right) H(t) + i\left(a^* - a\right) W(t), \tag{6.8}$$

where $H(t)$ and $W(t)$ are independent white noise coupled to two quadratures $a^* + a$ and $i(a^* - a)$, whose correlation are given by

$$\overline{H(t)H\left(t'\right)} = D\delta\left(t - t'\right), \tag{6.9}$$

$$\overline{W(t)W\left(t'\right)} = D\delta\left(t - t'\right), \tag{6.10}$$

$$\overline{W(t)H\left(t'\right)} = 0, \tag{6.11}$$

where $\overline{(\cdots)}$ indicates the statistical average of the randomness and D is a coefficient describing the strength of the randomness of the white noise fields. Under the Hamiltonian equation of motion with added dissipation terms with rate κ, we have:

$$\dot{a}(t) = -i\frac{\partial \mathcal{H}}{\partial a^*} - \kappa a = -i\left(\omega_b a(t) + H(t) + iW(t)\right) - \kappa a, \tag{6.12}$$

$$\dot{a}^*(t) = +i\frac{\partial \mathcal{H}}{\partial a} - \kappa a^* = +i\left(\omega_b a^*(t) + H(t) - iW(t)\right) - \kappa a^*, \tag{6.13}$$

where the dot above the character indicates time derivative. Solving this result in the following:

$$a(t) = \int_{-\infty}^{t} d\tau e^{-i\omega_b(t-\tau) - \kappa(t-\tau)}(W(\tau) - iH(\tau)), \tag{6.14}$$

$$a^*(t) = \int_{-\infty}^{t} d\tau e^{+i\omega_b(t-\tau) - \kappa(t-\tau)}(W(\tau) + iH(\tau)). \tag{6.15}$$

Using the white noise relation Eqs. (6.9)-(6.11), we obtain

$$\overline{a(t)a\left(t'\right)} = 0, \tag{6.16}$$

$$\overline{a^{*}(t)a\left(t'\right)} = \frac{D}{\kappa}e^{+i\omega_b\left(t-t'\right)}e^{-\kappa\left|t-t'\right|}. \tag{6.17}$$

Choosing the parameter D to be $D = \kappa k_B T/\omega_b$, where k_B is the Boltzmann constant and T is temperature, we obtain

$$\overline{a^{*}(0)a\left(0\right)} = k_B T/\omega_b, \tag{6.18}$$

which is the high-temperature limit of the quantum result $\langle a^{\dagger}a\rangle = 1/[\exp(\beta\omega) - 1]$.

When squeezed interaction is turned on, the story is slightly different. The Hamiltonian is modified to

$$\mathcal{H} = \omega_b a^{*}a + \frac{g}{2}\left(aa + a^{*}a^{*}\right) + \left(a^{*} + a\right)H(t) + i\left(a^{*} - a\right)W(t), \tag{6.19}$$

where g is the parameter for squeezing. In this situation, the normal modes are new complex canonical variables b and b^{*} with

$$b = \lambda a + \mu a^{*}, \qquad a = \lambda b - \mu b^{*}, \tag{6.20}$$

$$b^{*} = \mu a + \lambda a^{*} \qquad a^{*} = -\mu b + \lambda b^{*}, \tag{6.21}$$

with real parameters $(\lambda,\ \mu)$ under the constraint $\lambda^2 - \mu^2 = 1$. Appropriate choice of the coefficients to diagonalize the bear boson Hamiltonian (absence of noise H and W) is

$$\lambda = \cosh\theta; \quad \mu = \sinh\theta, \tag{6.22}$$

$$\tanh 2\theta = g/\omega_b. \tag{6.23}$$

Under this transformation coefficients, the Hamiltonian becomes

$$\mathcal{H} = \widetilde{\omega}_b b^* b + (\lambda - \mu)\,(b^* + b)\,H(t) + i(\lambda + \mu)\,(b^* - b)\,W(t), \tag{6.24}$$

where $\widetilde{\omega}_b = \sqrt{\omega_b^2 - g^2}$ is the new boson frequency. In the same way as before, we can check the correlation function. Adding the dissipation terms by hand, the Hamiltonian equation of motion becomes:

$$\dot{b}(t) = -i\frac{\partial \mathcal{H}}{\partial b^*} - \kappa b = -i\left(\widetilde{\omega}_b b(t) + (\lambda - \mu)H(t) + i(\lambda + \mu)W(t)\right) - \kappa b(t), \tag{6.25}$$

$$\dot{b}^*(t) = +i\frac{\partial \mathcal{H}}{\partial b} - \kappa b^* = +i\left(\widetilde{\omega}_b b^*(t) + (\lambda - \mu)H(t) - i(\lambda + \mu)W(t)\right) - \kappa b^*(t). \tag{6.26}$$

Solving this result in the following:

$$b(t) = \int_{-\infty}^{t} d\tau e^{-i\widetilde{\omega}_b(t-\tau)-\kappa(t-\tau)}((\lambda + \mu)W(\tau) - i(\lambda - \mu)H(\tau)), \tag{6.27}$$

$$b^*(t) = \int_{-\infty}^{t} d\tau e^{+i\widetilde{\omega}_b(t-\tau)-\kappa(t-\tau)}((\lambda + \mu)W(\tau) + i(\lambda - \mu)H(\tau)). \tag{6.28}$$

Using Eqs. (6.9)-(6.11), the correlation functions become the following due to the squeezed coefficient (Bogoliubov coefficient):

$$\overline{b(t)b\,(t')} = \frac{2D\lambda\mu}{i\widetilde{\omega}_b + \kappa} e^{-i(\widetilde{\omega}_b - i\kappa)|t-t'|}, \tag{6.29}$$

$$\overline{b^*(t)b\,(t')} = \frac{D}{\kappa}\left(\lambda^2 + \mu^2\right) e^{+i\widetilde{\omega}_b(t-t')} e^{-\kappa|t-t'|}. \tag{6.30}$$

Here, Eqs. (6.29) and (6.30) are different from the results when assuming the thermal state of the boson, which can be seen from the case $t = t'$. To avoid these confusion, in our simulation we simply assumed the thermal occupation of magnon modes, though the calculations based on the white-noise and LLG dynamics as in Ref. [142] may give different results from our simulations. We also support our approach by commenting that Ref. [184] (in Chapter 1) employs a noise model such that the Bogoliubov-transformed variables b and b^* take the

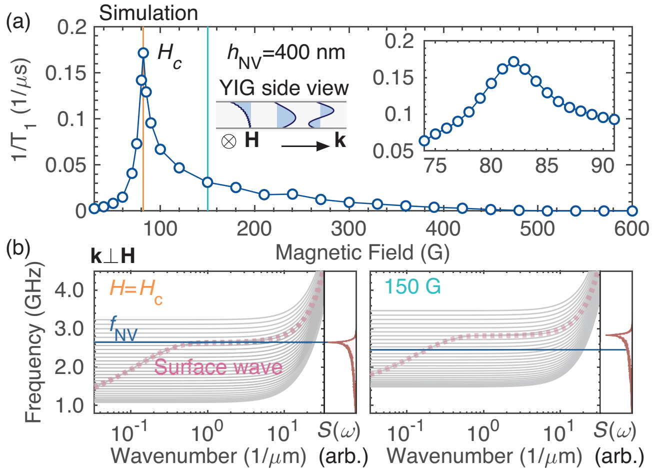

Figure 6.5: (a) Simulation of the T_1 relaxation rate of the NV centers caused by the magnetic noise generated by the magnons in the 3-μm-thick YIG. The simulations are performed under the same field conditions as in Fig. 6.3(b) and the intervals are interpolated linearly. The drawing shows the side view of the YIG with typical mode profilesof the magnon modes. (b) Dispersion relation of the magnons with wave vector perpendicular to the external magnetic field $\mathbf{k} \perp \mathbf{H}$ and the noise spectrum $S(\omega)$ at the NV position at the peak field $H_c = 82\ \mathrm{G}/\mu_0$ (left panel) and at 150 G (right panel). The surface magnon branch is highlighted with the dotted pink curve and the NV frequency is shown with the horizontal blue line.

standard statistical-mechanical thermal correlations as in Eqs. (6.18). Overall, the difference between the two approaches appears to be small.

As shown in Fig. 6.5(a), the simulation agrees well with the experimental observation presented in Fig. 6.3(b). We note that although the matching of the peak field H_c is due to the choice of the saturation magnetization parameter M_s in the model, which is the only variable parameter in the model and we use $M_s = 1718\ \mathrm{G}/\mu_0$ in the simulation, the qualitative and quantitative agreement of the amplitude of the decay rates are not the consequence of the free parameter in the model: for example, there is no overall scaling factor of the amplitude of the simulated T_1 decay rates. To study the origin of the peaked behavior in the longitudinal decay rate, we plot in Fig. 6.5(b) the magnon dispersion relation and the noise spectrum $S(\omega)$ [note the relation $1/T_1 = 2S(\omega = \omega_{\mathrm{NV}})$] at the NV position at the peak field $H_{\mathrm{ext}} = H_c (= 82\ \mathrm{G}/\mu_0)$ and at 150 G. In the visualization of the dispersion relation, the surface magnon mode branch is highlighted with a dotted pink curve, whose typical mode profile is shown in the leftmost drawing shown in Fig. 6.5(a). The other gray

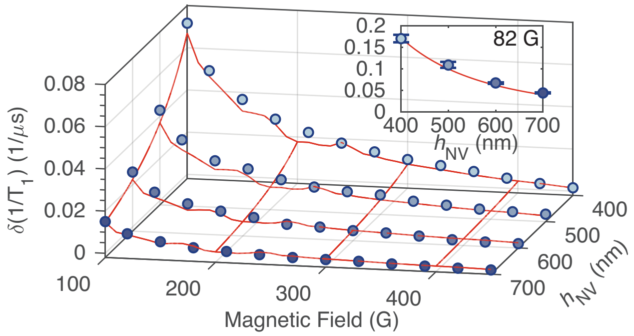

Figure 6.6: Magnetic field and the NV height dependencies of the longitudinal relaxation rate of the NV center $\delta(1/T_1)$, where $\delta(1/T_1) = 1/T_1 - 1/T_1(600\ \mathrm{G})$ is the deviation from the value at the highest field (600 G) in the measurement. The inset shows the NV height dependence of $\delta(1/T_1)$ at the peak field $H_c = 82\ \mathrm{G}/\mu_0$. The red curves are the simulation and the blue plots are the experimental observation. The non-smoothness of the red curves are due to the limited sampling of the numerical integration and diagonalization of the magnon matrix.

curves are (thickness-direction) modes orthogonal to the surface mode whose typical mode profile is shown in the middle and the right drawings in Fig. 6.5(a). Based on the left panel of Fig. 6.5(b), we find that the peaked behavior in the longitudinal decay rate is due to the crossing of the NV transition frequency and the plateau of the surface magnon dispersion. This also indicates that we are observing the signature of the interaction between NV centers and thermally occupied surface magnons.

To confirm the consistency between the experimental observation and the simulation results, we varied the height of the NV center h_{NV} from the YIG surface, and the resulting longitudinal relaxation rates in the field range $100\ \mathrm{G} \leq \mu_0 H_{\mathrm{ext}} \leq 450\ \mathrm{G}$ are shown in Fig. 6.6. Here, the red curves are the simulation results and the blue plots are the experimental observation, and we subtracted the offset relaxation rate $1/T(600\ \mathrm{G})$ from the measurement, at which field there is no overlap between the magnon band and the lower transition frequency of the NV center and thus there is no on-resonant magnons causing the strong T_1 decay. We also show in the inset of Fig. 6.6 the NV height dependency of the longitudinal relaxation rate at the peak field $H_c = 82\ \mathrm{G}/\mu_0$. The agreement between the experiment and the simulation supports the accuracy of the model provided in Eqs. (6.1)-(6.4).

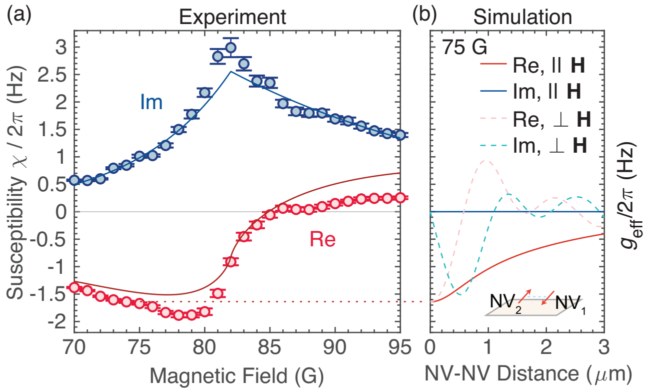

Figure 6.7: (a) NV center's susceptibility due to the self response mediated by the surface magnons in the YIG film. The blue and the red markers represent the imaginary part and the real part of the succeptibility, respectively. The blue curve is the fit with two exponential functions and the red curve is derived using the Kramers-Kronig relation to the fit equation. (b) Simulated NV-NV interaction mediated by the magnons in the YIG film as a function of the NV-NV distance under the condition where two NV centers are placed on top of the YIG as drawn in the bottom part of the figure. The real part (imaginary part) of the NV-NV coupling strength g_{eff} when the NV-NV displacement is along the external magnetic field direction is shown with a solid red (solid red) curve, where both of the NV axises are kept parallel to the external magnetic field. The real part and the imaginary part for the case with NV-NV displacement perpendicular to the external magnetic field direction are drawn with dashed sky blue and dashed pink curves, respectively. The simulation is performed for a 75-G-field condition, and the guide to the eyes is drawn with a horizontal red line to indicate the equivalence of the real part of the susceptibility and the magnon-mediated NV-NV coupling constant at zero distance.

6.5 Self-interaction of an NV center mediated by surface magnons

We have characterized the surface magnon induced enhancement of the T_1 decay rates so far. In this section, we obtain more useful information about the NV-magnon coupling in the system and the expected NV-NV interaction mediated by the surface magnons with the use of the fluctuation-dissipation relation and the Kramers-Kronig relation. As discussed in Chapter 3, the T_1 decay rate is related to the imaginary part of the self response function, or the susceptibility χ, via the fluctuation-dissipation relation:

$$\chi'' = T_1^{-1}/(2\coth(\beta\omega_{\text{NV}}/2)), \tag{6.31}$$

where the double prime indicates the imaginary part. While this captures the dissipation property of the magnon-mediated interaction, we are more interested in the coherent property of the interaction captured by its real part. Due to the causality of the response function, we can obtain this real part of the susceptibility with the use of the Kramers-Kronig relation. Although one needs to have access to the frequency dependence of χ'' to directly apply this relation, because changing the external magnetic field allows us to probe the response function under a different frequency input, we can apply the Kramers-Kronig relation in the magnetic field:

$$\chi'(H) = \mathcal{P} \int \frac{dH'}{\pi} \frac{\chi''(H')}{H - H'}, \tag{6.32}$$

where $\mathcal{P}$ represents the Cauchy's principal value integral. This frequency-field conversion in the Kramers-Kronig relation is verified or supported by the shift in the noise spectrum shown in Fig. 6.6(b), where the magnon spectrum simply shift due to the Zeeman energy when changing the external magnetic field.

In Fig. 6.7(a), we show the real and the imaginary part of the susceptibility calculated from Eqs. (6.31) and (6.32), where the red and the blue markers are the real part and the imaginary part, respectively. When applying the Kramers-Kronig relation Eq. (6.32) to the experimental data, we employed the procedure using the Maclaurin's rule with the elimination of the pole contribution provided in Ref. [185]. We also fit the imaginary part of the susceptibility with two exponential functions with different slopes for the two opposite directions:

$$\chi''(H) = A\left(\theta(H - H_c)\text{exp}[-|H - H_c|/H_R] + \theta(H_c - H)\text{exp}[-|H - H_c|/H_L]\right), \tag{6.33}$$

where $\theta(\cdots)$ is the Heaviside step function and $\{A,\ H_c,\ H_R,\ H_L\}$ are the fit parameters. The fit result is shown with the solid blue curve in Fig. 6.7(a). Applying the Kramers-Kronig relation to this functional form, we obtain

$$\chi'(H) = \frac{A}{\pi}\left(e^{-(H-H_c)/H_R}\mathrm{Ei}((H-H_c)/H_R) - e^{(H-H_c)/H_L}\mathrm{Ei}(-(H-H_c)/H_L)\right), \quad (6.34)$$

where $\mathrm{Ei}(\cdots)$ is the exponential integral function. This result is shown with the solid red curve in Fig. 6.7(a). The difference between the red marker and the red curve is due to the contribution from outside the field range shown in Fig. 6.7(a) in the Kramers-Kronig relation Eq. (6.32). Therefore, the overall agreement between the red marker and the red curve in Fig. 6.7(a) indicates that the real part of the susceptibility in the figure is mostly originating from the surface magnons in the shown field range.

As discussed in Chapter 3, the real part of the self interaction can be used to estimate the strength of the possible magnon-mediated NV-NV interaction for the case where there are two NV centers placed on top of the YIG structure. More specifically, we have the relation:

$$g_{\mathrm{eff}} = \chi', \text{ for } \mathbf{r}_{\mathrm{NV}_1} = \mathbf{r}_{\mathrm{NV}_2}, \quad (6.35)$$

where $\mathbf{r}_{\mathrm{NV}_1}$ and $\mathbf{r}_{\mathrm{NV}_2}$ are the position of two NV cneters with label $i = 1, 2$ and g_{eff} is the effective NV-NV coupling appearing in the interaction of form

$$\mathcal{H}_{\mathrm{NV-NV}} = -(g_{\mathrm{eff}}\sigma^{+}_{\mathrm{NV}_1}\sigma^{-}_{\mathrm{NV}_2} + \mathrm{H.c.}), \quad (6.36)$$

where $\sigma^{-}_{\mathrm{NV}_i} = |S_z = 0\rangle_i\langle S_z = -1|$ and $\sigma^{+}_{\mathrm{NV}_i} = (\sigma^{-}_{\mathrm{NV}_i})^{\dagger}$. As the absolute amplitude of the NV-NV effective coupling is typically largest for $\mathbf{r}_{\mathrm{NV}_1} = \mathbf{r}_{\mathrm{NV}_2}$, i.e., when the two NV centers are at zero distance, the real part of the susceptibility can be used to estimate the maximum possible NV-NV coupling strength for the system. This is made more explicit by showing the simulation of the NV-NV distance dependence of the effective coupling in Fig. 6.7(b).

Here, we use the result from the derivation of the Markovian Lindblad master equation:

$$g_{\text{eff}} = \sum_{n=1}^{N} \int \frac{d\mathbf{k}}{(2\pi)^2} \mathcal{P} \frac{|g_{n,\mathbf{k}}|^2 \exp[i\mathbf{k} \cdot (\mathbf{r}_{\text{NV}_1} - \mathbf{r}_{\text{NV}_2})]}{\omega_{n,\mathbf{k}} - \omega_{\text{NV}}}, \tag{6.37}$$

for different direction of the NV-NV displacement $\mathbf{r}_{\text{NV}_1} - \mathbf{r}_{\text{NV}_2}$. For the numerical evaluation of Eq. (6.37), we avoided the pole contribution by replacing $1/(\omega_{n,\mathbf{k}} - \omega_{\text{NV}})$ to $(\omega_{n,\mathbf{k}} - \omega_{\text{NV}})/[(\omega_{n,\mathbf{k}} - \omega_{\text{NV}})^2 + \delta^2]$ for small δ. The simulation is performed for a 75-G-field condition, and the real (imaginary) part of g_{eff} for $(\mathbf{r}_{\text{NV}_1} - \mathbf{r}_{\text{NV}_2}) \parallel \mathbf{H}$ and $(\mathbf{r}_{\text{NV}_1} - \mathbf{r}_{\text{NV}_2}) \perp \mathbf{H}$ are shown with a solid red (blue) and a dashed pink (sky blue) curves, respectively, as a function of the NV-NV distance $|\mathbf{r}_{\text{NV}_1} - \mathbf{r}_{\text{NV}_2}|$. As indicated by the horizontal dashed line, the real part of the susceptibility is measuring the $\mathbf{r}_{\text{NV}_1} = \mathbf{r}_{\text{NV}_2}$ part of the NV-NV effective coupling g_{eff}, and this provides an estimate of the strength of the NV-NV interaction mediated by magnons when there are two NV centers on top of the YIG structure. While the strength of the self response χ is small for our system as the magnon is not confined in the in-plane direction, the procedure used in this study to quantify the real part of the susceptibility χ with the fluctuation-dissipation relation and the Kramers-Kronig relation can be applied to more advanced YIG nanostructures for achieving the long-distance NV-NV entanglement, such as the YIG bar and waveguide structures as suggested in Ref. [2].

6.6 Conclusion

We have studied the interplay between NV centers in diamond and the magnons in a 3-μm-thick YIG film using the longitudinal relaxometry. The simulated T_1 decay rates using the magnetically-coupled NV-magnon model well captures the experimentally observed behavior of the field and the NV-YIG distance dependencies of the longitudinal relaxation rates. Based on the simulated magnon dispersion and the magnetic noise spectrum, we find the observed peak in the T_1 decay rate as a function of the external magnetic field is due to the crossing of the NV-center's transition frequency relative to the surface magnon dispersion's plateau.

With the use of the fluctuation-dissipation relation and the Kramers-Kronig relation, we obtain a real part of the susceptibility χ due to the self-response mediated by the surface magnons, which provides an estimate of the NV-NV effective coupling strength when there are two NV centers on top of the YIG film. This analysis scheme is applicable to a wider class of quantum systems where an energy transfer between qubits and boson modes are relevant, for example to characterize the spin-phonon interaction [186]. Furthermore, by applying these two relations to the two-NV correlated decay rates, we may obtain the full NV-NV distance dependency of the effective coupling strength (See Chapter 3). Although the susceptibility $|\chi|/2\pi \lesssim 2$ Hz obtained in our system is small as magnons are not confined in the in-plane direction of the YIG film, unlike the proposal in Ref. [2], the procedure of characterizing the NV-magnon coupling strength provided in this study is expected to be applicable to the future exploration of the YIG nanodevices to enable the magnon-mediated NV-NV entanglement generation.

Appendix A

Second quantization of magnetistatic surface spin waves and its coupling to NV centers

In this appendix, we perform a canonical quantization of the magnetistatic surface spin waves (MSSW) in ferromagnet (yttrium iron garnet, YIG) and show its coupling to a single NV center in diamond placed on top of the YIG. We show that a strong coupling between the MSSW and a collective excitation of an ensemble of NV centers may be realized, indicating that they form a hybridized quasiparticle of a ferromagnetic magnon and a dispersionless magnon of quantum impurities.

Firstly, we compute the coupling between the magnetostatic surface spin wave (MSSW) in YIG slab and a single NV center in diamond placed on the YIG, as illustrated in the Fig. A.1(a). We apply an external magnetic field to $\hat{z}$ direction, $\mathbf{H}_0 = H_0\hat{z}$, where the MSSW propagates along $\pm\hat{y}$ direction. Magnetization $\mathbf{M}(\mathbf{r})$ exist in $-d/2 \leq x \leq d/2$. At equilibrium, $\mathbf{M}(\mathbf{r})$ is along $\hat{z}$ axis, $\mathbf{M}(\mathbf{r}) = M_{\mathrm{s}}\hat{z}$, and we denote its deviation as $\delta M_{x,y} = m_{x,y}$ and $\delta M_z = (M_s^2 - m_x^2 - m_y^2)^{1/2} - M_{\mathrm{s}}$, where M_{s} is the saturation magnetization. The classical

Hamiltonian is given by $\mathcal{H} = \int dx \sum_{\mathbf{k}} \mathcal{H}_{\mathrm{F}}^{\mathbf{k}}(x) + \mathcal{H}_{\mathrm{NV}} + \mathcal{H}_{\mathrm{int}}$ with

$$\mathcal{H}_{\mathrm{F}}^{\mathbf{k}}(x) \approx \frac{\mu_0}{2}\left[\frac{H_0}{M_{\mathrm{s}}}\mathbf{m}_{-\mathbf{k}}(x)\cdot\mathbf{m}_{\mathbf{k}}(x) - \mathbf{m}_{-\mathbf{k}}(x)\cdot\mathbf{H}_{\mathbf{k}}^{\mathrm{d}}[\mathbf{m}](x)\right], \tag{A.1}$$

$$\mathcal{H}_{\mathrm{NV}} = DS_z^2 + \gamma\mu_0\mathbf{H}_0\cdot\mathbf{S}_{\mathrm{NV}}, \tag{A.2}$$

$$\mathcal{H}_{\mathrm{int}} = \gamma\mu_0\mathbf{H}_{\mathbf{r_0}}^{\mathrm{d}}[\delta\mathbf{M}]\cdot\mathbf{S}_{\mathrm{NV}}. \tag{A.3}$$

Here, we have ignored higher-order terms in $m_{x,y}$ in the ferromagnet Hamiltonian $\mathcal{H}_{\mathrm{F}}^{\mathbf{k}}(x)$, and we will regard $m^{\pm} = m_x \pm im_y$ as proportional to the complex canonical variables, which corresponds to dropping higher-order terms in the Holstein-Primakoff transformation. $\mathbf{k}$ is the in-plane wave vector, $\mathbf{m}_{\mathbf{k}}(x)$ is the Fourier transform of $\mathbf{m}(\mathbf{r}) = m_x(\mathbf{r})\hat{x} + m_y(\mathbf{r})\hat{y}$, $D = 2\pi \times 2.87$ GHz is the zero-field splitting of the NV center, $\gamma = 2\pi \times 28$ MHz/mT is the absolute value of the electron gyromagnetic ratio, $\mathbf{S}_{\mathrm{NV}}$ is the NV spin, and $\mathbf{H}_{\mathbf{r}}^{\mathrm{d}}[\mathbf{X}]$ is the demagnetization field generated by $\mathbf{X}(\mathbf{r}) = \delta\mathbf{M}(\mathbf{r})$ or $\mathbf{m}(\mathbf{r})$ under the magnetostatic approximation [149] ($\nabla \times \mathbf{H}_{\mathbf{r}}^{\mathrm{d}} = 0$). Its two-dimensional Fourier transform $\mathbf{H}_{\mathbf{k}}^{\mathrm{d}}[\mathbf{X}]$ can be written as

$$\mathbf{H}_{\mathbf{k}}^{\mathrm{d}}[\mathbf{X}](x) = \int dx'\hat{D}_{\mathbf{k}}(x-x')\cdot\mathbf{X}_{\mathbf{k}}(x') \tag{A.4}$$

$$\hat{D}_{\mathbf{k}}(x) = \frac{ke^{-k|x|}}{2}\sigma_{\mathbf{k}}^{-\mathrm{sgn}(x)}\otimes\sigma_{\mathbf{k}}^{-\mathrm{sgn}(x)} - \hat{x}\otimes\hat{x}\delta(x) \tag{A.5}$$

where $\sigma_{\mathbf{k}}^{\pm} \equiv \hat{x} \pm i\hat{\mathbf{k}}$.

To study the coupling between the MSSW and a single NV center, we focus on the momentum sector $\mathbf{k} = k_y\hat{y} = \nu k\hat{y}$ with $k = |\mathbf{k}|$ and $\nu = \pm 1$. We perform the following classical Bogoliubov transformation:

$$\frac{m_{\nu k\hat{y}}^{-}(x)}{\sqrt{2\gamma M_s}} = \sum_{\mu=0}^{\infty}\left[\xi_{\nu k}^{(\mu)}(x)\alpha_{\nu k,\mu} + \eta_{-\nu k}^{(\mu)}(x)\alpha_{-\nu k,\mu}^{*}\right], \tag{A.6}$$

$$\frac{m_{\nu k\hat{y}}^{+}(x)}{\sqrt{2\gamma M_s}} = \sum_{\mu=0}^{\infty}\left[\eta_{\nu k}^{(\mu)}(x)\alpha_{\nu k,\mu} + \xi_{-\nu k}^{(\mu)}(x)\alpha_{-\nu k,\mu}^{*}\right], \tag{A.7}$$

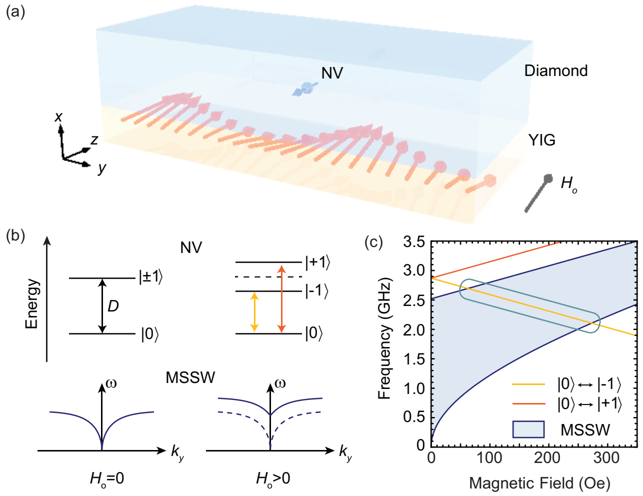

Figure A.1: (a) Schematic of the MSSW in YIG coupled to a single NV center in diamond on the YIG. External magnetic field is applied to $+\hat{z}$ direction. (b) Energy levels and the dispersion relation of an NV center and the MSSW with and without an external magnetic field H_0. (c) Magnetic field dependence of the NV-center transitions and the MSSW resonances. MSSW resonances form a band, where the low frequency bound corresponds to $k_y \to 0$ and the high frequency bound correspond to $k_y \to \infty$. Frequency overlap is marked with a rounded rectangle. $\mu_0 M_s = 180$ mT is used for the calculation.

where $\xi^{(\mu)}_{\nu k}(x)$ and $\eta^{(\mu)}_{\nu k}(x)$ satisfies proper orthogonality relations to make the transformation canonical [For detail, see Sec. A.0.1]. The MSSW mode corresponds to $\mu = 0$. With this transformation, the ferromagnet Hamiltonian can be written as

$$\int dx \left[\mathcal{H}_{\mathrm{F}}^{k\hat{y}}(x) + \mathcal{H}_{\mathrm{F}}^{-k\hat{y}}(x)\right] = \sum_{\nu,\mu} \omega_\mu(k) \alpha^*_{\nu k,\mu} \alpha_{\nu k,\mu}, \tag{A.8}$$

where the MSSW energy is given by

$$\omega_0(k) = \sqrt{\omega_H(\omega_H + \omega_M) + \omega_M^2 (1 - e^{-2kd})/4}, \tag{A.9}$$

with $\omega_M = \gamma \mu_0 M_{\mathrm{s}}$ and $\omega_H = \gamma \mu_0 H_0$. We can compute the interaction Hamiltonian between the NV center and the spin waves with momentum $\mathbf{k} \parallel \hat{y}$ by calculating the demagnetization field generated at the position of the NV center $h^{\pm}_{\mathrm{d}}(\boldsymbol{\rho}_0; h_0) = (\hat{x} \pm i\hat{y}) \cdot \mathbf{H}^{\mathrm{d}}_{\mathbf{r_0}}[\delta \mathbf{M}]$, and we

obtain

$$h_{\mathrm{d}}^{-}(\boldsymbol{\rho}_0; h_0) = \sum_{\mathbf{k}} h_{\mathrm{d},\mathbf{k}}^{-} e^{i\mathbf{k}\cdot\boldsymbol{\rho}_0}, \tag{A.10}$$

$$h_{\mathrm{d}}^{+}(\boldsymbol{\rho}_0; h_0) = \sum_{\mathbf{k}} h_{\mathrm{d},\mathbf{k}}^{+} e^{i\mathbf{k}\cdot\boldsymbol{\rho}_0}, \tag{A.11}$$

$$h_{\mathrm{d},\mathbf{k}=\nu k\hat{y}}^{-} = (\mathcal{A}_{-k}\alpha_{-k,0} + \mathcal{A}_{+k}\alpha_{+k,0}^{*})\delta_{\nu,-1}, \tag{A.12}$$

$$h_{\mathrm{d},\mathbf{k}=\nu k\hat{y}}^{+} = (\mathcal{A}_{+k}\alpha_{+k,0} + \mathcal{A}_{-k}\alpha_{-k,0}^{*})\delta_{\nu,+1}, \tag{A.13}$$

where

$$\mathcal{A}_{\nu k} = \sqrt{2\gamma M_s/V}\mathcal{M}_{\nu k}\sqrt{kd}e^{-kh_0}. \tag{A.14}$$

Here, V is the volume of the ferromagnet. Spin waves with $\mu \neq 0$ does not generate magnetic field outside the ferromagnetic film and does not contribute to the interaction. The equations (A.10) and (A.11) are linear in $\alpha_{\nu k,0}$, $\alpha_{\nu k,0}^{*}$ because δM_z vanishes in the inter product $\sigma_{\pm k\hat{y}}^{-} \cdot \delta\mathbf{M} = (\hat{x} \pm i\hat{y}) \cdot \delta\mathbf{M}$ in the equation (A.4), as well as because we have ignored higher order terms in the Holstein-Primakoff transformation. $\mathcal{M}_{\nu k}$ is given by

$$\mathcal{M}_{\nu k} = \nu\sqrt{\left(e^{-kd}\sinh kd\right)(\chi_0 + 2 - \nu\kappa_0)(\chi_0 + \nu\kappa_0)/4\kappa_0}, \tag{A.15}$$

where $\chi_0 = \omega_H\omega_M/(\omega_H^2 - \omega_0^2)$ and $\kappa_0 = \omega_0\omega_M/(\omega_H^2 - \omega_0^2)$. Note that $\mathcal{M}_{-k}$ is smaller than $\mathcal{M}_{+k}$ due to the chirality of the magnetic field generated by the magnetization texture. In the long-wavelength limit $k \to 0$, we obtain $\mathcal{M}_{\nu k} \to (1/2)(\sqrt{\omega_H/\omega_{\mathrm{K}}} + \nu\sqrt{\omega_{\mathrm{K}}/\omega_H})\sqrt{kd}$, where $\omega_{\mathrm{K}} = \lim_{k\to 0}\omega_0(k) = \sqrt{\omega_H(\omega_H + \omega_M)}$ is the Kittel frequency. In the short-wavelength limit $k \to \infty$, we obtain $\mathcal{M}_{+k} \to 1/\sqrt{2}$ and $\mathcal{M}_{-k} \to -(\omega_M/(2\omega_H + \omega_M))e^{-kd}/2\sqrt{2}$.

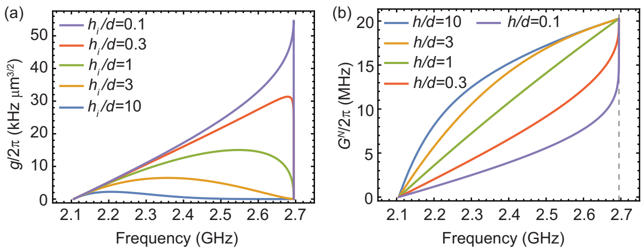

Figure A.2: (a) Coupling $g(k(\omega), h_i)$ between a single NV center and the MSSW as a function the frequency $\omega/2\pi$ under the overlap condition marked in Fig. A.1(c). Multiple curves under different hight of NV centers h_i/d are shown, where d is the YIG film thickness. The sharp cutoff on the high frequency side is due to the plateau of the MSSW dispersion at $k_y \to \infty$. (b) Collective coupling $G^N(k(\omega))$ as a function of frequency $\omega/2\pi$ under multiple diamond thickness h/d. The density of the NV centers is set $n_{\rm NV} = 2 \times 10^6\ \mu{\rm m}^{-3}$.

Substituting equations (A.10)-(A.13) into the interaction Hamiltonian $\mathcal{H}_{\rm int}$, we obtain

$$\mathcal{H}_{\rm int}^{\mathbf{k}\parallel\hat{y}} = \frac{\omega_M}{\sqrt{n_{\rm spin}V}} \sum_{k\geq 0} \sqrt{kd}\, e^{-kh_0}[S^-_{\rm NV}(\mathcal{M}_{+k}\alpha_{+k,0} + \mathcal{M}_{-k}\alpha^*_{-k,0})e^{iky_0} + {\rm H.c.}], \tag{A.16}$$

where $n_{\rm spin} = M_s/\mu_B$ is the spin density of the ferromagnet. Promoting the classical variables $\alpha^*_{\nu k\hat{y}}$, $\alpha_{\nu k\hat{y}}$ into the quantum-mechanical creation/annihilation operators $\alpha^\dagger_{\nu k\hat{y}}$, $\alpha_{\nu k\hat{y}}$, equations (A.2), (A.8), and (A.16) give the quantum-mechanical Hamiltonians of the MSSW-NV center hibrid system. We note that the Hamiltonian is problematic in a large momentum regime because the classical description of the magnetization is correct in a continuum limit $k \ll 1/a_{\rm F}$, where $a_{\rm F}$ is the spacing of the ferromagnetic spins. In addition, we have ignored the exchange interaction in the Hamiltonian, which is not accurate when $\gamma D k^2 \gtrsim \omega_M$, where D is the exchange stiffness (for YIG, $\gamma D/\omega_M \simeq 3 \times 10^{-4} \mu{\rm m}^2$). We also note that the magnetostatic approximation implies $k \gg \omega/c$, where c is the speed of light. So the currently studied model describes the real material when $\omega/c \ll k \ll \sqrt{\gamma D/\omega_M}$.

Next, we introduce an ensemble of NV centers and calculate the collective coupling between the MSSW and NV centers. Figure A.1(b) shows the schematic of the transition frequencies of an NV center and the MSSW dispersion. In the following, We adjust an external magnetic field $\mathbf{H}_0$ such that the NV-center transition $|0\rangle \leftrightarrow |-1\rangle$ is close to the

MSSW resonance, as marked in the Fig. A.1(c). We denote the Pauli operator of the NV-center spin as $\sigma_+^i = |-1\rangle\langle 0| = S_{\mathrm{NV},i}^-/\sqrt{2}$, where i is the label of NV centers and the factor of $\sqrt{2}$ is the coefficient due to the spin-1 nature of the NV center. Under the rotating wave approximation, the interaction Hamiltonian between the MSSW and an ensemble of NV centers becomes

$$\mathcal{H}_{\mathrm{int}}^{\mathbf{k}\|\hat{y},N} = \sum_{i,k\geq 0} \frac{g(k,h_i)}{\sqrt{V}} (\sigma_+^i \alpha_{+k,0} e^{iky_i} + \mathrm{H.c.}), \tag{A.17}$$

$$g(k,h_i) = \frac{\omega_M}{\sqrt{n_{\mathrm{spin}}}} \sqrt{2kd} e^{-kh_i} \mathcal{M}_{+k}. \tag{A.18}$$

We introduce a collective excitation operator of NV centers $\beta_k^\dagger$, which creates a dispersionless magnon with momentum $+k\hat{y}$ formed by NV centers [133]:

$$\beta_k^\dagger = \frac{1}{\sqrt{N} g^N(k)} \sum_i g(k,h_i) \sigma_+^i e^{iky_i}, \tag{A.19}$$

where $g^N(k) = \sqrt{\sum_i |g(k,h_i)|^2/N}$. The operator $\beta_k^\dagger$ creates an orthogonal spin wave in a limit where NV centers are fully polarized under a continuum limit of NV centers $k \ll 1/a_{\mathrm{NV}}$, where a_{NV} is the average distance of the NV centers. The spin waves formed by NV centers have a flat dispersion because we have not taken into account the NV-NV interaction, which is small when a_{NV} is not too short. Then we can rewrite the interaction Hamiltonain as

$$\mathcal{H}_{\mathrm{int}}^{\mathbf{k}\|\hat{y},N} = \sum_{k\geq 0} G^N(k) (\beta_k^\dagger \alpha_{+k,0} + \mathrm{H.c.}). \tag{A.20}$$

Here, the collective coupling strength is given by

$$\begin{aligned} G^N(k) &= g^N(k)\sqrt{N/V} = \sqrt{\frac{1}{V}\sum_i |g(k,h_i)|^2}, \\ &= \sqrt{\frac{n_{\rm NV}/4}{d}\int_0^h dz|g(k,z)|^2}, \\ &= \omega_M\sqrt{\frac{n_{\rm NV}/4}{n_{\rm spin}}}\mathcal{M}_{+k}\sqrt{1-e^{-2kh}}, \end{aligned} \tag{A.21}$$

where $n_{\rm NV}$ is the density of NV centers and h is the diamond thickness. The factor of 1/4 inside the square root is because only one out of four orientations of NV centers is aligned to the $\hat{z}$ axis. The couplings $g(k,h_i)$ and $G^N(k)$ are shown in the Fig. A.2(a) and A.2(b), respectively. Dispersion relation of the coupled magnon-magnon mode is shown in the Fig. A.3. We observe that the collective excitation of NV centers with momentum $-k\hat{y}$ does not couple to the MSSW due to the asymmetry of the coupling.

To see that the collective coupling $G^N(k)$ may result in a strong coupling, we compare the coupling $G^N(k)$ with the ensemble dephasing rate of NV centers γ_s and the damping rate $\kappa_{\rm MSSW}$ of the MSSW in YIG. The strong coupling is realized when $G^N(k) > \gamma_s,\ \kappa_{\rm MSSW}$. For NV centers, recent experiments have demonstrated $\gamma_s \simeq 2\pi \times 3$ MHz [187]. For the MSSW, the lower bound for $\kappa_{\rm MSSW}$ can be estimated by the Gilbert damping $\alpha \simeq 1\times 10^{-5}$ of YIG [188] by the relation $\kappa_{\rm MSSW} \geq 2\pi \times \alpha f_{\rm MSSW} \simeq 2\pi \times 25$ kHz, where $f_{\rm MSSW}$ is the MSSW frequency. Since the collective coupling can take $G^N(k) > 2\pi \times 15$ MHz, we expect the strong coupling to be realized in the NV-MSSW hybrid system.

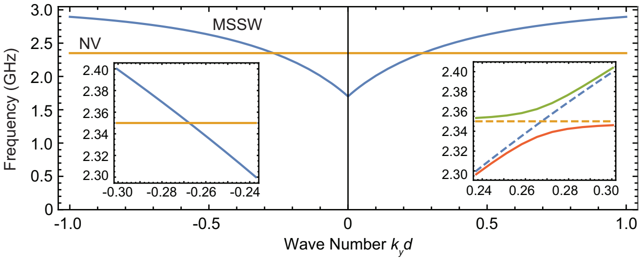

Figure A.3: Dispersion relation of the MSSW and the collective excitation of NV centers at small momentum regime. The curves are calculated under the external magnetic field $H_0 \simeq$ 185 Oe and the thickness of the diamond is set large enough $h/d \gg 1$. NV centers construct a flat dispersion because the NV-NV interaction is small. Inset shows the intersections of the two dispersions. Due to the asymmetry of the coupling, only $k_y > 0$ side form the hybridization.

A.0.1 Bogoliubov transformation of the MSSW

In this section, we show the functions that define the Bogoliubov transformation in the equation (A.6).

$$\xi_{\nu k}^{(\mu)}(x) = \begin{cases} \frac{-1}{\sqrt{(\chi_0^2-\kappa_0^2)4\kappa_0}}(\chi_0+\kappa_0)q(+)h_{\nu k}(x) & ,\mu = 0 \\ \frac{-1}{\sqrt{4\chi_\mu\kappa_\mu}}(\chi_\mu+\kappa_\mu)f_{\mu,\nu k}(x) & ,\mu \in (2\mathbb{Z}_+ - 1) \\ \frac{-1}{\sqrt{4\chi_\mu\kappa_\mu}}(\chi_\mu+\kappa_\mu)g_{\mu,\nu k}(x) & ,\mu \in 2\mathbb{Z}_+ \end{cases} \tag{A.22}$$

$$\eta_{\nu k}^{(\mu)}(x) = \begin{cases} \frac{-1}{\sqrt{(\chi_0^2-\kappa_0^2)4\kappa_0}}(\chi_0-\kappa_0)q(-)h_{-\nu k}(x) & ,\mu = 0 \\ \frac{-1}{\sqrt{4\chi_\mu\kappa_\mu}}(\chi_\mu-\kappa_\mu)f_{\mu,-\nu k}(x) & ,\mu \in (2\mathbb{Z}_+ - 1) \\ \frac{-1}{\sqrt{4\chi_\mu\kappa_\mu}}(\chi_\mu-\kappa_\mu)g_{\mu,-\nu k}(x) & ,\mu \in 2\mathbb{Z}_+ \end{cases} \tag{A.23}$$

$$q(\nu) = \sqrt{(\chi_0 + 2 - \nu\kappa_0)(\chi_0 - \nu\kappa_0)} \tag{A.24}$$

$$\chi_\mu = \frac{\omega_H\omega_M}{\omega_H^2 - \omega_\mu^2}; \quad \kappa_\mu = \frac{\omega_\mu\omega_M}{\omega_H^2 - \omega_\mu^2} \tag{A.25}$$

$$\omega_\mu(k) = \begin{cases} \sqrt{\omega_H(\omega_H+\omega_M) + \omega_M^2(1-e^{-2kd})/4} & ,\mu = 0 \\ \sqrt{\omega_H(\omega_H+\omega_M)} & ,\mu \neq 0 \end{cases} \tag{A.26}$$

$$\omega_M = \gamma\mu_0 M_\mathrm{s}; \quad \omega_H = \gamma\mu_0 H_0, \tag{A.27}$$

where $\mu = 0$ corresponds to the MSSW and $\mu \neq 0$ are modes which does not generate the magnetic field outside the ferromagnet. $\mathbb{Z}_+$ is the set of positive integers. The functions $\{f_{\mu,\nu k}(x), g_{\mu,\nu k}(x), h_{\nu k}(x)\}$ are non-zero only when $-d/2 \leq x \leq d/2$ and are given by

$$f_{\mu,\nu k}(x) = \sqrt{\frac{2d}{d^2k^2 + \mu^2\pi^2}} \left(\frac{\mu\pi}{d} \sin \frac{\mu\pi x}{d} - \nu k \cos \frac{\mu\pi x}{d}\right) \tag{A.28}$$

$$g_{\mu,\nu k}(x) = \sqrt{\frac{2d}{d^2k^2 + \mu^2\pi^2}} \left(\frac{\mu\pi}{d} \cos \frac{\mu\pi x}{d} + \nu k \sin \frac{\mu\pi x}{d}\right) \tag{A.29}$$

$$h_{\nu k}(x) = \sqrt{\frac{1}{d}\frac{kd}{\sinh kd}} e^{\nu k x} \tag{A.30}$$

The set of functions $\{f_{2n-1,\nu k}(x), g_{2n,\nu k}(x), h_{\nu k}(x) | n \in \mathbb{Z}_+\}$ form a complete orthonormal basis with the conventional inner product $\langle \phi | \phi' \rangle = \int dx \phi(x)\phi'(x)$. Therefore, functions $\{\xi^{(\mu)}_{\nu k}(x), \eta^{(\mu)}_{\nu k}(x) | \mu \in \mathbb{Z}_{\geq 0}\}$ satisfies

$$\int_{-d/2}^{d/2} dx \left[\xi^{(\mu)}_{\nu k} \xi^{(\mu')}_{\nu k} - \eta^{(\mu)}_{\nu k} \eta^{(\mu')}_{\nu k}\right] = \delta_{\mu,\mu'} \tag{A.31}$$

$$\int_{-d/2}^{d/2} dx \left[\xi^{(\mu)}_{\nu k} \eta^{(\mu')}_{-\nu k} - \eta^{(\mu)}_{\nu k} \xi^{(\mu')}_{-\nu k}\right] = 0, \tag{A.32}$$

which preserves the Poisson bracket relation in the classical Hamiltonian mechanics. Here, $\mathbb{Z}_{\geq 0}$ is the set of non-negative integers.

A.0.2 Driving NV centers with MSSW

In this section, we compute the magnetic field response to a current flowing through a microstrip line (MSL) fabricated on the YIG mediated by the MSSW. We model the current density as $j = (I/w)\theta(y + w/2)\theta(w/2 - y)\delta(x - d/2)$, where I is the net current, w is the width of the MSL, and $\theta(\cdot)$ is the Heaviside step function. Magnetic field generated by the

MSL is

$$
\begin{aligned}
\mathbf{H}_{\mathrm{MSL}} &= \frac{I}{2L}\sum_{\nu,k}\frac{\sin(kw/2)}{kw/2} i\nu\sigma_{\nu}^{-}(x)e^{i\nu ky-|k(x-\frac{d}{2})|}, && \text{(A.33)}\\
\sigma_{\nu}^{-}(x) &= \hat{x}-i\nu\mathrm{sgn}(x-d/2)\hat{y}. && \text{(A.34)}
\end{aligned}
$$

One obtains the interaction Hamiltonian by calculating $\mathcal{H}_{\mathrm{MSL}} = -\mu_0\int d\mathbf{r}\cdot\mathbf{H}_{\mathrm{MSL}}\cdot\delta\mathbf{M}$, and it reads

$$
\mathcal{H}_{\mathrm{MSL}} = -\sum_{\nu,k} i[\mathcal{F}_{\nu k}(\alpha_{\nu k,0}-\alpha_{\nu k,0}^{\dagger})]I \equiv -\hat{A}I, \qquad \text{(A.35)}
$$

where

$$
\mathcal{F}_{\nu k} = -\nu\frac{\mu_0}{2}\sqrt{2\gamma M_s}\frac{\sin(kw/2)}{kw/2}\mathcal{M}_{\nu k}\sqrt{1/k}. \qquad \text{(A.36)}
$$

Based on the linear response theory (Kubo formula), when we drive the current $I = I_0 e^{-i\omega t}$, the response of the field $\hat{h}_{\mathrm{d}}^{+} = \hat{h}_{\mathrm{d}}^{+}(\boldsymbol{\rho}_0; h_0)$ is given by

$$
\begin{aligned}
\delta\langle\hat{h}_{\mathrm{d}}^{+}(t)\rangle &= \chi_{h_{\mathrm{d}}^{+}A}(\omega)I_0e^{-i\omega t} && \text{(A.37)}\\
\chi_{h_{\mathrm{d}}^{+}A}(\omega) &= i\int_{-\infty}^{\infty} dt e^{i\omega t}\langle[\hat{h}_{\mathrm{d}}^{+}(t),\hat{A}(0)]\rangle_{\mathrm{eq}}\theta(t)\\
&= \int_0^{\infty} dk\left[\frac{L\mathcal{A}_{+k}\mathcal{F}_{+k}}{2\pi}\frac{i}{\omega-\omega_0(k)+i\epsilon}+\frac{L\mathcal{A}_{-k}\mathcal{F}_{-k}}{2\pi}\frac{i}{\omega+\omega_0(k)+i\epsilon}\right]e^{iky_0} && \text{(A.38)}\\
\frac{L\mathcal{A}_{\nu k}\mathcal{F}_{\nu k}}{2\pi} &= -\nu\omega_M\frac{\sin(kw/2)}{kw/2}\frac{\left(e^{-kd}\sinh kd\right)(\chi_0+2-\nu\kappa_0)(\chi_0+\nu\kappa_0)}{4\kappa_0}e^{-kh_0}, && \text{(A.39)}
\end{aligned}
$$

where $\langle\cdots\rangle_{\mathrm{eq}}$ represents the equilibrium average. This result is consistent with the classical calculation in ref.[138], where the field $H_{+}^{\mathrm{I}}(x,y)$ above the ferromagnetic film (equation (7),

(8) and (12) in ref.[138]) can be rewritten as (in our coordinate system)

$$H_{+}^{\mathrm{I}}(h_0+d/2,y_0)=H_x+iH_y=\int_0^{\infty}dk\frac{2iC_1(k)e^{-kh_0}}{\sqrt{2\pi}}e^{iky_0} \tag{A.40}$$

$$\frac{2iC_1(k)e^{-kh_0}}{\sqrt{2\pi}}=\left[\frac{L\mathcal{A}_{+k}\mathcal{F}_{+k}}{2\pi}\frac{i}{\omega-\omega_0(k)}+\frac{L\mathcal{A}_{-k}\mathcal{F}_{-k}}{2\pi}\frac{i}{\omega+\omega_0(k)}\right]I_0+\frac{iI_0}{2\pi}\frac{\sin(kw/2)}{kw/2}e^{-kh_0}, \tag{A.41}$$

where the last term corresponds to the field generated directly by the MSL.

A.0.3 Radiation resistance of the microstrip antenna due to the emission of MSSW

In this section, we show that the above Hamiltonian formalism of spin waves can successfully derive the radiation resistance due to the radiation of MSSW presented in various literatures [149]. To this end, we consider applying current $I=I_0(e^{-i\omega_{\mathrm{d}}t}+e^{+i\omega_{\mathrm{d}}t})\theta(t)$ in (A.35). From the Hamiltonian equation of motion, we obtain

$$\alpha_{\nu k,\mu}(t)=e^{-i\omega_\mu t}\alpha_{\nu k,\mu}(0)+I_0\mathcal{F}_{\nu k}\delta_{\mu,0}\int_0^t d\tau e^{-i\omega_\mu(t-\tau)}\left(e^{-i\omega_{\mathrm{d}}\tau}+e^{+i\omega_{\mathrm{d}}\tau}\right), \tag{A.42}$$

$$\alpha^*_{\nu k,\mu}(t)=e^{+i\omega_\mu t}\alpha^*_{\nu k,\mu}(0)+I_0\mathcal{F}_{\nu k}\delta_{\mu,0}\int_0^t d\tau e^{+i\omega_\mu(t-\tau)}\left(e^{-i\omega_{\mathrm{d}}\tau}+e^{+i\omega_{\mathrm{d}}\tau}\right). \tag{A.43}$$

Taking the long time limit $t\to\infty$ and assuming $\alpha_{\nu k,\mu}(0)=\alpha^*_{\nu k,\mu}(0)=0$, we obtain

$$\alpha_{\nu k,\mu}(t)=I_0\mathcal{F}_{\nu k}\delta_{\mu,0}e^{-i(\omega_\mu+\omega_{\mathrm{d}})t/2}\frac{\sin\left[\left(\omega_\mu-\omega_{\mathrm{d}}\right)t/2\right]}{\left(\omega_\mu-\omega_{\mathrm{d}}\right)/2}. \tag{A.44}$$

Now, the energy E_{F} radiated into the ferromagnet is

$$\begin{aligned}
E_{\mathrm{F}} &= \sum_{k,\nu,\mu} \omega_{\mu}(k)|\alpha_{\nu k,\mu}|^2, \\
&\to tL \int_0^{\infty} \frac{dk}{2\pi} \sum_{\nu=\pm 1} \omega_0(k)\left|I_0 \mathcal{F}_{\nu k}\right|^2 \delta\left(\omega_0(k)-\omega_{\mathrm{d}}\right), \\
&= tL \sum_{\nu=\pm 1} \frac{\omega_{\mathrm{d}}}{v_0\left(k_{\mathrm{d}}\right)}\left|I_0 \mathcal{F}_{\nu k_{\mathrm{d}}}\right|^2, \qquad \text{(A.45)}
\end{aligned}$$

where $t \to \infty$ is used in the second line, $k_{\mathrm{d}} \geq 0$ is the wavenumber of the on-resonant MSSW, i.e., $\omega_0(k_{\mathrm{d}}) = \omega_{\mathrm{d}}$, and $v_0(k) = d\omega_0(k)/dk$ is the MSSW group velocity. The radiation power per unit length is

$$P/L = E_{\mathrm{F}}/tL = \sum_{\nu=\pm 1} \frac{\omega_{\mathrm{d}}}{v_0\left(k_{\mathrm{d}}\right)}\left|I_0 \mathcal{F}_{\nu k_{\mathrm{d}}}\right|^2, \qquad \text{(A.46)}$$

and the radiation resistance per unit length is

$$\begin{aligned}
R/L &= \frac{P/L}{\bar{I}_0^2} = \frac{P/L}{2I_0^2}, \\
&= \sum_{\nu=\pm 1} \frac{\omega_{\mathrm{d}}}{2v_0\left(k_{\mathrm{d}}\right)}\left|\mathcal{F}_{\nu k_{\mathrm{d}}}\right|^2, \\
&= \frac{\mu_0 \omega_M}{4} \sum_{\nu=\pm 1} \frac{\omega_{\mathrm{d}}/k_{\mathrm{d}}}{v_0\left(k_{\mathrm{d}}\right)}\left|\mathcal{M}_{\nu k_{\mathrm{d}}}\right|^2 \left|\left(\frac{\sin k_{\mathrm{d}} w/2}{k_{\mathrm{d}} w/2}\right)\right|^2, \qquad \text{(A.47)}
\end{aligned}$$

where $\bar{I}_0 = \sqrt{2} I_0$ is the root-mean-square current [note that we have $I = 2I_0 \cos(\omega_{\mathrm{d}} t)$]. The radiation resistance we obtained in (A.47) is identical to that presented in [149] except that we are considering a specific geometry of the MSL.

Appendix B

Preparation of a diamond membrane with NV axis parallel to the diamond surface

In this appendix, we describe the preparation of the diamond membrane with NV axis [i.e., NV center's main symmetry axis, which is an equivalent direction to the (111) direction of the diamond] parallel to the diamond surface. The diamond membrane used in the experiments shown in Chapter 6 is cut out of a 2 mm × 2 mm × 0.5 mm diamond stone (electric grade, Sumitomo) with the top surface (001) and the side surfaces (110) and $(1\bar{1}0)$, where the bar above the number represents the negative direction (See Fig. B.1). The diamond membrane is laser cut and both the top and the bottom surfaces are polished (SYNTEK CO. LTD.). To remove the polishing damage, the diamond membrane goes through reactive-ion etching (RIE). After the RIE process, the diamond membrane is irradiated with nitrogen [^{15}N, 5 keV (on average ≈ 7.7 nm from the diamond surface based on the SRIM simulation), 10^{13} ions/cm^2 creating an ensemble NVs (≈ 2000 NV centers in a 1-μm-diameter focused laser spot) with a 7° tilt of the nitrogen implantation angle]. After the nitrogen implantation, the sample goes through tri-acid etching to maintain the surface clenliness, annealing [1200

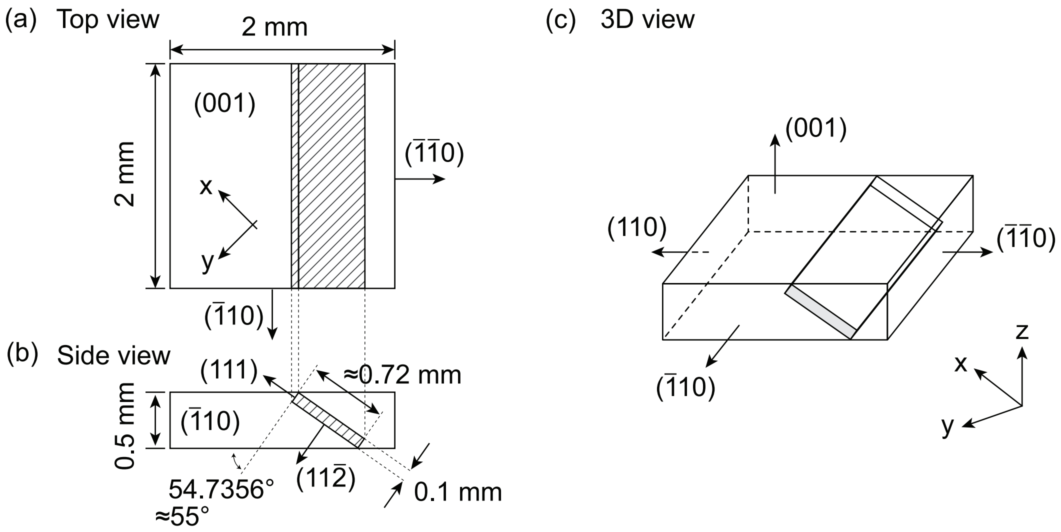

Figure B.1: (a) Top view of a 2 mm × 2 mm × 0.5 mm diamond stone. The shaded area represents the part that will be cut into a diamond membrane. (b) Side view of the diamond stone. (c) Three-dimensional view of the diamond stone.

°C in argon forming gas (95% argon, 5% H_2)], and tri-acid etching again to remove the graphitized layer.

References

[1] Masaya Fukami, Jonathan Karsch, Leah Weiss, and David D. Awschalom. Surface-magnon mediated self interaction of spin qubits in diamond revealed by longitudinal relaxometry. *in preparation*, 2022.

[2] Masaya Fukami, Denis R. Candido, David D. Awschalom, and Michael E. Flatté. Opportunities for long-range magnon-mediated entanglement of spin qubits via on- and off-resonant coupling. *PRX Quantum*, 2:040314, Oct 2021.

[3] Brian B. Zhou, Paul C. Jerger, Kan-Heng Lee, Masaya Fukami, Fauzia Mujid, Jiwoong Park, and David D. Awschalom. Spatiotemporal mapping of a photocurrent vortex in monolayer mos$_2$ using diamond quantum sensors. *Phys. Rev. X*, 10:011003, Jan 2020.

[4] M. Fukami, C.G. Yale, P. Andrich, X. Liu, F.J. Heremans, P.F. Nealey, and D.D. Awschalom. All-optical cryogenic thermometry based on nitrogen-vacancy centers in nanodiamonds. *Phys. Rev. Applied*, 12:014042, Jul 2019.

[5] Emanuel Knill, Raymond Laflamme, and Gerald J Milburn. A scheme for efficient quantum computation with linear optics. *nature*, 409(6816):46–52, 2001.

[6] Dik Bouwmeester, Jian-Wei Pan, Klaus Mattle, Manfred Eibl, Harald Weinfurter, and Anton Zeilinger. Experimental quantum teleportation. *Nature*, 390(6660):575–579, 1997.

[7] Akira Furusawa, Jens Lykke Sørensen, Samuel L Braunstein, Christopher A Fuchs,

H Jeff Kimble, and Eugene S Polzik. Unconditional quantum teleportation. *science*, 282(5389):706–709, 1998.

[8] J. I. Cirac and P. Zoller. Quantum computations with cold trapped ions. *Phys. Rev. Lett.*, 74:4091–4094, May 1995.

[9] Steven Olmschenk, DN Matsukevich, P Maunz, D Hayes, L-M Duan, and C Monroe. Quantum teleportation between distant matter qubits. *Science*, 323(5913):486–489, 2009.

[10] Jiehang Zhang, Guido Pagano, Paul W Hess, Antonis Kyprianidis, Patrick Becker, Harvey Kaplan, Alexey V Gorshkov, Z-X Gong, and Christopher Monroe. Observation of a many-body dynamical phase transition with a 53-qubit quantum simulator. *Nature*, 551(7682):601–604, 2017.

[11] Marco Anderlini, Patricia J Lee, Benjamin L Brown, Jennifer Sebby-Strabley, William D Phillips, and James V Porto. Controlled exchange interaction between pairs of neutral atoms in an optical lattice. *Nature*, 448(7152):452–456, 2007.

[12] Alpha Gaetan, Yevhen Miroshnychenko, Tatjana Wilk, Amodsen Chotia, Matthieu Viteau, Daniel Comparat, Pierre Pillet, Antoine Browaeys, and Philippe Grangier. Observation of collective excitation of two individual atoms in the rydberg blockade regime. *Nature Physics*, 5(2):115–118, 2009.

[13] Hannes Bernien, Sylvain Schwartz, Alexander Keesling, Harry Levine, Ahmed Omran, Hannes Pichler, Soonwon Choi, Alexander S Zibrov, Manuel Endres, Markus Greiner, et al. Probing many-body dynamics on a 51-atom quantum simulator. *Nature*, 551(7682):579–584, 2017.

[14] Yasunobu Nakamura, Yu A Pashkin, and JS Tsai. Coherent control of macroscopic quantum states in a single-cooper-pair box. *nature*, 398(6730):786–788, 1999.

[15] Andreas Wallraff, David I Schuster, Alexandre Blais, Luigi Frunzio, R-S Huang, Johannes Majer, Sameer Kumar, Steven M Girvin, and Robert J Schoelkopf. Strong coupling of a single photon to a superconducting qubit using circuit quantum electrodynamics. *Nature*, 431(7005):162–167, 2004.

[16] Frank Arute, Kunal Arya, Ryan Babbush, Dave Bacon, Joseph C Bardin, Rami Barends, Rupak Biswas, Sergio Boixo, Fernando GSL Brandao, David A Buell, et al. Quantum supremacy using a programmable superconducting processor. *Nature*, 574(7779):505–510, 2019.

[17] Daniel Loss and David P. DiVincenzo. Quantum computation with quantum dots. *Phys. Rev. A*, 57:120–126, Jan 1998.

[18] Ilya Fushman, Dirk Englund, Andrei Faraon, Nick Stoltz, Pierre Petroff, and Jelena Vuckovic. Controlled phase shifts with a single quantum dot. *science*, 320(5877):769–772, 2008.

[19] Mete Atature, Jan Dreiser, Antonio Badolato, Alexander Hogele, Khaled Karrai, and Atac Imamoglu. Quantum-dot spin-state preparation with near-unity fidelity. *Science*, 312(5773):551–553, 2006.

[20] Neil A Gershenfeld and Isaac L Chuang. Bulk spin-resonance quantum computation. *science*, 275(5298):350–356, 1997.

[21] A Gruber, A Drabenstedt, C Tietz, L Fleury, J Wrachtrup, and C von Borczyskowski. Scanning confocal optical microscopy and magnetic resonance on single defect centers. *Science*, 276(5321):2012–2014, 1997.

[22] Bas Hensen, Hannes Bernien, Anaïs E Dréau, Andreas Reiserer, Norbert Kalb, Machiel S Blok, Just Ruitenberg, Raymond FL Vermeulen, Raymond N Schouten, Carlos Abellán, et al. Loophole-free bell inequality violation using electron spins separated by 1.3 kilometres. *Nature*, 526(7575):682–686, 2015.

[23] Michael A Nielsen and Isaac Chuang. Quantum computation and quantum information, 2002.

[24] Asher Peres. Separability criterion for density matrices. *Physical Review Letters*, 77(8):1413, 1996.

[25] John S Bell. On the einstein podolsky rosen paradox. *Physics Physique Fizika*, 1(3):195, 1964.

[26] John F. Clauser, Michael A. Horne, Abner Shimony, and Richard A. Holt. Proposed experiment to test local hidden-variable theories. *Phys. Rev. Lett.*, 23:880–884, Oct 1969.

[27] Alain Aspect, Jean Dalibard, and Gérard Roger. Experimental test of bell's inequalities using time-varying analyzers. *Phys. Rev. Lett.*, 49:1804–1807, Dec 1982.

[28] Mary A Rowe, David Kielpinski, Volker Meyer, Charles A Sackett, Wayne M Itano, Christopher Monroe, and David J Wineland. Experimental violation of a bell's inequality with efficient detection. *Nature*, 409(6822):791–794, 2001.

[29] Markus Ansmann, H Wang, Radoslaw C Bialczak, Max Hofheinz, Erik Lucero, Matthew Neeley, Aaron D O'Connell, Daniel Sank, Martin Weides, James Wenner, et al. Violation of Bell's inequality in Josephson phase qubits. *Nature*, 461(7263):504–506, 2009.

[30] Julian Hofmann, Michael Krug, Norbert Ortegel, Lea Gérard, Markus Weber, Wenjamin Rosenfeld, and Harald Weinfurter. Heralded entanglement between widely separated atoms. *Science*, 337(6090):72–75, 2012.

[31] Peter W Shor. Polynomial-time algorithms for prime factorization and discrete logarithms on a quantum computer. *SIAM review*, 41(2):303–332, 1999.

[32] Lov K Grover. A fast quantum mechanical algorithm for database search. In *Proceedings of the twenty-eighth annual ACM symposium on Theory of computing*, pages 212–219, 1996.

[33] Edward Farhi, Jeffrey Goldstone, and Sam Gutmann. A quantum approximate optimization algorithm. *arXiv preprint arXiv:1411.4028*, 2014.

[34] Matthew P Harrigan, Kevin J Sung, Matthew Neeley, Kevin J Satzinger, Frank Arute, Kunal Arya, Juan Atalaya, Joseph C Bardin, Rami Barends, Sergio Boixo, et al. Quantum approximate optimization of non-planar graph problems on a planar superconducting processor. *Nature Physics*, 17(3):332–336, 2021.

[35] Peter W. Shor and John Preskill. Simple proof of security of the bb84 quantum key distribution protocol. *Phys. Rev. Lett.*, 85:441–444, Jul 2000.

[36] Charles H. Bennett, Gilles Brassard, Claude Crépeau, Richard Jozsa, Asher Peres, and William K. Wootters. Teleporting an unknown quantum state via dual classical and einstein-podolsky-rosen channels. *Phys. Rev. Lett.*, 70:1895–1899, Mar 1993.

[37] Charles H. Bennett and Stephen J. Wiesner. Communication via one- and two-particle operators on einstein-podolsky-rosen states. *Phys. Rev. Lett.*, 69:2881–2884, Nov 1992.

[38] C. L. Degen, F. Reinhard, and P. Cappellaro. Quantum sensing. *Rev. Mod. Phys.*, 89:035002, Jul 2017.

[39] Matteo Pompili, Sophie LN Hermans, Simon Baier, Hans KC Beukers, Peter C Humphreys, Raymond N Schouten, Raymond FL Vermeulen, Marijn J Tiggelman, Laura dos Santos Martins, Bas Dirkse, et al. Realization of a multinode quantum network of remote solid-state qubits. *Science*, 372(6539):259–264, 2021.

[40] Peter C. Humphreys, Norbert Kalb, Jaco P. J. Morits, Raymond N. Schouten, Raymond F. L. Vermeulen, Daniel J. Twitchen, Matthew Markham, and Ronald Han-

son. Deterministic delivery of remote entanglement on a quantum network. *Nature*, 558(7709):268–273, 2018.

[41] Andreas Reiserer, Norbert Kalb, Machiel S. Blok, Koen J. M. van Bemmelen, Tim H. Taminiau, Ronald Hanson, Daniel J. Twitchen, and Matthew Markham. Robust quantum-network memory using decoherence-protected subspaces of nuclear spins. *Phys. Rev. X*, 6:021040, Jun 2016.

[42] Robert Beals, Stephen Brierley, Oliver Gray, Aram W Harrow, Samuel Kutin, Noah Linden, Dan Shepherd, and Mark Stather. Efficient distributed quantum computing. *Proceedings of the Royal Society A: Mathematical, Physical and Engineering Sciences*, 469(2153):20120686, 2013.

[43] Michael A Perlin, Zhen-Yu Wang, Jorge Casanova, and Martin B Plenio. Noise-resilient architecture of a hybrid electron-nuclear quantum register in diamond. *Quantum Science and Technology*, 4(1):015007, sep 2018.

[44] CE Bradley, SW de Bone, PFW Moller, S Baier, MJ Degen, SJH Loenen, HP Bartling, M Markham, DJ Twitchen, R Hanson, et al. Robust quantum-network memory based on spin qubits in isotopically engineered diamond. *arXiv preprint arXiv:2111.09772*, 2021.

[45] Xueshi Guo, Casper R Breum, Johannes Borregaard, Shuro Izumi, Mikkel V Larsen, Tobias Gehring, Matthias Christandl, Jonas S Neergaard-Nielsen, and Ulrik L Andersen. Distributed quantum sensing in a continuous-variable entangled network. *Nature Physics*, 16(3):281–284, 2020.

[46] Li-Zheng Liu, Yu-Zhe Zhang, Zheng-Da Li, Rui Zhang, Xu-Fei Yin, Yue-Yang Fei, Li Li, Nai-Le Liu, Feihu Xu, Yu-Ao Chen, et al. Distributed quantum phase estimation with entangled photons. *Nature Photonics*, 15(2):137–142, 2021.

[47] Christopher D Wilen, S Abdullah, NA Kurinsky, C Stanford, L Cardani, G d'Imperio, C Tomei, L Faoro, LB Ioffe, CH Liu, et al. Correlated charge noise and relaxation errors in superconducting qubits. *Nature*, 594(7863):369–373, 2021.

[48] Marcus W Doherty, Neil B Manson, Paul Delaney, and Lloyd CL Hollenberg. The negatively charged nitrogen-vacancy centre in diamond: the electronic solution. *New Journal of Physics*, 13(2):025019, 2011.

[49] Jeronimo R Maze, Adam Gali, Emre Togan, Yiwen Chu, Alexei Trifonov, Efthimios Kaxiras, and Mikhail D Lukin. Properties of nitrogen-vacancy centers in diamond: the group theoretic approach. *New Journal of Physics*, 13(2):025025, 2011.

[50] Peter Christian Maurer, Georg Kucsko, Christian Latta, Liang Jiang, Norman Ying Yao, Steven D Bennett, Fernando Pastawski, David Hunger, Nicholas Chisholm, Matthew Markham, et al. Room-temperature quantum bit memory exceeding one second. *Science*, 336(6086):1283–1286, 2012.

[51] Nir Bar-Gill, Linh M Pham, Andrejs Jarmola, Dmitry Budker, and Ronald L Walsworth. Solid-state electronic spin coherence time approaching one second. *Nat. Commun.*, 4(1):1743, 2013.

[52] A. Jarmola, V. M. Acosta, K. Jensen, S. Chemerisov, and D. Budker. Temperature- and magnetic-field-dependent longitudinal spin relaxation in nitrogen-vacancy ensembles in diamond. *Phys. Rev. Lett.*, 108:197601, May 2012.

[53] T. Rosskopf, A. Dussaux, K. Ohashi, M. Loretz, R. Schirhagl, H. Watanabe, S. Shikata, K. M. Itoh, and C. L. Degen. Investigation of surface magnetic noise by shallow spins in diamond. *Phys. Rev. Lett.*, 112:147602, Apr 2014.

[54] E D Herbschleb, H Kato, Y Maruyama, T Danjo, T Makino, S Yamasaki, I Ohki, K Hayashi, H Morishita, M Fujiwara, et al. Ultra-long coherence times amongst room-temperature solid-state spins. *Nat. Commun.*, 10(1):3766, 2019.

[55] Giuseppe Grosso and Giuseppe Pastori Parravicini. *Solid state physics*. Academic press, 2013.

[56] Piers Coleman. *Introduction to many-body physics*. Cambridge University Press, 2015.

[57] Michael E Peskin. *An introduction to quantum field theory*. CRC press, 2018.

[58] Jørgen Rammer. Quantum field theory of non-equilibrium states. *Quantum Field Theory of Non-equilibrium States*, 2011.

[59] Alexei Alexeyevich Abrikosov, Lev Petrovich Gorkov, and Igor Ekhielevich Dzyaloshinski. *Methods of quantum field theory in statistical physics*. Courier Corporation, 2012.

[60] Alexander L Fetter and John Dirk Walecka. *Quantum theory of many-particle systems*. Courier Corporation, 2012.

[61] Heinz-Peter Breuer, Francesco Petruccione, et al. *The theory of open quantum systems*. Oxford University Press on Demand, 2002.

[62] Girish S Agarwal. *Quantum optics*. Cambridge University Press, 2012.

[63] Jiaxuan Wang, Hui Dong, and Sheng-Wen Li. Magnetic dipole-dipole interaction induced by the electromagnetic field. *Phys. Rev. A*, 97:013819, Jan 2018.

[64] Z. Ficek, R. Tanaś, and S. Kielich. Quantum beats and superradiant effects in the spontaneous emission from two nonidentical atoms. *Physica A: Statistical Mechanics and its Applications*, 146(3):452–482, 1987.

[65] K Uchida, S Takahashi, K Harii, J Ieda, W Koshibae, Kazuya Ando, S Maekawa, and E Saitoh. Observation of the spin seebeck effect. *Nature*, 455(7214):778–781, 2008.

[66] CM Jaworski, J Yang, S Mack, DD Awschalom, RC Myers, and JP Heremans. Spin-seebeck effect: A phonon driven spin distribution. *Physical review letters*, 106(18):186601, 2011.

[67] Michael Schreier, Akashdeep Kamra, Mathias Weiler, Jiang Xiao, Gerrit E. W. Bauer, Rudolf Gross, and Sebastian T. B. Goennenwein. Magnon, phonon, and electron temperature profiles and the spin seebeck effect in magnetic insulator/normal metal hybrid structures. *Phys. Rev. B*, 88:094410, Sep 2013.

[68] Brandon L. Giles, Zihao Yang, John S. Jamison, Juan M. Gomez-Perez, Saül Vélez, Luis E. Hueso, Fèlix Casanova, and Roberto C. Myers. Thermally driven long-range magnon spin currents in yttrium iron garnet due to intrinsic spin seebeck effect. *Phys. Rev. B*, 96:180412, Nov 2017.

[69] Arati Prakash, Benedetta Flebus, Jack Brangham, Fengyuan Yang, Yaroslav Tserkovnyak, and Joseph P. Heremans. Evidence for the role of the magnon energy relaxation length in the spin seebeck effect. *Phys. Rev. B*, 97:020408, Jan 2018.

[70] Gang-Qin Liu, Xi Feng, Ning Wang, Quan Li, and Ren-Bao Liu. Coherent quantum control of nitrogen-vacancy center spins near 1000 kelvin. *Nature communications*, 10(1):1–8, 2019.

[71] Paolo Andrich, Jiajing Li, Xiaoying Liu, F Joseph Heremans, Paul F Nealey, and David D Awschalom. Microscale-resolution thermal mapping using a flexible platform of patterned quantum sensors. *Nano Letters*, 18(8):4684–4690, 2018.

[72] Paolo Andrich, F. Charles, Xiaoying Liu, Hope L. Bretscher, Jonson R. Berman, F. Joseph Heremans, Paul F. Nealey, and David D. Awschalom. Long-range spin wave mediated control of defect qubits in nanodiamonds. *npj Quantum Inf.*, 3(1):28, 2017.

[73] X-D Chen, C-H Dong, F-W Sun, C-L Zou, J-M Cui, Z-F Han, and G-C Guo. Temperature dependent energy level shifts of nitrogen-vacancy centers in diamond. *Applied Physics Letters*, 99(16):161903, 2011.

[74] Taras Plakhotnik, Haroon Aman, and Huan-Cheng Chang. All-optical single-nanoparticle ratiometric thermometry with a noise floor of 0.3 k hz- 1/2. *Nanotechnology*, 26(24):245501, 2015.

[75] Taras Plakhotnik, Marcus W Doherty, Jared H Cole, Robert Chapman, and Neil B Manson. All-optical thermometry and thermal properties of the optically detected spin resonances of the NV^--center in nanodiamond. *Nano letters*, 14(9):4989–4996, 2014.

[76] Christian T Nguyen, Ruffin E Evans, Alp Sipahigil, Mihir K Bhaskar, Denis D Sukachev, Viatcheslav N Agafonov, Valery A Davydov, Liudmila F Kulikova, Fedor Jelezko, and Mikhail D Lukin. All-optical nanoscale thermometry with silicon-vacancy centers in diamond. *Applied Physics Letters*, 112(20):203102, 2018.

[77] Masfer Alkahtani, Ivan Cojocaru, Xiaohan Liu, Tobias Herzig, Jan Meijer, Johannes Küpper, Tobias Lühmann, Alexey V Akimov, and Philip R Hemmer. Tin-vacancy in diamonds for luminescent thermometry. *Applied Physics Letters*, 112(24):241902, 2018.

[78] Jing-Wei Fan, Ivan Cojocaru, Joe Becker, Ilya V Fedotov, Masfer Hassan A Alkahtani, Abdulrahman Alajlan, Sean Blakley, Mohammadreza Rezaee, Anna Lyamkina, Yuri N Palyanov, et al. Germanium-vacancy color center in diamond as a temperature sensor. *ACS Photonics*, 5(3):765–770, 2018.

[79] Toan Trong Tran, Blake Regan, Evgeny A Ekimov, Zhao Mu, Yu Zhou, Wei-bo Gao, Prineha Narang, Alexander S Solntsev, Milos Toth, Igor Aharonovich, et al. Anti-stokes excitation of solid-state quantum emitters for nanoscale thermometry. *Science advances*, 5(5):eaav9180, 2019.

[80] Pei-Chang Tsai, Chandra P Epperla, Jo-Shan Huang, Oliver Y Chen, Chih-Che Wu, and Huan-Cheng Chang. Measuring nanoscale thermostability of cell membranes

with single gold–diamond nanohybrids. *Angewandte Chemie International Edition*, 56(11):3025–3030, 2017.

[81] D. B. Fitchen, R. H. Silsbee, T. A. Fulton, and E. L. Wolf. Zero-phonon transitions of color centers in alkali halides. *Phys. Rev. Lett.*, 11:275–277, Sep 1963.

[82] Thomas H. Keil. Shapes of impurity absorption bands in solids. *Phys. Rev.*, 140:A601–A617, Oct 1965.

[83] Kyongmo An, Kevin S. Olsson, Annie Weathers, Sean Sullivan, Xi Chen, Xiang Li, Luke G. Marshall, Xin Ma, Nikita Klimovich, Jianshi Zhou, et al. Magnons and phonons optically driven out of local equilibrium in a magnetic insulator. *Phys. Rev. Lett.*, 117:107202, Aug 2016.

[84] Adam Gali. Theory of the neutral nitrogen-vacancy center in diamond and its application to the realization of a qubit. *Physical Review B*, 79(23):235210, 2009.

[85] S. Felton, A. M. Edmonds, M. E. Newton, P. M. Martineau, D. Fisher, and D. J. Twitchen. Electron paramagnetic resonance studies of the neutral nitrogen vacancy in diamond. *Phys. Rev. B*, 77:081201, Feb 2008.

[86] Nabeel Aslam, Gerhald Waldherr, Philipp Neumann, Fedor Jelezko, and Joerg Wrachtrup. Photo-induced ionization dynamics of the nitrogen vacancy defect in diamond investigated by single-shot charge state detection. *New Journal of Physics*, 15(1):013064, 2013.

[87] David A Hopper, Richard R Grote, Samuel M Parks, and Lee C Bassett. Amplified sensitivity of nitrogen-vacancy spins in nanodiamonds using all-optical charge readout. *ACS nano*, 12(5):4678–4686, 2018.

[88] Xiang-Dong Chen, Shen Li, Ao Shen, Yang Dong, Chun-Hua Dong, Guang-Can Guo, and Fang-Wen Sun. Near-infrared-enhanced charge-state conversion for low-power

optical nanoscopy with nitrogen-vacancy centers in diamond. *Phys. Rev. Applied*, 7:014008, Jan 2017.

[89] Xiang-Dong Chen, Lei-Ming Zhou, Chang-Ling Zou, Cong-Cong Li, Yang Dong, Fang-Wen Sun, and Guang-Can Guo. Spin depolarization effect induced by charge state conversion of nitrogen vacancy center in diamond. *Phys. Rev. B*, 92:104301, Sep 2015.

[90] Hu Yang, Quang Trong Nguyen, YaDi Ding, YingCai Long, and Zhenghua Ping. Investigation of poly (dimethyl siloxane)(pdms)–solvent interactions by dsc. *Journal of Membrane Science*, 164(1-2):37–43, 2000.

[91] James E Mark. Overview of siloxane polymers. 2000.

[92] John D. Dow and David Redfield. Toward a unified theory of urbach's rule and exponential absorption edges. *Phys. Rev. B*, 5:594–610, Jan 1972.

[93] Gordon Davies. The jahn-teller effect and vibronic coupling at deep levels in diamond. *Reports on Progress in Physics*, 44(7):787, 1981.

[94] SO Hruszkewycz, W Cha, P Andrich, CP Anderson, A Ulvestad, R Harder, PH Fuoss, DD Awschalom, and FJ Heremans. In situ study of annealing-induced strain relaxation in diamond nanoparticles using bragg coherent diffraction imaging. *APL Materials*, 5(2):026105, 2017.

[95] Elizabeth A Donley and Taras Plakhotnik. Statistics for single molecule spectroscopy data. *Single Molecules*, 2(1):23–30, 2001.

[96] Georg Kucsko, Peter C Maurer, Norman Ying Yao, MICHAEL Kubo, Hyun Jong Noh, Po Kam Lo, Hongkun Park, and Mikhail D Lukin. Nanometre-scale thermometry in a living cell. *Nature*, 500(7460):54–58, 2013.

[97] V. M. Acosta, E. Bauch, M. P. Ledbetter, A. Waxman, L.-S. Bouchard, and D. Budker. Temperature dependence of the nitrogen-vacancy magnetic resonance in diamond. *Phys. Rev. Lett.*, 104:070801, Feb 2010.

[98] Philipp Neumann, Ingmar Jakobi, Florian Dolde, Christian Burk, Rolf Reuter, Gerald Waldherr, Jan Honert, Thomas Wolf, Andreas Brunner, Jeong Hyun Shim, et al. High-precision nanoscale temperature sensing using single defects in diamond. *Nano letters*, 13(6):2738–2742, 2013.

[99] David M Toyli, F Charles, David J Christle, Viatcheslav V Dobrovitski, and David D Awschalom. Fluorescence thermometry enhanced by the quantum coherence of single spins in diamond. *Proceedings of the National Academy of Sciences*, 110(21):8417–8421, 2013.

[100] Ning Wang, Gang-Qin Liu, Weng-Hang Leong, Hualing Zeng, Xi Feng, Si-Hong Li, Florian Dolde, Helmut Fedder, Jörg Wrachtrup, Xiao-Dong Cui, Sen Yang, Quan Li, and Ren-Bao Liu. Magnetic criticality enhanced hybrid nanodiamond thermometer under ambient conditions. *Phys. Rev. X*, 8:011042, Mar 2018.

[101] M. W. Doherty, V. M. Acosta, A. Jarmola, M. S. J. Barson, N. B. Manson, D. Budker, and L. C. L. Hollenberg. Temperature shifts of the resonances of the nv^- center in diamond. *Phys. Rev. B*, 90:041201, Jul 2014.

[102] AT Collins, MF Thomaz, and Maria Isabel B Jorge. Luminescence decay time of the 1.945 ev centre in type ib diamond. *Journal of Physics C: Solid State Physics*, 16(11):2177, 1983.

[103] Taras Plakhotnik and Daniel Gruber. Luminescence of nitrogen-vacancy centers in nanodiamonds at temperatures between 300 and 700 k: perspectives on nanothermometry. *Physical Chemistry Chemical Physics*, 12(33):9751–9756, 2010.

[104] D. M. Toyli, D. J. Christle, A. Alkauskas, B. B. Buckley, C. G. Van de Walle, and D. D. Awschalom. Measurement and control of single nitrogen-vacancy center spins above 600 k. *Phys. Rev. X*, 2:031001, Jul 2012.

[105] Chris S Wolfe, Vidya P Bhallamudi, Hilong L Wang, Chunhui H Du, Sergei Manuilov, RM Teeling-Smith, AJ Berger, R Adur, FY Yang, and Peter Christopher Hammel. Off-resonant manipulation of spins in diamond via precessing magnetization of a proximal ferromagnet. *Physical Review B*, 89(18):180406, 2014.

[106] Chunhui Du, Toeno Van der Sar, Tony X Zhou, Pramey Upadhyaya, Francesco Casola, Huiliang Zhang, Mehmet C Onbasli, Caroline A Ross, Ronald L Walsworth, Yaroslav Tserkovnyak, et al. Control and local measurement of the spin chemical potential in a magnetic insulator. *Science*, 357(6347):195–198, 2017.

[107] Ken-ichi Uchida, Shunsuke Daimon, Ryo Iguchi, and Eiji Saitoh. Observation of anisotropic magneto-peltier effect in nickel. *Nature*, 558(7708):95–99, 2018.

[108] J. Flipse, F. K. Dejene, D. Wagenaar, G. E. W. Bauer, J. Ben Youssef, and B. J. van Wees. Observation of the spin peltier effect for magnetic insulators. *Phys. Rev. Lett.*, 113:027601, Jul 2014.

[109] Shunsuke Daimon, Ryo Iguchi, Tomosato Hioki, Eiji Saitoh, and Ken-ichi Uchida. Thermal imaging of spin peltier effect. *Nature communications*, 7(1):1–7, 2016.

[110] F. Jelezko, T. Gaebel, I. Popa, A. Gruber, and J. Wrachtrup. Observation of coherent oscillations in a single electron spin. *Phys. Rev. Lett.*, 92:076401, Feb 2004.

[111] Torsten Gaebel, Michael Domhan, Iulian Popa, Christoffer Wittmann, Philipp Neumann, Fedor Jelezko, James R Rabeau, Nikolas Stavrias, Andrew D Greentree, Steven Prawer, et al. Room-temperature coherent coupling of single spins in diamond. *Nat. Phys.*, 2(6):408–413, 2006.

[112] R. Hanson, F. M. Mendoza, R. J. Epstein, and D. D. Awschalom. Polarization and readout of coupled single spins in diamond. *Phys. Rev. Lett.*, 97:087601, Aug 2006.

[113] R. Hanson, V. V. Dobrovitski, A. E. Feiguin, O. Gywat, and D. D. Awschalom. Coherent dynamics of a single spin interacting with an adjustable spin bath. *Science*, 320(5874):352–355, 2008.

[114] G. D. Fuchs, V. V. Dobrovitski, D. M. Toyli, F. J. Heremans, and D. D. Awschalom. Gigahertz dynamics of a strongly driven single quantum spin. *Science*, 326(5959):1520–1522, 2009.

[115] J. M. Taylor, Paola Cappellaro, L. Childress, Liang Jiang, Dmitry Budker, P. R. Hemmer, Amir Yacoby, R. Walsworth, and M. D. Lukin. High-sensitivity diamond magnetometer with nanoscale resolution. *Nat. Phys.*, 4(10):810–816, 2008.

[116] A. Sipahigil, M. L. Goldman, E. Togan, Y. Chu, M. Markham, D. J. Twitchen, A. S. Zibrov, A. Kubanek, and M. D. Lukin. Quantum interference of single photons from remote nitrogen-vacancy centers in diamond. *Phys. Rev. Lett.*, 108:143601, Apr 2012.

[117] Hannes Bernien, Bas Hensen, Wolfgang Pfaff, Gerwin Koolstra, Machiel S. Blok, Lucio Robledo, T H Taminiau, Matthew Markham, Daniel J Twitchen, Lilian Childress, et al. Heralded entanglement between solid-state qubits separated by three metres. *Nature*, 497(7447):86–90, 2013.

[118] W. Pfaff, B. J. Hensen, H. Bernien, S. B. van Dam, M. S. Blok, T. H. Taminiau, M. J. Tiggelman, R. N. Schouten, M. Markham, D. J. Twitchen, et al. Unconditional quantum teleportation between distant solid-state quantum bits. *Science*, 345(6196):532–535, 2014.

[119] Francesco Casola, Toeno van der Sar, and Amir Yacoby. Probing condensed matter physics with magnetometry based on nitrogen-vacancy centres in diamond. *Nature Reviews Materials*, 3(1):17088, 2018.

[120] David D Awschalom, Ronald Hanson, Jörg Wrachtrup, and Brian B Zhou. Quantum technologies with optically interfaced solid-state spins. *Nat. Photonics*, 12(9):516–527, 2018.

[121] T. Mittiga, S. Hsieh, C. Zu, B. Kobrin, F. Machado, P. Bhattacharyya, N. Z. Rui, A. Jarmola, S. Choi, D. Budker, et al. Imaging the local charge environment of nitrogen-vacancy centers in diamond. *Phys. Rev. Lett.*, 121:246402, Dec 2018.

[122] H. P. Bartling, M. H. Abobeih, B. Pingault, M. J. Degen, S. J. H. Loenen, C. E. Bradley, J. Randall, M. Markham, D. J. Twitchen, and T. H. Taminiau. Coherence and entanglement of inherently long-lived spin pairs in diamond. *arXiv:2103.07961*, 2021.

[123] F. Jelezko, T. Gaebel, I. Popa, M. Domhan, A. Gruber, and J. Wrachtrup. Observation of coherent oscillation of a single nuclear spin and realization of a two-qubit conditional quantum gate. *Phys. Rev. Lett.*, 93:130501, Sep 2004.

[124] L. Childress, M. V. Gurudev Dutt, J. M. Taylor, A. S. Zibrov, F. Jelezko, J. Wrachtrup, P. R. Hemmer, and M. D. Lukin. Coherent dynamics of coupled electron and nuclear spin qubits in diamond. *Science*, 314(5797):281–285, 2006.

[125] P. Neumann, N. Mizuochi, F. Rempp, P. Hemmer, H. Watanabe, S. Yamasaki, V. Jacques, T. Gaebel, F. Jelezko, and J. Wrachtrup. Multipartite entanglement among single spins in diamond. *Science*, 320(5881):1326–1329, 2008.

[126] P. Neumann, R. Kolesov, B. Naydenov, J. Beck, F. Rempp, M. Steiner, V. Jacques, G. Balasubramanian, M. L. Markham, D. J. Twitchen, et al. Quantum register based on coupled electron spins in a room-temperature solid. *Nat. Phys.*, 6(4):249–253, 2010.

[127] T van der Sar, Z. H. Wang, M. S. Blok, H. Bernien, T. H. Taminiau, D. M. Toyli, D. A. Lidar, D. D. Awschalom, R. Hanson, and V. V. Dobrovitski. Decoherence-protected quantum gates for a hybrid solid-state spin register. *Nature*, 484(7392):82–86, 2012.

[128] Florian Dolde, Ingmar Jakobi, Boris Naydenov, Nan Zhao, Sebastien Pezzagna, Christina Trautmann, Jan Meijer, Philipp Neumann, Fedor Jelezko, and Jörg Wrachtrup. Room-temperature entanglement between single defect spins in diamond. *Nat. Phys.*, 9(3):139–143, 2013.

[129] David M. Toyli, Christoph D. Weis, Gregory D. Fuchs, Thomas Schenkel, and David D. Awschalom. Chip-scale nanofabrication of single spins and spin arrays in diamond. *Nano Lett.*, 10(8):3168–3172, 2010.

[130] Peng-Bo Li, Yong-Chun Liu, S.-Y. Gao, Ze-Liang Xiang, Peter Rabl, Yun-Feng Xiao, and Fu-Li Li. Hybrid quantum device based on NV centers in diamond nanomechanical resonators plus superconducting waveguide cavities. *Phys. Rev. Applied*, 4:044003, Oct 2015.

[131] Peng-Bo Li, Ze-Liang Xiang, Peter Rabl, and Franco Nori. Hybrid quantum device with nitrogen-vacancy centers in diamond coupled to carbon nanotubes. *Phys. Rev. Lett.*, 117:015502, Jun 2016.

[132] M.-A. Lemonde, S. Meesala, A. Sipahigil, M. J. A. Schuetz, M. D. Lukin, M. Loncar, and P. Rabl. Phonon networks with silicon-vacancy centers in diamond waveguides. *Phys. Rev. Lett.*, 120:213603, May 2018.

[133] Peng-Bo Li and Franco Nori. Hybrid quantum system with nitrogen-vacancy centers in diamond coupled to surface-phonon polaritons in piezomagnetic superlattices. *Phys. Rev. Applied*, 10:024011, Aug 2018.

[134] D. A. Lidar, I. L. Chuang, and K. B. Whaley. Decoherence-free subspaces for quantum computation. *Phys. Rev. Lett.*, 81:2594–2597, Sep 1998.

[135] Luka Trifunovic, Fabio L. Pedrocchi, and Daniel Loss. Long-distance entanglement of spin qubits via ferromagnet. *Phys. Rev. X*, 3:041023, Dec 2013.

[136] B. Flebus and Y. Tserkovnyak. Quantum-impurity relaxometry of magnetization dynamics. *Phys. Rev. Lett.*, 121:187204, Nov 2018.

[137] B. Flebus and Y. Tserkovnyak. Entangling distant spin qubits via a magnetic domain wall. *Phys. Rev. B*, 99:140403, Apr 2019.

[138] Clara Mühlherr, V. O. Shkolnikov, and Guido Burkard. Magnetic resonance in defect spins mediated by spin waves. *Phys. Rev. B*, 99:195413, May 2019.

[139] Ji Zou, Se Kwon Kim, and Yaroslav Tserkovnyak. Tuning entanglement by squeezing magnons in anisotropic magnets. *Phys. Rev. B*, 101:014416, Jan 2020.

[140] Denis R. Candido, Gregory D. Fuchs, Ezekiel Johnston-Halperin, and Michael E Flatté. Predicted strong coupling of solid-state spins via a single magnon mode. *Mat. Quantum Technol.*, 1(1):011001, dec 2021.

[141] T. Neuman, Derek S. Wang, and Prineha Narang. Nanomagnonic cavities for strong spin-magnon coupling and magnon-mediated spin-spin interactions. *Phys. Rev. Lett.*, 125:247702, Dec 2020.

[142] Avinash Rustagi, Iacopo Bertelli, Toeno van der Sar, and Pramey Upadhyaya. Sensing chiral magnetic noise via quantum impurity relaxometry. *Phys. Rev. B*, 102:220403(R), Dec 2020.

[143] C Gonzalez-Ballestero, Toeno van der Sar, and O Romero-Isart. Towards a quantum interface between spin waves and paramagnetic spin baths. *arXiv:2012.00540*, 2020.

[144] Derek S. Wang, Tomáš Neuman, and Prineha Narang. Spin emitters beyond the point dipole approximation in nanomagnonic cavities. *J. Phys. Chem. C*, 125(11):6222–6228, 2021.

[145] Abhishek Bharatbhai Solanki, Simeon I Bogdanov, Avinash Rustagi, Neil R Dilley, Tingting Shen, Mohammad Mushfiqur Rahman, Wenqi Tong, Punyashloka Debashis,

Zhihong Chen, Joerg Appenzeller, et al. Electric field control of interaction between magnons and quantum spin defects. *arXiv:2012.01497*, 2020.

[146] Toeno Van der Sar, Francesco Casola, Ronald Walsworth, and Amir Yacoby. Nanometre-scale probing of spin waves using single electron spins. *Nature communications*, 6:7886, 2015.

[147] C. S. Wolfe, S. A. Manuilov, C. M. Purser, R. Teeling-Smith, C. Dubs, P. C. Hammel, and V. P. Bhallamudi. Spatially resolved detection of complex ferromagnetic dynamics using optically detected nitrogen-vacancy spins. *Appl. Phys. Lett.*, 108(23):232409, 2016.

[148] B A Kalinikos and A N Slavin. Theory of dipole-exchange spin wave spectrum for ferromagnetic films with mixed exchange boundary conditions. *J. Phys. C: Solid State Phys.*, 19(35):7013–7033, dec 1986.

[149] Daniel D Stancil and Anil Prabhakar. *Spin Waves*, volume 5. Springer, 2009.

[150] A. A. Serga, A. V. Chumak, and B. Hillebrands. YIG magnonics. *J. Phys. D: Appl. Phys.*, 43(26):264002, 2010.

[151] J. H. P. Colpa. Diagonalization of the quadratic boson hamiltonian. *Physica A: Stat. Mech. Appl.*, 93(3-4):327–353, 1978.

[152] T. M. Nguyen and M. G. Cottam. Spectral intensities and frequencies of spin waves in ferromagnetic cylinders: Application to nickel nanowires. *Phys. Rev. B*, 72:224415, Dec 2005.

[153] Ryuichi Shindou, Ryo Matsumoto, Shuichi Murakami, and Jun-ichiro Ohe. Topological chiral magnonic edge mode in a magnonic crystal. *Phys. Rev. B*, 87:174427, May 2013.

[154] Q. Wang, B. Heinz, R. Verba, M. Kewenig, P. Pirro, M. Schneider, T. Meyer, B. Lägel,

C. Dubs, T. Brächer, et al. Spin pinning and spin-wave dispersion in nanoscopic ferromagnetic waveguides. *Phys. Rev. Lett.*, 122:247202, Jun 2019.

[155] Sergey Bravyi, David P. DiVincenzo, and Daniel Loss. Schrieffer-Wolff transformation for quantum many-body systems. *Ann. Phys.*, 326(10):2793–2826, 2011.

[156] G. Vidal and R. F. Werner. Computable measure of entanglement. *Phys. Rev. A*, 65:032314, Feb 2002.

[157] F. Dolde, H. Fedder, M. W. Doherty, T. Nöbauer, F. Rempp, G. Balasubramanian, T. Wolf, F. Reinhard, L. C. L. Hollenberg, F. Jelezko, et al. Electric-field sensing using single diamond spins. *Nat. Phys.*, 7(6):459–463, 2011.

[158] J. Teissier, A. Barfuss, P. Appel, E. Neu, and P. Maletinsky. Strain coupling of a nitrogen-vacancy center spin to a diamond mechanical oscillator. *Phys. Rev. Lett.*, 113:020503, Jul 2014.

[159] Yutaka Tabuchi, Seiichiro Ishino, Toyofumi Ishikawa, Rekishu Yamazaki, Koji Usami, and Yasunobu Nakamura. Hybridizing ferromagnetic magnons and microwave photons in the quantum limit. *Phys. Rev. Lett.*, 113:083603, Aug 2014.

[160] Kenichi Ohno, F. Joseph Heremans, Lee C. Bassett, Bryan A. Myers, David M. Toyli, Ania C. Bleszynski Jayich, Christopher J. Palmstrøm, and David D. Awschalom. Engineering shallow spins in diamond with nitrogen delta-doping. *Appl. Phys. Lett.*, 101(8):082413, 2012.

[161] Jean-Michel Raimond and Serge Haroche. Exploring the quantum. *Oxford University Press*, 82:86, 2006.

[162] Mika A. Sillanpää, Jae I. Park, and Raymond W. Simmonds. Coherent quantum state storage and transfer between two phase qubits via a resonant cavity. *Nature*, 449(7161):438–442, 2007.

[163] Tom Manovitz, Amit Rotem, Ravid Shaniv, Itsik Cohen, Yotam Shapira, Nitzan Akerman, Alex Retzker, and Roee Ozeri. Fast dynamical decoupling of the Mølmer-Sørensen entangling gate. *Phys. Rev. Lett.*, 119:220505, Nov 2017.

[164] C. Leroux, L. C. G. Govia, and A. A. Clerk. Enhancing cavity quantum electrodynamics via antisqueezing: Synthetic ultrastrong coupling. *Phys. Rev. Lett.*, 120:093602, Mar 2018.

[165] William D. Oliver, Yang Yu, Janice C. Lee, Karl K. Berggren, Leonid S. Levitov, and Terry P. Orlando. Mach-Zehnder interferometry in a strongly driven superconducting qubit. *Science*, 310(5754):1653–1657, 2005.

[166] Jing Xu, Changchun Zhong, Xu Han, Dafei Jin, Liang Jiang, and Xufeng Zhang. Floquet cavity electromagnonics. *Phys. Rev. Lett.*, 125:237201, Dec 2020.

[167] G. Lindblad. On the generators of quantum dynamical semigroups. *Commun. Math. Phys.*, 48(2):119–130, 1976.

[168] Ryszard Horodecki, Pawel Horodecki, and Michal Horodecki. Violating Bell inequality by mixed spin-$\frac{1}{2}$ states: Necessary and sufficient condition. *Physics Lett. A*, 200(5):340–344, 1995.

[169] Karol Bartkiewicz, Bohdan Horst, Karel Lemr, and Adam Miranowicz. Entanglement estimation from Bell inequality violation. *Phys. Rev. A*, 88:052105, Nov 2013.

[170] Michael A Nielsen. A simple formula for the average gate fidelity of a quantum dynamical operation. *Phys. Lett. A*, 303(4):249–252, 2002.

[171] Dany Lachance-Quirion, Samuel Piotr Wolski, Yutaka Tabuchi, Shingo Kono, Koji Usami, and Yasunobu Nakamura. Entanglement-based single-shot detection of a single magnon with a superconducting qubit. *Science*, 367(6476):425–428, 2020.

[172] R. E. Evans, M. K. Bhaskar, D. D. Sukachev, C. T. Nguyen, A. Sipahigil, M. J. Burek, B. Machielse, G. H. Zhang, A. S. Zibrov, E. Bielejec, et al. Photon-mediated interactions between quantum emitters in a diamond nanocavity. *Science*, 362(6415):662–665, 2018.

[173] Jonas N. Becker, Benjamin Pingault, David Groß, Mustafa Gündoğan, Nadezhda Kukharchyk, Matthew Markham, Andrew Edmonds, Mete Atatüre, Pavel Bushev, and Christoph Becher. All-optical control of the silicon-vacancy spin in diamond at millikelvin temperatures. *Phys. Rev. Lett.*, 120:053603, Jan 2018.

[174] Manish Kumar Singh, Abhinav Prakash, Gary Wolfowicz, Jianguo Wen, Yizhong Huang, Tijana Rajh, David D Awschalom, Tian Zhong, and Supratik Guha. Epitaxial Er-doped Y_2O_3 on silicon for quantum coherent devices. *APL Materials*, 8(3):031111, 2020.

[175] Vikas K. Sewani, Rainer J. Stöhr, Roman Kolesov, Hyma H. Vallabhapurapu, Tobias Simmet, Andrea Morello, and Arne Laucht. Spin thermometry and spin relaxation of optically detected Cr^{3+} ions in ruby Al_2O_3. *Phys. Rev. B*, 102:104114, Sep 2020.

[176] S. Kosen, A. F. van Loo, D. A. Bozhko, L. Mihalceanu, and A. D. Karenowska. Microwave magnon damping in YIG films at millikelvin temperatures. *APL Materials*, 7(10):101120, 2019.

[177] David D Awschalom, C H R Du, Rui He, F J Heremans, Axel Hoffmann, J T Hou, Hidekazu Kurebayashi, Yi Li, Luqiao Liu, Valentine Novosad, et al. Quantum engineering with hybrid magnonics systems and materials. *arXiv:2102.03222*, 2021.

[178] C. L. Jermain, S. V. Aradhya, N. D. Reynolds, R. A. Buhrman, J. T. Brangham, M. R. Page, P. C. Hammel, F. Y. Yang, and D. C. Ralph. Increased low-temperature damping in yttrium iron garnet thin films. *Phys. Rev. B*, 95:174411, May 2017.

[179] Christoph Hauser, Tim Richter, Nico Homonnay, Christian Eisenschmidt, Mohammad Qaid, Hakan Deniz, Dietrich Hesse, Maciej Sawicki, Stefan G. Ebbinghaus, and Georg Schmidt. Yttrium iron garnet thin films with very low damping obtained by recrystallization of amorphous material. *Sci. Rep.*, 6(1):20827, 2016.

[180] Alexander Altland and Ben D Simons. *Condensed matter field theory*. Cambridge university press, 2010.

[181] Rep Kubo. The fluctuation-dissipation theorem. *Reports on progress in physics*, 29(1):255, 1966.

[182] Eric Lee-Wong, Ruolan Xue, Feiyang Ye, Andreas Kreisel, Toeno van Der Sar, Amir Yacoby, and Chunhui Rita Du. Nanoscale detection of magnon excitations with variable wavevectors through a quantum spin sensor. *Nano Letters*, 20(5):3284–3290, 2020.

[183] Daisuke Kikuchi, Dwi Prananto, Kunitaka Hayashi, Abdelghani Laraoui, Norikazu Mizuochi, Mutsuko Hatano, Eiji Saitoh, Yousoo Kim, Carlos A Meriles, and Toshu An. Long-distance excitation of nitrogen-vacancy centers in diamond via surface spin waves. *Applied Physics Express*, 10(10):103004, 2017.

[184] Victor S L'vov. *Wave turbulence under parametric excitation: applications to magnets*. Springer Science & Business Media, 2012.

[185] CA Emeis, LJ Oosterhoff, and Gonda De Vries. Numerical evaluation of kramers-kronig relations. *Proceedings of the Royal Society of London. Series A. Mathematical and Physical Sciences*, 297(1448):54–65, 1967.

[186] Samuel J Whiteley, Gary Wolfowicz, Christopher P Anderson, Alexandre Bourassa, He Ma, Meng Ye, Gerwin Koolstra, Kevin J Satzinger, Martin V Holt, F Joseph Heremans, et al. Spin-phonon interactions in silicon carbide addressed by gaussian acoustics. *Nature Physics*, 15(5):490–495, 2019.

[187] Y Kubo, FR Ong, Patrice Bertet, Denis Vion, V Jacques, D Zheng, A Dréau, J-F Roch, Alexia Auffèves, Fedor Jelezko, et al. Strong coupling of a spin ensemble to a superconducting resonator. *Physical review letters*, 105(14):140502, 2010.

[188] Houchen Chang, Peng Li, Wei Zhang, Tao Liu, Axel Hoffmann, Longjiang Deng, and Mingzhong Wu. Nanometer-thick yttrium iron garnet films with extremely low damping. *IEEE Magnetics Letters*, 5:1–4, 2014.